STUDIES OF TURBULENCE STRUCTURE USING WELL-RESOLVED SIMULATIONS WITH AND WITHOUT EFFECTS OF A MAGNETIC FIELD

A Dissertation
Presented to
The Academic Faculty

By

X.M. Zhai

In Partial Fulfillment
of the Requirements for the Degree
Doctor of Philosophy in the
School of Aerospace Engineering

Georgia Institute of Technology

May 2019

STUDIES OF TURBULENCE STRUCTURE USING WELL-RESOLVED SIMULATIONS WITH AND WITHOUT EFFECTS OF A MAGNETIC FIELD

Approved by:

Prof. P. K. Yeung, Advisor
Schools of Aerospace Engineering and Mechanical Engineering
Georgia Institute of Technology

Prof. Katepalli R. Sreenivasan
Tandon School of Engineering, Graduate School of Arts and Sciences, and Courant Institute of Mathematical Sciences
New York University

Prof. Joseph Oefelein
School of Aerospace Engineering
Georgia Institute of Technology

Prof. Devesh Ranjan
Schools of Mechanical Engineering and Aerospace Engineering
Georgia Institute of Technology

Prof. John Wise
School of Physics
Georgia Institute of Technology

Date Approved: December 10, 2018

The path to the truth is a long way to go, I shall search high and low.

Yuan QU, c.340-278 BC, poet and idealist

To my beloved parents, Wenshang Zhai and Pan Guo

ACKNOWLEDGEMENTS

This work was supported by Grants ACI-1036170 and 1640771 under the Petascale Resource Allocations Program, and Grant CBET-1510749 under the Fluid Dynamics Program, both funded by the National Science Foundation (NSF). The computations and data analyses reported in this thesis were primarily performed using BlueWaters at the National Center for Supercomputing Applications (NCSA) funded by NSF in the University of Illinois at Urbana-Champaign, and Stampede1 and 2 at the Texas Advanced Computation Center (TACC) in the University of Texas at Austin under the XSEDE program supported by NSF. The supercomputing resources provided by the Argonne Leadership Computing Facility in the Argonne National Lab, the National Institute for Computational Sciences (NICS) and the National Energy Research Scientific Computing Center (NERSC) are also acknowledged.

I would like to express my gratitude to everyone whose help of various kinds has made this work possible. First I would like to thank my Ph.D. advisor Prof. P. K. Yeung, for his careful supervision and constant support over the years. From him I learned to set ambitious goals, diligently work towards them and persevere through hard times. Most importantly I picked up the scientific attitude as demonstrated by him everyday: that is to embrace a research topic passionately, to tackle a science problem with curiosity and rigor, and to always scrutinize the results in the pursuit of a thorough understanding. This scientific attitude that Prof. Yeung instilled in me will greatly benefit my career in the long run. I am also grateful to him for connecting me to some of the best minds in the research field, most notably Prof. K. R. Sreenivasan who also serves in the thesis committee. I am privileged to have spent a total of five months to work with him directly at the New York University, and I thank him for his care and hospitality during my stay. It is also within those periods of time that contents in chapter three of the thesis progressed to completion. One important aspect that I learned from him is to ask the right questions that touch the essence of a problem right away. This unconscious teaching from him will have a positive impact on me. The time and service from the other committee members, Professors Joseph Oefelein, Devesh Ranjan and John Wise are also gratefully acknowledged. I am indebted to them for their encouragement and help in my Ph.D. journey.

Over the years I have also benefited from the collaborations and interactions with other people

in the research and supercomputing community. I spent a wonderful summer in 2015 with Dr. Susan Kurien at the New Mexico Consortium, and I thank her for the support and the opportunity to work on topics outside of my thesis and get the results published. I am also grateful to the consultants at the supercomputer centers whose help is always quick and effective. In particular, I thank Drs. Jing Li, Rob Sisneros, David Semeraro at NCSA for their help with the visualization work presented in the thesis.

I have had a pleasant time at Georgia Tech, and I thank Prof. Lakshmi Sankar who granted me admission in the first place. I also appreciate the kind help of Profs. Jeff Jagoda and Vigor Yang in working out funding opportunities in my early years. Special thanks to the lab mates, Dr. Kartik Iyer, Dr. Dhawal Buaria, Dr. Matthew Clay, Jacob Sebastian, Mer-Win Cheong, Kiran Ravikumar and Bichuan Mo, for the interesting discussions and the help with everything. Over the years I have never felt lonely, thanks to my friends at Tech and the alumni from my undergraduate university of the Hong Kong University of Science and Technology (HKUST). As the local host of the HKUST alumni group supported by the Development and Alumni Office at HKUST and assisted by fellow alumni, I enjoy meeting new friends from HKUST every semester.

Most importantly, I would like to thank my family, especially my parents who stand firmly behind me and endure all it takes to support my studies in Hong Kong, and eventually the completion of a doctoral study in the United States. As the first generation college students at their times, their vision and emphasis on education have played a major part in shaping who I am today. I would also like to thank my girlfriend, Ms. Chong Zhou, who brings much happiness to my life. Since she will soon become a Ph.D. in computational fluid dynamics, we will for sure talk about turbulence for a long long time.

TABLE OF CONTENTS

Acknowledgments v

List of Tables xi

List of Figures xiii

Chapter 1: Introduction 1

1.1 Background and Motivation 1

1.2 Objectives and Outline 7

Chapter 2: Governing Equations and Direct Numerical Simulations 9

2.1 Velocity field in isotropic turbulence and numerical approach 9

2.2 Parallel implementations and formation of subcubes 12

2.3 Velocity and scalar field in low-R_m MHD turbulence 16

Chapter 3: Structure of small-scales in isotropic turbulence 19

3.1 Resolution effects on the structures of extreme events 19

3.1.1 Introduction of past results on the extreme events 19

3.1.2 New visualization results at improved temporal/spatial resolution 24

3.1.3 Summary of the resolution effects on the extreme events 32

3.2 Sign oscillation characteristics in the small-scales 35

3.2.1 Mathematical background and computational formulation 36

3.2.2 Results of cancellation exponents in isotropic turbulence 39

3.2.3 Cancellation exponent in low-R_m MHD turbulence 44

3.2.4 summary of sign oscillations in the small-scales 47

Chapter 4: Turbulence structure subject to a magnetic field 49

4.1 Introduction 49

4.2 Quantities used to examine anisotropy 52

4.3 Initial conditions and domain aspect ratio 53

4.4 Anisotropy Development Under a Magnetic Field 59

4.4.1 Reynolds stress budget and anisotropy tensor 60

4.4.2 Small scales and velocity gradient statistics 61

4.4.3 Anisotropy in spectral space 67

4.5 Effects of the Magnetic Interaction Parameter 75

4.6 Summary 78

Chapter 5: Relaxation of strained MHD turbulence 83

5.1 Introduction 83

5.2 Simulation set up and parameters 83

5.3 Anisotropy development 87

5.3.1 Results of strained MHD turbulence when the magnetic field is parallel to the direction of extensive strain 87

5.3.2 Results of strained MHD turbulence when the magnetic field is perpendicular to the direction of extensive strain 93

5.4 Summary 96

Chapter 6: Passive scalar mixing in MHD turbulence 98

6.1 Introduction 98

6.2 Simulation set up and parameters 99

6.3 Scalar mixing in MHD turbulence without a mean scalar gradient 101

6.4 Scalar mixing in MHD turbulence with a uniform mean scalar gradient parallel to the magnetic field 102

6.5 Summary 109

Chapter 7: Conclusions and further work 110

7.1 Summary of the main conclusions 110

7.1.1 Resolution effects on the structures of extreme events 110

7.1.2 Sign oscillation characteristics in the small-scales 111

7.1.3 Turbulence structure subject to a magnetic field 111

7.1.4 Relaxation of strained MHD turbulence 112

7.1.5 Passive scalar mixing in MHD turbulence 112

7.2 Future work 113

Appendix A: Extreme Events in Computational Turbulence 117

Appendix B: Cancellation exponents in isotropic turbulence and magnetohydrodynamic turbulence 118

Appendix C: The evolution of anisotropy in direct numerical simulations of MHD turbulence in a strong magnetic field on elongated periodic domains 119

Appendix D: Extreme events and small-scale structure in computational turbulence . . 120

Appendix E: The structure of MHD turbulence under an external magnetic field: results from simulations on elongated domains 121

Appendix F: Effects of a strong magnetic field on turbulence subjected to axisymmetric contraction. 122

Appendix G: Cancellation exponent in isotropic turbulence and MHD turbulence . . . 123

References 123

Vita 132

LIST OF TABLES

3.1 Parameters of the simulations in the study 25

3.2 Summary of visualization results at different spatial and temporal resolution. If the conventional picture that dissipation sheets wrap enstrophy filaments is observed with no sign of topological features of "chunky" structures, a "✓" is tabulated. . . 33

3.3 Data sets of isotropic turbulence used in the analysis. R_λ is the Taylor-scale Reynolds number. Spatial resolution is denoted by $k_{max}\eta$. N is the number of grid points along each side of the cubic domain. N_R denotes the number of realizations used for ensemble-averaging. 40

3.4 Cancellation exponent κ for vorticity obtained from past experiments, using 1D ($D = 1$) and 2D ($D = 2$) measurements. 42

4.1 Parameters of pre-simulations for domains of aspect ratio 8 (with shortest side fixed at 2π): viscosity, Taylor-scale Reynolds number $(R_\lambda)_b$ before the pre-simulation begins, followed by various parameters (as discussed in the text) at the end of the pre-simulation. 55

4.2 Table of parameters for production MHD simulations studied in this study. 56

4.3 Development of terms in the Reynolds stress budget and anisotropy tensor element, from 16384×2048^2 simulation with $\Lambda = 8$, $N = 1$. The data are listed at several normalized time instants (which are not uniformly spaced). 60

4.4 Skewness (μ_3) and flatness (μ_4) factors of the velocity gradients, classified according to statistical axisymmetry as referenced earlier in Chap. 4.4.2 66

5.1 Parameters for simulations where the magnetic field is parallel to the direction of extensive strain (x_1). Pre-contraction denoted by subscript or superscript a while post-contraction denoted by subscript or superscript b. R_λ^0 is the Taylor-scale Reynolds number at the start of the pre-simulation. In the first block, the number of grid points and grid metric factors are N_α and β_α^b. In the second block, $L_\alpha = 2\pi/\beta_\alpha$ is the domain size. l_{11} and l_{22} are the longitudinal integral length scales in the x_1 and x_2 directions, while l_{21} is the transverse integral length scales in the x_1 direction. Grid spacing is $\Delta_\alpha = 2\pi/N_\alpha$ and η is the Kolmogorov length scales. The third block lists the post to pre-contraction ratios of turbulence kinetic energy K, viscous dissipation rate ϵ and mean-square of velocity $\langle u_\alpha^2 \rangle$. The fourth block shows ratios of variances of velocity gradient $u_{i,j} = \partial u_i/\partial x_j$ and the skewness (S) and flatness (F) of the longitudinal velocity gradients. 84

5.2 Parameters for simulations where the magnetic field is parallel to the direction of compressive strain (x_3). Pre-contraction denoted by subscript or superscript a while post-contraction denoted by subscript or superscript b. R_λ^0 is the Taylor-scale Reynolds number at the start of the pre-simulation. In the first block, the number of grid points and grid metric factors are N_α and β_α^b. In the second block, $L_\alpha = 2\pi/\beta_\alpha$ is the domain size. l_{11} and l_{22} are the longitudinal integral length scales in the x_1 and x_2 directions, while l_{21} is the transverse integral length scales in the x_1 direction. Grid spacing is $\Delta_\alpha = 2\pi/N_\alpha$ and η is the Kolmogorov length scales. The third block lists the post to pre-contraction ratios of turbulence kinetic energy K, viscous dissipation rate ϵ and mean-square of velocity $\langle u_\alpha^2 \rangle$. The fourth block shows ratios of variances of velocity gradient $u_{i,j} = \partial u_i/\partial x_j$ and the skewness (S) and flatness (F) of the longitudinal velocity gradients. 85

LIST OF FIGURES

2.1 Mapping the N^3 domain into a 2D computational grid with $P = M_1 \times M_2$ parallel processes. In this example $M_1 = M_2 = 4$. 13

2.2 Illustration of the formation of subcubes (enclosed in red dashed lines) from a 2D domain decomposition. 15

3.1 Ensemble-averaged PDFs of normalized dissipation (red) and enstrophy (blue) from 8192^3 simulation at $R_\lambda \approx 1300$, with $k_{max}\eta \approx 2$. Inset shows data for 0 to 16 times of the mean value. Dashed curves in the inset show positive halves of Gaussian distributions with equal variances. 20

3.2 Perspective views of 3D contour surfaces of dissipation (red) and enstrophy (cyan) extracted from a randomly chosen (but representative) 8192^3 instantaneous snapshot, at different thresholds (in multiples of mean values) and for different sized subcubes: (a) 10, 768^3; (b) 30, 256^3; (c) 100, 256^3; (d), (e) and (f): 300, 51^3; (g) 600, 51^3; (h) 4800, 31^3; (i) 9600, 31^3. Both dissipation and enstrophy are shown in all frames but (d) and (e). 22

3.3 Color contours based on three instantaneous snapshots (frames a, b, c) from the 8192^3 simulation at $R_\lambda \approx 1300$, contrasted with data from (d) 2048^3 simulation at $R_\lambda \approx 400$. The contour thresholds used were 300 for data at $R_\lambda \approx 1300$, and 70 for data at $R_\lambda \approx 400$. The sub-cubes are 51^3 in extent in frames (a), (b) and (c), 31^3 in (d). 23

3.4 Overlaid contour plots of normalized dissipation $\epsilon/\langle\epsilon\rangle$ (red) and enstrophy $\Omega/\langle\Omega\rangle$ (cyan). Contour levels of $\epsilon/\langle\epsilon\rangle = 150$, $\Omega/\langle\Omega\rangle = 300$. LHS at original spatial resolution of $k_{max}\eta \approx 2.8$; RHS at truncated resolution of $k_{max}\eta \approx 1.4$. Zoomed-in region of most extreme enstrophy at $k_{max}\eta \approx 2.8$. $R_\lambda = 390$, 2048^3, $k_{max}\eta \approx 2.8$, $C = 0.15$. 26

3.5 Contour levels of $\epsilon/\langle\epsilon\rangle = 150$ (red), $\Omega/\langle\Omega\rangle = 300$ (cyan). LHS at original spatial resolution of $k_{max}\eta \approx 2.8$; RHS at truncated resolution of $k_{max}\eta \approx 1.4$. Zoomed-in region of most extreme dissipation at $k_{max}\eta \approx 2.8$. $R_\lambda = 390$, 2048^3, $k_{max}\eta \approx 2.8$, $C = 0.15$. 27

3.6 Contour levels of $\epsilon/\langle\epsilon\rangle = 150$ (red), $\Omega/\langle\Omega\rangle = 300$ (cyan). LHS at original spatial resolution of $k_{max}\eta \approx 2.8$; RHS at truncated resolution of $k_{max}\eta \approx 1.4$. $R_\lambda = 390$, 2048^3, $k_{max}\eta \approx 2.8$, $C = 0.6$. 27

3.7 All at original spatial resolution of $k_{max}\eta \approx 2.8$. The same contour level is used for dissipation $\epsilon/\langle\epsilon\rangle$ (red) and enstrophy $\Omega/\langle\Omega\rangle$ (cyan), at 300 (left), 600 (middle) and 1200 (right). $R_\lambda = 390$, 2048^3, $k_{max}\eta \approx 2.8$, $C = 0.6$. 27

3.8 Contour levels of $\epsilon/\langle\epsilon\rangle = 150$ (red), $\Omega/\langle\Omega\rangle = 300$ (cyan). Spatial resolution of $k_{max}\eta \approx 5.4$ (left), and truncated to 2.8 (middle) and 1.4 (right). Zoomed-in region of most extreme enstrophy at $k_{max}\eta \approx 5.4$. $R_\lambda = 390$, 4096^3, $k_{max}\eta \approx 5.4$, $C = 0.15$. 28

3.9 Contour levels of $\epsilon/\langle\epsilon\rangle = 150$ (red), $\Omega/\langle\Omega\rangle = 300$ (cyan). Spatial resolution of $k_{max}\eta \approx 5.4$ (left), and truncated to 2.8 (middle) and 1.4 (right). Zoomed-in region of most extreme dissipation at $k_{max}\eta \approx 5.4$. $R_\lambda = 390$, 4096^3, $k_{max}\eta \approx 5.4$, $C = 0.15$. 28

3.10 Contour levels of $\epsilon/\langle\epsilon\rangle = 150$ (red), $\Omega/\langle\Omega\rangle = 300$ (cyan). Spatial resolution of $k_{max}\eta \approx 5.4$ (left), and truncated to 2.8 (middle) and 1.4 (right). Zoomed-in region of most extreme enstrophy at $k_{max}\eta \approx 5.4$. $R_\lambda = 390$, 4096^3, $k_{max}\eta \approx 5.4$, $C = 0.6$. 29

3.11 Contour levels of $\epsilon/\langle\epsilon\rangle = 150$ (red), $\Omega/\langle\Omega\rangle = 300$ (cyan). Spatial resolution of $k_{max}\eta \approx 5.4$ (left), and truncated to 2.8 (middle) and 1.4 (right). Zoomed-in region of most extreme dissipation at $k_{max}\eta \approx 5.4$. $R_\lambda = 390$, 4096^3, $k_{max}\eta \approx 5.4$, $C = 0.6$. 29

3.12 Contour levels of $\epsilon/\langle\epsilon\rangle = 150$ (red), $\Omega/\langle\Omega\rangle = 300$ (cyan). LHS at original spatial resolution of $k_{max}\eta \approx 2.8$; RHS at truncated resolution of $k_{max}\eta \approx 1.4$. Zoomed-in region of most extreme enstrophy at $k_{max}\eta \approx 2.8$. $R_\lambda = 650$, 4096^3, $k_{max}\eta \approx 2.8$, $C = 0.15$. 30

3.13 Contour levels of $\epsilon/\langle\epsilon\rangle = 150$ (red), $\Omega/\langle\Omega\rangle = 300$ (cyan). LHS at original spatial resolution of $k_{max}\eta \approx 2.8$; RHS at truncated resolution of $k_{max}\eta \approx 1.4$. Zoomed-in region of most extreme dissipation at $k_{max}\eta \approx 2.8$. $R_\lambda = 650$, 4096^3, $k_{max}\eta \approx 2.8$, $C = 0.15$. 30

3.14 The same as before, but use only one set of contour levels $\epsilon/\langle\epsilon\rangle = 150$ (red), $\Omega/\langle\Omega\rangle = 300$ (cyan). $R_\lambda = 650$, 4096^3, $k_{max}\eta \approx 2.8$, $C = 0.6$. 31

3.15 At the original resolution of $k_{max}\eta \approx 2.8$, but with the same contour level for dissipation $\epsilon/\langle\epsilon\rangle$ (red) and enstrophy $\Omega/\langle\Omega\rangle$ (cyan), at 300, 600,1200 and 12000. $R_\lambda = 650$, 4096^3, $k_{max}\eta \approx 2.8$, $C = 0.6$. 31

3.16 Contour levels of $\epsilon/\langle\epsilon\rangle = 150$, $\Omega/\langle\Omega\rangle = 300$ (top); $\epsilon/\langle\epsilon\rangle = 300$, $\Omega/\langle\Omega\rangle = 600$ (middle row); $\epsilon/\langle\epsilon\rangle = 600$, $\Omega/\langle\Omega\rangle = 1200$ (bottom); Spatial resolution of $k_{max}\eta \approx 5.4$ (left), and truncated to 2.8 (center) and 1.4 (right). The most extreme enstrophy (cyan) and dissipation (red) are roughly co-located at $k_{max}\eta \approx 5.4$ in this simulation. $R_\lambda = 650$, 8192^3, $k_{max}\eta \approx 5.4$, $C = 0.15$. 33

3.17 Contour levels of $\epsilon/\langle\epsilon\rangle = 150$, $\Omega/\langle\Omega\rangle = 300$ (top); $\epsilon/\langle\epsilon\rangle = 300$, $\Omega/\langle\Omega\rangle = 600$ (bottom). Spatial resolution of $k_{max}\eta \approx 5.4$ (left), and truncated to 2.8 (middle) and 1.4 (right). The most extreme enstrophy (cyan) and dissipation (red) are roughly co-located at $k_{max}\eta \approx 5.4$ in this simulation. $R_\lambda = 650$, 8192^3, $k_{max}\eta \approx 5.4$, $C = 0.6$. 34

3.18 All at $k_{max}\eta \approx 5.4$, but the same contour levels of $\epsilon/\langle\epsilon\rangle = \Omega/\langle\Omega\rangle$ (from left to right) 600, 1200 and 2400. $R_\lambda = 650$, 8192^3, $k_{max}\eta \approx 5.4$, $C = 0.6$. 34

3.19 Signals of (a) a square wave with magnitude of unity; (b) a sinusoidal wave $y(x) = \sin\big((2\pi/100)x\big)$ with a period of 100; (c) a standard Wiener process (Brownian motion) where the inset shows the ratio of step-wise increment and unit step size. For brevity, (a) (b) show only a few periods of the signal. Partition functions ($\chi(l)$) of signal (a-c) are shown in (d-f). Dashed lines mark power-law behaviors. 37

3.20 Line traces of (a) longitudinal velocity gradient $\partial u/\partial x$ and (b) vorticity component $\omega_z = \partial u/\partial y - \partial v/\partial x$ from a simulation of isotropic turbulence at $R_\lambda = 400$ on a 2048^3 grid. 38

3.21 (a) Partition function and (b) cancellation exponent κ (see Eqs. 3.3 and 3) for measures of $1D$ ($\square$), $2D$ ($\triangle$) and $3D$ ($\bigcirc$). Horizontal dashed line marks $2/3$, and solid line marks 0.639 as a result of log-normal correction for intermittency with the exponent $\mu = 0.25$. Data are ensemble averaged at $R_\lambda = 650$, 4096^3. 40

3.22 Cancellation exponent κ of (a) longitudinal velocity gradients and (b) transverse velocity gradients for measures of $1D$ ($\square$), $2D$ ($\triangle$) and $3D$ ($\bigcirc$). Horizontal dashed and solid lines mark $2/3$ and 0.639, respectively, as in Fig. 3.21. Data are ensemble averaged at $R_\lambda = 650$, 4096^3. 41

3.23 Reynolds number dependence of cancellation exponents for vorticity (top row), longitudinal velocity gradients (middle row), and transverse velocity gradients (bottom row). From left to right, different columns denote measures in 1D, 2D and 3D; with Reynolds number R_λ increasing in the direction of the arrow for 140, 240, 400, 650 and 1300. Horizontal dashed and solid lines mark $2/3$ and 0.639, respectively, as in Fig. 3.21. 43

3.24 Left column: visualization of normalized enstrophy $\Omega/\langle\Omega\rangle = 5$ in MHD turbulence with the magnetic field along the x-direction (vertical); middle column: cancellation exponent of the x-component vorticity ω_x; right column: averaged cancellation exponent of ω_y and ω_z. Measures used are $1D$ ($\square$), $2D$ ($\triangle$) and $3D$ ($\bigcirc$). From top to bottom, $t/(\mathcal{L}/\mathcal{U}) = 0$, 12, 24 and 36. 46

3.25 PDFs of the length of intervals over which the signal retains the same sign in one dimension. Solid curves denote longitudinal velocity gradients and dashed curves denote transverse velocity gradients. Arrows point in the direction of increasing R_λ : 140 (red), 400 (blue) and 1300 (green). In (a) L is normalized by the domain length (L_0) while in (b) it is normalized by the Kolmogorov length scale (η). . . . 47

4.1 (a) Taylor-scale Reynolds number and (b) flatness factor of longitudinal velocity gradients in pre-simulations where $n_y = n_z = 256$, 512, 1024, 2048 (from bottom to top). With $n_x = \Lambda n_y$, results for $\Lambda = 1$ and $\Lambda = 8$ are indicated by solid lines and dashed lines respectively. The time axis (t') is normalized by initial values of K and $\langle\epsilon\rangle$ in the pre-simulation. The meanings of the circles on each curve are addressed in the text. 54

4.2 (a) Turbulence kinetic energy (K), (b) integral length scales L_{11} and L_{22} of velocity components u_1 and u_2, and (c) Reynolds stress anisotropy tensor elements (b_{11} (red), b_{22} and b_{33} (blue)) in 8192×1024^2 simulation on a $16\pi \times (2\pi)^2$ domain with $N = 1$. Time t is measured from the beginning of the pre-simulation, and the magnetic field is turned on at $t = t_0$. In (a) and (b) solid lines represent the pre-simulation (if extended), while dashed line represents MHD results. In (b) L_{11} L_{22} under the magnetic field are indicated by long and short dashed lines respectively. 57

4.3 (a) L_{11}/π, (b) $\langle J\rangle/\langle J\rangle_0$, (c) $\langle\epsilon\rangle/\langle\epsilon\rangle_0$ versus normalized time $t^* = (t - t_0)/(T_E)_0$ since when the magnetic field is turned on. Domain aspect ratio Λ increases from 1 to 64 in the direction of the arrow. Short horizontal bars in (a) mark maximum possible values for each Λ. 58

4.4 Contour plots of axisymmetric spectra of Joule dissipation (left frames) and viscous dissipation (right frames), from late-time data in simulations with three different aspect ratios, corresponding to grid resolutions 256^3, 2048×256^2 and 16384×256^2, with $N = 1$ and $(R_\lambda)_0 = 21$. 59

4.5 Development of anisotropy of velocity gradient and vorticity variances, for the same simulation as in Table 4.3. (a) $\langle u^2_{\parallel,\parallel}\rangle$ (•), $\langle u^2_{\parallel,\perp}\rangle$ (■), $\langle u^2_{\perp,\parallel}\rangle$ (△), $\langle(u^L_{\perp,\perp})^2\rangle$ (□), $\langle(u^T_{\perp,\perp})^2\rangle$ (○), all normalized by $\langle\epsilon\rangle/15\nu$; (b) Ratios between variance of velocity gradients: $\langle u^2_{\parallel,\parallel}\rangle/\langle(u^L_{\perp,\perp})^2\rangle$ (•), $\langle u^2_{\perp,\parallel}\rangle/\langle u^2_{\parallel,\perp}\rangle$ (■), for $2\langle u^2_{\parallel,\parallel}\rangle/\langle u^2_{\parallel,\perp}\rangle$ (△), $\langle u^2_{\parallel,\perp}\rangle/\langle(u^T_{\perp,\perp})^2\rangle$ (□), $2\langle(u^L_{\perp,\perp})^2\rangle/\langle(u^T_{\perp,\perp})^2\rangle$ (○); (c) $\langle\omega^2_\parallel\rangle$ (solid lines) and $\langle\omega^2_\perp\rangle$ (dashed lines), both normalized by $\langle\omega_i\omega_i\rangle$. 62

4.6 Development of anisotropy of velocity gradient and vorticity variances under a magnetic field, on domains with aspect ratio $\Lambda = 1$ (red), 8 (green) and 64 (blue) with the shortest dimension having 256 grid points. (a) $\langle u^2_{\perp,\parallel}\rangle$ (△), $\langle(u^T_{\perp,\perp})^2\rangle$ (○), all normalized by $\langle\epsilon\rangle/15\nu$; (b) Ratios between variance of velocity gradients: $2\langle u^2_{\parallel,\parallel}\rangle/\langle u^2_{\parallel,\perp}\rangle$ (△), $\langle u^2_{\parallel,\perp}\rangle/\langle(u^T_{\parallel,\perp})^2\rangle$ (□), $2\langle(u^L_{\perp,\perp})^2\rangle/\langle(u^T_{\perp,\perp})^2\rangle$ (○); (c) $\langle\omega^2_\parallel\rangle$ (solid lines) and $\langle\omega^2_\perp\rangle$ (dashed lines), both normalized by $\langle\omega_i\omega_i\rangle$. 63

4.7 Visualizations of normalized enstrophy $\Omega/\langle\Omega\rangle$ showing development of coherent vortical structures in MHD turbulence in domains of different aspect ratios. The brighest red and darkest blue represent $\Omega/\langle\Omega\rangle > 10$ and < 0.05 respectively. Each frame is a pair of 2 images in $y-z$ (square, on left) and $x-z$ planes (rectangle, on right.) Frames (a) and (b) are from 2048^3 grid with $\Lambda = 1$, with $N = 1$, at $t^* = 12.58$ and 41.52 respectively; while frames (c), (d), (e) are from 16384×2048^2 grid with $\Lambda = 8$, with $N = 1$, at $t^* = 0$, 12.58 and 41.52. Frames (f) and (g) are similar to (d) and (e), but from simulation at $N = 8$. 64

4.8 (a) Evolution of $\epsilon_\parallel/\langle\omega_\perp^2\rangle$ (△), $\epsilon_\perp/\langle\omega_\parallel^2\rangle$ (◯) and $(\epsilon_\parallel/\epsilon_\perp)(\langle\omega_\parallel^2\rangle/\langle\omega_\perp^2\rangle)$ (□). Horizontal dashed lines are at values 0.5 and 2.0. (b) Anisotropy tensor elements $d_\parallel = \epsilon_\parallel/(2\epsilon) - 1/3$ for dissipation (▲), $v_\parallel = \langle\Omega_\parallel\rangle/\langle\Omega\rangle - 1/3$ for vorticity covariance (•), and their sum $d_\parallel + v_\parallel$ (dashed line). 65

4.9 Compensated 1D spectra $k_1E_{\alpha\alpha}(k_1)$: solid and dashed lines for $\alpha = 1$ and $\alpha = 2$ respectively. From (a) to (c): at $t^* = 0$, 2.06, 26.25, normalized by the instantaneous kinetic energy. 68

4.10 Terms contributing to the evolution of 1D compensated spectra: (a), (c) and (e) for $d\big(k_1E_{11}(k_1)\big)/dt$, (b), (d) and (f) for $d\big(k_1E_{22}(k_1)\big)/dt$, at normalized times (from top to bottom) $t^* = 0$, 2.06, 26.25. Different curves denote time rate of change (black), viscous dissipation (red), Joule dissipation (blue), non-linear transfer (green) and pressure strain correlation (magenta). All are normalized by the instantaneous viscous dissipation. 69

4.11 Evolution of (left) compensated 1D transfer spectra of (a) $k_1T_{11}(k_1)$, (c) $k_1T_{22}(k_1)$, and (right) compensated radial transfer spectra of (b) $k_rT_{11}(k_r)$, (d) $k_rT_{22}(k_r)$. All the spectra shown are normalized by instantaneous viscous dissipation. Lines in red, green, blue and black denote times $t^* = 0$, 2.06, 6.86 and 26.25 respectively. . 71

4.12 Contours of axisymmetric energy spectrum $E_A(k_1, k_r)$ at times (from left to right) $t^* = 2.06$, 6.86, 26.25. Contour levels are set at logarithmically-spaced intervals, decreasing by successive factors of 10 outwards from near the origin. (Note the diffeernces among different frames in the upper limits of the coordinate axes shown. In frame (a) maximum values of both k_1 and k_r are both 960.) 72

4.13 Axisymmetric spectra of TKE. From left to right, $t^* = 0$, 2.06, 6.86, 26.25. 72

4.14 Axisymmetric spectra of the terms in the energy budget equation. From left to right: (negative of) rate of change, viscous dissipation, Joule dissipation, and positive values of spectral transfer. From top to bottom $t^* = 0$, 2.06, 6.86, 26.25. 74

4.15 Evolution of (a) normalized integral length scale and (b) Reynolds stress anisotropy tensor element, in the direction of the magnetic field, with arrows pointing in the direction of increasing N (0.5, 1, 2, 4, 8, . . . , 256). In (a), sloping dashed line has slope of 0.5, horizontal dashed lines are at heights 0.25 and 0.5. In (b), solid circles indicate time instants when L_{11} exceeds 1/4 of $\mathcal{L}_{0x}$ as seen in (a). The upper dashed line is at height 1/6. 76

4.16 Evolution of (a) $\langle u^2_{\parallel,\parallel}\rangle/\langle (u^L_{\perp,\perp})^2\rangle$, (b) $\langle (u^L_{\perp,\perp})^2\rangle/\langle (u^T_{\perp,\perp})^2\rangle$. Arrows point in the direction of increasing N $(1, 2, 4, 8)$, for the same 16384×2048^2 domain of $\Lambda = 8$. In (b) the horizontal dashed line denotes $1/3$, which is the value in 2D isotropic turbulence. 77

4.17 Terms contributing to the evolution of 1D compensated spectra of: $d\big(k_1 E_{11}(k_1)\big)/dt$: (a) $t^* = 0$, with $N = 1$; (b) $t^* = 3.29$, with $N = 1$; (c) $t^* = 0$, with $N = 8$; (d) $t^* = 3.29$, with $N = 8$. Different curves denote time rate of change (black), viscous dissipation (red), Joule dissipation (blue), non-linear transfer (green) and pressure strain correlation (magenta). All curves are normalized by the instantaneous viscous dissipation. 78

4.18 Axisymmetric spectra of the terms in the energy budget equation at $N = 8$. From left to right: (negative of) rate of change, viscous dissipation, Joule dissipation, and positive values of spectral transfer. Top row for results at $t^* = 0$, bottom row for $t^* = 26.25$. 79

5.1 Evolution of the averaged transverse integral length scales l_{21} and l_{31} in the x_1 direction. Magnetic interaction parameter $N = 0$ (red), 1 (green) and 4 (blue). The horizontal solid line denotes $1/4$ of the domain size in the x_1 direction at 4π. Results are taken from run 5 in Table 5.1 of 1024^3 grids on a $16\pi \times (4\sqrt{2}\pi)^2$ domain. 88

5.2 Evolution of (a) turbulence kinetic energy K normalized by the post-contraction value (denoted by K_b), (b) viscous dissipation rate $\langle\epsilon\rangle$ and (c) Joule dissipation rate $\langle J\rangle$. Magnetic interaction parameter $N = 0$ (red), 1 (green) and 4 (blue). Results are taken from run 5 in Table 5.1 of 1024^3 grids on a $16\pi \times (4\sqrt{2}\pi)^2$ domain. . . 89

5.3 Evolution of (a) components of the Reynolds stress anisotropy tensor, and (b) second and third invariants of the Reynolds stress anisotropy tensor. Magnetic interaction parameter $N = 0$ (red), 1 (green) and 4 (blue). In (a) solid and dashed curves denote b_{11} and b_{22} and in (b) solid and dashed curves denote η and $-\xi$. Results are taken from run 5 in Table 5.1 of 1024^3 grids on a $16\pi \times (4\sqrt{2}\pi)^2$ domain. 89

5.4 Evolution of components of the vorticity covariance tensor parallel (solid) and perpendicular (dashed) to the magnetic field direction. Magnetic interaction parameter $N = 0$ (red), 1 (green) and 4 (blue). Results are taken from run 5 in Table 5.1 of 1024^3 grids on a $16\pi \times (4\sqrt{2}\pi)^2$ domain. 90

5.5 Evolution of ratios of velocity gradient variances of (a) $\langle u^2_{1,1}\rangle/\langle u^2_{1,3}\rangle$, (b) $\langle u^2_{2,1}\rangle/\langle u^2_{2,3}\rangle$, and (c) $\langle u^2_{2,2}\rangle/\langle u^2_{2,3}\rangle$. Magnetic interaction parameter $N = 0$ (red), 1 (green) and 4 (blue). The solid horizontal lines denote values expected at an isotropic state. The dashed horizontal line in (c) marks $1/3$. Results are taken from run 5 in Table 5.1 of 1024^3 grids on a $16\pi \times (4\sqrt{2}\pi)^2$ domain. 91

5.6 Evolution of the (a) skewness and (b) flatness of longitudinal velocity gradients. Solid curves for $\partial u_1/\partial x_1$ and dashed curves for $\partial u_3/\partial x_3$. Magnetic interaction parameter $N = 1$, and the Reynolds numbers ${R_\lambda}^0$ are at 39.7 (red), 67.7 (green) and 113 (blue). Results are taken from runs 5rd2, 6 and 9 in Table 5.1. 91

5.7 Evolution of ratios of velocity gradient variances of (a) $\langle u^2_{\parallel,\parallel}\rangle/\langle u^2_{\parallel,\perp}\rangle$, (b) $\langle u^2_{\perp,\parallel}\rangle/\langle {u^T_{\perp,\perp}}^2\rangle$, and (c) $\langle {u^L_{\perp,\perp}}^2\rangle/\langle {u^T_{\perp,\perp}}^2\rangle$. The solid horizontal lines denote values expected at an isotropic state. The dashed horizontal line in (c) marks $1/3$. Magnetic interaction parameter $N = 1$, and the Reynolds numbers ${R_\lambda}^0$ are at 39.7 (red), 67.7 (green) and 113 (blue). Results are taken from runs 5rd2, 6 and 9 in Table 5.1. 92

5.8 Evolution of axisymmetric energy spectra at $t/(2K/\langle\epsilon\rangle)_0 = 0$, 0.5, 2, 10, and 40 (from left to right). Results are taken rom run 9 in Table 5.1. 93

5.9 Evolution of integral length scales (a) l_{33}, (b) l_{13} and (c) l_{11}, where $L_{\alpha\alpha,\beta}$ denotes the α-th velocity component separated in the β direction. The initial Reynolds numbers ${R_\lambda}^0$ are at 39.7 (red), 67.7 (green) and 113 (blue), while magnetic interaction parameters are all at $N = 1$. The solid horizontal lines denote $1/4$ of the domain size in the corresponding direction. Results are taken from runs 1rd3, 2 and 3 in Table 5.2. 94

5.10 Anisotropy invariant map. The initial Reynolds numbers ${R_\lambda}^0$ are at 39.7 (red), 67.7 (green) and 113 (blue), while magnetic interaction parameters are all at $N = 1$. The black solid curves mark the boundary of the Lumley triangle (see discussions in the text). The middle arrows marked by R_λ points in the direction of increasing Reynolds number. The arrows on the side mark the start and end of the curves. Results are taken from runs 1rd3, 2 and 3 in Table 5.2. 94

5.11 Evolution of ratios of velocity gradient variances (a) $\langle u^2_{\parallel,\parallel}\rangle/\langle u^2_{\parallel,\perp}\rangle$, (b) $\langle u^2_{\perp,\parallel}\rangle/\langle {u^T_{\perp,\perp}}^2\rangle$, and (c) $\langle {u^L_{\perp,\perp}}^2\rangle/\langle {u^T_{\perp,\perp}}^2\rangle$, where L and T denotes longitudinal and transverse respectively. The initial Reynolds numbers ${R_\lambda}^0$ are at 39.7 (red), 67.7 (green) and 113 (blue), while magnetic interaction parameters are all at $N = 1$. The dashed horizontal line in (c) marks $1/3$. Results are taken from runs 1rd3, 2 and 3 in Table 5.2. 95

6.1 Evolution of scalar variance in the absence of a mean scalar gradient. Solid curves denote scalars with $Sc = 0.1$, and dashed curves denote scalars with $Sc = 1$. Magnetic interaction parameters are $N = 0$ (red), 1 (blue) and 4 (green). Results are taken from a 2048×256^2 grid on a $16\pi \times (2\pi)^2$ domain. 100

6.2 Relaxation of PDFs of $\phi/(\langle\phi^2\rangle)^{1/2}$ for (a) $Sc = 0.1$ (b) $Sc = 1$ from initial "double delta" shape to a distribution close to Gaussian (dashed curves). The same time instants are used at $t/\tau_\eta = 0$ (red),2 (blue),4 (green), 6 (black),8 (magenta). Results are taken from simulations at $N = 1$ on a 2048×256^2 grid. 101

6.3 Evolution of scalar gradient variances with (a) $Sc = 0.1$ (b) $Sc = 1$. Solid curves denote $\langle(\nabla_{\|}\phi)^2\rangle$ and dashed curves denote $\langle(\nabla_{\perp}\phi)^2\rangle$. Inset shows ratios of $\langle(\nabla_{\|}\phi)^2\rangle/\langle(\nabla_{\perp}\phi)^2\rangle$. Arrow points along increasing magnetic interaction parameters of $N = 0$ (red), 1 (blue) and 4 (green). Results are taken from simulations at $N = 1$ on a 2048×256^2 grid. 102

6.4 Evolution of integral length scales in the x_1 direction for (a) $Sc = 1/16$ (b) $Sc = 1$. Solid and dashed curves denote integral length scales of scalar and velocity respectively. Magnetic interaction parameter $N = 0$ (red) and $N = 1$ (blue). The horizontal solid line denotes $1/4$ of the domain size at 4π. Results are taken from 4096×512^2 grids on a $32\pi \times (4\pi)^2$ domain. 102

6.5 Evolution of averaged integral length scales in the x_2 and x_3 directions for (a) $Sc = 1/16$ (b) $Sc = 1$. Solid and dashed curves denote integral length scales of scalar and velocity respectively. Magnetic interaction parameter $N = 0$ (red) and $N = 1$ (blue). The horizontal solid line denotes $1/4$ of the domain size at $\pi/2$. Results are taken from 4096×512^2 grids on a $32\pi \times (4\pi)^2$ domain. 103

6.6 Evolution of scalar variances with (a) $Sc = 1/16$ (b) $Sc = 1$. Solid curves denote $N = 0$ and dashed curves denote $N = 1$. Results are taken from 4096×512^2 grids on a $32\pi \times (4\pi)^2$ domain. 103

6.7 Evolution of (a, b) scalar production and (c, d) scalar dissipation. The Schmidt number $Sc = 1/16$ (a, c) and $Sc = 1$ (b, d). Solid curves denote $N = 0$ and dashed curves denote $N = 1$. Results are taken from 4096×512^2 grids on a $32\pi \times (4\pi)^2$ domain. 104

6.8 Evolution of the time rate of change of scalar variance for (a) $Sc = 1/16$ and (b) $Sc = 1$. Solid curves denote $N = 0$ and dashed curves denote $N = 1$. Results are taken from 4096×512^2 grids on a $32\pi \times (4\pi)^2$ domain. 105

6.9 Evolution of the scalar gradient variances $\langle(\nabla_{\|}\phi)^2\rangle$ (solid) and $\langle(\nabla_{\perp}\phi)^2\rangle$ (dashed) where the insets show the ratio of $\langle(\nabla_{\|}\phi)^2\rangle/\langle(\nabla_{\|}\phi)^2\rangle$. Frame (a) $Sc = 1/16$ and (b) $Sc = 1$. Magnetic interaction parameter $N = 0$ (red) and $N = 1$ (blue). Results are taken from 4096×512^2 grids on a $32\pi \times (4\pi)^2$ domain. 105

6.10 Evolution of the PDFs of the normalized intermediate strain rate $\hat{\beta}$ for (a) $N = 0$ and (b) $N = 1$. In (a), curves A-D denote $t/(2K/\langle\epsilon\rangle)_0 \approx 3.76$, 12.43, 25.54 and 45.25. In (b), curves A-F denote $t/(2K/\langle\epsilon\rangle)_0 \approx 0.52$, 1.30, 3.76, 12.43, 25.54 and 45.25. Results are taken from 4096×512^2 grids on a $32\pi \times (4\pi)^2$ domain. 106

6.11 Evolution of the PDFs of directional cosines $\cos(\nabla\phi, \mathbf{e}_k)$ for $k = \alpha$, β and γ for $N = 0$, at $t/(2K/\langle\epsilon\rangle)_0$ of (a) 3.76 and (b) 45.25. Curves A-C represent eigenvectors $\mathbf{e}_\alpha$, $\mathbf{e}_\beta$, $\mathbf{e}_\gamma$ for $Sc = 1/16$, while curves D-F give corresponding data for $Sc = 1$. Results are taken from 4096×512^2 grids on a $32\pi \times (4\pi)^2$ domain. 107

6.12 Evolution of the PDFs of directional cosines $\cos(\nabla\phi, \mathbf{e}_k)$ for $k = \alpha$, β and γ for $N = 1$, at $t/(2K/\langle\epsilon\rangle)_0$ of (a) 0.52, (b) 3.76 and (c) 45.25. Curves A-C represent eigenvectors $\mathbf{e}_\alpha$, $\mathbf{e}_\beta$, $\mathbf{e}_\gamma$ for $Sc = 1/16$, while curves D-F give corresponding data for $Sc = 1$. Results are taken from 4096×512^2 grids on a $32\pi \times (4\pi)^2$ domain. . 108

SUMMARY

This thesis presents results from a large-scale computational study motivated to advance understanding of turbulence structure in isotropic turbulence as well as in magnetohydrodynamic (MHD) turbulence at low magnetic Reynolds number. Direct numerical simulations (DNS) are performed using state-of-the-art massively parallel computers with the care in the choice of the simulation parameters so that the small scales are adequately resolved and the large scales are well contained in the simulation domains. Results of isotropic turbulence provide clarifications not only on the topological features of the small scale motions that take large amplitudes, but also on the values of cancellation exponent which quantifies the sign oscillation characteristics. For topics in MHD turbulence, a central theme is the anisotropy development from initial conditions that are either isotropic, or those that contain some degree of anisotropy resulting from axisymmetric contraction. Scalar mixing in MHD turbulence is also studied briefly, with or without a mean scalar gradient.

The first half of the thesis contains discussions of turbulence structure in isotropic turbulence, with a focus on the highly intermittent small scales, especially at higher Reynolds numbers. In previous studies geometrical structures of "sheets" and "filaments" were identified in intense energy dissipation rate and enstrophy density (vorticity squared) respectively. However large simulations of isotropic turbulence using 8192^3 grid points seem to suggest a change in the topological feature of the extreme events, in the form of somewhat "chunky" structures, as the Reynolds number increases. Since the extreme events are highly localized in space and possess fast dynamics, resolution effects in both space and time are critical. It was found recently that inadequate resolution over-estimates the likelihood for the extreme events to occur. In this thesis, a new investigation of the resolution effects on the topological features of the extreme events using three dimensional (3D) visualizations show that, when the time step is made smaller and the grid spacing is refined the dominant geometrical features are consistent with the classical picture of extreme dissipation, in the form of sheets, wrapped around filaments of extreme enstrophy,

In addition to the occurrences of large amplitude events, small scale quantities exhibit frequent sign oscillations in both space and time, which can be quantified by the cancellation exponent which measures the propensity for opposite signs to cancel each other at varying scale sizes. Values of cancellation exponents measured experimentally in the past were dependent of the dimensionality of the

spatial region considered. This thesis presents a systematic study of cancellation exponents where values computed in one dimensional (1D), 2D and 3D are compared over a wide range of Reynolds numbers for vorticity, longitudinal and transverse velocity gradients. It is found that 2D and 3D measures of cancellation exponents of vorticity and transverse velocity gradients give values close to theoretical predictions, while values of 1D measure are smaller. However longitudinal velocity gradients have similar cancellation exponents regardless of the dimensionality of the measure. The results suggest measures in higher dimensions are generally needed to give more accurate cancellation exponents. The simulation results also show that weakened sign cancellation accompanies an increased degree of coherency, and therefore the elongated filament-like structures are likely the cause of smaller cancellation exponents measured in 1D for vorticity and transverse velocity gradients.

The second half of the thesis presents results of MHD turbulence, which concerns the flow of electrically conducting fluids in a magnetic field. One key feature in MHD turbulence is the development of anisotropy, which results from the Lorentz force of electromagnetic induction and occurs at all scales. Since in most terrestrial applications advective transport is much weaker than the diffusion of the magnetic field, a low magnetic Reynolds number is assumed and the main interest is on the evolution of the velocity field. Specifically, DNS of decaying MHD turbulence at a low magnetic Reynolds number are performed on initially isotropic turbulence and anisotropic turbulence after axisymmetric contraction. To allow the integral length scales to develop naturally, a strong emphasis in the study is on the use of domains elongated in the direction of the magnetic field. For the isotropic initial condition, grids with up to 32768×4096^2 points are employed and the domain aspect ratio was 8. It is found that elements of the Reynolds stress anisotropy tensor flip signs during the evolution, while the small scales display axisymmetry about the magnetic field direction. Velocity gradients along the magnetic field decrease strongly, while the parallel vorticity component becomes dominant. In the wavenumber space the axisymmetric energy spectra become highly anisotropic too. At later times the turbulence approaches a state of quasi-two-dimensionality. Elongated domains that help reduce confinement issues have enabled useful results at longer times compared to previous work.

With an anisotropic initial condition obtained after axisymmetric contraction, the anisotropy development depends on whether the imposed magnetic field is in the extensive versus compressive

direction. For the parallel case, results of simulations with up to 8192×4096^2 grid points show while both the large and small scales possess trends of return to isotropy at intermediate times, relations representing axisymmetry are well maintained. Behaviors at late times are similar to those in MHD turbulence from isotropic initial conditions, which suggests the initial anisotropy produced by axisymmetric contraction is not strong enough to affect the long-time dynamics. In comparison when the magnetic field is applied in the compressive strain direction, results of simulations with up to $(2048)^2 \times 16384$ grid points show the initial axisymmetry vanishes, but a new type of axisymmetry develops about the magnetic field direction at later times. Regardless of turbulence conditions prior to the activation of the magnetic field, rapid growth of the integral length scales along the magnetic field, accompanied by a state of local axisymmetry about the same direction in the small scales, is consistently observed.

Scalar mixing in MHD turbulence is also briefly studied with or without a uniform mean scalar gradient which acts as a source term in producing the scalar variance. Due to the large molecular diffusivities of liquid metals, scalar mixing in MHD turbulence occurs at low Schmidt numbers. While MHD effects do not act on the scalars directly, preliminary results show that in the absence of a mean scalar gradient, scalar mixing becomes less efficient with the application of a magnetic field, and scalar gradients decrease in the magnetic field direction. These effects seem stronger at a larger Schmidt number when molecular diffusion is less dominant. When a uniform mean scalar gradient is supplied along the magnetic field, scalar variance that starts from a zero initial condition develops steadily. A parallel magnetic field slows down the growth of scalar variance, and leads to departures from local isotropy in the small scales of the scalars.

CHAPTER 1
INTRODUCTION

1.1 Background and Motivation

Turbulence is ubiquitous in nature and engineering such as in the atmosphere, water bodies, aerospace applications, combustion devices etc. One of the most notable characteristics of turbulent flows is that fluid motions have three-dimensional disorderly fluctuations that span a wide range of scales in space and time (Tennekes and Lumley, 1972). Even though the Navier-Stokes equations — the governing equations of turbulence and fluid motions in general — have been known for some two centuries, our understanding of turbulent flows is still not complete. Over the years various approaches have been taken to improve our understanding of turbulence, including theoretical studies (Monin and Yaglom, 1975; Sreenivasan and Antonia, 1997), experimental measurements (Warhaft, 2000) and computer simulations (Moin and Mahesh, 1998). In particular, great advances in high-performance computing (Ishihara, Gotoh, and Kaneda, 2009) have allowed close examination of the turbulence problem in unprecedented detail.

One central issue in turbulence research is the interaction among different scales, and the degree of scale separation can be measured by the Reynolds number $Re = \mathcal{U}\mathcal{L}/\nu$ where $\mathcal{U}$ and $\mathcal{L}$ denote characteristic velocity and length scales respectively, and ν is the kinematic viscosity. In a classical picture by Richardson (1926), energy associated with large eddies cascades to smaller and smaller eddies, until eventually dissipated by viscosity. More formally, Kolmogorov (1941) hypothesized that at high Reynolds numbers, the influence of large scale anisotropy is weakened as energy cascades to smaller eddies, and the small scales are statistically isotropic (i.e. locally isotropy) and exhibit universal scaling properties only as a function of scale size and mean dissipation rate $\langle\epsilon\rangle$ ($\langle\cdot\rangle$ denotes averaged quantities). Good understanding of the small scales is not only important in turbulence theories (Sreenivasan and Antonia, 1997), but also has practical implications such as in rain formation (Shaw, 2003), alternative fuels (Oefelein, Chen, and Sankaran, 2009), wind power (Castillo et al., 2013) and marine zooplakton ecology (Rothschild and Osborn, 1988). At even higher Reynolds numbers, scale separation becomes more pronounced, and Kolmogorov (1962) hy-

pothesized that an inertial range arises where turbulence statistics are minimally affected by viscous effects and only depend on the scale size. Usually, the small scales are studied in isotropic turbulence, where the effect of any large-scale anisotropy is minimal. However in many applications in nature and engineering, body forces such as those representing gravity or magnetic fields, can lead to substantial anisotropy. As a result, in anisotropic turbulence, the small scales may no longer display universality and turbulence structure can become more complex. The focus of this thesis is to study the turbulence structure, especially that of the small scales, with and without effects of a magnetic field.

A key feature of the small scales is the highly intermittent behavior (Frisch, 1995) where small scale motions can take extremely large amplitude, leading to non-Gaussian statistics, especially at high Reynolds numbers. For example, energy dissipation rate and enstrophy (vorticity squared) are two small-scale descriptors of the strength of local straining and rotation respectively (Sreenivasan and Antonia, 1997). Past studies suggest their magnitude can attain $\mathcal{O}(10^4)$ times of their mean values (Donzis, Yeung, and Sreenivasan, 2008; Yeung, Donzis, and Sreenivasan, 2012), thus giving the notion of "extreme events". Such intense dissipation rate can tear apart flame surfaces and lead to extinction in combustion systems, while strong enstrophy can result in preferential concentration of inertial particles. In addition to applications noted above, understanding the extreme events is also of some theoretical interest. In particular Nelkin (1999) argued that in the high Reynolds number limit, dissipation and enstrophy must scale similarly. This argument received support from past numerical simulations (Donzis, Yeung, and Sreenivasan, 2008; Yeung, Donzis, and Sreenivasan, 2012; Yeung, Zhai, and Sreenivasan, 2015), as the probability density functions (PDFs) of dissipation and enstrophy approach each other at large magnitudes at high Reynolds numbers.

One natural question that follows is how the extreme events look like and how their occurrences relate to each other. In fact a variety of spatial structures have been identified in the high-amplitude small-scale quantities, such as dissipation sheets and vortex filaments (Siggia, 1981; Kerr, 1985; Vincent and Meneguzzi, 1991; Jimenez and Wray, 1998). Elongated vortex filaments are formed as fluid elements undergo spiral motions (She, Jackson, and Orszag, 1990), and dissipation sheets tend to wrap around the vortex filaments (Kawahara, 2005). However recent computational work (Yeung, Zhai, and Sreenivasan, 2015) suggests a change in the topological features of the extreme events at higher Reynolds numbers. In particular, amplitudes of extreme dissipation and enstrophy

can reach $\mathcal{O}(10^5)$ of their mean values, and topologically the two quantities are co-located in space and assume a somewhat "chunky" structure, notably different from the conventional picture at lower Reynolds numbers where elongated vortex filaments are wrapped around by dissipation sheets. This finding seems to suggest that more complicated structural changes accompany an increase of the Reynolds number, in addition to an extended inertial range.

Since extreme events are highly localized in space, resolution of the small scales in simulations is crucial, especially at higher Reynolds numbers when resolution requirements become more stringent (Yakhot and Sreenivasan, 2005). More recently Yeung, Sreenivasan, and Pope (2018) found that inadequate spatial and temporal resolution can lead to overestimation of the most extreme events. Moreover it is seen that dissipation and enstrophy do not scale similarly in the far tail of the PDFs as spatial and temporal resolution are improved. Since the co-location of extreme dissipation and enstrophy is in good agreement with the collapse of the PDF tails, the different scalings in the far tail of PDFs call for a re-examination of the accuracy of the results, including the topological features. One objective of the thesis is to assess systematically the resolution effects in time and space on the extreme events of dissipation and enstrophy. Visualization techniques are used mainly to study how the topological features are affected by resolution as it is varied.

The small scales of fluid turbulence not only fluctuate strongly in magnitude, but also exhibit frequent oscillations in sign if not sign-definite, such as vorticity and velocity gradients. At high Reynolds numbers, the sign changes can be characterized by a cancellation exponent (Ott et al., 1992), which measures the propensity of the quantity considered to cancel out when averaged over a region of space or interval of time. Consider cancellation of signs over some spatial extent, a natural distinction arises when sign cancellations are measured along lines (one-dimensional, 1D), across areas (2D) or over volumes (3D). Both theoretical analysis (Vainshtein et al., 1994) and experimental data (Vainshtein, Du, and Sreenivasan, 1994; Sreenivasan, Juneja, and Suri, 1995) suggest that cancellation exponents depend on the dimensionality considered. However past experiments only have results up to 2D, partly due to difficulties in making measurements in 3D, and there still lacks a systematic study of cancellation exponents using measures in 1D, 2D and 3D. In comparison, computing cancellation exponents in 3D is convenient, despite its own computational challenges. Moreover, since cancellation exponent is defined in the inertial range, high Reynolds number is important for accurate results. Another objective of the thesis is to take advantage of the

rich simulation database that spans a wide range of Reynolds numbers, and study how cancellation exponents depend on the dimensionality of the measures and the Reynolds number.

As noted previously, turbulence structure can depart from classical descriptions and become anisotropic when body forces arise. In particular electrically conducting fluids in a magnetic field are subjected to the Lorentz force of electromagnetic induction, which leads to anisotropy at all scales (Davidson, 2001). The study of magnetohydrodynamic (MHD) turbulence is thus of importance in applications such as metallurgical processing, nuclear reactors and convection in the Earth's liquid core. In general MHD flows involve a two-way coupling between the fluctuating velocity and magnetic fields. A critical parameter is the magnetic Reynolds number (R_m), which is a measure of the strength of advective transport compared with magnetic diffusion. In most terrestrial applications R_m is much lower than unity, such that the effect of the fluid motion on the magnetic field is minimal, and it is appropriate to only focus on how the magnetic field affects the flow. A measure of the strength of the imposed magnetic field is the magnetic interaction parameter N, defined to be the ratio of large-eddy turnover time to Joule damping time. The latter time scale characterizes the Joule dissipation which arises due to the Lorentz force and, unlike viscous dissipation, acts at all scales. Many attempts have been made to understand MHD turbulence. However, past theoretical studies were mostly restricted to linearized problems in the limit of large N, whereas experimental studies are difficult since liquid metals are often opaque and corrosive. As a result, numerical simulations, if formulated properly and executed efficiently, have particular appeal as a tool of investigation (Knaepen and Moreau, 2008).

Past numerical studies (Zikanov and Thess, 1998; Ishida and Kaneda, 2007; Okamoto, Davidson, and Kaneda, 2010; Burattini, Zikanov, and Knaepen, 2010) investigating the response of isotropic turbulence to an external magnetic field have reported various trends towards a state of two-dimensionalization. For example, the integral length scales, as a measure of the large scales, grow preferentially along the magnetic field direction. The small scales deviate from local isotropy, characterized by a preferential damping of the velocity gradients in the magnetic field direction. However simulations in the past often employ cubic grids, which may not represent the highly anisotropic MHD turbulence field faithfully when the rapidly-growing integral length scales reach a significant percentage of the domain size. Also, numerical forcing used in some previous works inevitably introduces numerical artifacts to Joule dissipation that acts at all scales, and thus may not

be ideal. As a result to better understand the anisotropy evolution at all scales and the underlying physical mechanisms, and there is a need to simulate MHD turbulence on grids strongly elongated along the magnetic field direction free of numerical forcing.

It is well known that turbulence promotes efficient mixing, where turbulent transport breaks large-scale non-uniformities into increasingly smaller fragments, which are ultimately smoothed by molecular diffusivity (D). A measure of the relative strengths of viscous and molecular diffusion is the Schmidt number $Sc \equiv \nu/D$. Important examples of turbulent mixing include bringing segregated species together for chemical reactions to occur at molecular level, and scattering pollutants in the air. Despite extensive studies of scalar mixing in non-conducting fluids (Warhaft, 2000), mixing in MHD turbulence, which occurs at low Sc due to high molecular diffusivity of liquid metals, is not well understood. Even though the magnetic field does not act on the scalars directly, changes in the structure of the velocity field by the magnetic field can have strong effects on the mixing of scalars. Past study by Kinet et al. (2008) in the absence of a mean scalar gradient, suggests the magnetic field slows down scalar mixing by modifying energy transfers in the spectral space. However the Reynolds number obtained was low compared to what can be reached today. Furthermore, much remains unknown if a mean scalar gradient is present which provides a production mechanism for scalar variance. One objective of the thesis is to study the anisotropy development in both the velocity and scalar field in decaying low-R_m MHD turbulence with isotropic initial conditions.

Although studies of the response of isotropic turbulence to a magnetic field provide important information on the anisotropy development, in applications anisotropy of various origins can be present as well. For example, many engineering devices involve passing fluids into a straight conduit through a contracting entry section. In particular, axisymmetric contraction causes anisotropy to develop at all scales (Ayyalasomayajula and Warhaft, 2006; Clay and Yeung, 2016), but the anisotropy weakens in the straight section as the mean strain is removed. In some nuclear fusion engineering applications, the conducting fluid may be subjected to a magnetic field in the straight section (Alberts-Chico et al., 2013), and the combined effects of strains and MHD can lead to further complexities. Since both axisymmetric contraction and the magnetic field possess preferred directions, turbulence evolution will depend on whether the magnetic field is acting along the extensional or contracting directions, and on the relative strengths of such effects. Building on the understanding of MHD turbulence from isotropic initial conditions, the last objective of the the-

sis is to study the anisotropy evolution in MHD turbulence from an initial turbulent state that just undergoes axisymmetric contraction.

In this thesis, direct numerical simulations (DNS) are used to study turbulence structure with and without a magnetic field. Due to the need to resolve a wide range of scales, DNS is computationally intensive (Moin and Mahesh, 1998). Yet recent advances in high performance parallel computing have now made it possible to perform simulations of isotropic turbulence on grids up to 8192^3 points, and on a similar scale for anisotropic MHD turbulence. Certainly the large amount of data involved can only be processed when distributed over hundreds of thousands of processors by a domain decomposition, and efficient simulations require advanced parallel programming models such as Message Passing Interface (MPI) and OpenMP shared-memory library. While the details of the numerical schemes are given in Chap. 2, an important aspect of the DNS reported in this thesis is the use of periodic domains, which explores periodic the boundary conditions and allows the use of highly accurate pseudo-spectral method (Rogallo, 1981). Use of periodic boundary conditions are convenient for the study of the small-scales. However, in MHD turbulence it is important that the integral length scales do not become too large relative to the size of the domain. To visualize the highly localized extreme events, subcubes are formed from the larger simulation domains. Since data in a particular subcube may lie in multiple processors, efficient communication is key to the study. To this end, one-sided communication such as Coarray Fortran (CAF) and MPI_Get are employed in subcube formation. When cancellation exponents are computed which involve averaging over lines, areas and volumes, the prefix sum strategy is used to reduce computational cost and decrease the message size for faster communication. With the presence of the magnetic field, numerical simulations of decaying MHD turbulence are performed from isotropic initial conditions or those after axisymmetric strain, with and without scalars. A solution domain elongated along the magnetic field direction is used to help minimize numerical artifacts of finite domain size. Given the massive scales of the simulations presented in the thesis, this work required the use of supercomputers including Blue Waters at the National Center for Supercomputing Applications and Stampede1 & 2 at the Texas Advanced Computing Center.

In summary, this thesis presents a numerical study of turbulence structure, especially the small scales, with and without the effects of a magnetic field, in isotropic turbulence and MHD turbulence respectively. In the present study of isotropic turbulence, the focus is on the large magnitude and

frequent sign oscillations of the small scales. For extreme events of dissipation and enstrophy in high Reynolds number isotropic turbulence, a systematic investigation is performed to examine the resolution effects in space and time, by visualizing and comparing the extreme events at different spatial and temporal resolutions. For small scale quantities that oscillate rapidly in sign, cancellation exponents that quantify the sign oscillation characteristics are computed in all three dimensions and over a wide range of Reynolds numbers. In MHD turbulence, simulations have been carried out using isotropic turbulence or anisotropic turbulence subjected to axisymmetric contraction as initial condition. Since the Lorentz force induces anisotropy at all scales of motion, characterizations of anisotropy development go beyond the small scales. Furthermore to alleviate finite domain effects that arise with periodic boundary conditions, the solution domain is elongated in the direction of the magnetic field. Mixing in MHD turbulence is also studied, with and without a mean scalar gradient which produces scalar variance. The products of the code development undertaken in this work, including forming subcubes and calculations of cancellation exponents, are expected to be useful for further research, such as the structure of the scalar dissipation rate.

1.2 Objectives and Outline

There are three major objectives in this thesis:

1. To study the structure of the small-scales in isotropic turbulence. When events of large amplitude are considered, the objective is to examine, by performing 3D visualizations, how the spatial and temporal resolution affect the topological features of the extreme events. As to sign-oscillation properties of the small-scales, the objective is to compare values of cancellation exponents measured in one, two or three dimensional space, and understand why the values differ.

2. To study the anisotropy development in decaying MHD turbulence from isotropic states. An emphasis in the study is the use of an elongated domain to allow natural development of anisotropy at all scales of motion. In addition to the velocity field, scalar mixing in MHD turbulence with or without a mean scalar gradient is also studied, with emphasis on examining how the mixing of scalars with different Schmidt number Sc is affected by a magnetic field.

3. To study the effects of a magnetic field on the evolution of anisotropic turbulence subjected to axisymmetric contraction. Comparison will be made with the anisotropy development of initially

isotropic turbulence. Furthermore, this study examines different configurations of the mean strain being parallel or perpendicular to the magnetic field.

The remaining chapters of the thesis are organized as follows. Chapter 2 gives an overview of the governing equations and direct numerical simulations. In Chap. 3, the structure of small-scales in isotropic turbulence is studied, with emphasis on the resolution effects in space and time on the extreme events, and on the sign oscillation characteristics of the small scale quantities. Chapter 4 is focused on the anisotropy development in decaying MHD turbulence. A highlight of the study is the use of domains elongated in the magnetic field direction to produce reliable statistics that describe the anisotropy in the large and small scales in both physical and wavenumber spaces. Chapter 5 shows preliminary results of scalar mixing in MHD turbulence and Chap. 6 presents the evolution of strained MHD turbulence. A summary of the thesis and suggestions of future work are given in Chap. 7.

While the work reported in this thesis has spanned several different topics, it is worth re-emphasizing that the subject material of most of the following chapters can be considered as covering two main areas of research. In particular, the material in Chapter 3 is focused (mainly) on small-scale structure in isotropic turbulence (re: Objective 1 noted at the beginning of this subsection), while the material in Chapters 4 to 6 collectively addresses several fundamental, but related aspects of MHD turbulence (re: Objectives 2 and 3).

CHAPTER 2

GOVERNING EQUATIONS AND DIRECT NUMERICAL SIMULATIONS

In this chapter, the governing equations of fluid flows are first introduced in both physical and wavenumber space, along with details of setting the simulation domain size, temporal and spatial resolution as well as numerical forcing. Then an overview of direct numerical simulation (DNS) using massively parallel supercomputers follows, with special attention to the formation of subcubes using one-sided communication, which greatly facilitates the visualization of the extreme events. With the presence of a strong magnetic field, the modified governing equations that include the Lorentz force are presented, followed by discussions of specific numerical aspects in scalar mixing in MHD turbulence. Details of computing cancellation exponents are postponed to Chap. 3 where the formal definition is given.

2.1 Velocity field in isotropic turbulence and numerical approach

The governing equations of fluid flows are the Navier-Stokes equations, a set of partial differential equations that express principles of the conservation of mass and momentum. Assuming a constant density flow with no mean velocity, the fluctuating velocity field evolve by the following equations, written in Cartesian tensor notation as

$$\frac{\partial u_i}{\partial x_i} = 0 \tag{2.1}$$

$$\frac{\partial u_i}{\partial t} + u_j \frac{\partial u_i}{\partial x_j} = -\frac{1}{\rho}\frac{\partial p}{\partial x_i} + \nu \frac{\partial^2 u_i}{\partial x_j \partial x_j} \,, \tag{2.2}$$

where u_i denotes fluctuating velocity component in the ith direction, p is the fluctuating pressure, and density (ρ) and kinematic viscosity (ν) are constant. Repeated indices imply summation throughout the thesis.

As discussed in Chap. 1, periodic boundary conditions in all three dimensions are used, which

allows a Fourier series representation of the velocity field as

$$u_j(\mathbf{x},t) = \sum_{\mathbf{k}} \hat{u}_j(\mathbf{k},t) e^{i\mathbf{k}\cdot\mathbf{x}} \ , \tag{2.3}$$

where $\mathbf{k}$ denotes a wavenumber vector, caret denotes Fourier coefficient and $i = \sqrt{-1}$ is the imaginary unit. Since variables like $\mathbf{u}(\mathbf{x},t)$ are real-valued, their Fourier coefficients satisfy conjugate symmetry, $\hat{\mathbf{u}}(-\mathbf{k},t) = \hat{\mathbf{u}}^*(\mathbf{k},t)$, where the asterisk denotes a complex conjugate. In isotropic turbulence, statistics are unchanged upon the rotation of the reference frame. As a result there is no reason to favor a particular direction, and it is common to use a cubic domain of size L_0^3 discretized by N^3 grid points. In physical space, the grid points are located at $(l_1\Delta, l_2\Delta, l_3\Delta)$ where integers l_1, l_2 and l_3 range from 0 to $N-1$, and $\Delta = L_0/N$ is the uniform grid spacing. In wavenumber space, there exists N^3 discrete wavenumbers in the form of $(m_1\beta, m_2\beta, m_3\beta)$, where integers m_1, m_2 and m_3 range from $-N/2+1$ to $N/2$, and $\beta = 2\pi/L_0$ is the grid metric factor, which is also the smallest non-zero wavenumber. For isotropic turbulence, a $(2\pi)^3$ domain with $\beta = 1$ is often used, but in general the domain size, grid spacing and grid metric factor can differ in different directions.

For turbulence simulations with periodic boundary conditions, to avoid finite-domain effects care must be taken to ensure that the large scales of turbulence remain small compared to the domain size. The characteristic length scale of the large eddies in turbulence is the integral length scale L_1, and in simulations of isotropic turbulence the ratio L_0/L_1 is preferably at least $5-6$ (Pope, 2000). However in many other scenarios the large scales of turbulence can grow strongly, such as those in flows subject to solid-body rotation or a magnetic field. To allow more room for the large scales to grow naturally, in MHD turbulence the simulation domain is made longer in the direction of the magnetic field. Moreover the elongated domain is accompanied by a proportional increase of grid points N such that the grid spacings remain the same along different directions.

The Fourier series representation allows the use of highly accurate Fourier pseudo-spectral methods (Rogallo, 1981). Specifically in wavenumber space Eq. 2.1 and 2.2 are transformed to

$$k_i \hat{u}_i = 0 \tag{2.4}$$

$$\Big(\frac{d}{dt} + \nu k^2\Big)\hat{u}_i(\mathbf{k},t) = -\Big(\delta_{ij} - \frac{k_i k_j}{k^2}\Big)\hat{G}_j(\mathbf{k},t) \ , \tag{2.5}$$

where δ_{ij} is the kronecker delta tensor, and $\hat{G}_j(\mathbf{k}, t)$ is the Fourier transform of the nonlinear term in Eq. 2.2 and is given by

$$\hat{G}_j(\mathbf{k}, t) = ik_m \sum_{\mathbf{k}'} \hat{u}_j(\mathbf{k}', t)\hat{u}_m(\mathbf{k} - \mathbf{k}', t) \ . \tag{2.6}$$

As Eq. 2.6 shows, the nonlinear term involves non-local interactions among wavenumber triads $\mathbf{k}$, $\mathbf{k}'$ and $\mathbf{k}''$, such that $\mathbf{k}' + \mathbf{k}'' = \mathbf{k}$. In Eq. 2.5, the pressure term is eliminated as $\left(\delta_{ij} - k_i k_j / k^2\right)$ projects the nonlinear term to the plane perpendicular to $\mathbf{k}$, but the pressure can be recovered by a Poisson equation as follows

$$k^2 \hat{p} = ik_j \hat{G}_j \ . \tag{2.7}$$

For N^3 discrete wavenumbers, the convolution sum in Eq. 2.6 requires $\mathcal{O}(N^6)$ operations, which is prohibitively expensive. Instead, a pseudo-spectral method is used where the nonlinear term is formed in physical space and then transformed into wavenumber space, reducing the number of operations down to $\mathcal{O}(N^3 log_2 N)$. However aliasing errors are introduced with this approach, and a combination of phase shifting and spherical truncation are used to reduce aliasing errors. As a result, the highest resolvable wavenumber becomes $k_{max} = \sqrt{2}N\beta/3$ (Canuto et al., 1988).

While the Navier-Stokes equations are partial differential equations, in wavenumber space Eq. 2.4 and 2.5 become ordinary differential equations. Nonlinear terms are integrated in time using an explicit Runge-Kutta method while viscous terms are addressed exactly via an integrating factor. In general, numerical stability is controlled by the Courant number C, defined as

$$C = \Delta t \left[\frac{|u|}{\Delta x} + \frac{|v|}{\Delta y} + \frac{|w|}{\Delta z} \right]_{max} \ , \tag{2.8}$$

where Δt is the time step, u, v, w are the three velocity components, and a maximum is taken over all the grid points. In the past $C = 0.6$ was often used in simulations of isotropic turbulence, yet the recent work of Yeung, Sreenivasan, and Pope (2018) shows that $C = 0.6$ may not give adequate temporal resolution to faithfully simulate the evolution of the extreme events at higher Reynolds numbers. In addition to temporal resolution, spatial resolution requirements also become more stringent as Reynolds number increases (Yakhot and Sreenivasan, 2005). The small scale resolution is often expressed by the dimensionless parameter $k_{max}\eta$, where $\eta = (\nu^3/\langle\epsilon\rangle)^{1/4}$ is the Kolmogorov

length scale that represents small scales. Using the relation $\Delta = 2\pi/(\beta N)$ and $k_{max} = \sqrt{2}N\beta/3$ as given above, the ratio of grid spacing to the Kolmogorov scale can be expressed as

$$\Delta/\eta = \frac{2\sqrt{2}\pi}{3}\frac{1}{k_{max}\eta} \approx \frac{2.96}{k_{max}\eta} \,. \tag{2.9}$$

For simulations aimed at increasing the Reynolds number, $k_{max}\eta$ is often of the order 1.5 or less (Ishihara et al., 2016), or effectively $\Delta/\eta \approx 2$. An important objective in this thesis (Chap. 3) is to examine the resolution effects in time and space on the evolution of extreme events at different Reynolds numbers.

In the absence of a mechanism of energy production (such as mean velocity gradients), turbulence decays and Reynolds number decreases. To maintain the Reynolds number, it is common to apply numerical forcing to the velocity field at the large scales. One approach employed successfully in the past is the scheme of Eswaran and Pope (1988a) which uses Uhlenbeck-Ornstein random processes to inject energy to Fourier modes at the smallest few wavenumbers. However such stochastic processes can cause substantial temporal variations of turbulence statistics, such as in the turbulent kinetic energy and the dissipation rate. To reduce the temporal oscillations, Donzis and Yeung (2010) proposed a forcing scheme that freezes the energy spectrum at the lowest wavenumbers. In general as the energy dissipation reaches equilibrium with the energy injection at the large scales, a statistically stationary state can be obtained. Snapshots of the simulation are then saved over several large eddy-turnover times $T_E = L_1/u'$ (where u' is the root-mean-square (r.m.s.) of the velocity fluctuations) and more detailed analysis can be performed using post-processing. To improve statistical sampling, post-processed results are ensemble averaged over a number of realizations. This is particularly important for the statistics of the extreme events since they are rare in nature.

2.2 Parallel implementations and formation of subcubes

Turbulence simulations at the scales performed in this thesis cannot be achieved without an efficient and scalable parallel implementation using high-performance computing (HPC). Two widely used programming models in the HPC community are distributed and shared memory computing, and both are employed in our Pseudo-Spectral Direct Numerical Simulation (PSDNS) codes. The first,

also known as single program multiple data (SPMD) programming model, involves a partition of the entire domain and a binding of partial data to each computing process locally. With the computing processes executing a single program in SPMD, accessing data non-local to the computing process is achieved through communication. For example, the Message Passing Interface (MPI) standard provides high level application program interfaces (API) that allow communication among computing processes. The second programming model — shared memory computing — differs from the first by granting all computing processes access to a shared memory. Specifically the OpenMP software library is used to create a so-called "parallel region" where computing processes known as threads share computational workload. In general each MPI process (also known as an MPI task) executes the entire code while OpenMP threads are active only within a parallel region.

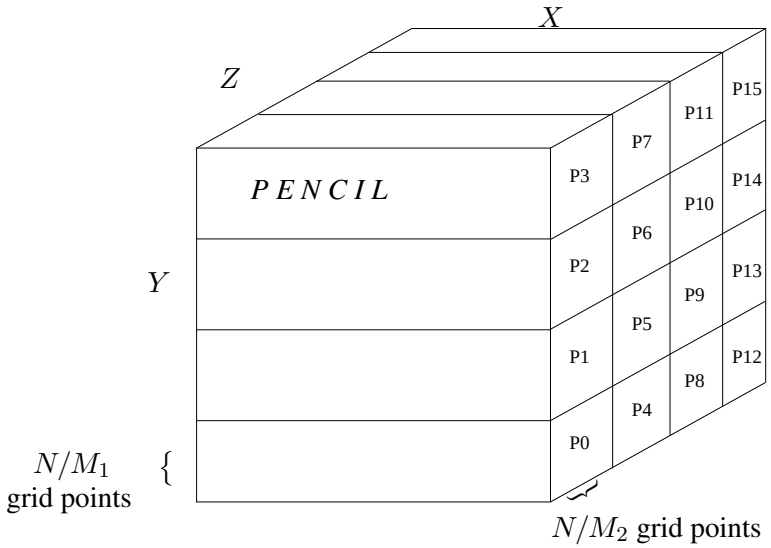

Figure 2.1: Mapping the N^3 domain into a 2D computational grid with $P = M_1 \times M_2$ parallel processes. In this example $M_1 = M_2 = 4$.

As discussed previously, the use of MPI is contingent on a partition of data. In this thesis a 2D domain decomposition is used (Donzis, Yeung, and Pekurovsky, 2008) as illustrated in Fig. 2.1. Take the cubic domain as an example, a total of N^3 grid points are equally divided by $P = M_1 \times M_2$ parallel processes, forming "pencils" of size $N \times (N/M_1) \times (N/M_2)$. Since each pencil is bound to an MPI task placed on a CPU, complete "lines" of data in one direction are local to the CPU's memory, which greatly facilitates efficient computation of Fast Fourier Transform (FFT) (Cooley and Tukey, 1965) along the pencil direction. However to complete FFTs in all three directions, it is necessary to re-arrange the data in the form of pencils aligned in different directions. This is

achieved by collective communication of the "all-to-all" type (e.g. the MPI_ALLTOALL). Often M_1 is made smaller than or equal to the number of cores per node so that the M_1 MPI tasks could be placed within a single node. Such a choice allows one transpose to take place within a node, which is more efficient.

While the current PSDNS code uses a 2D domain decomposition, the domain can be decomposed into 1D slabs or 3D sub-volumes, depending on the need and computational constraints. For example, 1D domain decomposition divides N^3 grid points into P slabs and each slab consists of $N \times N \times N/P$ grid points. Since each slab holds data that span two directions entirely, FFTs along the two directions within the slab can be readily performed, and only one transpose is needed to complete FFT in the third direction, thus saving communication time. However the 1D decomposition is restricted to a maximum number of N MPI tasks, while in contrast a 2D decomposition allows up to N^2 MPI tasks, which has potential for a higher degree of parallelism. Yet as computing hardware evolves, especially given the current trend of many core per node configurations (such as in Stampede2 of the Texas Advanced Computing Center), it may be worthwhile to revert to 1D domain decomposition in the future. This is because as each node has more memory, it may be possible to use fewer MPI processes, or perhaps the entire slab of data can fit within a compute node. Savings in communication overhead as a result of one fewer transpose may be significant.

In addition to 1D and 2D domain decompositions, 3D domain decomposition can be useful, especially in visualizing turbulence structures. For example, when 262144 MPI tasks are used in the simulation on a 8192^3 grid, the processor grid is 32×8192 and the resulting pencils are of size $8192 \times 256 \times 1$. Clearly, visualizing a pencil, with one side containing only one grid point, does not reveal important physics. However on the other hand visualizing the entire 8192^3 is not helpful either: not only is the procedure prohibitively expensive, but also the rich structures of various scale sizes in the turbulence field present too much information to draw useful conclusions. As a result, when highly localized extreme events are of interest as in this thesis, it is useful to form "subcubes" out of the entire simulation domain. The subcubes are computationally efficient to visualize, and allow a focused study of extreme events in turbulence. The formation of subcubes in fact is closely tied to a 3D domain decomposition.

To demonstrate how to obtain 3D subcubes, Fig. 2.2 shows a domain that is decomposed to $8 \times 8 = 64$ pencils, with a subcube sample enclosed by red dashed lines. Since subcubes of

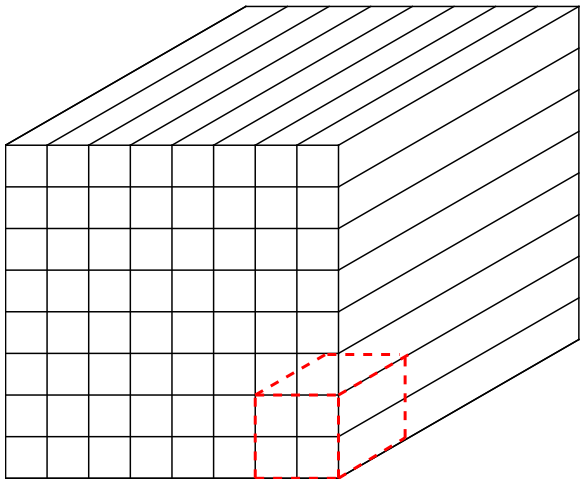

Figure 2.2: Illustration of the formation of subcubes (enclosed in red dashed lines) from a 2D domain decomposition.

equal size are to be formed, the natural choice is to place 4 subcubes in each direction and as a result there are $4 \times 4 \times 4 = 64$ subcubes in total. In fact because the number of MPI tasks is the same as the number of pencils and subcubes, the formation of subcubes in general requires the use of l^3 MPI tasks, where l is an integer, and the size of the subcube is N/l. To form the subcube in Fig. 2.2, communication is needed to collect data distributed in four pencils. Often communication among different MPI tasks is two-sided, meaning each MPI task both receives and sends data to other MPI tasks. To ensure the memory location contains the intended data after communication, synchronizations of MPI processes immediately follow the data movement in two-sided communications. However at larger problem sizes as the pencil size becomes much smaller, the number of messages in communication can become very large, and the overhead incurred can be substantial. Instead one-sided communication can achieve better performance with less overhead, as demonstrated in previous studies (Buaria, 2016). A key characteristic of one-sided communication is the decoupling of data movement and process synchronization. Users can set up rules for data movement and delay the actual communication until explicit synchronization calls are made. In particular, Co-array Fortran (CAF), known as a partitioned global address space (PGAS) language is used where memory defined with CAF is accessible by all MPI tasks. Specifically variables declared with CAF have a co-dimension, where an identification number indicates which MPI task to access. Variables declared with CAF are allocated some global memory, but the memory address space is logically partitioned so that each portion of it has affinity for the corresponding MPI process.

Co-array Fortran has become a Fortran 2008 standard, but it does require compiler support such as on BlueWaters at the National Center for Scientific Applications. On machines where CAF is not supported, a similar approach is available by the use of the MPI_GET subroutine, which is a part of the MPI standard.

2.3 Velocity and scalar field in low-R_m MHD turbulence

Since MHD turbulence concerns the flows of electrically-conducting fluids, additional equations – the Maxwell equations – are needed to describe the physics of electrodynamics. The set of reduced Maxwell equations can be written as (Davidson, 2001):

$$\nabla \cdot \mathbf{E} = 0 \qquad \text{Gauss's law} \tag{2.10}$$

$$\nabla \times \mathbf{E} = -\frac{\partial \mathbf{B}}{\partial t} \qquad \text{Faraday's law} \tag{2.11}$$

$$\mathbf{J} = \sigma \left(\mathbf{E} + \mathbf{u} \times \mathbf{B} \right) \qquad \text{Ohm's law} \tag{2.12}$$

$$\nabla \times \mathbf{B} = \mu \mathbf{J} \qquad \text{Ampere's law} \tag{2.13}$$

where $\mathbf{E}$ is the electric field, $\mathbf{B}$ is the magnetic field, $\mathbf{J}$ is the current density, σ is the magnetic conductivity, $\mathbf{u}$ is the velocity of the conducting fluid and μ is the permeability of free space. Combining Faraday's law, Ohm's law and Ampere's law to cancel E and J, the evolution equation of the magnetic field is:

$$\frac{\partial \mathbf{B}}{\partial t} = \nabla \times (\mathbf{u} \times \mathbf{B}) + \lambda \nabla^2 \mathbf{B} \, , \tag{2.14}$$

where the magnetic diffusivity $\lambda = (\mu\sigma)^{-1}$.

A distinctive feature of MHD turbulence is the Lorentz force (per volume) $\mathbf{F} = \mathbf{J} \times \mathbf{B}/\rho$, which arises due to the relative motion between the velocity field and the magnetic field. Substituing $\mathbf{J}$ using Ohm's law, the Lorentz force is split into irrotational and rotational parts $(\mathbf{B}\cdot\nabla\mathbf{B} - \nabla(B^2/2))/\mu$. Consequently the momentum equation is modified as

$$\frac{D\mathbf{u}}{Dt} = -\frac{1}{\rho}\nabla(p + \frac{B^2}{2\mu}) + \nu\nabla^2\mathbf{u} + \frac{1}{\rho\mu}\mathbf{B}\cdot\nabla\mathbf{B} \tag{2.15}$$

where the magnetic pressure $B^2/(2\mu)$ is lumped together with pressure p.

In general, the motions of an electrically conducting fluid under the external magnetic field produce an electric field and hence a current, which induces a secondary fluctuating magnetic field (Eq. 2.14). The secondary magnetic field would act back on the velocity field via Eq. 2.15, thus leading to a two-way coupling. However the equations are de-coupled if advective transport of the magnetic field is weak. In particular, the total magnetic field $\mathbf{B}$ can be decomposed into a steady and uniform mean field $\mathbf{B_0}$ and the fluctuating magnetic field $\mathbf{b}$. Define magnetic Reynolds number $R_m = \mathcal{U}\mathcal{L}/\lambda$ where $\mathcal{U}$, $\mathcal{L}$ are characteristic velocity and length scales. Physically, at vanishingly small R_m any localized large fluctuations $\mathbf{b}$ are quickly diffused by magnetic diffusivity λ such that $\mathbf{b} \ll \mathbf{B_0}$. Further apply the quasi-static approximation that $\partial\mathbf{b}/\partial t$ is small, Eq. 2.14 becomes

$$0 = \mathbf{B_0} \cdot \nabla\mathbf{u} + \lambda\nabla^2\mathbf{b} \, . \tag{2.16}$$

Equation 2.16 can be used to simplify the last term in Eq. 2.15 as

$$\mathbf{B} \cdot \nabla\mathbf{B} \approx \mathbf{B_0} \cdot \nabla\mathbf{b} = -\frac{1}{\lambda}\nabla^{-2}\left[(\mathbf{B_0} \cdot \nabla)^2\mathbf{u}\right] \, , \tag{2.17}$$

and the momentum equation becomes

$$\frac{D\mathbf{u}}{Dt} = -\frac{1}{\rho}\nabla(p + \frac{B^2}{2\mu}) + \nu\nabla^2\mathbf{u} + \frac{\sigma}{\rho}\left[(\mathbf{B_0} \cdot \nabla)^2(\nabla^{-2}\mathbf{u})\right] \, . \tag{2.18}$$

As the two-way coupling of the velocity and magnetic field vanishes, the key question is to study how the velocity field is affected by the external magnetic field. Specifically the modified momentum equation Eq. 2.18 is solved, together with the incompressibility condition $\nabla \cdot \mathbf{u} = 0$. Since the assumption of vanishingly small R_m makes the Lorentz term linear (see Eq. 2.16), it can be integrated exactly in time (similar to the viscous term), via a modified integrating factor of the form $exp\left(\int(\nu k^2 + \sigma B_0^2/\rho)dt\right)$, without major changes in the code.

In the study of scalar mixing in MHD turbulence, the advection-diffusion equation describes the evolution of fluctuating scalar ϕ as

$$\partial\phi/\partial t + \mathbf{u} \cdot \nabla\phi = -\mathbf{u} \cdot \nabla\Phi + D\nabla^2\phi \, , \tag{2.19}$$

where D is the molecular diffusivity and $\nabla\Phi$ is a uniform mean scalar gradient, which can act as a source term to produce scalar fluctuations. Even though the magnetic field does not affect scalar evolution directly, MHD effects are felt through the velocity field and eventually have an influence on scalar mixing. The scalar field is treated in a similar manner as the velocity field, including the periodic boundary conditions and the use of Fourier series representation.

Since liquid metals often have very large molecular diffusivity D, which leads to a low Schmidt number $Sc = \nu/D \ll 1$, special care must be taken in the simulation of low-Sc scalar mixing. For example, the scalar integral length scales (L_ϕ) are known to grow with decreasing Schmidt number (Yeung and Sreenivasan, 2014), and as a result the domain size needs to be made longer to allow L_ϕ evolve naturally. For Sc of order one or less, since the smallest scale is the Obukhov-Corrsin scale $\eta_{OC} = \eta Sc^{-3/4}$ (Obukhov, 1949; Corrsin, 1951), the small scales of the scalar field are better resolved than those of the velocity field on the same grid. However, at $Sc \ll 1$ temporal resolution requirements become more demanding, as strong molecular diffusion introduces very small time scales. In simulations of low-Sc scalar mixing in forced isotropic turbulence, Δt has to satisfy $D\Delta t/\Delta^2 \leq 0.5$ to achieve numerical stability (Yeung and Sreenivasan, 2014).

In the study of MHD turbulence with or without scalars, forcing is not applied as in high Reynolds number isotropic turbulence simulations. The reason is that numerical forcing could obscure the role of the Lorentz force, which acts at all scales. As the MHD turbulence decays, spatial resolution continues to improve over time, and the constraint on time step $D\Delta t/\Delta^2 \leq 0.5$ needs to be re-examined. However convergence tests are always performed to ensure that results computed with larger Δt are similar to those obtained with smaller Δt.

CHAPTER 3

STRUCTURE OF SMALL-SCALES IN ISOTROPIC TURBULENCE

As discussed in Chap. 1, the small scales in turbulence can form different structures, and their geometrical features may depend on the Reynolds number, resolution of the simulation as well as the intensity of the small-scale motions being probed. The first half of the chapter provides discussions of the structures of extreme energy dissipation rate and enstrophy. Since extreme events are highly localized in space and sensitive to the Reynolds number, effects of spatial and temporal resolution require careful consideration. In particular, geometrical features of the extreme events observed in 3D visualization may be sensitive to resolution. Another aspect is that, compared to the characterization of magnitude variations of the small-scales which has received much attention, the sign oscillations of the small scale motions (such as velocity gradients and vorticity) is less studied. A quantitative measure of sign oscillations, known as cancellation exponent, is used to characterize the propensity of the cancellations of opposite signs. The second half of the chapter presents results of cancellation exponent, where the measure can be computed in the full 3D space, or taken as 1D or 2D cuts of the 3D solution domain. Since studies of the magnitude variations and sign oscillations are both focused on the small scales, it is useful to consider isotropic turbulence in a wide range of Reynolds numbers.

3.1 Resolution effects on the structures of extreme events

3.1.1 Introduction of past results on the extreme events

In this section, extreme events of two small-scale descriptors of turbulence — energy dissipation rate ϵ and enstrophy Ω — are considered. They are defined respectively as

$$\epsilon = 2\nu s_{ij} s_{ij} \; ; \quad \Omega = \omega_i \omega_i \; , \tag{3.1}$$

where ν is the kinematic viscosity, s_{ij} is the rate of strain tensor $(\partial u_i/\partial x_j + \partial u_j/\partial x_i)/2$ and ω_i is the vorticity. Even though the two quantities represent different effects of local straining and

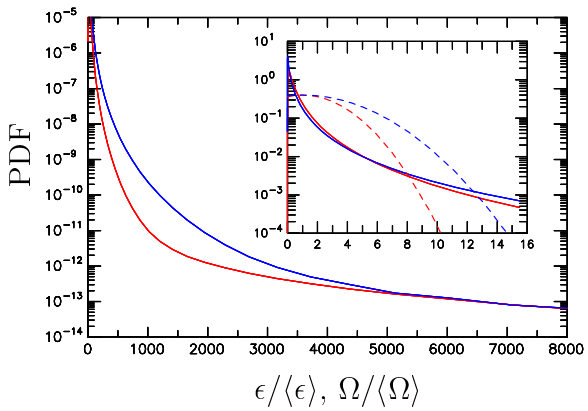

Figure 3.1: Ensemble-averaged PDFs of normalized dissipation (red) and enstrophy (blue) from 8192^3 simulation at $R_\lambda \approx 1300$, with $k_{max}\eta \approx 2$. Inset shows data for 0 to 16 times of the mean value. Dashed curves in the inset show positive halves of Gaussian distributions with equal variances.

rotation, their mean values satisfy $\nu\langle\epsilon\rangle = \langle\Omega\rangle$ in homogeneous isotropic turbulence. Both quantities are known to be highly intermittent (Donzis, Yeung, and Sreenivasan, 2008; Yeung, Donzis, and Sreenivasan, 2012), and their peak amplitudes become larger at higher Reynolds numbers. To demonstrate the intermittent behavior, Fig. 3.1 shows the probability density functions (PDFs) of normalized dissipation and enstrophy. It can be seen that events of magnitude on the order of tens of thousands of the mean value occur, although with a low probability. Moreover as the inset to Fig. 3.1 shows, rare events (e.g. those with larger magnitude) occur much more frequently than in the case of Gaussian-distributed random variables. Figure 3.1 also shows that events of moderately large intensity (of order tens to hundreds of the mean value) are more likely for enstrophy than for dissipation, while for the truly extreme events, both PDFs tend to converge. The coincidence of the PDF tails only occurs at high Reynolds numbers, and suggests that at higher Reynolds numbers higher order moments of dissipation and enstrophy would be nearly identical as larger magnitude events contribute more. Results of the PDFs shown support theoretical arguments that at sufficiently high Reynolds numbers, dissipation and enstrophy should scale similarly (Nelkin, 1999). However a very recent study (Yeung, Sreenivasan, and Pope, 2018) suggests that coincidence of the PDF tails may be a result of inadequate resolution.

Conventionally, structures of intense vortex motions (corresponding to intense enstrophy) are often found to have the shape of filaments (Siggia, 1981; Kerr, 1985; Vincent and Meneguzzi, 1991; Jimenez and Wray, 1998). Visualization of the streamlines shows that fluid elements un-

dergo spiral motions around the filaments, producing enstrophy of large magnitude (She, Jackson, and Orszag, 1990). Near the edges of such spiral motions intense dissipation arises in the form of sheets that wrap around the vortex filaments (Kawahara, 2005). Since visualization is key to revealing turbulence structures in the past, it is used in the current study to understand the geometrical properties of the extreme events. In particular, since the extreme events are known to be localized in space, it is useful to only visualize their intricate details using 3D subcubes formed using the procedures described in Chap. 2. To understand how the structures of the small-scales depend on the magnitude for both dissipation and enstrophy, Fig. 3.2 shows a collection of images where color surfaces at prescribed thresholds for $\epsilon/\langle\epsilon\rangle$ and $\Omega/\langle\Omega\rangle$ are used to visualize the structures of the small-scales. In frame (a) viewing from a subcube of 768^3 grid points at a low threshold level of 10, the spotty nature of ϵ and Ω exceeding this threshold is apparent, but this image does not reveal much about extreme events because the threshold chosen is low. To show the effect of increasing the threshold, the next two images on the top row of Fig. 3.2 use threshold of 30 in (b) and 100 in (c), and zoom in on a more compact subcube of 256^3 grid points. As expected the volume enclosed by contour surfaces shrinks substantially as the threshold is raised. Moreover at the threshold of 100, filament-like structures in enstrophy are quite visible in enstrophy. The fraction of space in cyan (for enstrophy) also becomes significantly larger than that in red (for dissipation), which is consistent with the contrast between probability of occurrence of ϵ and Ω around this threshold (see Fig. 3.1). At an increased threshold of 300, frames (d) to (f) zoom in to subcubes of 51^3 grid points where ϵ and Ω are rendered separately (d, e) as well as simultaneously (f). Both dissipation and enstrophy show somewhat "chunky" topological features which are only modestly elongated. This main structure is distinct from a thinner vortex filament seen near the upper-right corner of frame (e). In frame (f) where both quantities are shown, the chunky region roughly overlaps, but appears as mainly red, which implies that the dissipation contour surface subsumes the region of peak enstrophy. This observation is consistent with the notion that high-vorticity regions at this level of intensity tend to be wrapped around by sheets of intense dissipation (Kawahara, 2005). To focus on the most extreme events, frames (g) to (i) are based on yet higher thresholds. A comparison between (f) and (g) shows that some vortex filaments visible at threshold 300 are no longer present at threshold 600, while the main structure with a chunky appearance remains largely intact. In frame (h) as the threshold is raised further to 4800, the structure becomes somewhat slimmer although not

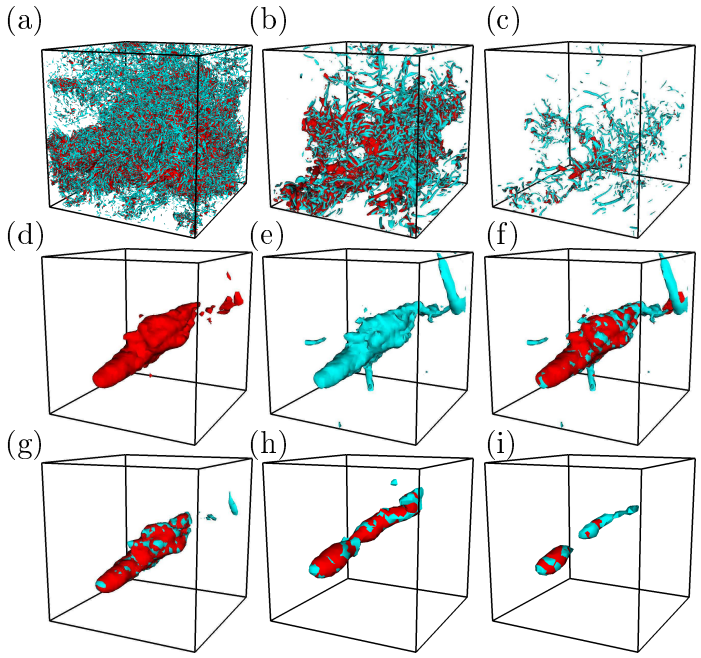

Figure 3.2: Perspective views of 3D contour surfaces of dissipation (red) and enstrophy (cyan) extracted from a randomly chosen (but representative) 8192^3 instantaneous snapshot, at different thresholds (in multiples of mean values) and for different sized subcubes: (a) 10, 768^3; (b) 30, 256^3; (c) 100, 256^3; (d), (e) and (f): 300, 51^3; (g) 600, 51^3; (h) 4800, 31^3; (i) 9600, 31^3. Both dissipation and enstrophy are shown in all frames but (d) and (e).

as slender as typical filament-like vortex filament (see Refs. Jimenez, 2003; Kaneda et al., 2003). In frame (i) at the threshold of 9600, the structure seems to break into two — one of which looks like a blob and and the other like a filament. The wrapping around of vortex filaments by sheet-like dissipation is now less pronounced, as the red color itself now covers the chunky main structure less completely. Closer examination (e.g. by raising the threshold further) indicates that the global maximum is located inside the blob-like region in the lower half of frame (i).

To ascertain that the snapshot used to produce Fig. 3.2 is representative, and to illustrate the effect of the Reynolds number, in Fig. 3.3 we show dissipation and enstrophy contour surfaces from three 8192^3 snapshots, and one 2048^3 at a lower Reynolds number. Frame (a) in this figure is the same as Fig. 3.2 (f) but is repeated here for convenience. All the frames (a) to (c) show a dominant chunky structure with some worm-like vortex filaments nearby. All three images are consistent with the scenario of sheets of intense dissipation being wrapped around a region of intense enstrophy. The chunky structure itself contains the grid location where both dissipation and enstrophy attain their maximum values. The near co-location of dissipation and enstrophy is apparently a very

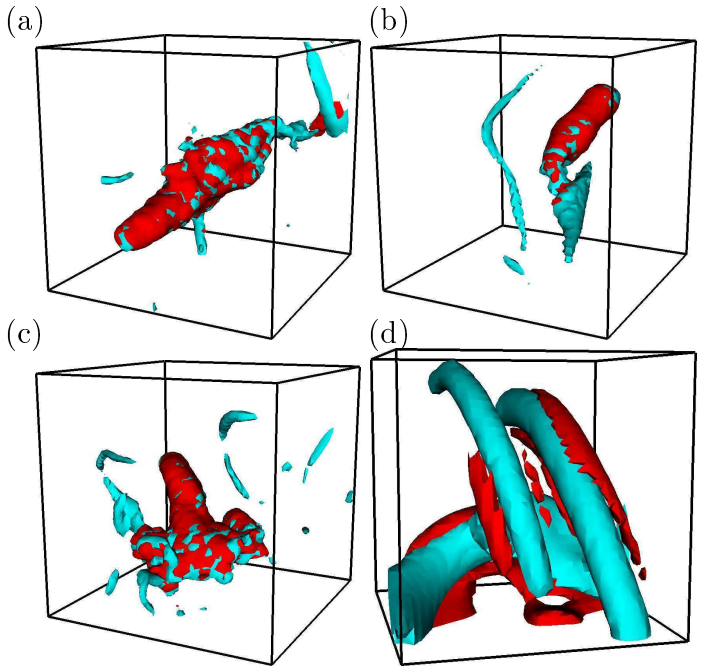

Figure 3.3: Color contours based on three instantaneous snapshots (frames a, b, c) from the 8192^3 simulation at $R_\lambda \approx 1300$, contrasted with data from (d) 2048^3 simulation at $R_\lambda \approx 400$. The contour thresholds used were 300 for data at $R_\lambda \approx 1300$, and 70 for data at $R_\lambda \approx 400$. The sub-cubes are 51^3 in extent in frames (a), (b) and (c), 31^3 in (d).

robust feature — in all the 8192^3 snapshots examined, the maxima of dissipation and enstrophy are located just one or two grid points apart. However, frame (d), for a lower Reynolds number, is characteristically different: the dominant structure there appears to be vortex filaments which are only partially surrounded by intense dissipation. Peak dissipation and peak enstrophy in the lower Reynolds number data are also not co-located.

The results shown above were reported in Yeung, Zhai, and Sreenivasan (2015), and they seem to suggest that complicated topological changes to the extreme events also accompany the increase of the Reynolds number, as opposed to the conventional notion that the main effect of a higher Reynolds number is a larger degree of scale separation. However recently Yeung, Sreenivasan, and Pope (2018) pointed out that requirements of spatial and temporal resolution become more stringent at high Reynolds numbers, and practices exercised successfully in previous simulations at lower Reynolds numbers need to be re-evaluated. Specifically they found that inadequate resolution in time leads to over-estimation of the occurrences of the most extreme events in dissipation and enstrophy. Moreover as resolution improves, the PDFs of dissipation and enstrophy do not approach

each other in the far tails at high Reynolds number. Since the new findings strongly suggest that errors may arise in the extreme events statistics, it is imperative to re-examine the visualization results of the extreme events at better resolution.

3.1.2 New visualization results at improved temporal/spatial resolution

Since the extreme events of the small-scales are highly localized in space, adequate spatial resolution is important to resolve the fine scale motions. As discussed previously, spatial resolution is expressed by $k_{max}\eta$, and its value is often around 1.5 in simulations aimed at attaining higher Reynolds numbers with a focus on lower order statistics (Ishihara et al., 2016). Even though the 8192^3 simulation uses an increased spatial resolution of $k_{max}\eta = 2$, it is possible that such resolution may still be inadequate to resolve the most extreme events, especially at the higher $R_\lambda = 1300$ when resolution requirements become more demanding at higher Reynolds numbers (Yakhot and Sreenivasan, 2005). In addition to spatial resolution, temporal resolution may also be an issue as extreme events are generally expected to evolve over short time scales. In past simulations, the time step Δt is determined by the Courant number C, which ensures the stability of the numerical scheme when $C < 1$. However whether such a choice would guarantee adequate temporal resolution for the extreme events needs to be further checked. Recently Yeung, Sreenivasan, and Pope (2018) have shown that, although a choice of $C = 0.6$ gives Δt of only around one percent of the Kolmogorov time scale τ_η, errors in time stepping can still be significant when extreme events are considered.

To examine the effects of spatial and temporal resolution, three approaches are taken. The first is to increase spatial resolution $k_{max}\eta$ but to hold the Courant number C and the Reynolds number R_λ fixed. This is a conventional way of assessing the effects of improved spatial resolution. Specifically the velocity field on a coarser grid is read into a finer grid, and the additional Fourier modes that are now present on the fine grid with larger wavenumeber magnitudes are filled with zeros. After some transient time on the order of a few Kolmogorov time scales, the small scales develop naturally and non-trivial values populate the additional Fourier modes. As a result, the spatial resolution $k_{max}\eta$ increases to a desired value set by the finer grid. The second approach is to vary the Courant number C with fixed $k_{max}\eta$ and R_λ, which is intended to study the effects of temporal resolution. Generally the same initial condition is used to run simulations with different Courant numbers that

decrease progressively, say by a factor of 2. For both of the approaches above, comparisons are made against cases of different $k_{max}\eta$ or C and require re-running the simulations. However it is also possible to study the resolution effects by post-processing, especially by filtering (truncating) the high wavenumber contribution progressively on existing snapshots so that spatial resolution is decreased. This approach is motivated by the fact that aliasing errors due to the pseudo-spectral numerical method (see Chap. 2) arise mainly at the high wavenumbers. If a specific topological feature vanishes upon filtering, it may have been contaminated by residual aliasing errors.

Table 3.1: Parameters of the simulations in the study

R_λ		390			650		1300
N	1024^3	2048^3	4096^3	2048^3	4096^3	8192^3	8192^3
$k_{max}\eta$	1.4	2.8	5.6	1.4	2.8	5.6	2.0

To allow direct comparisons with quantitative studies of Yeung, Sreenivasan, and Pope (2018), the same data sets are used in current visualization work. Table 3.1 shows the parameters of the simulations that were performed to address issues of spatial resolution. Since further increasing $k_{max}\eta$ for 8192^3 grids is extremely expensive, coarser grids are used and the Reynolds numbers simulated are lower than $R_\lambda = 1300$. However, $R_\lambda = 650$ is known to be sufficiently high to produce extreme events on the order of $\mathcal{O}(10^4)$ of their mean value, which also possess the "chunky" topological features, while the $R_\lambda = 390$ suite of simulations allow the study of resolution effects at a lower Reynolds number. For each Reynolds number, three values of $k_{max}\eta$ of 1.4, 2.8 and 5.6 are used, and the best spatial resolution resolves up to half of the Kolmogorov length scale $\Delta/\eta \approx 0.5$ (see Eq. 2.9). For each pair of Reynolds number and spatial resolution, three Courant numbers of $C = 0.6$, 0.3 and 0.15 are used to assess effects of temporal resolution. As a result, the combination of 2 Reynolds numbers, each with 3 spatial resolution and simulated with 3 choices of Courant numbers, requires a total of $2 \times 3 \times 3 = 18$ new simulations.

To perform visualizations, subcubes are first obtained using the procedures laid out in Chap. 2. Since the focus of the work is on the extreme events, specific subcubes that contain the most extreme dissipation and enstrophy are singled out for visualization. Generally when the Reynolds number is low, extreme dissipation and enstrophy may not occur in close vicinity and subcubes holding different extreme events are visualized separately. As the Reynolds number increases, there is a stronger tendency for extreme dissipation and enstrophy to be found within the same subcube.

Various visualization techniques have been used in past studies, and in this work contour plots at prescribed threshold are made such that only the structures of intensity above a given threshold are shown. In the previous subsection on results from 8192^3 simulations, the same threshold value was used for both dissipation and enstrophy. Such a choice shows clearly that the most extreme events of both quantities have somewhat chunky topological features that overlap in space. However as Yeung, Sreenivasan, and Pope (2018) have found, the PDFs of $2\epsilon/\langle\epsilon\rangle$ and $\Omega/\langle\Omega\rangle$ are remarkably similar in shape. As a result in the visualizations presented below, the threshold value of dissipation is chosen twice as small as that of enstrophy. Nevertheless it is still useful to use the same threshold values to detect spuriously strong extreme events, since it clearly shows the overlap of the "chunky" topological features, as will be seen later.

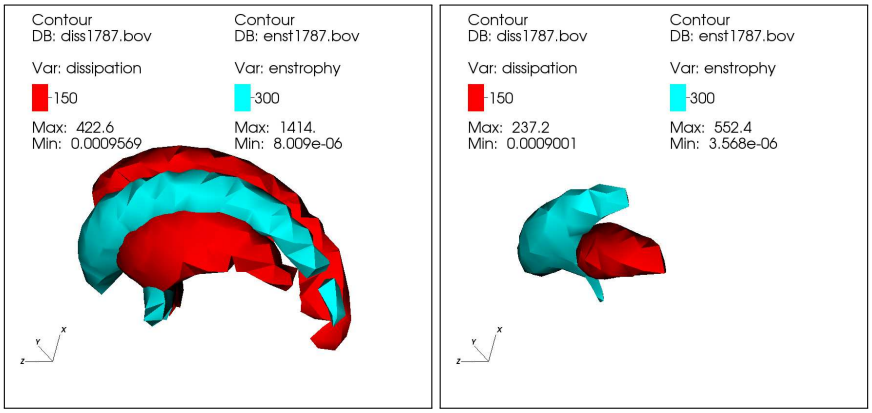

Figure 3.4: Overlaid contour plots of normalized dissipation $\epsilon/\langle\epsilon\rangle$ (red) and enstrophy $\Omega/\langle\Omega\rangle$ (cyan). Contour levels of $\epsilon/\langle\epsilon\rangle = 150$, $\Omega/\langle\Omega\rangle = 300$. LHS at original spatial resolution of $k_{max}\eta \approx 2.8$; RHS at truncated resolution of $k_{max}\eta \approx 1.4$. Zoomed-in region of most extreme enstrophy at $k_{max}\eta \approx 2.8$. $R_\lambda = 390$, 2048^3, $k_{max}\eta \approx 2.8$, $C = 0.15$.

At $R_\lambda = 390$ with spatial resolution $k_{max}\eta = 2.8$, the most extreme dissipation and enstrophy do not occur in the same subcube when simulated with $C = 0.15$, but they do with $C = 0.6$. At $C = 0.15$, Fig. 3.4 and 3.5 show the neighborhoods that contain the most extreme enstrophy and dissipation respectively. In the left frame of both figures, there is clear evidence that intense dissipation sheets at $\epsilon/\langle\epsilon\rangle = 150$ tend to wrap around enstrophy filaments at $\Omega/\langle\Omega\rangle = 300$. The right frame shows the same structures using the same threshold, but with the high wavenumber contribution truncated such that $k_{max}\eta$ is decreased to 1.4. In general the effect of truncating the high wavenumber contribution is to remove the most extreme oscillations from the turbulence signals. Therefore turbulence structures identified by volumes of space where intense activity occurs

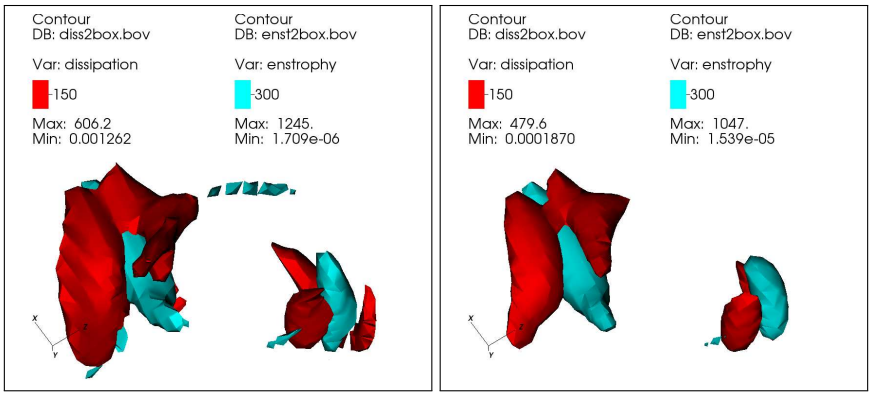

Figure 3.5: Contour levels of $\epsilon/\langle\epsilon\rangle = 150$ (red), $\Omega/\langle\Omega\rangle = 300$ (cyan). LHS at original spatial resolution of $k_{max}\eta \approx 2.8$; RHS at truncated resolution of $k_{max}\eta \approx 1.4$. Zoomed-in region of most extreme dissipation at $k_{max}\eta \approx 2.8$. $R_\lambda = 390$, 2048^3, $k_{max}\eta \approx 2.8$, $C = 0.15$.

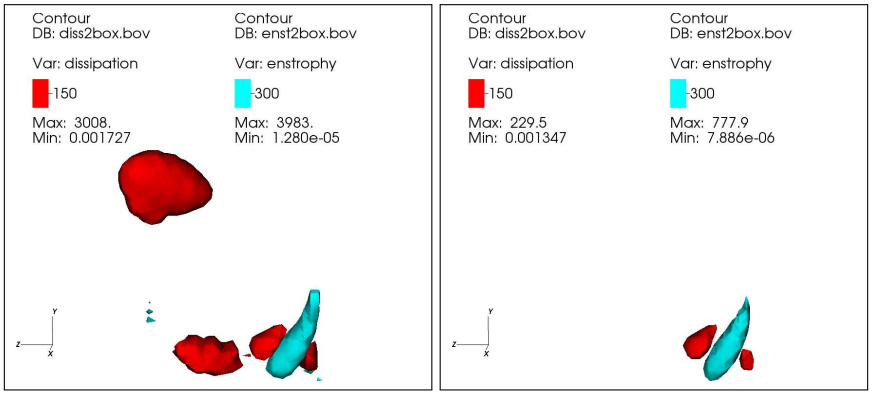

Figure 3.6: Contour levels of $\epsilon/\langle\epsilon\rangle = 150$ (red), $\Omega/\langle\Omega\rangle = 300$ (cyan). LHS at original spatial resolution of $k_{max}\eta \approx 2.8$; RHS at truncated resolution of $k_{max}\eta \approx 1.4$. $R_\lambda = 390$, 2048^3, $k_{max}\eta \approx 2.8$, $C = 0.6$.

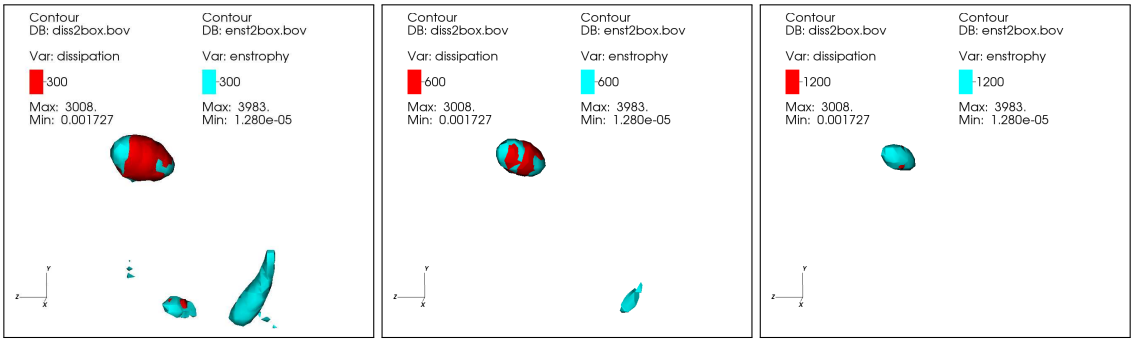

Figure 3.7: All at original spatial resolution of $k_{max}\eta \approx 2.8$. The same contour level is used for dissipation $\epsilon/\langle\epsilon\rangle$ (red) and enstrophy $\Omega/\langle\Omega\rangle$ (cyan), at 300 (left), 600 (middle) and 1200 (right). $R_\lambda = 390$, 2048^3, $k_{max}\eta \approx 2.8$, $C = 0.6$.

become smaller in size as the fluctuating signal is smoothed, which can be seen in the right frames of Fig. 3.4 and 3.5 where the geometrical features of sheets and filaments are relatively robust. In

comparison, at $C = 0.6$ the most extreme dissipation and enstrophy are co-located in space, and appears in a single figure as in Fig. 3.6. In addition to a tiny elongated enstrophy structure accompanied by dissipation blobs nearby, there is a region of intense dissipation that disappears when the high wavenumbers are truncated. In fact, using the same threshold values for $\epsilon/\langle\epsilon\rangle$ and $\Omega/\langle\Omega\rangle$, Fig. 3.7 shows that the region has the property that intense to extreme dissipation and enstrophy are co-located (shown as blobs colored by patches of red and cyan), with the most extreme events residing in the core. Even though this region does not appear "chunky", the geometrical feature is neither sheet-like nor filament-like, and is not robust with respect to a decrease of spatial resolution via filtering high wavenumber contribution. The observation strongly suggests that aliasing errors may have been the cause of such spurious topological features, in agreement with findings in Yeung, Sreenivasan, and Pope (2018).

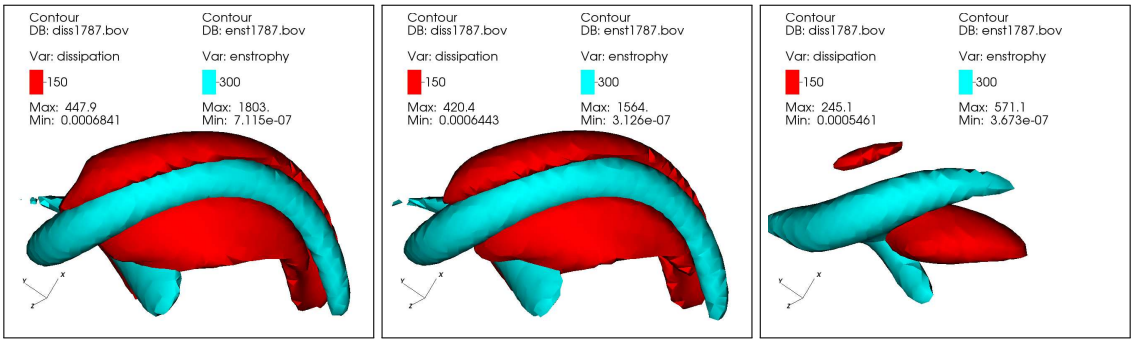

Figure 3.8: Contour levels of $\epsilon/\langle\epsilon\rangle = 150$ (red), $\Omega/\langle\Omega\rangle = 300$ (cyan). Spatial resolution of $k_{max}\eta \approx 5.4$ (left), and truncated to 2.8 (middle) and 1.4 (right). Zoomed-in region of most extreme enstrophy at $k_{max}\eta \approx 5.4$. $R_\lambda = 390$, 4096^3, $k_{max}\eta \approx 5.4$, $C = 0.15$.

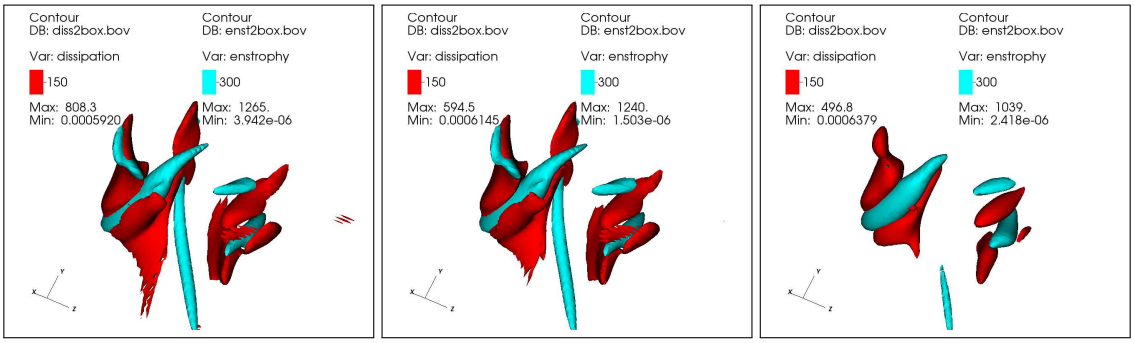

Figure 3.9: Contour levels of $\epsilon/\langle\epsilon\rangle = 150$ (red), $\Omega/\langle\Omega\rangle = 300$ (cyan). Spatial resolution of $k_{max}\eta \approx 5.4$ (left), and truncated to 2.8 (middle) and 1.4 (right). Zoomed-in region of most extreme dissipation at $k_{max}\eta \approx 5.4$. $R_\lambda = 390$, 4096^3, $k_{max}\eta \approx 5.4$, $C = 0.15$.

A similar analysis can be made starting from velocity field at the same $R_\lambda = 390$, but with an

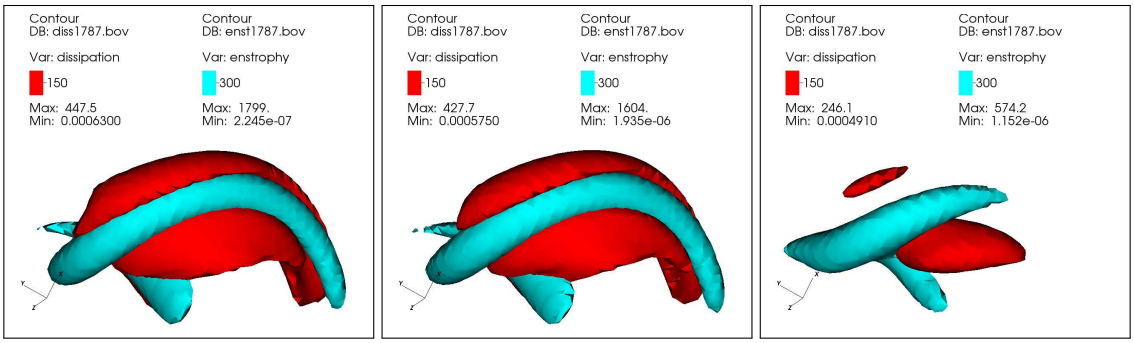

Figure 3.10: Contour levels of $\epsilon/\langle\epsilon\rangle = 150$ (red), $\Omega/\langle\Omega\rangle = 300$ (cyan). Spatial resolution of $k_{max}\eta \approx 5.4$ (left), and truncated to 2.8 (middle) and 1.4 (right). Zoomed-in region of most extreme enstrophy at $k_{max}\eta \approx 5.4$. $R_\lambda = 390$, 4096^3, $k_{max}\eta \approx 5.4$, $C = 0.6$.

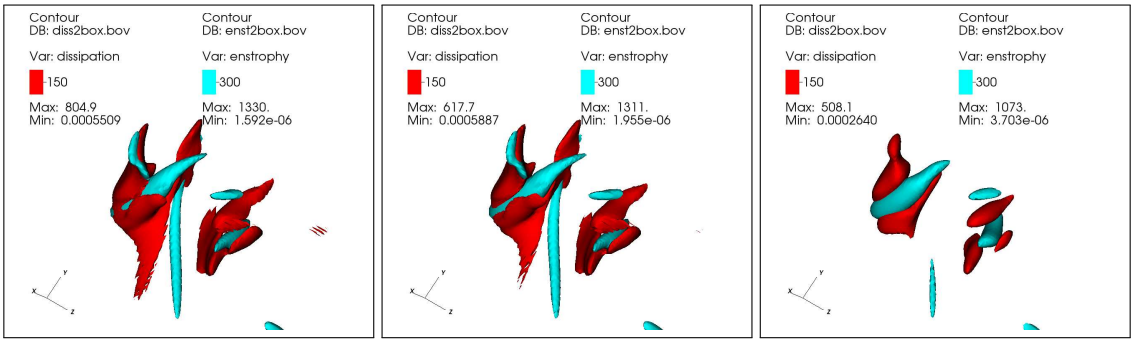

Figure 3.11: Contour levels of $\epsilon/\langle\epsilon\rangle = 150$ (red), $\Omega/\langle\Omega\rangle = 300$ (cyan). Spatial resolution of $k_{max}\eta \approx 5.4$ (left), and truncated to 2.8 (middle) and 1.4 (right). Zoomed-in region of most extreme dissipation at $k_{max}\eta \approx 5.4$. $R_\lambda = 390$, 4096^3, $k_{max}\eta \approx 5.4$, $C = 0.6$.

improved spatial resolution of $k_{max}\eta = 5.4$ such that two levels of truncation of the high wavenumber contribution give decreased $k_{max}\eta = 2.8$ and 1.4 respectively. Using threshold of $\epsilon/\langle\epsilon\rangle = 150$ and $\Omega/\langle\Omega\rangle = 300$, Fig. 3.8 and 3.9 show subcubes that hold the most extreme enstrophy and dissipation simulated with $C = 0.15$, and the same for Fig. 3.10 and 3.11 but with $C = 0.6$. Since most extreme events of dissipation and enstrophy do not occur in a close neighborhood with $k_{max}\eta = 5.4$ for either $C = 0.15$ or $C = 0.6$, two subcubes are visualized for each Courant number C. The observations are remarkably similar to those seen in $k_{max}\eta = 2.8$ and $C = 0.15$: in regions that contain extreme events, dissipation form sheet-like structures that wrap around enstrophy filaments. These geometrical structures become smaller in size upon filtering the high wavenumbers, but the main characteristics remain largely intact. In particular, with improved $k_{max}\eta = 5.4$ there is no evidence of "chunky" structure even when $C = 0.6$ is used. This is in clear contrast to cases with $k_{max}\eta = 2.8$ and $C = 0.6$, where Fig. 3.6 and 3.7 show spurious topological features that disap-

pear as high wavenumber contribution is filtered. The observation suggests that at a low Reynolds number of $R_\lambda = 390$, improved spatial resolution of $k_{max}\eta = 5.4$ allows the use of $C = 0.6$ in producing physical and robust visualization results.

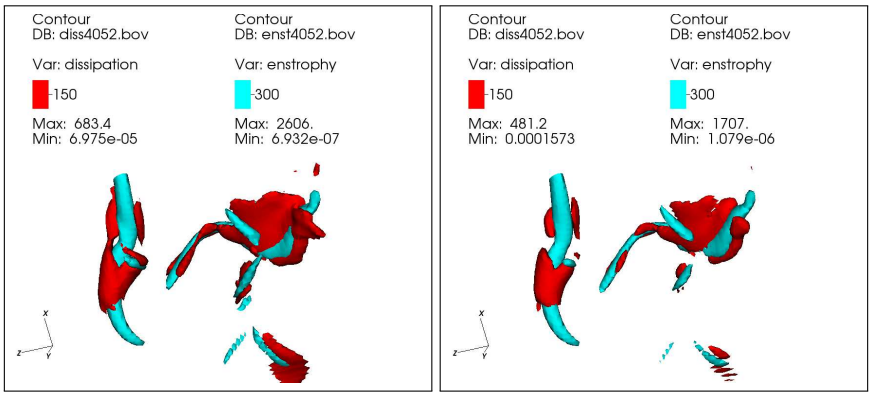

Figure 3.12: Contour levels of $\epsilon/\langle\epsilon\rangle = 150$ (red), $\Omega/\langle\Omega\rangle = 300$ (cyan). LHS at original spatial resolution of $k_{max}\eta \approx 2.8$; RHS at truncated resolution of $k_{max}\eta \approx 1.4$. Zoomed-in region of most extreme enstrophy at $k_{max}\eta \approx 2.8$. $R_\lambda = 650$, 4096^3, $k_{max}\eta \approx 2.8$, $C = 0.15$.

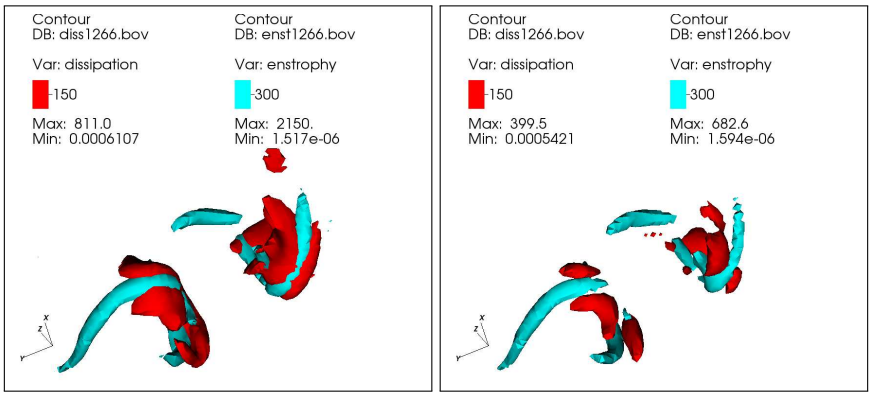

Figure 3.13: Contour levels of $\epsilon/\langle\epsilon\rangle = 150$ (red), $\Omega/\langle\Omega\rangle = 300$ (cyan). LHS at original spatial resolution of $k_{max}\eta \approx 2.8$; RHS at truncated resolution of $k_{max}\eta \approx 1.4$. Zoomed-in region of most extreme dissipation at $k_{max}\eta \approx 2.8$. $R_\lambda = 650$, 4096^3, $k_{max}\eta \approx 2.8$, $C = 0.15$.

In general, as the Reynolds number increases, the small scales become more intermittent, leading to extreme events of larger magnitude. As a result, higher threshold values of the contour surfaces can be used than those at lower Reynolds numbers. Fig. 3.12 and 3.13 show the neighborhoods that contain the most extreme enstrophy and dissipation respectively at a higher Reynolds number of $R_\lambda = 650$ with $k_{max}\eta = 2.8$ and $C = 0.15$. As with the case at $R_\lambda = 390$, when a small Courant number of $C = 0.15$ is used, intense dissipation sheets of $\epsilon/\langle\epsilon\rangle = 150$ tend to wrap around enstrophy filaments of $\Omega/\langle\Omega\rangle = 300$. Also these structures remain robust upon filtering the high

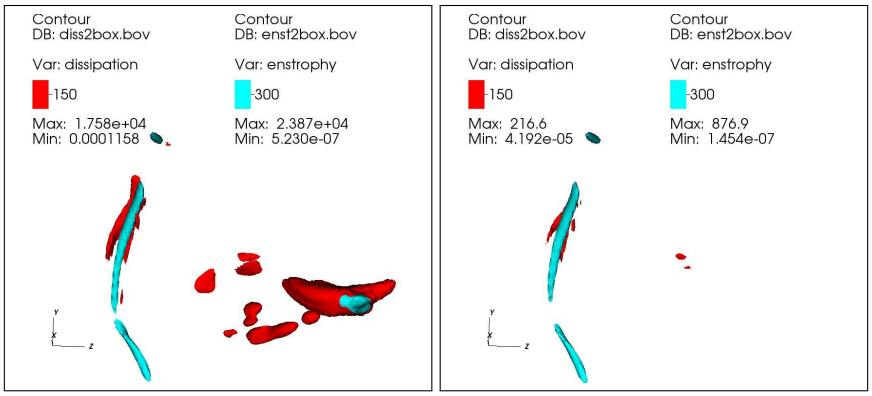

Figure 3.14: The same as before, but use only one set of contour levels $\epsilon/\langle\epsilon\rangle = 150$ (red), $\Omega/\langle\Omega\rangle = 300$ (cyan). $R_\lambda = 650$, 4096^3, $k_{max}\eta \approx 2.8$, $C = 0.6$.

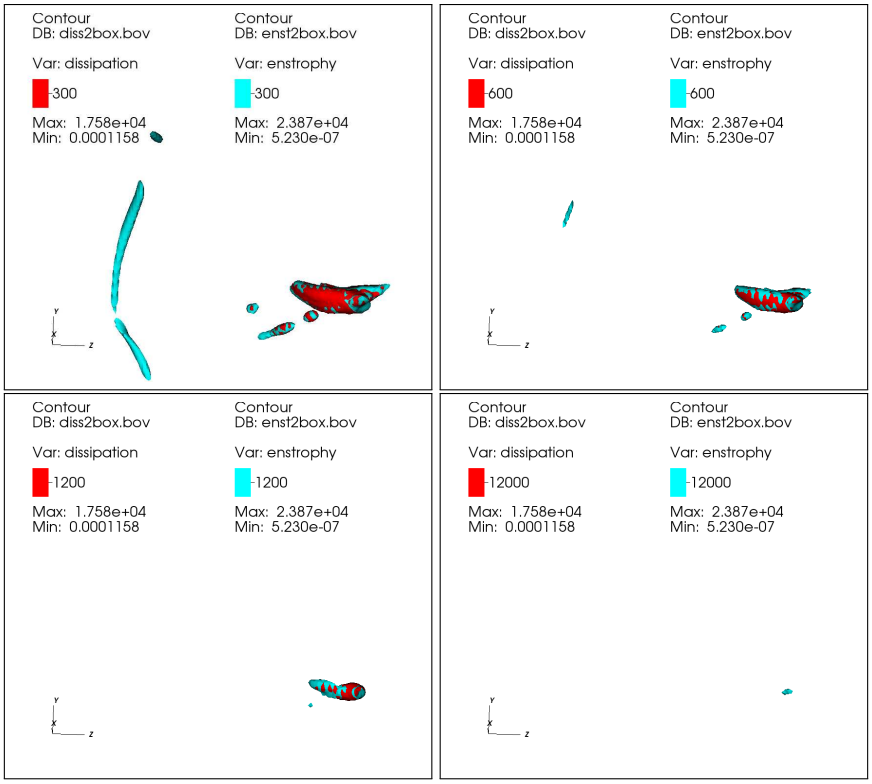

Figure 3.15: At the original resolution of $k_{max}\eta \approx 2.8$, but with the same contour level for dissipation $\epsilon/\langle\epsilon\rangle$ (red) and enstrophy $\Omega/\langle\Omega\rangle$ (cyan), at 300, 600,1200 and 12000. $R_\lambda = 650$, 4096^3, $k_{max}\eta \approx 2.8$, $C = 0.6$.

wavenumber contribution. However at this higher $R_\lambda = 650$, the volume of the intense events decreases less when the resolution is truncated to $k_{max}\eta = 1.4$, than that at a lower Reynolds number (e.g. see Fig. 3.4 and 3.5). Since $C = 0.6$ is seen to lead to spurious behaviors of the extreme events at $R_\lambda = 390$, it is expected that $C = 0.6$ is not adequate at a higher $R_\lambda = 650$ either, as resolution

requirements become more stringent. Indeed Fig. 3.14 shows the contour surfaces of $\epsilon/\langle\epsilon\rangle = 150$ and $\Omega/\langle\Omega\rangle = 300$ at $R_\lambda = 650$ with $k_{max}\eta = 2.8$ and $C = 0.6$. Even though the slender enstrophy filament and accompanied dissipation sheets decrease their volume minimally as spatial resolution is reduced to $k_{max}\eta = 1.4$, a somewhat "chunky" region, which was visible at original resolution of $k_{max}\eta = 2.8$, appears to vanish totally. Similar as before, to better show the co-location behavior of the "chunky" topological feature, Fig. 3.15 uses the same threshold values for $\epsilon/\langle\epsilon\rangle$ and $\Omega/\langle\Omega\rangle$ at the original resolution of $k_{max}\eta = 2.8$ with $C = 0.6$. It is evident that intense dissipation and enstrophy remain co-located as the threshold value increases, until the threshold value becomes too large to visualize the structures.

Earlier it is seen that at $R_\lambda = 390$ and with improved spatial resolution of $k_{max}\eta = 5.4$, there is no sign of "chunky" structures when either $C = 0.15$ or $C = 0.6$ is used. Now still with improved spatial resolution of $k_{max}\eta = 5.4$ but at a higher $R_\lambda = 650$, Fig. 3.16 shows visualization results with $C = 0.15$ while Fig. 3.17 and 3.18 for $C = 0.6$. When $C = 0.15$, three sets of threshold values for the contour surfaces are used in Fig. 3.16. It is seen that dissipation sheets wrap around enstrophy filaments, even up to $\epsilon/\langle\epsilon\rangle = 600$ and $\Omega/\langle\Omega\rangle = 1200$. The volume of the structures decreases as threshold value is increased, but no "chunky" structure is seen, which suggests $C = 0.15$ gives reliable results. In comparison when $C = 0.6$ is used, even though Fig. 3.17 appears to show similar behaviors of the extreme events as before, a close examination does reveal hints of spurious behavior. In particular, the peak amplitudes of dissipation and enstrophy are above 10^4 at the original spatial resolution of $k_{max}\eta = 5.4$ (left column), but the peak values decrease substantially below 2000 when high wavenumber contribution is truncated and $k_{max}\eta$ is reduced to 2.8 (center column). In fact using the same threshold values for dissipation and enstrophy, Fig. 3.18 shows that a "chunky" structure lies at the intersection of the two enstrophy filaments, which is not visible when lower threshold values are used. Increasing the threshold value, however, reveals its existence. The observation suggests that $C = 0.6$ can give un-physical results at $R_\lambda = 650$, despite of improved spatial resolution.

3.1.3 Summary of the resolution effects on the extreme events

Table 3.2 gives a summary of the visualization results shown so far, where "✓" denotes the observation of reliable results that dissipation sheets wrap around enstrophy filaments, without topological

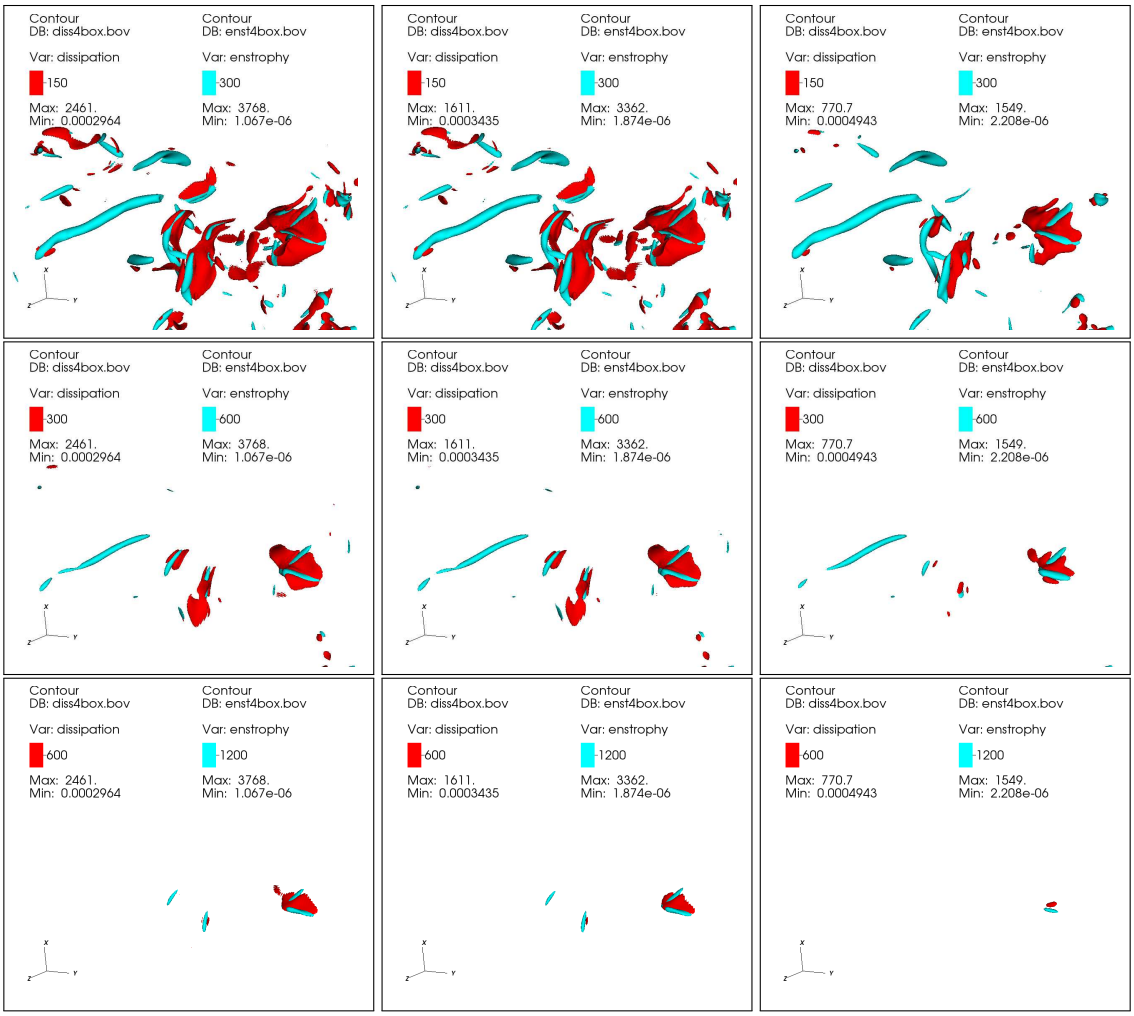

Figure 3.16: Contour levels of $\epsilon/\langle\epsilon\rangle = 150$, $\Omega/\langle\Omega\rangle = 300$ (top); $\epsilon/\langle\epsilon\rangle = 300$, $\Omega/\langle\Omega\rangle = 600$ (middle row); $\epsilon/\langle\epsilon\rangle = 600$, $\Omega/\langle\Omega\rangle = 1200$ (bottom); Spatial resolution of $k_{max}\eta \approx 5.4$ (left), and truncated to 2.8 (center) and 1.4 (right). The most extreme enstrophy (cyan) and dissipation (red) are roughly co-located at $k_{max}\eta \approx 5.4$ in this simulation. $R_\lambda = 650$, 8192^3, $k_{max}\eta \approx 5.4$, $C = 0.15$.

Table 3.2: Summary of visualization results at different spatial and temporal resolution. If the conventional picture that dissipation sheets wrap enstrophy filaments is observed with no sign of topological features of "chunky" structures, a "✓" is tabulated.

R_λ	grids	$k_{max}\eta$	C=0.15	C=0.6
390	2048^3	2.8	✓	
390	4096^3	5.4	✓	✓
650	4096^3	2.8	✓	
650	8192^3	5.4	✓	

features of "chunky" structures. It seems that $C = 0.15$ is generally a safe choice for all the spatial resolution and Reynolds numbers explored, while $C = 0.6$ is acceptable only when spatial reso-

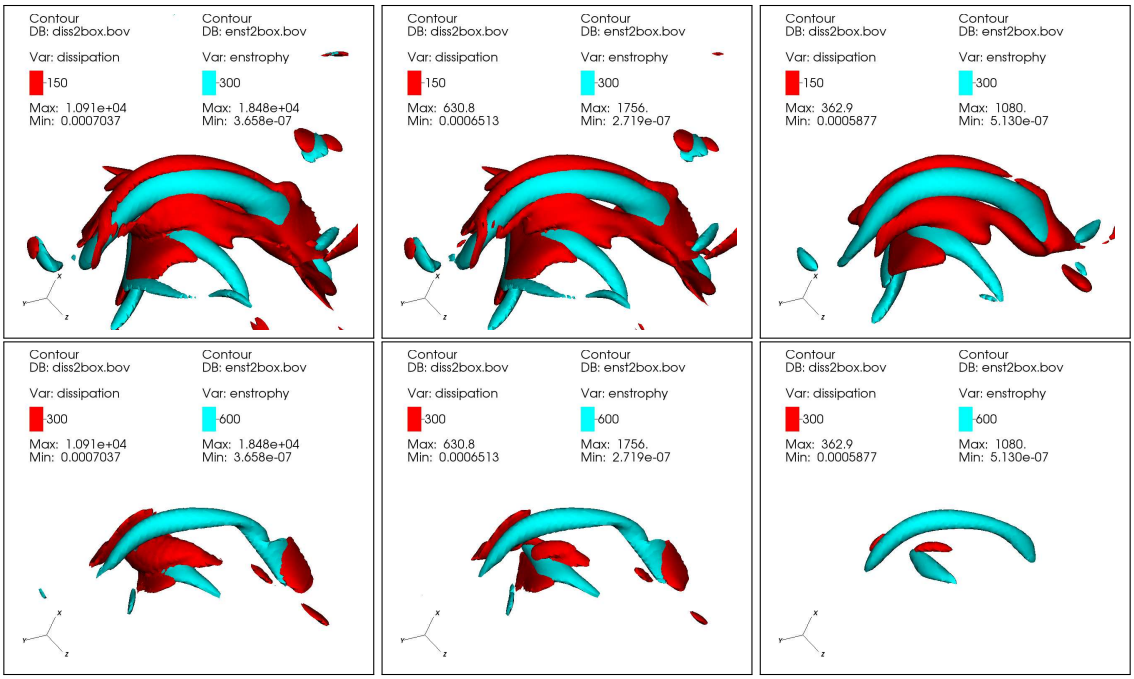

Figure 3.17: Contour levels of $\epsilon/\langle\epsilon\rangle = 150$, $\Omega/\langle\Omega\rangle = 300$ (top); $\epsilon/\langle\epsilon\rangle = 300$, $\Omega/\langle\Omega\rangle = 600$ (bottom). Spatial resolution of $k_{max}\eta \approx 5.4$ (left), and truncated to 2.8 (middle) and 1.4 (right). The most extreme enstrophy (cyan) and dissipation (red) are roughly co-located at $k_{max}\eta \approx 5.4$ in this simulation. $R_\lambda = 650$, 8192^3, $k_{max}\eta \approx 5.4$, $C = 0.6$.

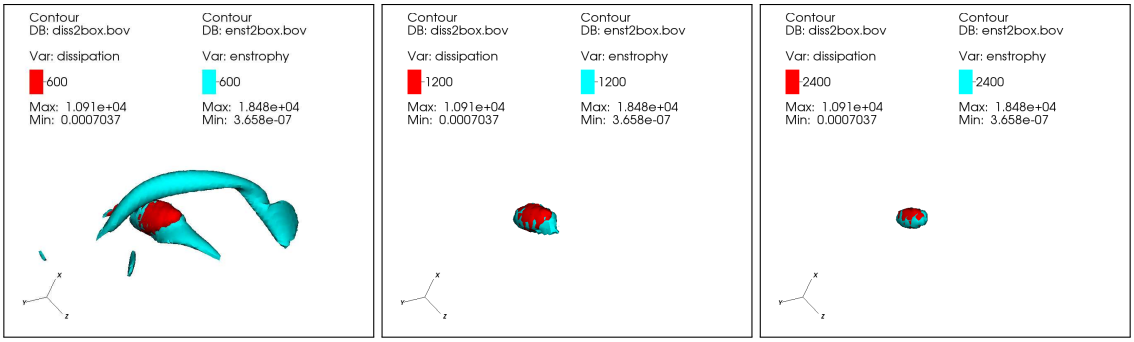

Figure 3.18: All at $k_{max}\eta \approx 5.4$, but the same contour levels of $\epsilon/\langle\epsilon\rangle = \Omega/\langle\Omega\rangle$ (from left to right) 600, 1200 and 2400. $R_\lambda = 650$, 8192^3, $k_{max}\eta \approx 5.4$, $C = 0.6$.

lution is much better (at $k_{max}\eta = 5.4$) than that often used, and also when the Reynolds number is low. For other combinations of spatial and temporal resolution, spurious behaviors may arise as evidenced by the "chunky" structures, which have two characteristics. First, they are highly susceptible to truncation of the high wavenumber contribution, and as a result vanish at reduced/truncated spatial resolution. Second, the "chunky" structures occupy a region where extreme dissipation and enstrophy are co-located, which is best seen when the same threshold values of contour surfaces

are used. In comparison, the choice of $2\epsilon/\langle\epsilon\rangle = \Omega/\langle\Omega\rangle$ in the threshold values generally shows dissipation sheets and enstrophy filaments well, and such a choice is consistent with the finding that PDFs of $2\epsilon/\langle\epsilon\rangle$ and $\Omega/\langle\Omega\rangle$ scale similarly (Yeung, Sreenivasan, and Pope, 2018).

Since the 8192^3 simulation (Yeung, Zhai, and Sreenivasan, 2015) used $C = 0.6$ at $R_\lambda = 1300$ and $k_{max}\eta = 2$, given the studies of resolution effects presented above it is highly likely that the extreme events may not have been adequately resolved both spatially and temporally, and therefore the visualization of the extreme events reported may not be physical. The visualization results presented here clarify that topological features of the extreme events are still sheet-like for dissipation and filament-like for enstrophy, at least up to $R_\lambda = 650$. The results also show how aliasing error may appear when inadequate resolution is used. Furthermore, the results support the notion that resolution requirements become more demanding as Reynolds number is increased (Yakhot and Sreenivasan, 2005; Yeung, Sreenivasan, and Pope, 2018), and advocate the use of finer grids and smaller time steps when even larger simulations are attempted in the future.

3.2 Sign oscillation characteristics in the small-scales

Velocity gradients representing small-scale motions in turbulence are typically characterized by substantial magnitude variations as shown in the previous section, as well as strong oscillations in sign. The sign oscillations can be studied by considering the averages of the signals over some interval in space or time, where cancellations between positive and negative signs occur. The characteristics of the sign cancellation which depend on the scale size of the averaging interval can be quantified by the cancellation exponent, whose values however depend on the dimensionality of the averaging interval. In this section, the concept of sign oscillation and cancellation exponent is first given. The focus here is on the differences of the values of cancellation exponents obtained in different dimensions. The prevalence of coherent structures with an increased degree of coherency in one direction is proposed as the cause. A specific example is provided by the elongated vortex structures aligned with a fixed magnetic field in magnetohydrodynamic turbulence.

3.2.1 Mathematical background and computational formulation

Small scale motions in fluid turbulence exhibit fluctuations of positive and negative signs, in both space and time. If oscillations in sign continue to occur no matter how small a spatial or temporal interval is probed, a form of singularity can be said to exist. which is known as sign-singularity (Ott et al., 1992; Du, Tél, and Ott, 1994; Vainshtein et al., 1994). Since oscillations of the sign introduce cancellation of the signal when averaged within a spatial or temporal interval, sign singularity can be quantified by the so called "cancellation exponent", which characterizes how the averaged signal depends on the scale size. Because turbulence signals are continuous at the smallest scales, in general a cancellation exponent is sought in the inertial range.

Mathematically the idea is made clear with the introduction of a signed measure $\mu_i(l)$ at some scale l:

$$\mu_i(l) = \frac{\int_{Q_i(l)} d\mathbf{r} f(\mathbf{r})}{\int_{Q(L)} d\mathbf{r} |f(\mathbf{r})|} \tag{3.2}$$

where $Q_i(l)$ denotes a hierarchy of disjoint subsets of size l covering the entire domain $Q(L)$ of size L, and $f(\mathbf{r})$ is a scalar field with a zero mean value. The denominator is chosen to bound $\mu_i(l)$ between $[-1, 1]$, thus making it a signed probability measure. The sum of the absolute values of all the signed probability measures gives rise to the partition function $\chi(l)$ defined as

$$\chi(l) = \sum_{Q_i(l)} |\mu_i(l)|. \tag{3.3}$$

Since $\chi(l) = 1$ if $f(\mathbf{r})$ is sign-definite, sign-singularity is readily reflected in non-unity $\chi(l)$, which is possible only when cancellations of opposite signs occur in the numerator of Eq. 3.2. Therefore, to measure the propensity of the quantity considered to cancel out when averaged over a region of space or an interval of time, the "cancellation exponent" κ is defined (Ott et al., 1992; Du, Tél, and Ott, 1994) via

$$\chi(l) \sim l^{-\kappa} \tag{3.4}$$

Clearly, sign-definite signals have $\kappa = 0$.

To help understand the properties of cancellation exponent, Fig. 3.19 shows simple 1D signals of square wave, sinusoidal wave and standard Wiener process (Brownian motion) as well as their

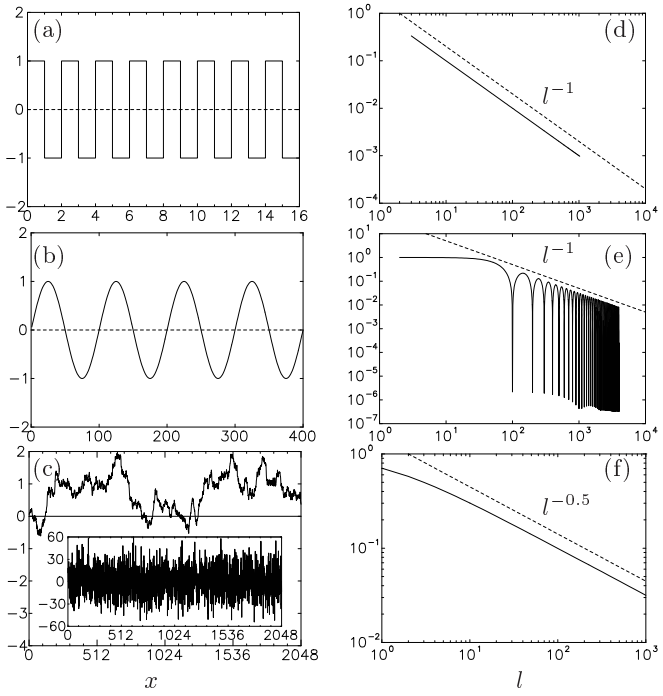

Figure 3.19: Signals of (a) a square wave with magnitude of unity; (b) a sinusoidal wave $y(x) = \sin\big((2\pi/100)x\big)$ with a period of 100; (c) a standard Wiener process (Brownian motion) where the inset shows the ratio of step-wise increment and unit step size. For brevity, (a) (b) show only a few periods of the signal. Partition functions ($\chi(l)$) of signal (a-c) are shown in (d-f). Dashed lines mark power-law behaviors.

partition functions. In Fig. 3.19 (a) for the square wave extending from $x = 0$ to $2n$ (where n is an integer), the signed measure $\mu_i(l)$ is zero when l is even, and $\pm 1/(2n)$ when l is odd. Since the number of disjoint subsets at size l is $(2n)/l$, following Eq. 3.3 the partition function $\chi(l) = \sum_{Q_i(l)} |\mu_i(l)| = (2n)/l \times 1/(2n) = 1/l$ for odd values of l, and zero otherwise. As a result, plotting $\chi(l)$ as a function of odd numbers of l only, Fig. 3.19 (d) shows that the cancellation exponent $\kappa = 1$, which is known to be the case for non-differentiable signals (Vainshtein et al., 1994). In Fig. 3.19 (b) for the sinusoidal wave with a period of 100, the integral in the numerator of Eq. 3.2 vanishes when the interval size l takes multiples of the period and $\chi(l)$ is zero. Indeed, very small values of $\chi(l)$ are seen in Fig. 3.19 (e) for l equal to any integral multiple of the period. Since finite numerical accuracy prevents the occurrence of exact zero, the small values of $\chi(l)$ appear as deep valleys. Furthermore, the signed measure $\mu_i(l)$ depends strongly on the interval size l, resulting in large variations of $\chi(l)$. The envelope, as expected, has a slope of -1. In Fig. 3.19 (c) for the standard Wiener process (Brownian motion), the ratio of the stepwise increment and step size (shown in the

inset) is highly oscillatory, and is known (Bertozzi and Chhabra, 1994) to correspond to $\kappa = 0.5$. Good agreement with $\kappa = 0.5$ can be seen in Fig. 3.19 (f).

The examples constructed above show that even simple signals can be sign-singular. In fact, sign-singularity is ubiquitous in nature, such as in more sophisticated signals in magnetohydrodynamics (MHD) (Sorriso-Valvo et al., 2002; Graham, Mininni, and Pouquet, 2005; Martin et al., 2013), solar activities (Carbone and Bruno, 1997; Consolini and Lui, 1999; Carbone et al., 2010; Sorriso-Valvo et al., 2015), geomagnetic field (De Michelis, Consolini, and Meloni, 1998), helical flows (Imazio and Mininni, 2010), rotating turbulence (Horne and Mininni, 2013) and aspects of classical turbulence (Ott et al., 1992; Du, Tél, and Ott, 1994; Vainshtein et al., 1994). As another example, Fig. 3.20 shows line traces of longitudinal velocity gradient $\partial u/\partial x$ and vorticity component $\omega_z = \partial u/\partial y - \partial v/\partial x$ from direct numerical simulations (DNS) of isotropic turbulence with a Taylor-scale Reynolds number $R_\lambda = 400$. Both quantities oscillate strongly in sign, with vorticity exhibiting greater intermittency than the longitudinal velocity gradient.

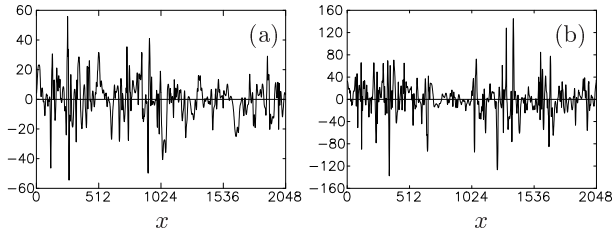

Figure 3.20: Line traces of (a) longitudinal velocity gradient $\partial u/\partial x$ and (b) vorticity component $\omega_z = \partial u/\partial y - \partial v/\partial x$ from a simulation of isotropic turbulence at $R_\lambda = 400$ on a 2048^3 grid.

One key element of the analysis is to contrast cancellation exponent κ obtained from 1D, 2D and 3D measures. As a result the meaning of $Q_i(l)$ and $Q(L)$ in Eq. 3.2 depends on the dimensionality of the measure: $Q_i(l)$ can come from line segments (1D), square areas (2D) and cubes (3D), all with edge length of l; $Q(L)$ can come from box length L, side area L^2 and volume L^3. The use of 2D domain decomposition (Donzis, Yeung, and Pekurovsky, 2008) in the simulations poses computational challenges for 2D and 3D measures as data needed for evaluating Eq. 3.2 may be distributed among multiple processors, but strategies such as prefix sums (Iyer, 2014) have been adopted to reduce computation and communication loads. To allow for direct comparisons with experiments (e.g. Vainshtein et al. (1994)), 2D measures are recovered through the application of Stokes theorem. Taking vorticity component as an example, the circulation $\Gamma_A(l)$ of the velocity

field $\mathbf{v}$ around a closed loop $\mathbf{s}$ surrounding an area $A = l^2$ is

$$\Gamma_A(l) = \oint \mathbf{v} d\mathbf{s} = \int_A \omega \cdot \mathbf{n} dA \tag{3.5}$$

If the circulation scales as $\langle |\Gamma_A(l)|^q \rangle \sim l^{\alpha_q}$ (where q is any real number), it is shown (Vainshtein et al., 1994) that $\alpha_q = (2-\kappa)q - (D - D_q)(q-1)$, where the space dimension $D = 3$ and D_q is the generalized dimension (Mandelbrot, 1974; Hentschel and Procaccia, 1983). For $q = 1$, clearly $\kappa = 2 - \alpha_1$.

An unresolved question in the study of cancellation exponents is whether and how different types of calculation methods affect the results. While some theoretical results connect lower dimensional results with those in three-dimensions (see, e.g., Mandelbrot (1974), Sreenivasan (1991), and Vainshtein et al. (1994)), it is not clear that they should work for real quantities in arbitrary flows. Experimental data analysis suggests that measurements over spatial extent of different dimensions are different. Past 2D measures of cancellation exponent for vorticity were larger, with $\kappa = 0.85$(Vainshtein et al., 1994), than 1D measures, $\kappa = 0.45$ (Ott et al., 1992) and $\kappa = 0.6$ (Vainshtein, Du, and Sreenivasan, 1994). These differences indicate that 1D measures are "blind" to structures with dimensions less than two, and assessment in higher dimensions might be quite necessary for turbulent quantities (Vainshtein et al., 1994). However, partly due to difficulties of experimentally making measurements in 3D, a thorough comparison of cancellation exponents measured in all three dimensions has not been made. It follows that the underlying causes of the differences by measures of different dimensions have not been clearly identified.

3.2.2 Results of cancellation exponents in isotropic turbulence

Table 3.3 summarizes the data used in the analysis from DNS of homogeneous isotropic turbulence that spans the Reynolds number R_λ range from 140 to 1300. Since the cancellation exponents are defined in the inertial range, resolution effects are mild. Nevertheless spatial resolution $k_{max}\eta \geq 2$ is used. To improve statistical sampling, results are averaged over N_R number of realizations.

Since cancellation exponents are simply the scaling exponents of the partition function, it is instructive to plot both quantities side by side, as shown in Fig. 3.21 for vorticity measured in 1D and 2D cuts as well in 3D in homogeneous isotropic turbulence at $R_\lambda = 650$. Instead of fitting straight

Table 3.3: Data sets of isotropic turbulence used in the analysis. R_λ is the Taylor-scale Reynolds number. Spatial resolution is denoted by $k_{max}\eta$. N is the number of grid points along each side of the cubic domain. N_R denotes the number of realizations used for ensemble-averaging.

R_λ	140	240	400	650	1300
$k_{max}\eta$	5.6	5.6	2.7	2.7	2
N	1024	2048	2048	4096	8192
N_R	8	14	16	12	6

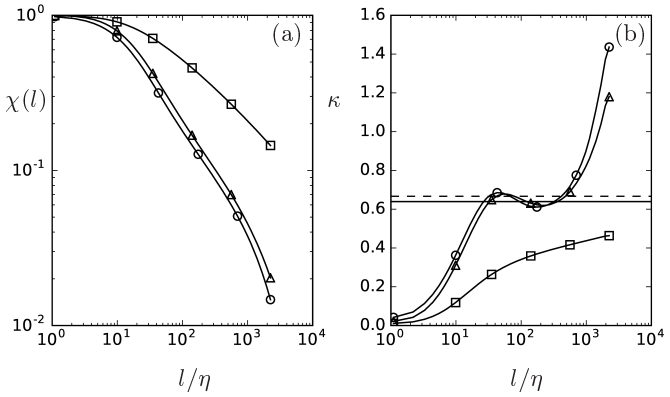

Figure 3.21: (a) Partition function and (b) cancellation exponent κ (see Eqs. 3.3 and 3) for measures of $1D$ ($\square$), $2D$ ($\triangle$) and $3D$ ($\bigcirc$). Horizontal dashed line marks $2/3$, and solid line marks 0.639 as a result of log-normal correction for intermittency with the exponent $\mu = 0.25$. Data are ensemble averaged at $R_\lambda = 650$, 4096^3.

lines in the log-log plots of $\chi(l)$, the plateau regions in the local slopes $-d\,log\,[\chi(l)]/d\,log\,(l)$ are used to obtain the value of cancellation exponent. For small values of l/η viscosity smooths the signals and weakens sign cancellations rendering $\chi(l)$ close to 1, as confirmed in Fig. 3.21 (a). Figure 3.21 (b) shows that plateaus indeed exist for 2D and 3D measures at around $50 < l/\eta < 400$, which is consistent with the inertial range identified in previous work (Iyer, Sreenivasan, and Yeung, 2017). Furthermore 2D and 3D measures give similar values of $\kappa \approx 2/3$, larger than what one may infer from the 1D measure, which does not show a convincing scaling in the first place.

The relationship between cancellation exponent and other scaling exponents in turbulence (Vainshtein, Du, and Sreenivasan, 1994; Vainshtein et al., 1994) can be used to explain the value of $2/3$. Consider the generalized structure function at order q where q is any real number (Vainshtein et al., 1994). In the inertial range, $\langle|\Delta u|^q\rangle \sim l^{\zeta_q}$ and the scaling exponent ζ_q is related to the cancellation exponent κ by

$$\zeta_q = (1-\kappa)q - (D - D_q)(q-1) \tag{3.6}$$

where dimension of space $D = 3$ and D_q is the generalized dimension (Mandelbrot, 1974; Hentschel and Procaccia, 1983). At $q = 1$, the equation becomes $\zeta_1 = 1 - \kappa$. If the effects of intermittency are neglected, Kolmogorov's hypothesis (Kolmogorov, 1941) gives $\zeta_1 = 1/3$ and thus $\kappa = 2/3$; whereas refined similarity hypothesis (Kolmogorov, 1962) gives $\zeta_1 = 0.361$ and $\kappa = 0.639$ (using lognormal correction as an example of intermittency model with intermittency exponent $\mu = 0.25$ (Sreenivasan and Kailasnatth, 1993)). It is clear from Fig. 3.21 (b) that cancellation exponents $\kappa \approx 2/3$ measured in 2D and 3D, but not the 1D measure, are in good agreement with theoretical expectations.

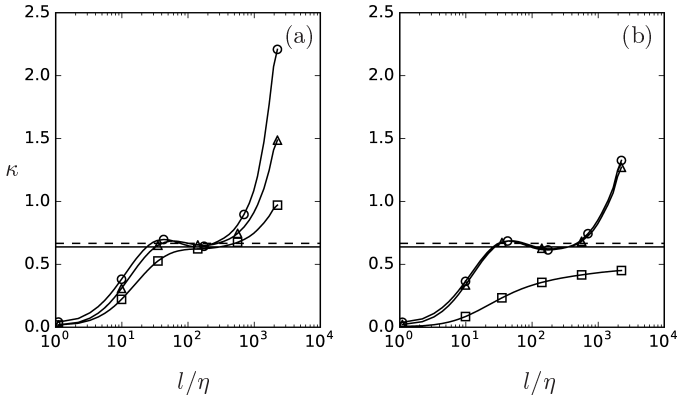

Figure 3.22: Cancellation exponent κ of (a) longitudinal velocity gradients and (b) transverse velocity gradients for measures of $1D$ (□), $2D$ (△) and $3D$ (◯). Horizontal dashed and solid lines mark $2/3$ and 0.639, respectively, as in Fig. 3.21. Data are ensemble averaged at $R_\lambda = 650$, 4096^3.

To see whether measurements in different dimensions have an effect on other small scale quantities, similar calculations for longitudinal and transverse velocity gradients have been performed. Figure 3.22 shows that while transverse velocity gradients behave similarly to vorticity, longitudinal velocity gradients are seen to have the same cancellation exponents $\kappa \approx 2/3$ for all three dimensions. To interpret the value of $2/3$ of the longitudinal velocity gradient using 1D measure, it may be noted that the Hölder exponent α (for the first order structure function) of the velocity increment is related to the cancellation exponent of the velocity derivative κ_1 as $\kappa_1 = 1 - \alpha$ (Bertozzi and Chhabra, 1994). Again by the Kolmogorov hypothesis (Kolmogorov, 1941), the Hölder exponent $\alpha = 1/3$ and $\kappa_1 = 2/3$. Figure 3.22 (a) suggests that this relation holds in 2D and 3D as well. The close similarity between cancellation exponents for transverse velocity gradients (Fig. 3.22 (b)) and for vorticity (Fig. 3.21) is perhaps not surprising, as vorticity is composed of algebraic combinations of transverse velocity gradients.

Table 3.4: Cancellation exponent κ for vorticity obtained from past experiments, using 1D ($D = 1$) and 2D ($D = 2$) measurements.

D	κ	experimental method
1	0.45	1D cuts of one vorticity component behind cylinder wake (Ott et al., 1992)
1	0.6	velocity difference over variable time interval $\Delta u/\Delta t$ in atmospheric flow (Ott et al., 1992; Vainshtein, Du, and Sreenivasan, 1994)
2	0.85	2D circulation data behind cylinder wake (Vainshtein et al., 1994; Sreenivasan, Juneja, and Suri, 1995)

To compare the results with past data, Table 3.4 lists the cancellation exponents κ of vorticity measured in past experiments with a brief summary of the experimental method employed. The lower value of $\kappa = 0.45$ is likely due to the use of 1D measure, as reproduced in Fig. 3.21. The data for $\kappa = 0.6$ comes from atmospheric flow measurements where velocity differences over variable sampling time interval (i.e. $\Delta u/\Delta t$) were actually measured (Ott et al., 1992). Yet, the data were previously interpreted as vorticity statistics et al. (Vainshtein, Du, and Sreenivasan, 1994), via the use of Taylor's frozen-turbulence hypothesis. Strictly speaking, the $\kappa = 0.6$ result is a confirmation of the relation between the Hölder exponent of a signal and its derivative (Bertozzi and Chhabra, 1994), similar to results of $\kappa \approx 2/3$ in longitudinal velocity gradients in Fig. 3.22 (a), rather than vorticity. The $\kappa = 0.85$ result measured from 2D circulation data behind cylinder wake (Sreenivasan, Juneja, and Suri, 1995) is qualitatively consistent with a larger cancellation exponents by 2D and 3D measures from numerical simulations (Fig. 3.21), but current numerical simulations do not have the anisotropy of the cylinder wake.

To examine the Reynolds number dependence of cancellation exponents, Fig. 3.23 shows cancellation exponents computed for vorticity, longitudinal and transverse velocity gradients using 1D, 2D and 3D measures, from $R_\lambda = 140$ to 1300. At higher Reynolds numbers a more extensive scaling range appears as expected, and coincides with the inertial range reported previously (Iyer, Sreenivasan, and Yeung, 2017). The general observation is that 2D and 3D cancellation exponents for vorticity and transverse velocity gradients give similar values but larger than 1D measure, which does not show convincing plateaus. In comparison for longitudinal velocity gradients, measures of different dimensions give similar cancellation exponents. The plateau is not perfect, but the values oscillate around $\kappa \approx 2/3$, perhaps due to a conspicuous bottleneck effect (Donzis and Sreenivasan,

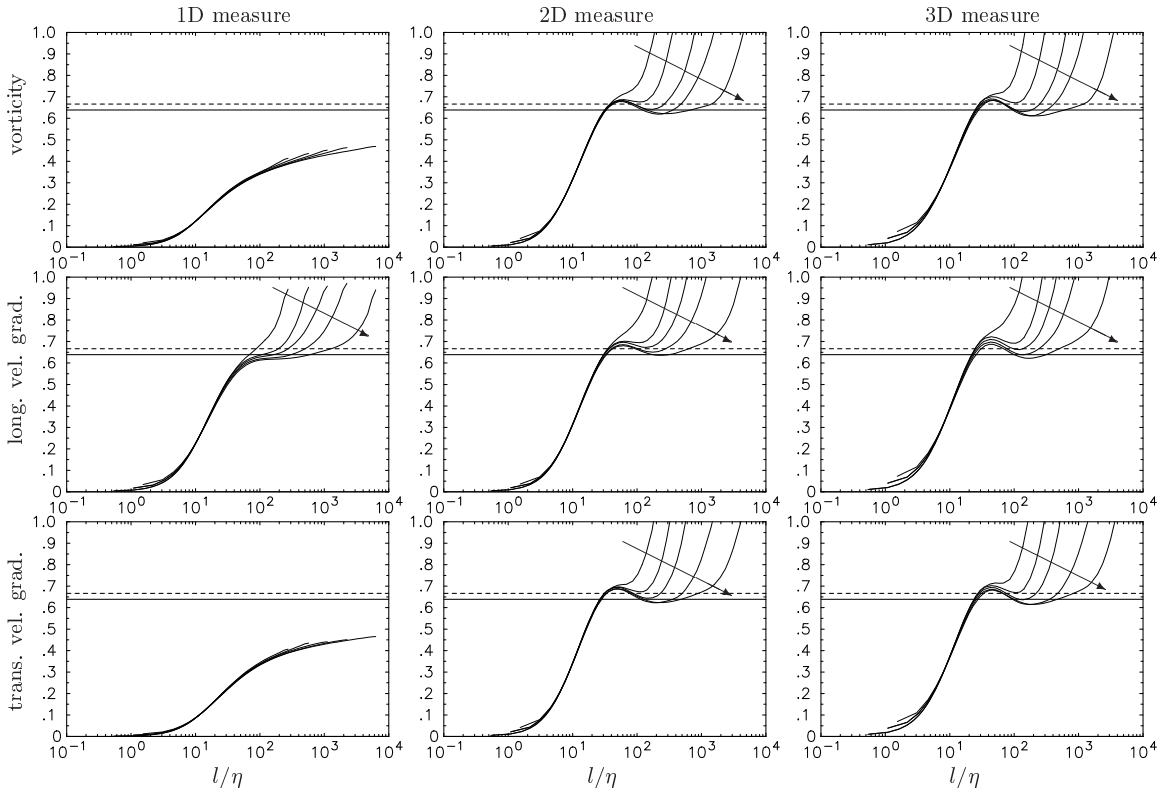

Figure 3.23: Reynolds number dependence of cancellation exponents for vorticity (top row), longitudinal velocity gradients (middle row), and transverse velocity gradients (bottom row). From left to right, different columns denote measures in 1D, 2D and 3D; with Reynolds number R_λ increasing in the direction of the arrow for 140, 240, 400, 650 and 1300. Horizontal dashed and solid lines mark $2/3$ and 0.639, respectively, as in Fig. 3.21.

2010).

3.2.3 Cancellation exponent in low-R_m MHD turbulence

The results so far suggest that 1D measures of cancellation exponent of vorticity take smaller values than those obtained from 2D and 3D measures, but the cause is not yet clear. Vainshtein et al. (1994) argued that 1D measure is "blind" to certain type of geometric structures. Martin et al. (2013) also argued that coherent turbulence structures are "smooth regions embedded in a highly fluctuating field" and as a result "their presence and characteristics will influence the statistical properties of the scale-dependent changes of the sign". Both arguments suggest a connection between cancellation exponents and the structures of turbulent motions.

Consider a turbulent structure of any sign-oscillating quantity that has considerable coherency in one dimension (say, the x-direction). Such a structure can be a 1D filament or a flat sheet that extends in the x-direction. It is expected that signals of the same sign are embedded in the coherent structure, whereas signals of opposite signs can be found in the neighborhood of the structure (if signals of the *same* sign are found in the neighborhood as well, the increased degree of coherency would extend beyond one dimension). When a 1D measure is used to quantify sign oscillations along the coherent structure, the persistence of the same sign reduces sign cancellations, leading to a smaller cancellation exponent. In contrast, 2D and 3D measures have more room in other dimension(s) for cancellation to take place, thus resulting in larger cancellation exponents.

Following this reasoning, the prevalence of vortex filaments in high Reynolds number isotropic turbulence may be thought to lead to differences in cancellation exponents measured in 1D versus higher dimensions. However, sign oscillation measures are taken along the coordinate axis while vortex filaments are randomly oriented in space. As a result there is only a fraction of coherent filaments that are aligned with the grid axis in any realization and may affect the cancellation exponent in the way described above. It is not clear if the use of many more realizations will solve this problem, but the reasoning can be tested if vortex structures grow preferentially along a specific direction. One example is low magnetic Reynolds number (R_m) MHD turbulence in which the vortex structures are forced to be along a chosen coordinate axis — since vortical structures are known to grow preferentially along the magnetic field direction (Zikanov and Thess, 1998; Reddy and Verma, 2014). While more details of MHD turbulence are given in Chap. 4, it suffices here to just focus on

how values of cancellation exponent of vorticity change as vortical structures grow.

Figure 3.24 shows the evolution of normalized enstrophy $\Omega = |\omega|^2$ as well as the cancellation exponents of ω_x and the average of exponents of ω_y and ω_z. Time is normalized by the ratio between integral length scale $\mathcal{L}$ and root-mean-square velocity $\mathcal{U}$, both computed at the instant of the application of the magnetic field (top row). At $t/(\mathcal{L}/\mathcal{U}) = 0$, small vortex filaments are space-filling, and similar values of cancellation exponents for ω_x and averaged ω_y and ω_z confirm that isotropy holds to an acceptable level. At this low $R_\lambda = 98$, cancellation exponents are qualitatively similar to those observed at $R_\lambda = 140$ for forced isotropic turbulence (compare the first row for vorticity in Fig. 3.23). As turbulence decays, vortical structures become increasingly elongated along the magnetic field direction (x-direction). Moreover as the flow evolves the range of scales (measured by the ratio l/η) decreases because η increases in time. The most notable change is that the 1D result of cancellation exponent for ω_x becomes significantly smaller than those for 2D and 3D measures (middle column). Yet the lack of any plateau in κ suggests that ω_x is not sign-singular. For completeness, the right column shows that for ω_y and ω_z, a clear plateau is only seen for 1D measure at intermediate and large scales. The inflections of the curves by 2D and 3D measures mimic those in Fig. 3.23, but better-defined plateaus may form at higher Reynolds numbers.

The example of low-R_m MHD turbulence confirms that an increased degree of coherence in turbulent structures can effectively reduce sign cancellations when the 1D measure along a specific direction is used. The coherent structures in low-R_m MHD turbulence are sheets elongated preferentially along one direction, whereas they are filaments for vorticity in isotropic turbulence. To examine the degree of coherency in one dimension for signals in isotropic turbulence, we consider the interval length L over which the signal retains the same sign. Since coherent structures are expected to be composed of events of the same sign, a higher likelihood of large L suggests a higher degree of spatial coherency. Fig. 3.25 shows the probability density functions (PDF) of the interval length (L) for longitudinal and transverse velocity gradients. The PDF of L/L_0 (the interval length normalized by the domain size L_0) in Fig. 3.25 (a) shows that, at higher Reynolds number, it is less likely for both longitudinal and transverse velocity gradients to maintain the same sign over extended scales, which is in agreement with the notion that turbulence tends to rupture coherent structures. When normalized by the Kolmogorov length scale η, Fig. 3.25 (b) shows that it is more likely for transverse velocity gradients to form longer coherent structures than longitudinal gradi-

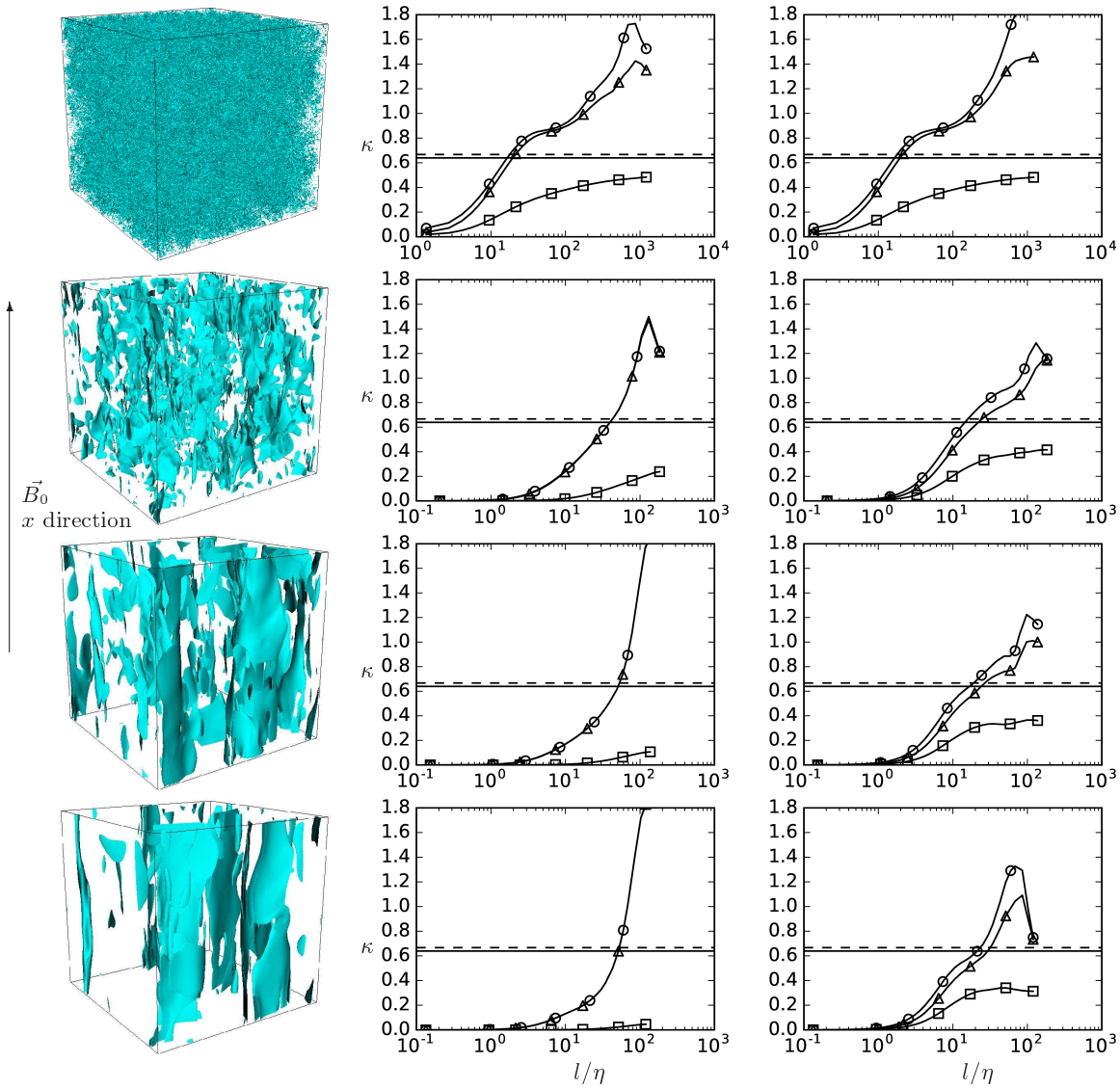

Figure 3.24: Left column: visualization of normalized enstrophy $\Omega/\langle\Omega\rangle = 5$ in MHD turbulence with the magnetic field along the x-direction (vertical); middle column: cancellation exponent of the x-component vorticity ω_x; right column: averaged cancellation exponent of ω_y and ω_z. Measures used are $1D$ (□), $2D$ (△) and $3D$ (◯). From top to bottom, $t/(\mathcal{L}/\mathcal{U}) = 0$, 12, 24 and 36.

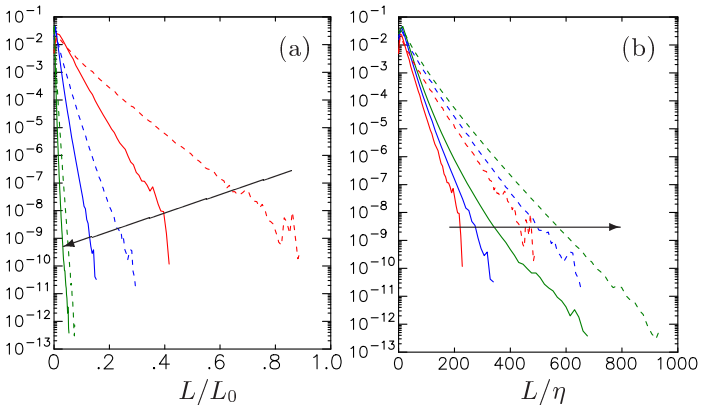

Figure 3.25: PDFs of the length of intervals over which the signal retains the same sign in one dimension. Solid curves denote longitudinal velocity gradients and dashed curves denote transverse velocity gradients. Arrows point in the direction of increasing R_λ : 140 (red), 400 (blue) and 1300 (green). In (a) L is normalized by the domain length (L_0) while in (b) it is normalized by the Kolmogorov length scale (η).

ents. Therefore, as longitudinal velocity gradients are more fragmented, the less coherent structures in 1D longitudinal velocity gradients have minimal effects on cancellation exponents measured in 1D, 2D and 3D.

3.2.4 summary of sign oscillations in the small-scales

In this section, cancellation exponents are computed using 1D and 2D cuts as well as full 3D space. The 3D measures are hardly attainable in experiments, but DNS results now help resolve the conflicts in previous data and allow a direct assessment on whether measures in higher dimensions are needed to measure cancellation exponents for turbulence processes (Vainshtein et al., 1994). Specifically, the results show that the answer depends on the quantity in question. For vorticity and transverse velocity gradients, 2D and 3D measures of cancellation exponents are close to $\kappa \approx 2/3$, and larger than the 1D measure. However, longitudinal velocity gradients have similar cancellation exponents of $\kappa \approx 2/3$ regardless of the dimensionality of the measure. By invoking connections to exponents of generalized structure functions(Vainshtein et al., 1994), it is seen that for vorticity the cancellation exponent should indeed be close to $2/3$; this reveals that the 1D measure is not sufficient. Results from simulations provide more insight on past experimental work. Specifically, in past experiments that quantify sign-oscillations in vorticity, the lower value of $\kappa = 0.45$ is likely due to the fact that 1D measure was used; on the other hand, a value of $\kappa = 0.6$, close to $2/3$,

obtained for longitudinal velocity gradients suggests that it is not as sensitive to the dimensionality. One possible reason for the discrepancies for quantities in different directions, as well as 1D, 2D and 3D measures, is the existence of persistent coherent structures.

To better understand the reasons underlying these differences, cancellation exponents of vorticity have also been computed in low-R_m MHD turbulence. Compared to forced isotropic turbulence where vortex filaments are randomly oriented in space, in low-R_m MHD turbulence vortical structures grow preferentially along the magnetic field direction. As a result, improved alignment of elongated coherent structures with the direction of 1D measure allows the assessment of whether increased degree of coherency leads to weakened sign-cancellation. Quantitatively, 1D measures of cancellation exponents are substantially reduced as elongated coherent vortical structures grow in the form of 1D filaments or 2D sheets, as confirmed by qualitative visualizations. It is thus very plausible that in homogeneous isotropic turbulence elongated vortical structures in the form of filaments are responsible for smaller cancellation exponents measured in 1D. In comparison, structures of longitudinal velocity gradients are more fragmented, leading to similar cancellation exponents regardless of the dimensionality of the measure.

CHAPTER 4

TURBULENCE STRUCTURE SUBJECT TO A MAGNETIC FIELD

As discussed previously, a magnetic field imposes a preferred direction for the electrically conducting fluid. As a result, anisotropy arises in both the large and small scales, and the turbulence deviates from the isotropic state as studied in the previous chapter. To delineate the effects of the magnetic field clearly, decaying isotropic turbulence free from forcing is first simulated from a model spectrum until non-Gaussian features become evident. Then as the magnetic field is applied along one coordinate direction, the anisotropy development is studied in all scales of motion, in both the physical and wavenumber spaces. The study of the response of turbulence structure subject to a magnetic field lays the foundation for Chap. 5 and 6 where the relaxation of strained MHD turbulence and the scalar mixing in MHD turbulence and are considered separately.

4.1 Introduction

The study of magnetohydrodynamic (MHD) turbulence of an electrically conducting fluid subjected to a magnetic field has numerous applications ranging from metallurgical processing to astrophysical phenomena (Davidson, 2013; Biskamp, 2003). The motion of the fluid produces an electric field, and hence a current, which modifies the character of the flow field dramatically through the Lorentz force that points in a direction orthogonal to both the electric current and magnetic field vectors. In general, the resulting flow phenomena depend strongly on the the magnetic Reynolds number (R_m), which is a measure of the strength of advective transport to that of diffusion of the magnetic field. However, in most terrestrial applications, including convection in the Earth's core, and nuclear reactor design, R_m is much smaller than unity — in which case the velocity field has only a minimal effect on the magnetic field. The main interest is then in how the velocity field is (in a one-way coupling) modified by the magnetic field. For MHD turbulence in this low magnetic Reynolds number regime the strength of MHD effects is expected to be a function of how the time scale of the magnetic field compares with the time scale(s) of the turbulence itself.

Since liquid metals are opaque and corrosive, experiments in MHD turbulence are much more

difficult than those involving ordinary fluids. As a result, direct numerical simulations, if formulated properly and executed efficiently, have particular appeal for understanding the fundamentals in this subject (Knaepen and Moreau, 2008). A number of authors have simulated MHD turbulence in a simplified geometry, namely a three-dimensional (3D) periodic domain, with (e.g. Refs. Zikanov and Thess, 1998; Ishida and Kaneda, 2007; Burattini et al., 2008; Reddy and Verma, 2014) or without (e.g. Refs. Schumann, 1976; Okamoto, Davidson, and Kaneda, 2010; Favier et al., 2010) numerical forcing that supplies energy to the large scales. These studies have shown, for instance, that length scales under MHD can grow rapidly, and that Joule dissipation arising from the Lorentz force causes the energetics of the flow to differ substantially from classical isotropic turbulence. However, although the use of (different types of) forcing as a means of achieving stationarity at high Reynolds number in hydrodynamic turbulence (Eswaran and Pope, 1988a; Kaneda et al., 2003) is well accepted, for MHD turbulence this may interfere with the physical effects of the Lorentz force, which acts at all scales. On the other hand, if the turbulence is allowed to decay without energy input the Reynolds number in numerical simulations often becomes quite low, especially if the range of scales is limited by a desire to minimize effects of finite domain size (Okamoto, Davidson, and Kaneda, 2010). At the same time, although (for this reason) computational requirements for MHD turbulence are greater than those for hydrodynamic turbulence, simulations of MHD turbulence have generally not yet reached the grid resolutions deployed for the latter (such as in Yeung, Donzis, and Sreenivasan (2012) and higher). Furthermore, in view of preferential growth of large-eddy length scales along the direction of the imposed magnetic field, cubic solution domains widely employed in the literature are physically not optimal.

The basic premise of the study is to improve understanding of MHD turbulence by conducting simulations of higher resolution than achieved before in this subject, using elongated solution domains of large aspect ratio, with initial flow conditions that are representative of natural, unforced isotropic turbulence. The first focus is on the anisotropy that develops at various scales as a result of the Lorentz force, through a dissipative mechanism which (unlike viscous dissipation) is inherently anisotropic. Previous works in the literature (Alemany et al., 1979; Sommeria and Moreau, 1982) have in fact suggested a trend towards quasi two-dimensionality (hereafter Q2D for short) if the magnetic field is sufficiently strong. To analyze the anisotropy one can consider the single-point Reynolds stress tensor, the statistics of velocity gradients under constraints due to axisymmetry

(George and Hussein, 1991), as well as evolution of spectral quantities in Fourier space (Verma, 2017). Anisotropy also implies that both magnitude and orientation in wavenumber space are important. As a result, tools of one-dimensional and axisymmetric spectra (Clay and Yeung, 2016) are used, which can provide information complementary to other descriptions such as a decomposition into toroidal and poloidal contributions (Favier et al., 2010), ring-to-ring energy transfer (Teaca et al., 2009; Verma, 2017), as well as wavelet analyses (Okamoto, K. Schneider, and Farge, 2014).

The second focus is to quantify the effects of the strength of the imposed magnetic field, through the magnetic interaction parameter (N), defined as the ratio of a large-eddy time scale of an initial turbulence state to the time scale (called Joule time) of the magnetic field. Although other authors have reported results for values of N much larger than unity before, results in this work show that simulation results at large N can be unreliable (except perhaps at early times) unless domain size requirements are addressed rigorously. For example, use of elongated domains allows comparisons with an asymptotic prediction by Moffatt (1967) for anisotropy development in the limit of infinitely large N. A more general question is whether changes in turbulence statistics scale with the Joule time of the magnetic field. For the study of effects of larger N the use of elongated domains to minimize the confinement effects on the turbulence structure due to insufficient domain size is even more important. It may be noted that such confinement effects may be avoided entirely in an alternative approach based on spectral closures (Favier et al., 2010; Favier et al., 2011), while other phenomena such as Hartmann layers are present in flows with actual solid boundaries (Pothérat and Kornet, 2015; Bandaru et al., 2016; Kobayashi, 2006). However those effects are not considered in this work.

This chapter presents results from a number of simulations. In each case, a pre-simulation of decaying isotropic turbulence is first performed to provide physically realistic initial conditions prior to the activation of the magnetic field. The domain aspect ratio is varied from 1 to 64, and the magnetic interaction parameter is varied from 1 to 256. After an assessment of the effects of aspect ratio on the development of basic quantities such as the turbulence kinetic energy and viscous and Joule dissipation rates, the highest grid resolution employed is 16384×2048^2, for simulations where the pre-MHD Taylor-scale Reynolds number is 98. At early times velocity fluctuations parallel to the imposed magnetic field are larger than those in the orthogonal directions, but the inequality is reversed at later times. In the literature this anisotropy reversal has been interpreted (Favier et al.,

2010) as the result of polarization in spectral space. However a more detailed analysis is attempted here, over a range of values of N as stated above. In particular, emphasis is placed on the direct and indirect effects of the Joule dissipation in the evolution of different terms in the Reynolds stress budget, and the development of Q2D behavior as well as departures from local isotropy at the small scales. Also results on one-dimensional and axisymmetric spectra (Clay and Yeung, 2016) of the turbulence kinetic energy as well as specific terms in the spectral energy budget are presented, including nonlinear spectral transfer and contributions from pressure-strain correlations. Furthermore, the effects of larger values of N are studied using two separate series of simulations at grid resolutions 4096×512^2 and 16384×2048^2.

4.2 Quantities used to examine anisotropy

The anisotropy development studied in this work can be quantified using several scale-dependent quantities in physical and spectral spaces, beginning with the Reynolds stress tensor, which evolves by

$$d\langle u_i u_j \rangle / dt = (2/\rho)\langle p s_{ij} \rangle - \langle J_{ij} \rangle - \langle \epsilon_{ij} \rangle \tag{4.1}$$

where $s_{ij} \equiv (\partial u_i/\partial x_j + \partial u_j/\partial x_i)/2$ is the strain rate tensor, and angled brackets represent averaging in space, and terms on the right are the pressure-strain correlation, Joule and viscous dissipation tensors respectively. The last two terms can be related to the velocity spectrum tensor $\Phi_{ij}(\mathbf{k})$ (whose integral is the Reynolds stress) by

$$\langle J_{ij} \rangle = 2(\sigma B_0^2/\rho) \iiint (k_x/k)^2 \Phi_{ij}(\mathbf{k})\, d\mathbf{k} \;\; ; \;\; \langle \epsilon_{ij} \rangle = 2\nu \iiint k^2 \Phi_{ij}(\mathbf{k})\, d\mathbf{k} \, . \tag{4.2}$$

Taking half of the traces of these relations gives the dissipation rates, via

$$\langle J \rangle = 2(\sigma B_0^2/\rho) \iiint (k_x/k)^2 E(\mathbf{k})\, d\mathbf{k} \;\; ; \;\; \langle \epsilon \rangle = 2\nu \iiint k^2 E(\mathbf{k})\, d\mathbf{k} \, , \tag{4.3}$$

where $E(\mathbf{k}) = \frac{1}{2}\Phi_{ii}(\mathbf{k})$ is the 3D energy spectrum.

Since MHD turbulence has very different length scales in different directions, representation of anisotropy as a function of wavenumber magnitude k in wavenumber space would not be satisfactory. Instead, since the turbulence studied is axisymmetric, with rotational symmetry(Batchelor,

1946) around the direction of the imposed magnetic field, the spectral content of the turbulence can be represented as a function of one-dimensional wavenumber k_1 (same as k_x, along the direction of the magnetic field) and a "radial" wavenumber $k_r = \sqrt{k_2^2 + k_3^2}$ in the transverse plane, as in Ref. Clay and Yeung, 2016. In this coordinate system $k_r = k \sin\phi$ where $0 \leq \phi \leq \pi$ is the co-latitude with respect to the k_1 axis, and $0 \leq \theta \leq 2\pi$ is the polar angle within the $k_2 - k_3$ plane. The axisymmetric spectrum tensor can be formed by integrating the velocity spectrum tensor over all values of θ, i.e.

$$A_{ij}(k_1, k_r) = \int_0^{2\pi} \Phi_{ij}(\mathbf{k}) k_r \, d\theta \, . \tag{4.4}$$

The velocity spectrum in one dimension can also be recovered by

$$\Phi_{ij}(k_1) = 2 \int_0^{\infty} A_{ij}(k_1, k_r) \, dk_r \tag{4.5}$$

where the factor of 2 accounts for contributions from both positive and negative k_1. Half of the trace of $A_{ij}(k_1, k_r)$ gives the axisymmetric energy spectrum, $E_A(k_1, k_r)$. If the turbulence is isotropic a contour plot of $E_A(k_1, k_r)/\sin\phi$ (Mininni, Rosenberg, and Pouquet, 2012) would show a pattern of concentric circles. Any deviation from such circular contours (except caused by a limited number of Fourier modes at low k_1 or low k_r) is then an indicator of anisotropy. A radial spectrum in k_r can also be defined, such that

$$\Phi'_{ij}(k_r) = \int_0^{\infty} A_{ij}(k_1, k_r) \, dk_1 \, . \tag{4.6}$$

In practice, the upper limits of the integrals in Eqs. (4.5) and (4.6) are replaced by the highest wavenumbers in k_1 or k_r represented in the code after treatment for aliasing errors(Rogallo, 1981).

4.3 Initial conditions and domain aspect ratio

To study the response of isotropic turbulence to the magnetic field it is important to begin with a physically realistic isotropic state — that can be represented well in an anisotropic domain of non-unity aspect ratio, with minimal numerical distortion. A pre-simulation where isotropic turbulence is allowed to evolve naturally is typically required. This section presents a summary of these pre-simulations and an assessment of how high an aspect ratio is required for reliable results.

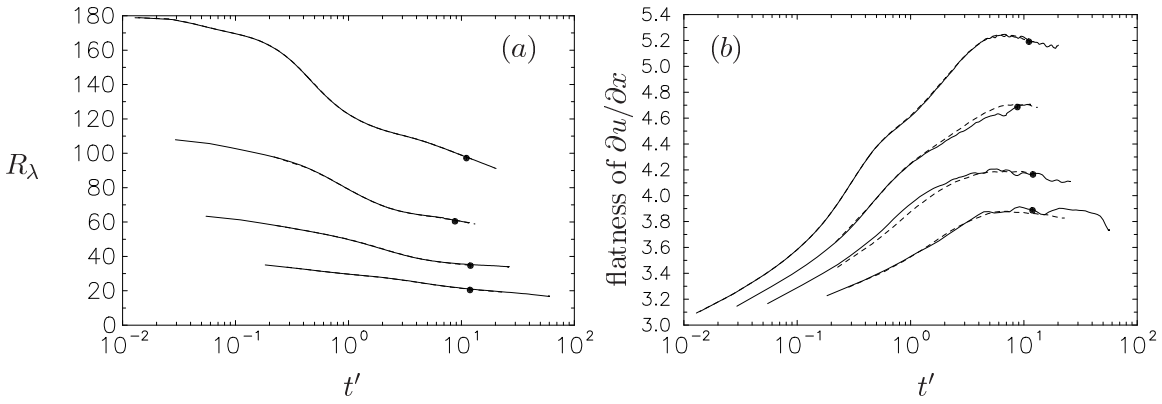

Figure 4.1: (a) Taylor-scale Reynolds number and (b) flatness factor of longitudinal velocity gradients in pre-simulations where $n_y = n_z = 256$, 512, 1024, 2048 (from bottom to top). With $n_x = \Lambda n_y$, results for $\Lambda = 1$ and $\Lambda = 8$ are indicated by solid lines and dashed lines respectively. The time axis (t') is normalized by initial values of K and $\langle\epsilon\rangle$ in the pre-simulation. The meanings of the circles on each curve are addressed in the text.

Consider solution domains of lengths $\mathcal{L}_{0x}$, $\mathcal{L}_{0y}$ $\mathcal{L}_{0z}$ in x, y, z directions with n_x, n_y and n_z grid points respectively, the magnetic field is applied in the x direction, on elongated domains of aspect ratio $\Lambda = \mathcal{L}_{0x}/\mathcal{L}_{0y} > 1$, while $\mathcal{L}_{0y} = \mathcal{L}_{0z}$. In each direction the number of grid points is proportional to the length of the solution domain, so that the grid spacings Δx, Δy and Δz are all equal. This ensures small-scale motions are equally well resolved in every coordinate direction, with the same highest wavenumbers in each. The domain sizes are set in $\mathcal{L}_{0y} = \mathcal{L}_{0z} = 2\pi$ units, with Λ increased from unity in powers of 2, as desired.

To achieve the objective of minimum numerical distortion, the large eddies prior to activation of the magnetic field must be very small compared with the dimensions of the solution domain. The purpose of the pre-simulations is to allow the turbulence to develop naturally towards a well-developed state, with initial parameters chosen to minimize numerical artifacts. The flow is initialized as a Gaussian velocity field with an energy spectrum function (which is the integral of $E(\mathbf{k})$ over a spherical shell of radius k in wavenumber space) of the form (Pope, 2000)

$$E(k) = C_K \langle\epsilon\rangle^{2/3}\, k^{-5/3} f_L(kL) f_\eta(k\eta) \tag{4.7}$$

where $C_K \approx 1.62$ (Ref.Yeung and Zhou, 1997) is the Kolmogorov constant for $E(k)$, L and η are initial (longitudinal) integral and Kolmogorov scales respectively, and $f_L(\cdot)$ and $f_\eta(\cdot)$ are semi-empirical fitting functions. As the turbulence decays all the length scales are expected to grow. It

is important to choose L here to be very small compared to the domain size in all directions, so that even at the end of the pre-simulation ample room remains for the large scales to grow during the subsequent MHD simulation. The pre-simulation can be considered complete when the kinetic energy shows a power-law decay while the Reynolds number drops slowly, and when clear non-Gaussianity in the velocity gradients has developed.

Figure 4.1 shows the evolution of Taylor-scale Reynolds number (R_λ) and flatness factor of longitudinal velocity gradients in several pre-simulations that began at different Reynolds numbers, with L taken to be 1/48 of the shortest sides of the domain. The gradient flatness increases from 3.0, towards a maximum and then decreases as a result of a slowly decreasing Reynolds number. Solid and dashed lines for pre-simulations on cubic and elongated domains with $\Lambda = 8$ (and $n_x = \Lambda n_y$) are in close agreement, thus showing that a proper isotropic state has been attained on an anisotropic solution domain. Velocity fields at time instants marked by solid circles are used as initial conditions for the MHD simulations.

Table 4.1: Parameters of pre-simulations for domains of aspect ratio 8 (with shortest side fixed at 2π): viscosity, Taylor-scale Reynolds number $(R_\lambda)_b$ before the pre-simulation begins, followed by various parameters (as discussed in the text) at the end of the pre-simulation.

Grid points	2048×256^2	4096×512^2	8192×1024^2	16384×2048^2
ν	0.0028	0.0011	0.000437	0.0001732
n_R	3	2	3	2
$(R_\lambda)_b$	36	62	105	173
$(R_\lambda)_0$	21	35	61	98
u'	0.393	0.350	0.428	0.383
v'	0.394	0.351	0.430	0.385
w'	0.394	0.350	0.430	0.386
L_1/L_2	1.999	1.941	2.026	1.981
$\langle(\nabla_\parallel \mathbf{u})^2\rangle/\langle(\nabla_\perp \mathbf{u})^2\rangle$	0.5001	0.4998	0.5000	0.4999
μ_3 of $\nabla_\parallel \mathbf{u}$	-0.497	-0.508	-0.519	-0.529
μ_4 of $\nabla_\parallel \mathbf{u}$	3.863	4.174	4.701	5.212
$\mathcal{L}_{0\parallel}/L_1$	130	134	166	163
$\mathcal{L}_{0\perp}/L_1$	16.3	16.8	20.8	20.4
$\Delta x/\eta$	1.479	1.302	1.519	1.356

Table 4.1 shows parameters for pre-simulations on domains of aspect ratio $\Lambda = 8$. As in simulations of forced isotropic turbulence (Yeung, Pope, and Sawford, 2006), higher Reynolds numbers are obtained on finer grids by reducing the viscosity (ν). Ensemble averaging is taken over modest number (n_R) of realizations initialized with different random number seeds. It is clear that, despite

the solution domain being highly anisotropic, the component r.m.s velocities, the ratio between longitudinal (L_1) and transverse (L_2) integral length scales, and the ratio between mean-squared longitudinal ($\nabla_{\parallel}\mathbf{u}$) and transverse ($\nabla_{\perp}\mathbf{u}$) velocity gradient fluctuations all agree very well with results in incompressible isotropic turbulence. The skewness (μ_3) and flatness (μ_4) factors of $\nabla_{\parallel}\mathbf{u}$ are also close to values at comparable Reynolds numbers in simulations of forced isotropic turbulence (Yeung, Girimaji, and Pope, 1989). The ratios of domain sizes to the integral length scales at the end of the pre-simulation are sufficiently large for the large scales to develop naturally under a magnetic field in the x direction. Resolution of the Kolmogorov scale is also adequate, and is expected to improve further as the turbulence continues to decay.

Table 4.2: Table of parameters for production MHD simulations studied in this study.

Grid	Λ	n_R	$(R_\lambda)_0$	N
256^3	1	3	21	0.5,1,2
512×256^2	2	3	21	1
1024×256^2	4	3	21	1
2048×256^2	8	3	21	1
4096×256^2	16	3	21	1
8192×256^2	32	4	21	1
16384×256^2	64	3	21	1
4096×512^2	8	2	34	0.5,1,2,4,8,16,32,64,128,256
2048×256^2	8	3	21	1
4096×512^2	8	2	34	0.5,1,2,4,8,16,32,64,128,256
8192×1024^2	8	3	59	0.1,0.5,1,2,5,10
16384×2048^2	8	2	98	1,2,4,8
2048^3	1	1	98	1,8

For a given pre-MHD turbulence state subjected to a magnetic field of strength B_0 in a fluid of density ρ and conductivity σ, MHD effects can be characterized by the magnetic interaction parameter (N) as the ratio of a large-eddy time scale to the Joule time $\tau_J \equiv \rho/(\sigma B_0^2)$. The choice of the eddy turnover time is $T_E = L_{11}/u'$ where L_{11} is a longitudinal length scale and u' is the r.m.s. velocity as the large-eddy time scale. Other definitions (such as $K/\langle\epsilon\rangle$) have been used by others as well but that will not change the results significantly. Some theoretical results are known for N of order unity (Ishida and Kaneda, 2007; Okamoto, Davidson, and Kaneda, 2010) as well as $N \to \infty$ (Moffatt, 1967). Stronger magnetic fields with shorter time scales lead to faster growth of the large-eddy length scales and hence turbulence statistics becoming contaminated by finite domain size effects earlier. Generally results are only shown at times before at least one integral

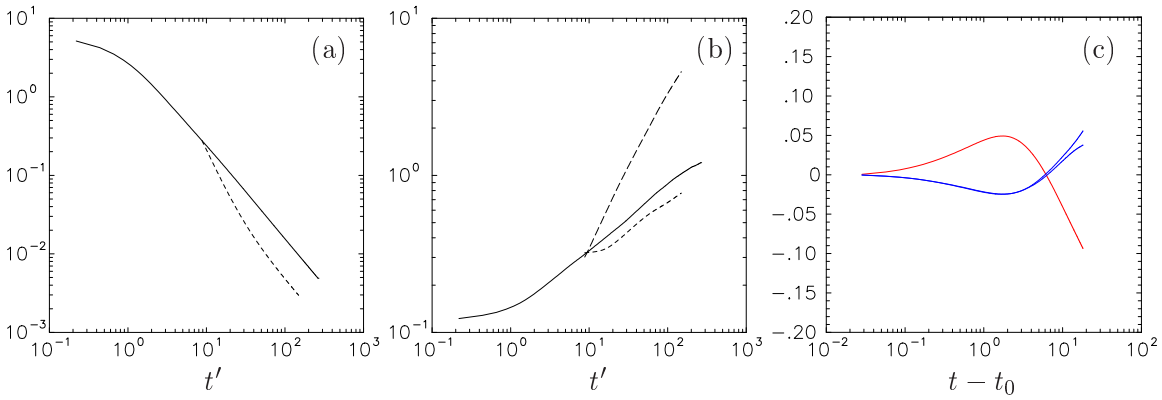

Figure 4.2: (a) Turbulence kinetic energy (K), (b) integral length scales L_{11} and L_{22} of velocity components u_1 and u_2, and (c) Reynolds stress anisotropy tensor elements (b_{11} (red), b_{22} and b_{33} (blue)) in 8192×1024^2 simulation on a $16\pi \times (2\pi)^2$ domain with $N = 1$. Time t is measured from the beginning of the pre-simulation, and the magnetic field is turned on at $t = t_0$. In (a) and (b) solid lines represent the pre-simulation (if extended), while dashed line represents MHD results. In (b) L_{11} L_{22} under the magnetic field are indicated by long and short dashed lines respectively.

length scale in the x direction exceeds 1/4 of $\mathcal{L}_{0x}$. For the same physical parameters a domain with larger Λ allows reliable results to be obtained for a longer period of time. Table 4.2 gives a list of the key simulations in this work, grouped into three categories used to study dependence on domain aspect ratio, magnetic interaction parameter and pre-MHD Reynolds number respectively. In the simulations, as the integral length scales grow while the turbulence decays, the value of N if based on instantaneous values of T_E can increase by 2 orders of magnitude of more (even more so than in simulations with forcing (Zikanov and Thess, 1998; Verma, 2017)). For convenience, and since the magnetic field itself is fixed, values of N are based on the value of T_E just before the magnetic field is applied.

Figure 4.2 gives, in three frames, a basic characterization of effects of MHD in the simulations. When the magnetic field is turned on (at time t_0), the kinetic energy decreases more quickly (as a direct result of the Joule dissipation) than in freely decaying isotropic turbulence but reverts later to power-law behavior. The integral length scales grow rapidly: in particular, L_{11} is seen to grow to 4.6 and beyond (which is 6 times of L_{22}), which would not have been captured if the solution domain were a cube of size $(2\pi)^3$. Anisotropy reflected by nonzero values of the Reynolds stress anisotropy tensor $b_{ij} = \langle u_i u_j \rangle / (2K) - (1/3)\delta_{ij}$, develops quickly when the magnetic field is turned on. At short times $t - t_0$ $b_{11} > 0$ while $b_{22} \approx b_{33} < 0$, but this anisotropy is reversed at later times.

To help quantify the sensitivity of numerical results to the domain aspect ratio, in Fig. 4.3 com-

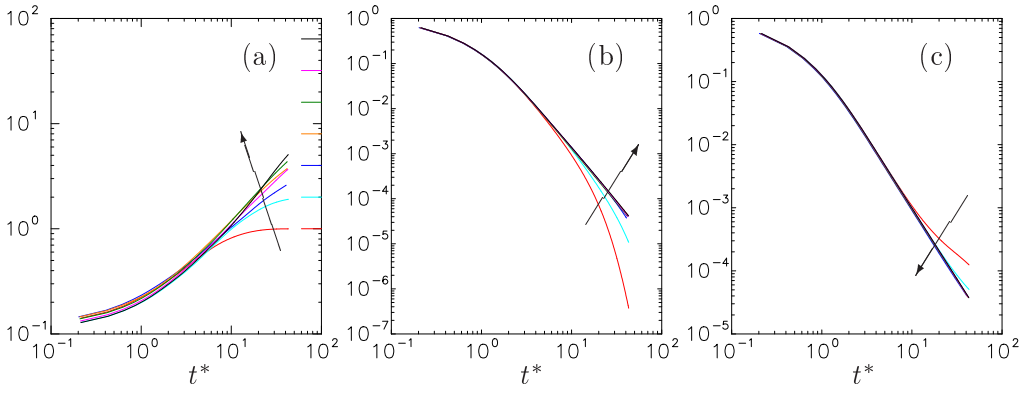

Figure 4.3: (a) L_{11}/π, (b) $\langle J\rangle/\langle J\rangle_0$, (c) $\langle\epsilon\rangle/\langle\epsilon\rangle_0$ versus normalized time $t^* = (t-t_0)/(T_E)_0$ since when the magnetic field is turned on. Domain aspect ratio Λ increases from 1 to 64 in the direction of the arrow. Short horizontal bars in (a) mark maximum possible values for each Λ.

parison is made for the evolution of (a) longitudinal integral length scale (L_{11}), (b) Joule dissipation and (c) viscous dissipation for simulations at Λ from 1 to 64 (in powers of 2), with $(R_\lambda)_0$ and N held fixed (at 21 and 1 respectively). In this and all subsequent figures normalized time t^* is defined as $(t-t_0)/(T_E)_0$ where the subscript 0 refers to pre-MHD conditions. Since L_{11} is an integral of the two-point correlation for spatial separation r_x from 0 to $\frac{1}{2}\mathcal{L}_{0x}$ its maximum possible value is $\frac{1}{2}\mathcal{L}_{0x}$ which is marked by short horizontal bars in frame (a). At early times, all curves agree closely with each other. (Conversely, the benefits of larger Λ may not be apparent if only results at early times were considered.) However, for $\Lambda = 1$ or 2 the growth of L_{11} is clearly constrained by the domain size at later times. It also appears that most results converge (or nearly so) for $\Lambda \geq 8$, at least up to the times shown in the figure.

In Fig. 4.3 it is worth noting that simulations of low Λ tend to underestimate the Joule dissipation ($\langle J\rangle$) but overestimate the viscous dissipation ($\langle\epsilon\rangle$). This observation can be explained by the forms of the integrands present in the definitions in Eq. (4.3). The value of $\langle J\rangle$ is determined by a selective sampling of the energy in each Fourier mode, via the factor $(k_x/k)^2$ which is largest for wavevectors pointing in or closely aligned with the k_x direction in wavenumber space. The 3D spectrum $E(\mathbf{k})$ itself takes largest values at low wavenumbers. In a domain of finite length $2\pi\Lambda$ in the x direction the lowest nonzero k_x is $1/\Lambda$. As a result, if Λ is low then some of the Fourier modes that should, via the factor $(k_x/k)^2$, contribute the most to $\langle J\rangle$ would not have been represented in the simulation.

In Fig 4.4, axisymmetric spectra (as functions of k_1 and k_r) are compared in simulations at $\Lambda =$ 1, 8 and 64 corresponding to conditions in Fig. 4.3. In the leftmost frame the space corresponding

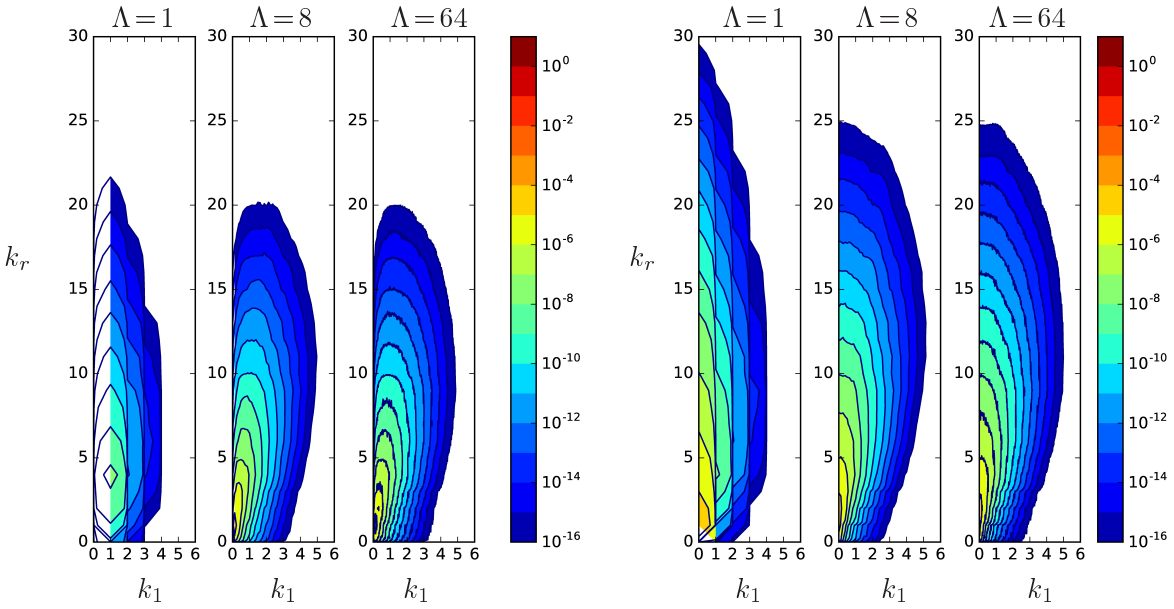

Figure 4.4: Contour plots of axisymmetric spectra of Joule dissipation (left frames) and viscous dissipation (right frames), from late-time data in simulations with three different aspect ratios, corresponding to grid resolutions 256^3, 2048×256^2 and 16384×256^2, with $N = 1$ and $(R_\lambda)_0 = 21$.

to $0 < k_x < 1$ is empty because no Fourier modes exist in that range when $\Lambda = 1$. This leads to an underestimate of $\langle J \rangle$ as suggested above. In contrast, for the viscous dissipation, because of the incompressibility condition $\mathbf{u} \perp \mathbf{k}$ in wavenumber space substantial contributions in the range $0 < k_1 < 1$ arise from wavenumber modes of nonzero $k_\perp$. This effect leads to a slight overestimate of $\langle \epsilon \rangle$, although the effect is weak because most of the spectral content of viscous dissipation lies at higher wavenumbers. As in the case of Fig. 4.3, differences between $\Lambda = 8$ and 64 in Fig. 4.4 are very small. This suggests $\Lambda = 8$ is likely to be adequate for minimizing effects of finite domain size in the simulation data presented in this study.

4.4 Anisotropy Development Under a Magnetic Field

The prime focus of investigation in this study is the nature of anisotropy development resulting from the magnetic field and its Lorentz force. Quantities sensitive to the large and small scales are considered, followed by a more complete description of scale dependence in spectral space. Most of the results in this section are taken by a simulation with 16384×2048^2 grid points, aspect ratio $\Lambda = 8$, and interaction parameter $N = 1$. Time evolution is expressed in terms of the normalized time t^* which was first used in Fig. 4.3 (Chap. 4.3). Questions of dependence on N and scaling

Table 4.3: Development of terms in the Reynolds stress budget and anisotropy tensor element, from 16384×2048^2 simulation with $\Lambda = 8$, $N = 1$. The data are listed at several normalized time instants (which are not uniformly spaced).

Normal stress parallel to the magnetic field

t^*	b_{11}	$\langle u_1^2 \rangle$	$2\langle (p/\rho) s_{11} \rangle$	$\langle J_{11} \rangle$	$\langle \epsilon_{11} \rangle$	relaxation	db_{11}/dt
0.00	-0.00126	0.14800	-8.052×10^{-4}	7.221×10^{-2}	1.334×10^{-1}	-2.537×10^{-1}	0.10600
1.08	0.03424	0.05275	-6.272×10^{-3}	1.756×10^{-2}	2.249×10^{-2}	-4.862×10^{-2}	0.01600
2.06	0.03890	0.02889	-2.656×10^{-3}	7.676×10^{-3}	7.602×10^{-3}	-1.776×10^{-2}	-0.00223
4.87	0.01321	0.01017	-3.842×10^{-4}	1.688×10^{-3}	1.200×10^{-3}	-2.837×10^{-3}	-0.01490
6.86	-0.01141	0.00646	-1.368×10^{-4}	8.525×10^{-4}	5.688×10^{-4}	-1.262×10^{-3}	-0.01480
12.58	-0.07078	0.00269	-4.342×10^{-6}	2.239×10^{-4}	1.517×10^{-4}	-2.779×10^{-4}	-0.00996
26.25	-0.14950	0.00083	5.204×10^{-6}	3.791×10^{-5}	2.845×10^{-5}	-3.994×10^{-5}	-0.00469
41.52	-0.19210	0.00039	2.780×10^{-6}	1.155×10^{-5}	9.121×10^{-6}	-1.168×10^{-5}	-0.00226

Normal stress perpendicular to the magnetic field

t^*	b_{22}	$\langle u_2^2 \rangle$	$2\langle (p/\rho) s_{22} \rangle$	$\langle J_{22} \rangle$	$\langle \epsilon_{22} \rangle$	relaxation	db_{22}/dt
0.00	0.00063	0.14890	4.026×10^{-4}	1.460×10^{-1}	1.334×10^{-1}	-2.546×10^{-1}	-0.05330
1.08	-0.01712	0.04538	3.136×10^{-3}	2.727×10^{-2}	1.884×10^{-2}	-4.536×10^{-2}	-0.00800
2.06	-0.01945	0.02436	1.328×10^{-3}	1.056×10^{-2}	5.658×10^{-3}	-1.643×10^{-2}	0.00112
4.87	-0.00661	0.00959	1.921×10^{-4}	1.982×10^{-3}	6.658×10^{-4}	-2.744×10^{-3}	0.00742
6.86	0.00571	0.00680	6.838×10^{-5}	9.752×10^{-4}	2.744×10^{-4}	-1.285×10^{-3}	0.00738
12.58	0.03539	0.00378	2.171×10^{-6}	2.792×10^{-4}	6.230×10^{-5}	-3.342×10^{-4}	0.00498
26.25	0.07475	0.00185	-2.602×10^{-6}	6.269×10^{-5}	1.275×10^{-5}	-6.541×10^{-5}	0.00235
41.52	0.09604	0.00118	-1.390×10^{-6}	2.581×10^{-5}	5.214×10^{-6}	-2.467×10^{-5}	0.00113

with respect to Joule time are considered later in Chap. 4.5.

4.4.1 Reynolds stress budget and anisotropy tensor

The Reynolds stress transport equation including the Joule dissipation tensor has already been given in Eq. (4.1). The corresponding equation for the anisotropy tensor elements is

$$\frac{db_{ij}}{dt} = \frac{1}{2K}\left[2\langle (p/\rho) s_{ij} \rangle - \langle J_{ij} \rangle - \langle \epsilon_{ij} \rangle - \frac{\langle u_i u_j \rangle}{K}\frac{dK}{dt}\right] , \tag{4.8}$$

where the last term represents a relaxation, or restoring effect. Table 4.3 shows, at selected normalized times t^*, values of the anisotropy tensor elements, mean-squared velocities, various terms in the Reynolds stress equation, and rate of change of anisotropy, in directions parallel and perpendicular to the magnetic field. In the perpendicular direction averaging over two coordinate components is performed. At $t^* = 0$ the anisotropy is very weak and nonzero only because of sampling errors. However for the Joule dissipation, initially (because of MHD is applied to an isotropic state) $\langle J_{22} \rangle \approx 2\langle J_{11} \rangle$. This causes $\langle u_2^2 \rangle$ to decrease faster than $\langle u_1^2 \rangle$, such that the anisotropy tensor elements b_{11} and b_{22} quickly become positive and negative, respectively. As the turbulence structure adjusts over time, $\langle J_{22} \rangle$ remains stronger than $\langle J_{11} \rangle$ but their difference becomes less dominant. The anisotropizing effect of Joule dissipation is resisted by the behavior of viscous dissipation which is

however relatively weak, while the re-distributive pressure-strain correlation is even weaker. It can be seen that at time $t^* \sim 1-2$ the relaxation term in Eq. (4.8) becomes strong enough such that both db_{11}/dt and db_{22}/dt undergo a change in sign, to be followed by b_{11} and b_{22} themselves at $t^* \approx 6$.

An important question is (e.g. Refs. Favier et al., 2011; Gallet and Doering, 2015) whether a strong magnetic field would cause the turbulence to take on a Q2D, or perhaps two-dimensional, three-component (2D-3C) character, where the three velocity components are comparable in magnitude but dependence on one coordinate becomes extremely weak. If strict two-dimensionality occurs then the anisotropy tensor elements would take the values $b_{11} = -1/3$ and $b_{22} = b_{33} = 1/6$. Data at later times in the simulations are qualitatively consistent with development of Q2D behavior. However for a given N the answer to this question requires a study of asymptotic behavior at large times for which domains of extremely large aspect ratios are required to avoid eventual contamination by finite domain-size effects. It is also possible that a higher Reynolds number with a wider range of scales may lead to different outcomes.

4.4.2 Small scales and velocity gradient statistics

Since the Lorentz force acts directly at all scale sizes, the small scales are expected to deviate from the classical picture of local isotropy at high Reynolds number. At the same time, because of axisymmetry due to the magnetic field it is useful to distinguish between the statistics of velocity gradients taken in directions parallel or perpendicular to the imposed magnetic field. As a result the notations $u_{\parallel,\parallel}$, $u_{\parallel,\perp}$, $u_{\perp,\parallel}$, $u^L_{\perp,\perp}$, $u^T_{\perp,\perp}$ are introduced, where subscripts $\parallel$ and $\perp$ refer to directions along and perpendicular to the magnetic field respectively, and the last two of these refer to longitudinal and transverse velocity gradients in the orthogonal plane. (In the simulations, for example, statistics of $u^T_{\perp,\perp}$ are obtained by taking samples over from $\partial u_2/\partial x_3$ and $\partial u_3/\partial x_2$.) Likewise, vorticity is studied via the statistics of $\omega_\parallel$ and $\omega_\perp$ in the respective directions.

Figure 4.5 shows information from the same simulation as in Table 4.3, on (a) the departure of gradient variances from standard isotropy relations, (b) the ratio between variances of different velocity gradients, and (c) the relative contributions from different vorticity components to mean-squared vorticity. In both (a) and (b) it is clear that gradients in the parallel direction become much smaller than those in the perpendicular directions. This implies dependence on x_1 becomes weak

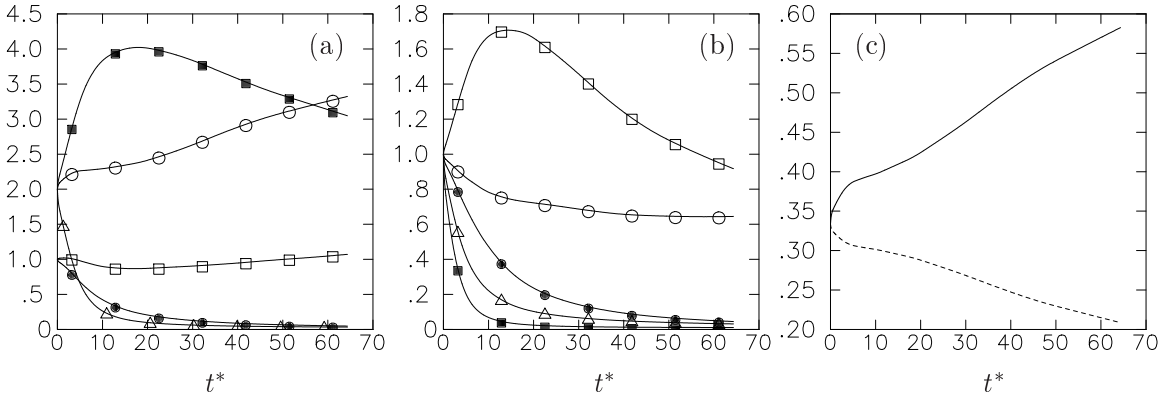

Figure 4.5: Development of anisotropy of velocity gradient and vorticity variances, for the same simulation as in Table 4.3. (a) $\langle u^2_{\parallel,\parallel}\rangle$ (•), $\langle u^2_{\parallel,\perp}\rangle$ (■), $\langle u^2_{\perp,\parallel}\rangle$ (△), $\langle (u^L_{\perp,\perp})^2\rangle$ (□), $\langle (u^T_{\perp,\perp})^2\rangle$ (○), all normalized by $\langle\epsilon\rangle/15\nu$; (b) Ratios between variance of velocity gradients: $\langle u^2_{\parallel,\parallel}\rangle/\langle (u^L_{\perp,\perp})^2\rangle$ (•), $\langle u^2_{\perp,\parallel}\rangle/\langle u^2_{\parallel,\perp}\rangle$ (■), for $2\langle u^2_{\parallel,\parallel}\rangle/\langle u^2_{\parallel,\perp}\rangle$ (△), $\langle u^2_{\parallel,\perp}\rangle/\langle (u^T_{\perp,\perp})^2\rangle$ (□), $2\langle (u^L_{\perp,\perp})^2\rangle/\langle (u^T_{\perp,\perp})^2\rangle$ (○); (c) $\langle\omega^2_{\parallel}\rangle$ (solid lines) and $\langle\omega^2_{\perp}\rangle$ (dashed lines), both normalized by $\langle\omega_i\omega_i\rangle$.

compared to x_2 and x_3. The strong decreases seen in $u_{\parallel,\parallel}$ and $u_{\perp,\parallel}$ are accompanied by a strong increase in $u_{\parallel,\perp}$, while the variance of $u_{\perp,\perp}$ shows relatively little change. However at sufficiently large times the transverse gradient in the orthogonal plane, i.e. $u^T_{\perp,\perp}$ ultimately becomes the largest. All of these observations are consistent with a trend towards two-dimensionality in the small scales. In fact for incompressible isotropic turbulence in two dimensions (Pope, 2000; Gotoh et al., 2007) the ratio between the mean-squares of transverse to longitudinal velocity gradients is 3.0, which is consistent with the ratio $2\langle (u^L_{\perp,\perp})^2\rangle/\langle (u^T_{\perp,\perp})^2\rangle$ approaching 2/3 closely as seen in frame (b) of this figure. In addition, Q2D behavior in the velocity gradients implies that one vorticity component ($\omega_{\parallel}$) becomes highly dominant, as seen in frame (c) especially at later times. This observation is consistent with the emergence of elongated vortical structures along the direction of the magnetic field, which can be explained by the principle of conservation of angular momentum (Davidson, 1997).

Since velocity gradient statistics are dominated by the small scales, one may ask if they may be not highly sensitive to effects of finite domain size nor forcing applied at the large scales. Indeed, several authors (Schumann, 1976; Zikanov and Thess, 1998; Vorobev et al., 2005; Favier et al., 2011) who used cubic domains or simulated forced MHD turbulence have reported results which are qualitatively similar those in Fig. 4.5. To check for domain size effects Fig. 4.6 shows several results obtained from domains of $\Lambda = 1$, 8, 64 (which were also used for other comparisons in

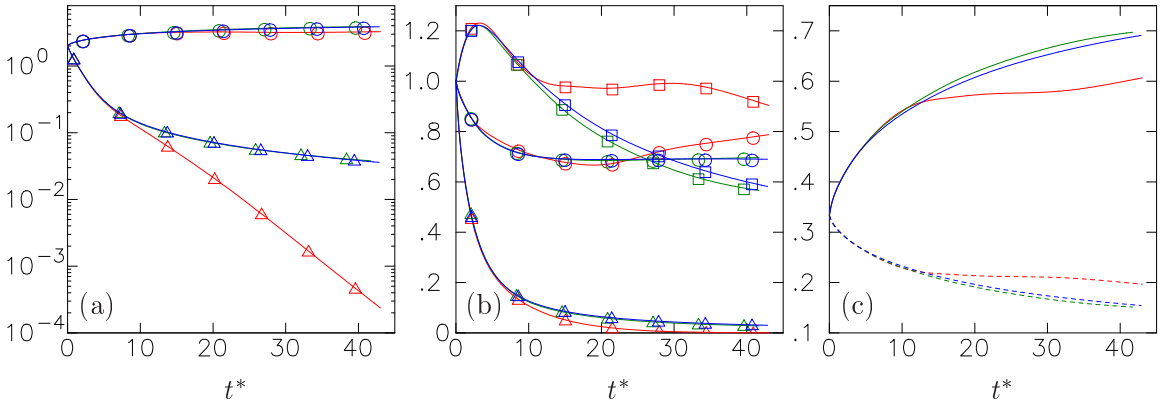

Figure 4.6: Development of anisotropy of velocity gradient and vorticity variances under a magnetic field, on domains with aspect ratio $\Lambda = 1$ (red), 8 (green) and 64 (blue) with the shortest dimension having 256 grid points. (a) $\langle u^2_{\perp,\parallel}\rangle$ ($\triangle$), $\langle (u^T_{\perp,\perp})^2\rangle$ ($\circ$), all normalized by $\langle\epsilon\rangle/15\nu$; (b) Ratios between variance of velocity gradients: $2\langle u^2_{\parallel,\parallel}\rangle/\langle u^2_{\parallel,\perp}\rangle$ ($\triangle$), $\langle u^2_{\parallel,\perp}\rangle/\langle (u^T_{\parallel,\perp})^2\rangle$ ($\square$), $2\langle (u^L_{\perp,\perp})^2\rangle/\langle (u^T_{\perp,\perp})^2\rangle$ ($\circ$); (c) $\langle\omega^2_\parallel\rangle$ (solid lines) and $\langle\omega^2_\perp\rangle$ (dashed lines), both normalized by $\langle\omega_i\omega_i\rangle$.

Fig. 4.3 and 4.4). Clearly, despite good agreement at early times substantial discrepancies are seen at later times. The differences seen indicate that Q2D character at later times is not as well defined in the case of $\Lambda = 1$. This is not surprising, since the confining effects of a finite domain size tends to prevent the flow structure to be extended in the parallel direction to greater lengths, thus acting to maintain a degree of dependence of the fluctuating velocity on the x_1 coordinate. Indeed, it is possible that more substantial domain size effects would arise in past simulations in the literature if they were extended to longer times.

As emphasized earlier, a long domain in the direction of magnetic field (i.e. one of large aspect ratio) is important in allowing the turbulence structure to evolve naturally. This effect can also be seen by visualization of the enstrophy (Ω, vorticity squared) within two-dimensional cuts taken in planes perpendicular or parallel to the magnetic field. For isotropic turbulence vortical structures are dominated by smaller scales and randomly oriented in space, but they are expected to be stretched out along the direction of the magnetic field. In Fig. 4.7, comparison of frames (a) and (b) (at two different times) for $\Lambda = 1$ shows that eventually some of the coherent vortical structures become as long as the domain itself (but, due to the nature of periodic boundary conditions, are not allowed to grow any further). This observation is reminiscent of past simulations where later-time results become strongly distorted by the confinement effects of periodic domains of finite size. (Zikanov and Thess, 1998; Reddy and Verma, 2014). In contrast, frames (c,d,e) show clearly that an elongated

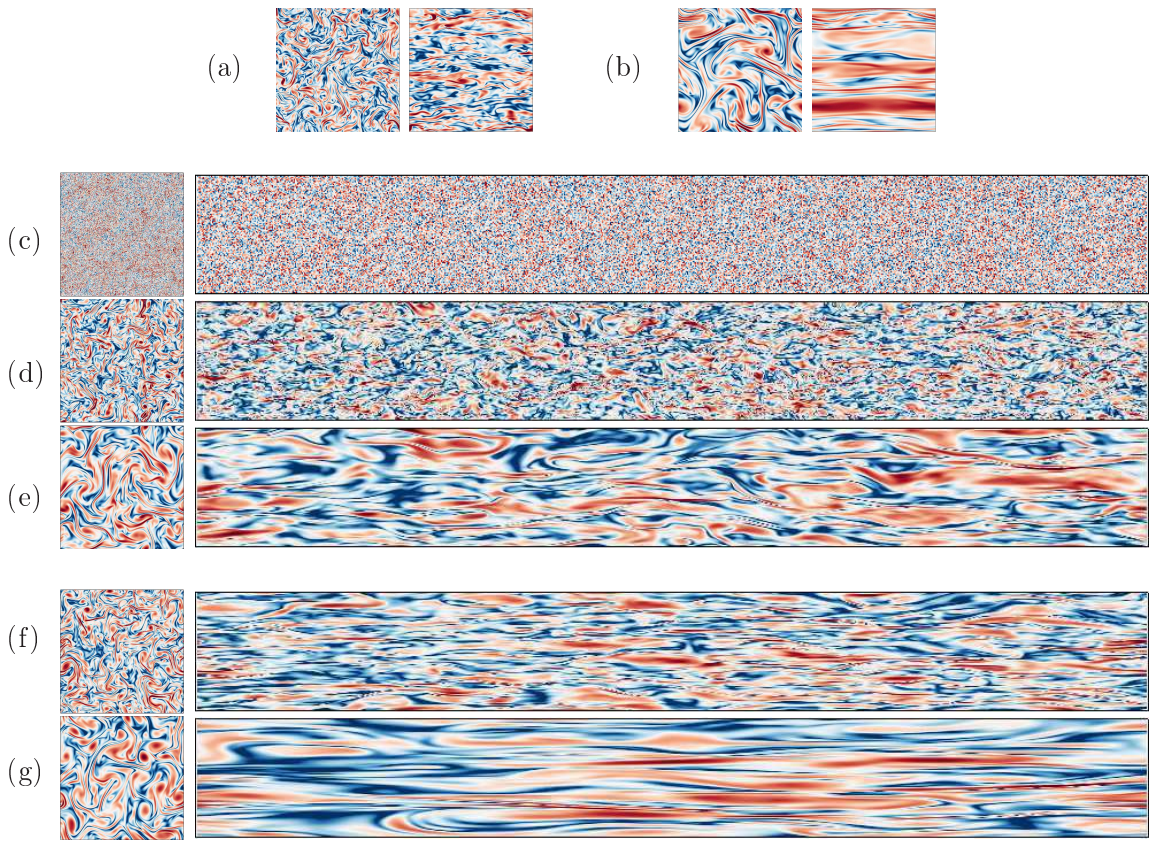

Figure 4.7: Visualizations of normalized enstrophy $\Omega/\langle\Omega\rangle$ showing development of coherent vortical structures in MHD turbulence in domains of different aspect ratios. The brighest red and darkest blue represent $\Omega/\langle\Omega\rangle > 10$ and < 0.05 respectively. Each frame is a pair of 2 images in $y-z$ (square, on left) and $x-z$ planes (rectangle, on right.) Frames (a) and (b) are from 2048^3 grid with $\Lambda = 1$, with $N = 1$, at $t^* = 12.58$ and 41.52 respectively; while frames (c), (d), (e) are from 16384×2048^2 grid with $\Lambda = 8$, with $N = 1$, at $t^* = 0$, 12.58 and 41.52. Frames (f) and (g) are similar to (d) and (e), but from simulation at $N = 8$.

domain (with $\Lambda = 8$) along the magnetic field allows the vortex filaments to grow beyond the limit imposed by a domain with $\Lambda = 1$. This contrast shows clearly the benefit of an elongated domain even for supposedly small-scale quantities such as the vorticity. The strong preferential orientation of the observed vortical structures also indicates strong anisotropy. It is also not surprising that this effect is even stronger for larger N, such as in frames (f,g) (for $N = 8$) versus frames (d,e) (for $N = 1$). The effects of large N will be addressed further in Chap. 4.5.

Local axisymmetry for small-scale statistics has some interesting implications for the diagonal elements of the dissipation tensor ($\epsilon_{ij} \equiv 2\nu\langle(\partial u_i/\partial x_k)(\partial u_j/\partial x_k)\rangle$) as well as those of the vorticity covariance tensor ($\langle\omega_i\omega_j\rangle$, whose trace gives the enstrophy, $\langle\Omega\rangle$). In particular, application of relations for locally axisymmetric turbulence derived by George and Hussein (1991) leads to the dissipation rates of velocity components parallel and perpendicular to the magnetic field and vorticity component variances being given by

$$\epsilon_\parallel = \langle(u_{\parallel,\parallel})^2\rangle + 2\langle(u_{\parallel,\perp})^2\rangle \,, \tag{4.9}$$

$$\epsilon_\perp = \langle(u_{\perp,\parallel})^2\rangle + (1/3)\langle(u_{\parallel,\parallel})^2\rangle + (4/3)\langle(u^T_{\perp,\perp})^2\rangle \,, \tag{4.10}$$

$$\langle\omega^2_\parallel\rangle = -(1/3)\langle u^2_{\parallel,\parallel}\rangle + (8/3)\langle(u^T_{\perp,\perp})^2\rangle \,, \tag{4.11}$$

$$\langle\omega^2_\perp\rangle = \langle u^2_{\parallel,\parallel}\rangle + \langle u^2_{\perp,\parallel}\rangle + \langle(u_{\parallel,\perp})^2\rangle \,. \tag{4.12}$$

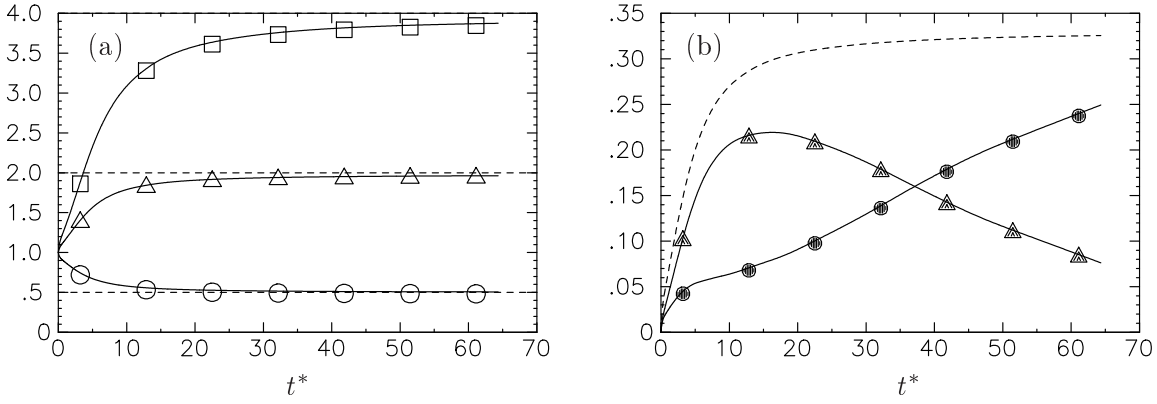

Figure 4.8: (a) Evolution of $\epsilon_\parallel/\langle\omega^2_\perp\rangle$ (△), $\epsilon_\perp/\langle\omega^2_\parallel\rangle$ (◯) and $(\epsilon_\parallel/\epsilon_\perp)(\langle\omega^2_\parallel\rangle/\langle\omega^2_\perp\rangle)$ (□). Horizontal dashed lines are at values 0.5 and 2.0. (b) Anisotropy tensor elements $d_\parallel = \epsilon_\parallel/(2\epsilon) - 1/3$ for dissipation (▲), $v_\parallel = \langle\Omega_\parallel\rangle/\langle\Omega\rangle - 1/3$ for vorticity covariance (•), and their sum $d_\parallel + v_\parallel$ (dashed line).

Since in MHD turbulence velocity gradients along the parallel direction are strongly suppressed,

Table 4.4: Skewness (μ_3) and flatness (μ_4) factors of the velocity gradients, classified according to statistical axisymmetry as referenced earlier in Chap. 4.4.2

t^*	$u_{\parallel,\parallel}$	$u^L_{\perp,\perp}$	$u_{\parallel,\parallel}$	$u^L_{\perp,\perp}$	$u_{\parallel,\perp}$	$u_{\perp,\parallel}$	$u^T_{\perp,\perp}$
	μ_3	μ_3	μ_4	μ_4	μ_4	μ_4	μ_4
0	-0.5290	-0.5286	5.230	5.227	7.345	7.343	7.348
1.08	-0.4611	-0.5507	4.941	4.963	6.593	6.928	6.836
2.06	-0.4173	-0.5605	4.929	4.925	6.427	6.936	6.710
4.87	-0.3309	-0.5299	5.183	4.708	6.333	7.269	6.274
6.86	-0.2783	-0.4844	5.463	4.490	6.452	7.404	5.919
12.58	-0.2138	-0.3443	5.994	3.950	6.894	6.499	5.237
26.25	-0.1023	-0.1643	5.429	3.419	6.940	4.830	4.444
41.52	-0.0211	-0.0901	4.894	3.179	6.480	4.438	4.115
61.44	0.0839	-0.0556	5.553	3.320	6.341	4.222	3.822

the relations above can be simplified by keeping the respective last terms which involve gradients in the perpendicular direction. It then follows that

$$\epsilon_\parallel/\langle\Omega_\perp\rangle \approx 2\ ,\ \ \epsilon_\perp/\langle\Omega_\parallel\rangle \approx 1/2 \tag{4.13}$$

(where, for brevity, denote $\omega^2_\parallel$ and $\omega^2_\perp$ by $\Omega_\parallel$ and $\Omega_\perp$ with $\Omega = \Omega_\parallel + 2\Omega_\perp$) and hence

$$(\epsilon_\parallel/\epsilon_\perp)(\langle\Omega_\parallel\rangle/\langle\Omega_\perp\rangle) \approx 4\ . \tag{4.14}$$

Equation (4.14) gives a relationship between elements of the anisotropy tensors for dissipation and vorticity covariance satisfying local axisymmetry: namely with $d_\parallel = \epsilon_\parallel/(2\epsilon) - 1/3$ and $v_\parallel = \langle\Omega_\parallel\rangle/\langle\Omega\rangle - 1/3$, if $\langle\Omega_\parallel\rangle/\langle\Omega_\perp\rangle = 4/(\epsilon_\parallel/\epsilon_\perp)$ an algebraic rearrangement leads to

$$d_\parallel + v_\parallel = 1/3\ . \tag{4.15}$$

Figure 4.8 shows comparisons of DNS data with (a) Eqs.(4.13)-(4.14) and (b) anisotropy tensor elements for the dissipation and vorticity covariance with Eq. (4.15). Both frames of this figure indicate very good agreement with the asymptotic results at large times.

In addition to second moments, third and fourth moments of the velocity gradients provide important information on nonlinear processes contributing to spectral transfer and intermittency. In 3D isotropic turbulence the longitudinal velocity gradient has a negative skewness of order -0.5

while the transverse velocity gradients have a higher flatness factor (that increases with the Reynolds number). Table 4.4 shows the skewnesses of $u_{\parallel,\parallel}$ and $u^L_{\perp,\perp}$ as well as the flatness factors of all five independent components of the velocity gradients under conditions of axisymmetry. It can be seen that the skewnesses are much reduced, which is consistent with the absence of a forward energy cascade in 2D turbulence. The flatnesses of gradients of $u_\parallel$ show no drastic change but those of the gradients of $u_\perp$ are strongly reduced. This apparent reduction of intermittency in the plane perpendicular to the magnetic field is also consistent with the general absence of intermittency (at least at high Reynolds numbers) in 2D turbulence (Boffetta and Ecke, 2012; Smith and Yakhot, 1994).

4.4.3 Anisotropy in spectral space

Results in the two preceding subsections indicate both the large scales and the small scales deviate (differently) from isotropy in response to the magnetic field. To characterize anisotropy as a function of scale size it is natural to use a spectral (wavenumber) space description. However, since the observed anisotropy is strong, both magnitude and orientation in wavenumber space should be considered. Information on orientation can be expressed by using the angle between the wavevector $\mathbf{k}$ and the k_1 axis, or by using both k_1 and k_r simultaneously. In practice, the first approach tends to give noisy results at low wavenumbers, since Fourier modes on a Cartesian grid are not uniformly distributed with respect to this nor other angles. In this work, the simultaneous use of k_1 and k_r is found to be more convenient. Specifically one-dimensional (1D) spectra (which depend on k_1 and k_r separately) and the axisymmetric energy spectrum (which depend on k_1 and k_r jointly) are examined, as the cumulative result of various physical processes represented in the spectral budget equations.

In isotropic turbulence 1D spectra can be classified as longitudinal and transverse, which are related to each other through a constraint based on incompressibility. The reversal of the Reynolds stress anisotropy noted in Chap. 4.4.1 suggests a qualitative change in how longitudinal and transverse spectra compare with each other, especially at low wavenumbers. Figure 4.9 shows the 1D spectra of u_1 and u_2, as a function of k_1. The scales chosen in the plot here are such that the integral under the curves (in log-linear scales) is equal to the variance of u_1 or u_2 normalized by $K(t)$. At $t^* = 0$ the areas under the two spectra are nearly equal, as required for isotropic turbulence.

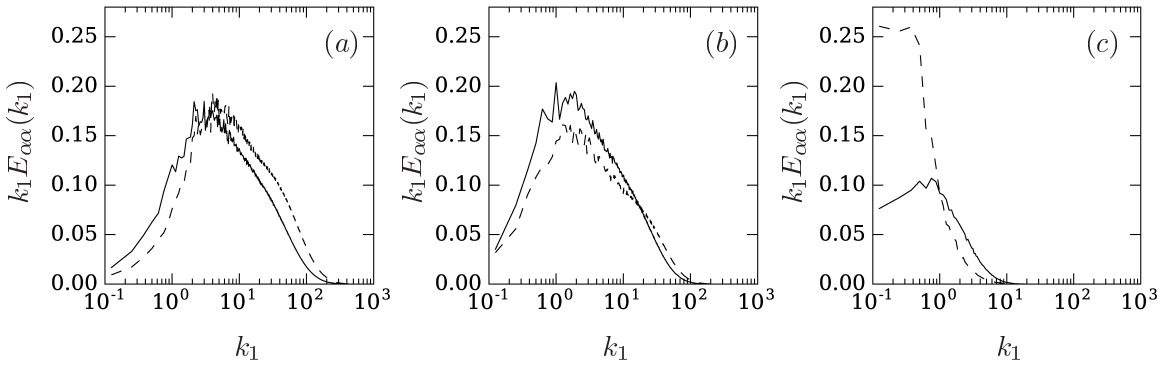

Figure 4.9: Compensated 1D spectra $k_1 E_{\alpha\alpha}(k_1)$: solid and dashed lines for $\alpha = 1$ and $\alpha = 2$ respectively. From (a) to (c): at $t^* = 0$, 2.06, 26.25, normalized by the instantaneous kinetic energy.

Subsequently, both spectra are shifted towards smaller k_1, as energy is increasingly concentrated in motions with a large length scale in the x_1 direction. At $t^* = 2.06$, when $\langle u_1^2 \rangle$ has become larger than $\langle u_2^2 \rangle$ (Table 4.3) the spectrum of u_1 is higher than that of u_2 up to $k_1 = 20$. In contrast, at a later time $t^* = 26.25$ when the anisotropy has reversed, the spectrum $E_{22}(k_1)$ has shifted so strongly to low k_1 that it is at least twice of $E_{11}(k_1)$ for $k_1 < 1$. Since integral length scales are proportional to the ratio of 1D spectrum at zero wavenumber to the mean-squared velocity, the features seen at this later time are consistent with a strong growth of integral length scales in the x_1 direction (for all velocity components). Furthermore, Fourier modes of $k_1 < 1$ are present only because the solution domain employed is longer than 2π in the x_1 direction — thus confirming again the importance of using larger or elongated solution domains in the study of MHD effects.

To understand the evolution of the 1D spectra, it is necessary to compute various terms in the spectral evolution equations. For each Fourier mode with wavevector $\mathbf{k}$, the energy spectrum tensor $E_{ij}(\mathbf{k}) \equiv \frac{1}{2}\langle \hat{u}_i^*(\mathbf{k})\hat{u_j}(\mathbf{k}) + \hat{u}_j^*(\mathbf{k})\hat{u}_i(\mathbf{k})\rangle$ (where asterisks for Fourier coefficients denote complex conjugates) evolves by

$$dE_{ij}(\mathbf{k})/dt = -D_{ij}^V(\mathbf{k}) - D_{ij}^J(\mathbf{k}) + \Pi_{ij}(\mathbf{k}) + T_{ij}(\mathbf{k}) \tag{4.16}$$

where terms on the r.h.s. defined by

$$D^V_{ij}(\mathbf{k}) = 2\nu k^2 E_{ij}(\mathbf{k}) \tag{4.17}$$

$$D^J_{ij}(\mathbf{k}) = 2(\sigma B_0^2/\rho)\,(k_1/k)^2\, E_{ij}(\mathbf{k}) \tag{4.18}$$

$$\Pi_{ij}(\mathbf{k}) = ik_i\langle \hat{u}^*_j(\mathbf{k})\hat{p}(\mathbf{k})\rangle - ik_j\langle \hat{u}^*_i(\mathbf{k})\hat{p}(\mathbf{k})\rangle \tag{4.19}$$

$$T_{ij}(\mathbf{k}) = -\left[\langle ik_m\hat{u}^*_i(\mathbf{k})\widehat{u_j u_m}\rangle + \langle ik_m\hat{u}^*_j(\mathbf{k})\widehat{u_i u_m}\rangle\right] \tag{4.20}$$

represent viscous dissipation, Joule dissipation, redistribution due to pressure fluctuations and non-linear spectral transfer respectively. For each term, a 1D spectrum can be formed by summing up contributions in the $k_2 - k_3$ plane at fixed k_1, while an axisymmetric spectrum can be formed by summing over annular rings within this plane.

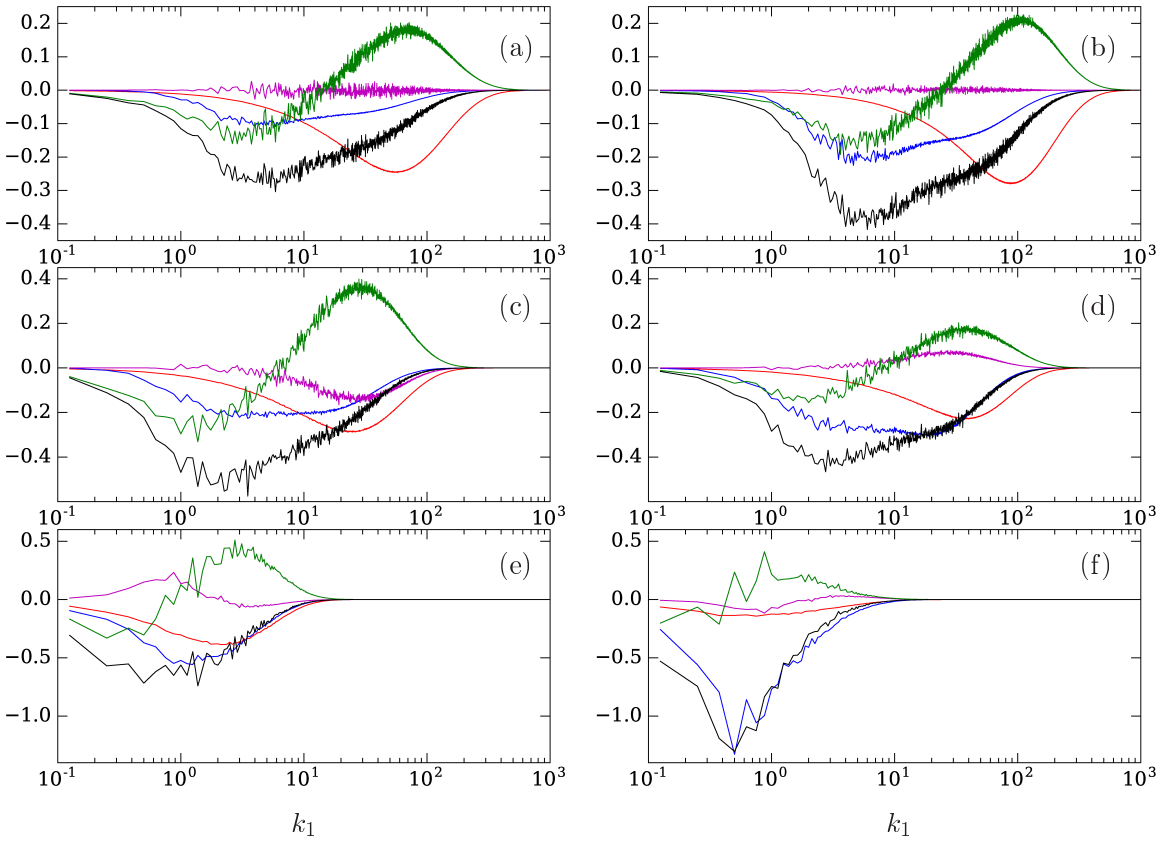

Figure 4.10: Terms contributing to the evolution of 1D compensated spectra: (a), (c) and (e) for $d\big(k_1 E_{11}(k_1)\big)/dt$, (b), (d) and (f) for $d\big(k_1 E_{22}(k_1)\big)/dt$, at normalized times (from top to bottom) $t^* = 0$, 2.06, 26.25. Different curves denote time rate of change (black), viscous dissipation (red), Joule dissipation (blue), non-linear transfer (green) and pressure strain correlation (magenta). All are normalized by the instantaneous viscous dissipation.

Figure 4.10 shows the budget of terms in Eq. (4.16) for the 1D spectra $E_{11}(k_1)$ (in frames (a,c,e)) and $E_{22}(k_1)$ (in frames (b,d,f)). In general the calculation of spectral quantities at low wavenumber can be affected by errors associated with the number of Fourier modes in a designated wavenumber interval being relatively small. For each given k_1 this effect is more significant if the 1D spectrum concerned is dominated by modes with small k_r. A slight degree of jaggedness is indeed apparent in all curves except for the viscous dissipation, which is dominated by modes of relatively large k_r. At $t^* = 0$ the rates of change of $E_{11}(k_1)$ and $E_{22}(k_2)$ differ mainly as a result of differences between $D^J_{11}(k_1)$ and $D^J_{22}(k_1)$, consistent with the relation $\langle J_{22} \rangle \approx 2\langle J_{11} \rangle$ as discussed in Sec. 4.4.1. The resulting difference between the rates of change of the two 1D spectra is such that $E_{22}(k_1)$ starts to fall more rapidly than $E_{11}(k_1)$ over a broad wavenumber range, leading to a degree of anisotropy that depends on scale size in the direction of the magnetic field.

It can be seen from frames (c) and (d) above that at $t^* = 2.06$ spectral transfer (green lines) of u_2 from low to high k_1 is significantly weaker than that of u_1. Reduced transfer of u_2 from low k_1 to high k_1 has the effect of slowing down the rate of decrease of $E_{22}(k_1)$ in time. Since this trend is opposite to that observed at $t^* = 0$, this contributes to a gradual weakening, and eventually reversal of anisotropy at later times. At $t^* = 26.25$ all the spectral activity has moved to considerably lower wavenumbers, while the Joule dissipation becomes highly dominant. Finally while pressure-strain correlation term (lines in magenta) is not dominant at any of the three time instants shown, its general effect is to re-distribute energy from the velocity component with more energy to that with less, as reflected in the general change in sign between frames (c,d) and (e,f).

A more direct illustration of changes in spectral transfer due to the magnetic field is given in Fig. 4.11, which shows 1D and radial transfer spectra at different times in each frame. In general, as MHD effects cause the turbulence length scales to grow, wavenumber ranges of significant transfer activity are shifted from higher to lower wavenumbers. As this shift to lower wavenumbers continues, energy also becomes increasingly dominated by a small number of Fourier modes, leading to numerical noise which is reflected by the jagged nature of lines in black in this figure. Despite this noise much of the spectral transfer is recognized as being of a "forward cascade" nature, i.e., negative at the lowest few k_1 or k_r values but generally positive for higher wavenumbers. However there is an important exception, in frame (d), where at late times $k_r T_{22}(k_r)$ is positive at the first few values of k_r. This indicates occurrence of backward transfer in the plane perpendicular to the mag-

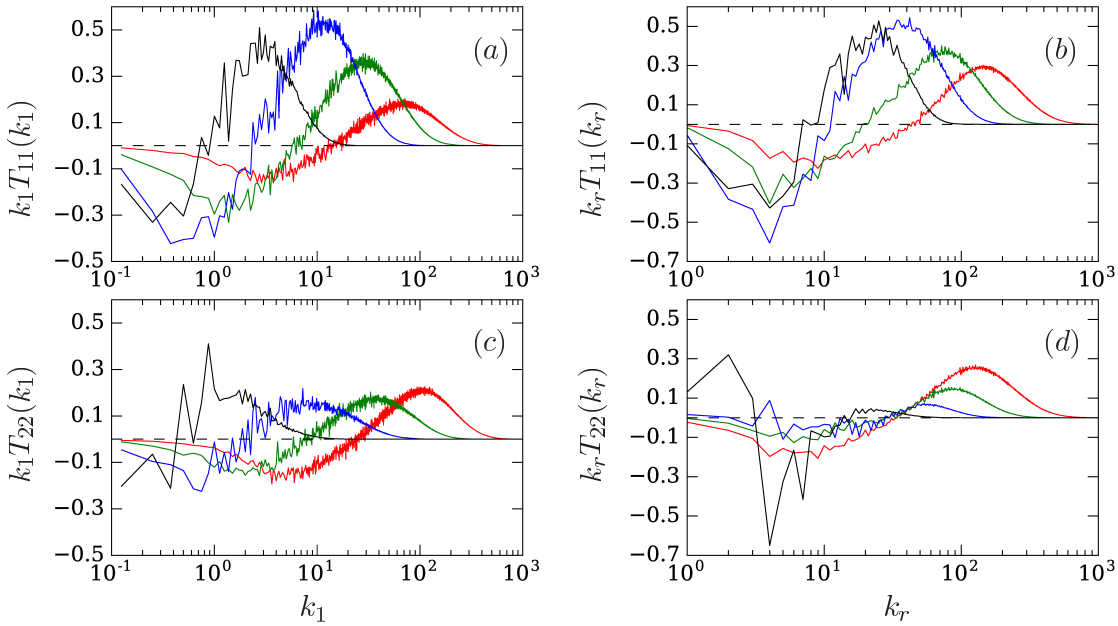

Figure 4.11: Evolution of (left) compensated 1D transfer spectra of (a) $k_1T_{11}(k_1)$, (c) $k_1T_{22}(k_1)$, and (right) compensated radial transfer spectra of (b) $k_rT_{11}(k_r)$, (d) $k_rT_{22}(k_r)$. All the spectra shown are normalized by instantaneous viscous dissipation. Lines in red, green, blue and black denote times $t^* = 0$, 2.06, 6.86 and 26.25 respectively.

netic field. This backward energy transfer in velocity perpendicular to the magnetic field has also been reported in forced simulations (Reddy, Kumar, and Verma, 2014), and is consistent with the transfer characteristics found in two-dimensional three-component turbulence (Montgomery and Turner, 1982; Favier et al., 2011). In addition, in this frame, transfer activity at intermediate to higher radial wavenumbers generally becomes weaker in time. This reduction of spectral transfer is consistent with weakened non-Gaussianity for velocity gradients in the orthogonal plane as seen earlier in Table 4.4.

Axisymmetric spectra can give more detailed information of energy distribution in Fourier space. Figure 4.12 shows contour lines of the axisymmetric energy spectrum $E_A(k_1, k_r)$ at three different times (from left to right). As noted in Chap. 4.3, departure from circular contours indicate anisotropy. At $t^* = 2.06$ most contours are at least mildly non-circular: e.g. the curve in red (second counting from outwards) intersects the wavenumber axes at $k_1 \approx 720$ but at $k_r \approx 820$. To facilitate comparisons in time, the same contour levels are used at different times. However at later times a zoom-in on lower and lower wavenumbers is needed in order to see all the important features. The contour lines are seen to increasingly deviate from circles. In frame (c) it is also seen that the

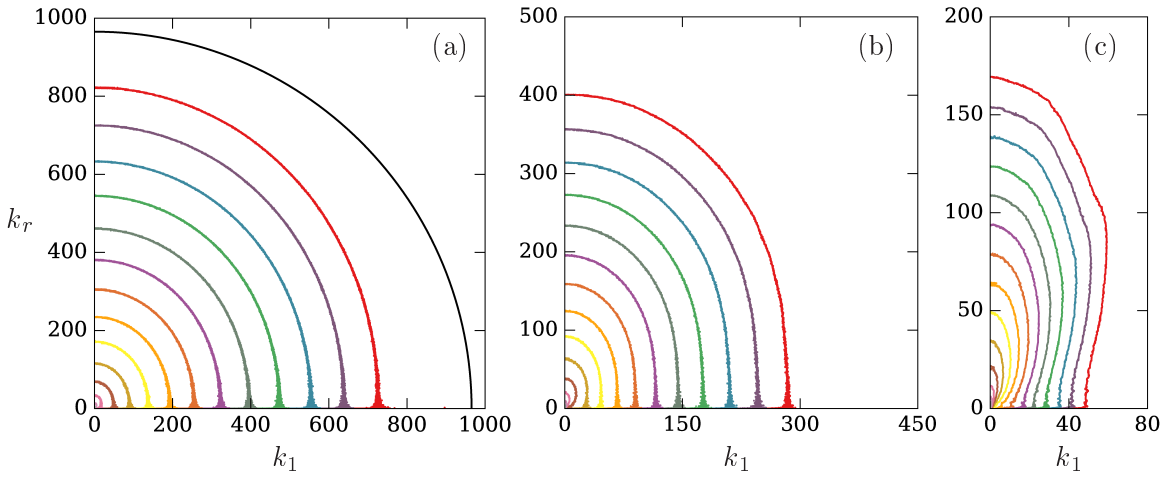

Figure 4.12: Contours of axisymmetric energy spectrum $E_A(k_1, k_r)$ at times (from left to right) $t^* = 2.06$, 6.86, 26.25. Contour levels are set at logarithmically-spaced intervals, decreasing by successive factors of 10 outwards from near the origin. (Note the diffeernces among different frames in the upper limits of the coordinate axes shown. In frame (a) maximum values of both k_1 and k_r are both 960.)

contour lines bend backwards towards smaller k_1 in the region where k_r is also small, showing that energy is increasingly concentrated in Fourier modes with low k_1, i.e. in the plane orthogonal to the magnetic field. These trends are consistent with those seen in forced simulations (Reddy, Kumar, and Verma, 2014).

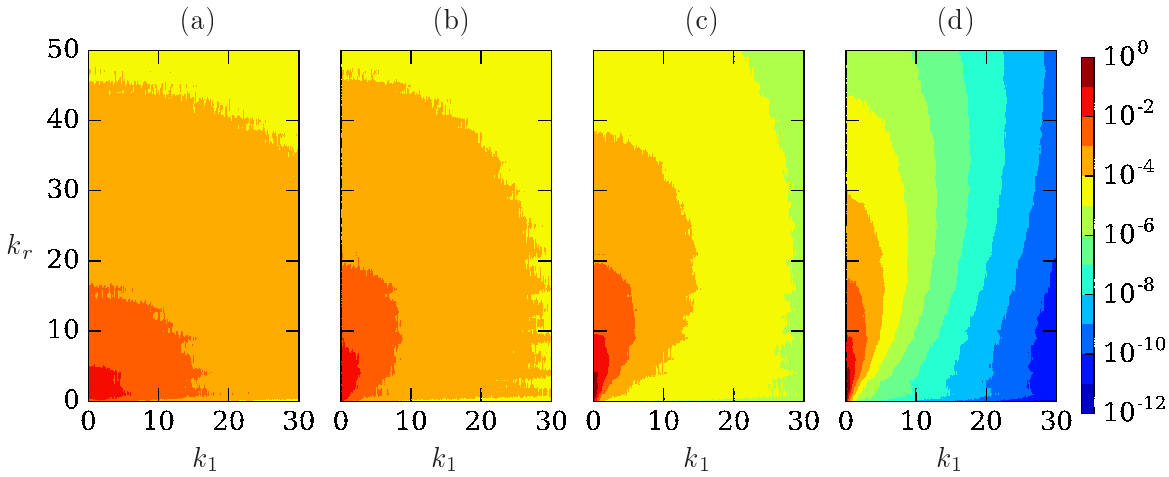

Figure 4.13: Axisymmetric spectra of TKE. From left to right, $t^* = 0$, 2.06, 6.86, 26.25.

Since the magnetic field causes energy to be concentrated at low wavenumbers, Fig. 4.13 shows some zoomed-in details for the same spectral region at different times in the simulation. At $t^* = 2.06$ (frame (b)), a departure from isotropy is already evident. At $t^* = 6.86$ (frame (c)) the property

of contour lines (at the boundaries between color-coded regions) bending backwards towards $k_1 \approx 0$ at low k_r is well developed. At the last time instant shown (frame (d)) it is clear that energy is increasingly concentrated in a narrow crescent-like region with very small k_1 but a large ratio between k_r and k_1. These results also reaffirm the importance of representing spectral regions of $k_1 < 1$ properly using a domain which is long in the x_1 direction.

To illustrate the effects of different terms in the spectral budget equation on the change of axisymmetric energy spectrum, Fig. 4.14 shows the axisymmetric spectrum of each term in Eq. (4.16). (The pressure-strain correlation term is not shown since it is traceless and does not contribute to changes in the kinetic energy.) To facilitate comparisons between these different terms the frames at a given time are placed horizontally next to each other, and in contrast to the arrangement in Fig. 4.13 now different upper limits are used on the k_r axis at different times. In Fig. 4.14, even at $t^* = 0$ the rate of change (frame (a)) already shows anisotropic character, in which the contours extend to larger k_1 than k_r. This behavior is due to that of the Joule dissipation, which (frame (c)) favors modes of larger k_1 for a given k if the initial velocity field is isotropic. For axisymmetric spectrum of energy transfer, while color contours are used to indicate magnitudes of positive transfers, blank regions indicate negative values — i.e. those modes which are losing energy as a result of the nonlinear interactions. Some degree of noise is present because the transfer is nearly zero in between spectral regions where the spectral transfer is primarily positive or negative respectively. Nevertheless in frame (d) modes losing energy (with negative transfer) can be seen to lie mostly in regions of low k_1 and low k_r, which is consistent with a conventional forward energy cascade.

As time proceeds, down successive rows of Fig. 4.14, all the axisymmetric spectra undergo substantial changes in both magnitude and shape. A most striking feature is that the spectra for Joule dissipation changes from one that favors modes lying close to the k_1 axis to one that favor modes lying close to the k_r axis. At late times (frame (o)) the Joule dissipation largely resides in a narrow strip next to the k_r axis. The spectrum of viscous dissipation also follows a similar pattern, but later, since it responds to the magnetic field only indirectly via changes in the energy spectrum itself. Zones of negative spectral transfer almost become mostly restricted to the narrow strip near the k_r axis — but it extends to higher values of k_r than seen in zones of highest activity in the other terms. In both frames (l) and (p), at very small k_1, there is a narrow range of k_r where a decrease of k_r leads to a change from negative to positive transfer, which can be taken as a directional form of

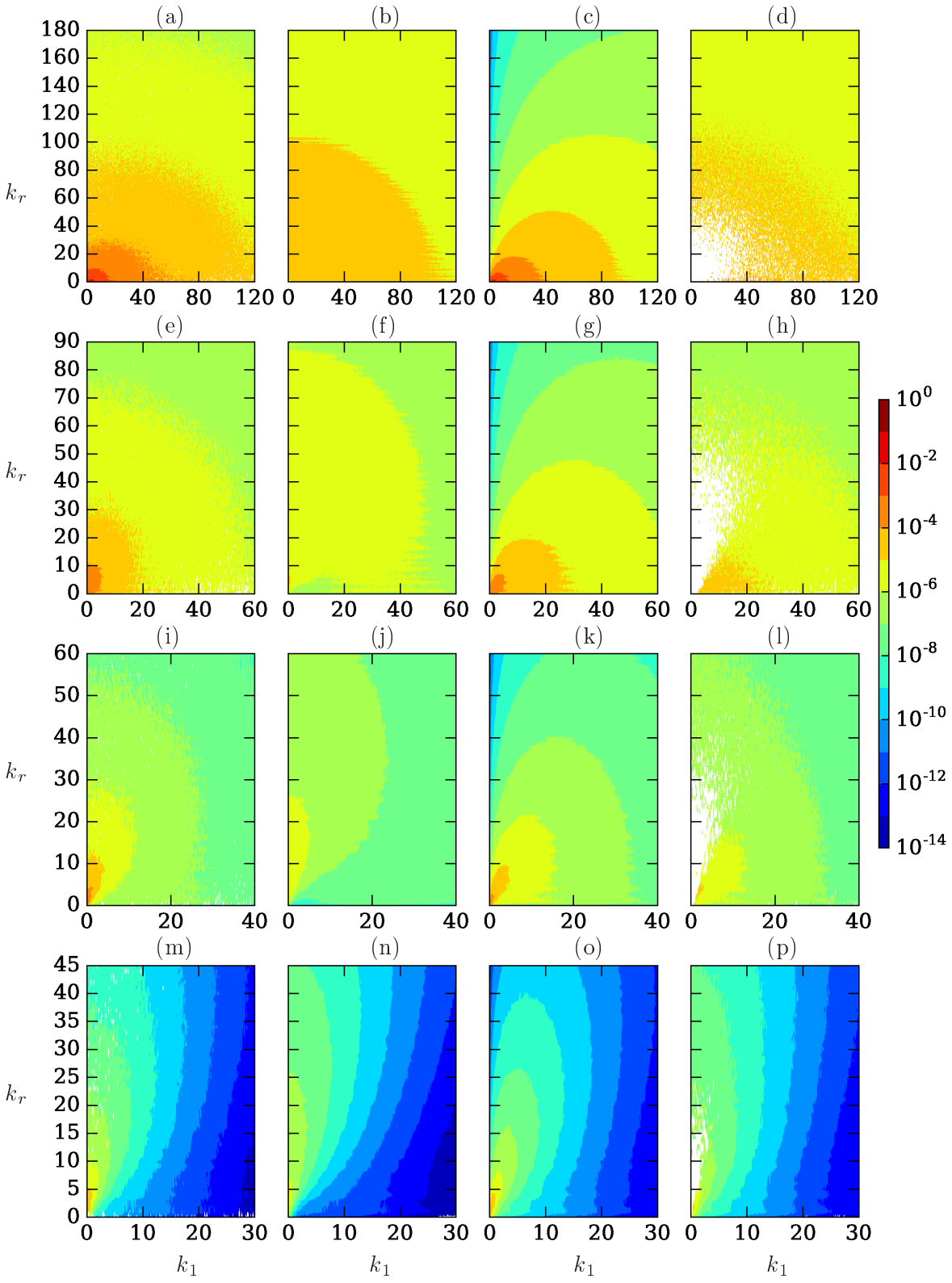

Figure 4.14: Axisymmetric spectra of the terms in the energy budget equation. From left to right: (negative of) rate of change, viscous dissipation, Joule dissipation, and positive values of spectral transfer. From top to bottom $t^* = 0$, 2.06, 6.86, 26.25.

reverse cascade. Previous studies (Alemany et al., 1979; Schumann, 1976; Caperan and Alemany, 1985; Knaepen and Moreau, 2008) have also suggested angular transfers from spectral regions with $k_r > k_1$ to $k_r < k_1$. Finally, it may be noted that the contour pattern in frame (m) of this figure (for the rate of change at $t^* = 26.25$) is qualitatively similar to that of the energy itself in frame (d) of Fig. 4.13. This suggests the shape of the energy spectrum is unlikely to change dramatically if the simulation were to be extended to longer times.

Although viscous dissipation is not the most important term in the discussion above it is worth noting that following the sequence of frames (b-f-j-n) in Fig. 4.14, this spectrum increasingly decreases with the wavenumber. In DNS, even in those with forcing, since the range of scales is limited, viscous dissipation spectrum usually peaks at a modest wavenumber. At $t^* = 0$ this peak is well within the pale-orange region in frame (b). Subsequently, since energy and dissipation spectra are related by a kinematic factor of $2\nu k^2$, as the energy spectrum becomes heavily concentrated at the lowest wavenumbers, the same feature occurs in the dissipation spectrum, as well. This explains why in frame (n) a strong decrease with increasing wavenumber is seen, especially with respect to k_1 since length scales grow most strongly in this direction.

4.5 Effects of the Magnetic Interaction Parameter

In Chap. 4.4 above the focus is on the case of $N = 1$, i.e. for the ratio of pre-MHD eddy turnover time $T_E = L_{11}/u'$ to Joule time $\tau_J \equiv \rho/(\sigma B_0^2)$ to be equal to unity. If $N > 1$ then the Lorentz force operates at a time scale shorter than the large eddy turnover time, such that the effects of the magnetic field are felt rapidly. As may be expected, a larger N will lead to a more rapid growth of integral length scales, which means numerical requirements in the form of elongated solution domains will become more demanding. Consequently only the data at modestly large values of N is presented while ensuring numerical results are not grossly contaminated by the effects of finite domain size. In this section the focus is whether the time evolution of some single-point statistics might scale with the Joule time (which is fixed in time), and how the evolution of some spectral quantities may depend qualitatively on N.

It is useful to compare results over a series of simulations where the initial turbulence state is the same but N is varied systematically. Per Table 4.2, similar calculations for 10 different values

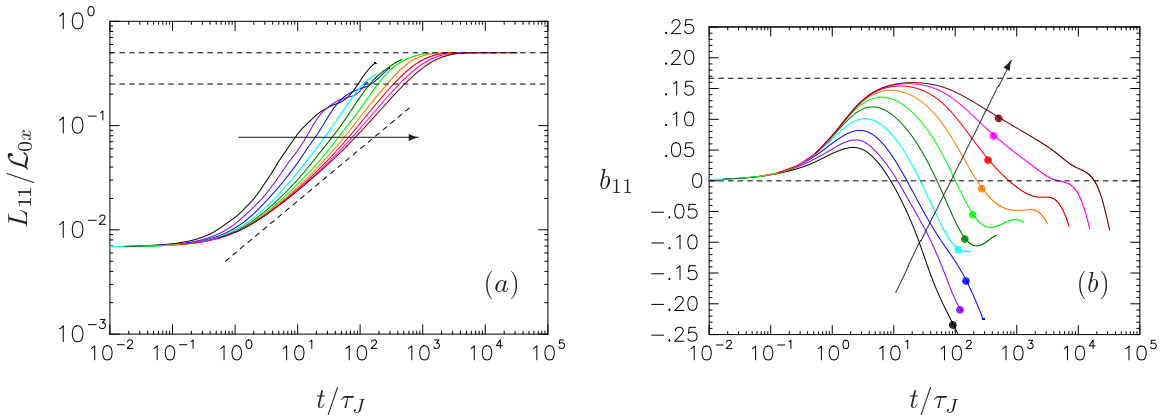

Figure 4.15: Evolution of (a) normalized integral length scale and (b) Reynolds stress anisotropy tensor element, in the direction of the magnetic field, with arrows pointing in the direction of increasing N (0.5, 1, 2, 4, 8, . . . , 256). In (a), sloping dashed line has slope of 0.5, horizontal dashed lines are at heights 0.25 and 0.5. In (b), solid circles indicate time instants when L_{11} exceeds 1/4 of $\mathcal{L}_{0x}$ as seen in (a). The upper dashed line is at height 1/6.

of N are performed, from 0.5 to 256 (in powers of 2), but at a lower grid resolution of 4096×512^2 and a lower pre-MHD Reynolds number. Figure 4.15 shows the evolution of the integral length scale along the direction of the magnetic field, and the anisotropy tensor element b_{11}, versus time normalized by τ_J. Scaling with Joule time would be indicated if curves for a wide range of N were to coincide. In both frames of this figure this scaling appears to hold better at large N but only at early times up to $t = O(\tau_J)$. In frame (a) a straight line of slope 0.5 on log-log scales is used to compare with a prediction by Okamoto, Davidson, and Kaneda (2010) that the ratio $L_{11}/\mathcal{L}_{0x}$ should be proportional to $(t/\tau_J)^{1/2}$ at large N and large t/τ_J. A modest degree of agreement is seen, but results at later times may also be contaminated by domain size effects as L_{11} grows past 1/4 of $\mathcal{L}_{0x}$ and eventually ceases to increase any further upon reaching its maximum possible value of $\mathcal{L}_{0x}/2$. In (b), at large N anisotropy is clearly very strong, with b_{11} almost reaching 1/6, which is the limiting value corresponding to the result $\langle u_1^2 \rangle = 2\langle u_2^2 \rangle$ predicted by the theory of Moffatt (1967) which assumes both viscous and nonlinear transfer effects to be vanishingly small. Another effect of large N is that the integral length scales grow extremely fast, eventually even reaching its maximum value of half of the length of the solution domain. Some of the less well-defined features in the curves for b_{11} at late times (beyond those values of t/τ_J marked by the solid circles on each line) are probably the result of finite domain size effects.

The results in Fig. 4.15 show how the large scale motions respond to magnetic fields of different

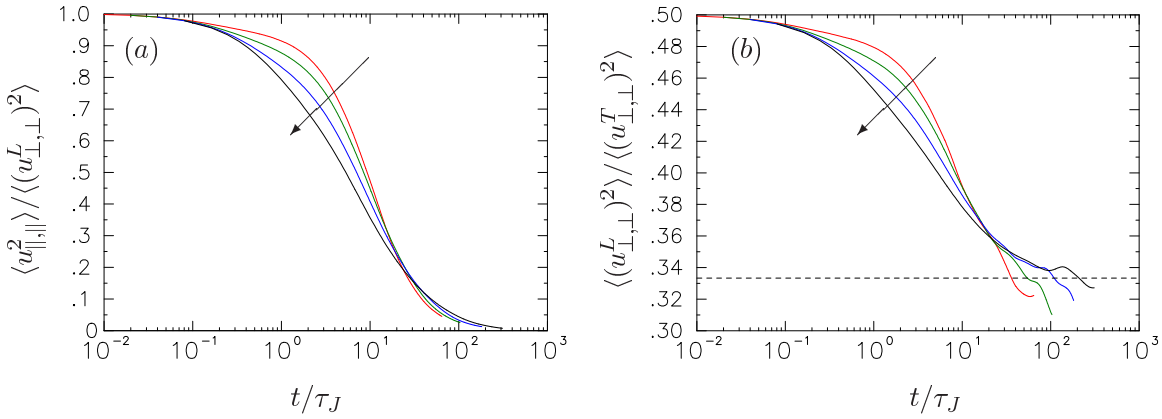

Figure 4.16: Evolution of (a) $\langle u^2_{\parallel,\parallel}\rangle/\langle(u^L_{\perp,\perp})^2\rangle$, (b) $\langle(u^L_{\perp,\perp})^2\rangle/\langle(u^T_{\perp,\perp})^2\rangle$. Arrows point in the direction of increasing N $(1, 2, 4, 8)$, for the same 16384×2048^2 domain of $\Lambda = 8$. In (b) the horizontal dashed line denotes $1/3$, which is the value in 2D isotropic turbulence.

strengths (even if the integral scales are still shorter than 1/4 of the domain size). To examine how the small scales respond Fig. 4.16 shows some ratios of the variances of velocity gradients. Since the main interest in the small scales is in departures from local isotropy, a larger grid of 16384×2048^2 with a higher pre-MHD Reynolds number is used. In both frames of Fig. 4.16 the main effect of a larger N is to accelerate, beyond slightly more than 0.1 τ_J, the transition from a state of local isotropy to a new asymptotic state of anisotropy. In frame (a) the ratio between longitudinal gradient variances beyond about 30 τ_J is almost independent of N. In frame (b) the ratio between longitudinal and transverse gradient variances in the orthogonal plane drops to values close to 1/3 (the value for 2D turbulence), although oscillations (presumably arising from finite domain size effects) develop from about 30 τ_J onwards. These results are consistent with a trend towards a Q2D state, whose development is hastened by stronger magnetic fields.

For spectral characteristics, Fig. 4.17 shows the spectral budget for 1D spectra (similar to those in Fig. 4.10) obtained with $N = 1$ versus $N = 8$. In frames (a) and (c) it is seen that at large N the Joule dissipation dominates the rate of change of the spectrum immediately from $t^* = 0$ onwards. At later times (here $t^* = 3.29$ corresponds to a time close to maximum anisotropy) the bulk of the spectral activity is clearly shifted to lower values of k_1. While both spectral transfer and viscous dissipation become more significant, for k_1 about 8 onwards these two contributions appear to cancel out each other, so that the Joule dissipation still dominates the rate of change overall.

Finally, Fig. 4.18 shows axisymmetric spectra of different terms in the spectral energy budget

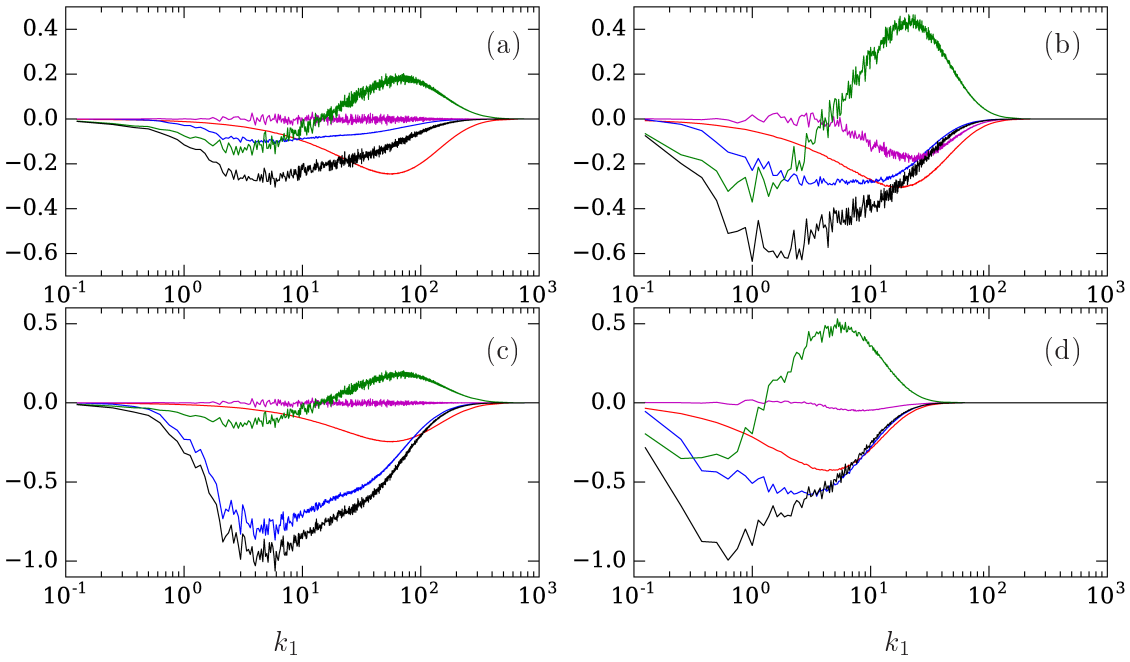

Figure 4.17: Terms contributing to the evolution of 1D compensated spectra of: $d\big(k_1 E_{11}(k_1)\big)/dt$: (a) $t^* = 0$, with $N = 1$; (b) $t^* = 3.29$, with $N = 1$; (c) $t^* = 0$, with $N = 8$; (d) $t^* = 3.29$, with $N = 8$. Different curves denote time rate of change (black), viscous dissipation (red), Joule dissipation (blue), non-linear transfer (green) and pressure strain correlation (magenta). All curves are normalized by the instantaneous viscous dissipation.

equation, at $N = 8$ in a manner similar to $N = 1$ results in Fig. 4.14. Frames a-d and e-h of Fig. 4.18 can be compared with frames a-d and m-p of Fig. 4.14 respectively, with the same color map being used in both figures. Comparison between frames (a) and (c) shows that at $t^* = 0$ the initial rate of change in regions of strongest activity is dominated by the Joule dissipation, except at very low k_1 and at higher values of k_r. The contours in frame (c) have the same shape as those in frame (c) of Fig. 4.14 but are at higher contour levels and hence shown in a different color. At the later time of $t^* = 26.25$ all four frames in the bottom row are very similar in shape, being concentrated in zones of low k_1 and large k_r. For spectral transfer, a narrow crescent-like region of negative values (in white) near the k_r axis persists but is now confined to yet smaller values of k_1.

4.6 Summary

In this chapter, results from direct numerical simulations of decaying magnetohydrodynamic (MHD) turbulence are presented for a study the response of isotropic turbulence to a strong external magnetic field, in the limit of low magnetic Reynolds number (R_m). This type of flow, to which a

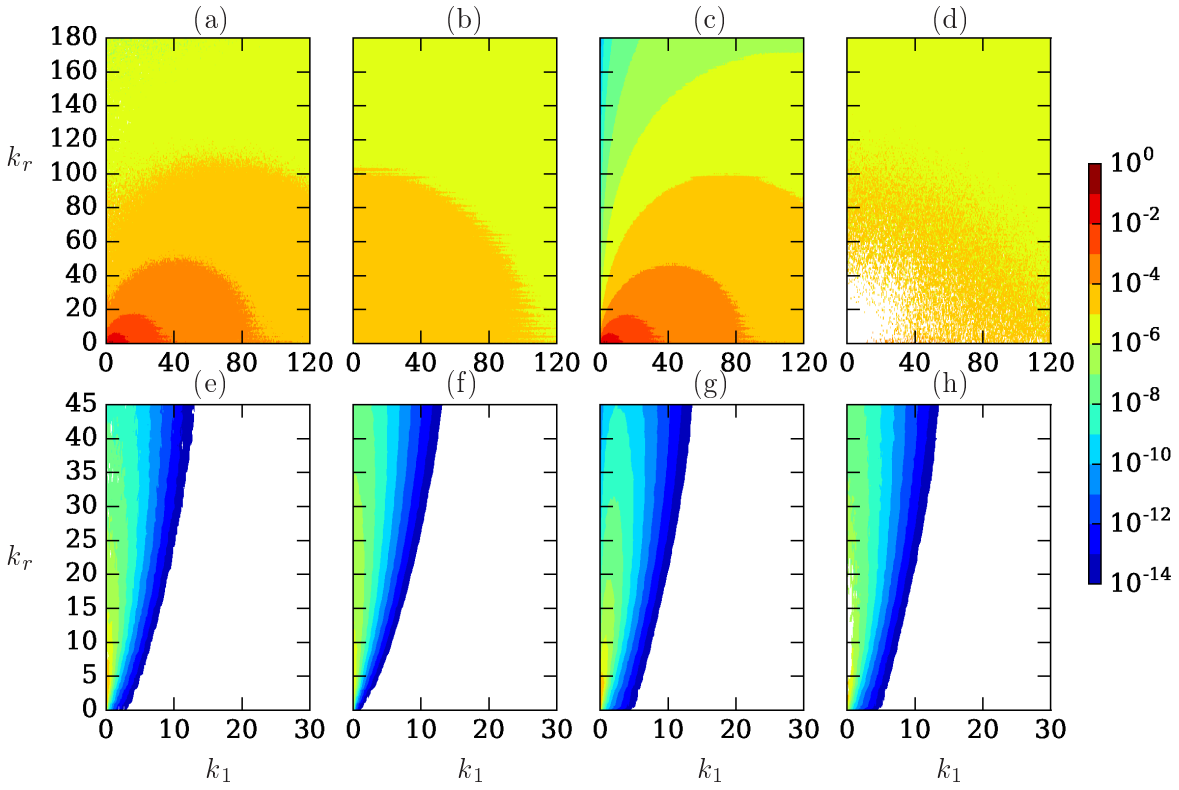

Figure 4.18: Axisymmetric spectra of the terms in the energy budget equation at $N = 8$. From left to right: (negative of) rate of change, viscous dissipation, Joule dissipation, and positive values of spectral transfer. Top row for results at $t^* = 0$, bottom row for $t^* = 26.25$.

quasi-static approximation applies, is relevant to many terrestrial applications including small-scale flow in planetary cores and industrial applications involving liquid metals. Although this subject has been studied by other authors before, preferential growth of large-eddy length scales in the direction of the magnetic field implies that accurate results cannot be readily obtained, especially at later times, unless the solution domain is very long in this direction. As a result, elongated solution domains of aspect ratio 8 are used for most purposes, and in some cases up to 64. The largest number of grid points was 16384×2048^2, which is much higher than in most previous works for this flow. The strength of the magnetic field is quantified by the magnetic interaction parameter (N) which is the ratio of pre-MHD eddy-turnover time to the Joule time of the magnetic field. A pre-simulation is conducted in a manner that minimizes any effects of numerical distortion. To facilitate a natural response to the magnetic field, no forcing is applied.

In low-R_m MHD turbulence the velocity field is modified by the magnetic field via the Lorentz force, which introduces anisotropy at all scales through the Joule dissipation. With the magnetic field in the x_1 direction, a reversal of Reynolds stress anisotropy is observed in which as $\langle u_1^2 \rangle > \langle u_2^2 \rangle$ at early times but $\langle u_1^2 \rangle < \langle u_2^2 \rangle$ later. Analysis of the Reynolds stress budget shows initially the larger Joule dissipation for u_2 leads to $\langle u_1^2 \rangle > \langle u_2^2 \rangle$, whereas relaxation terms are responsible for the reversal. The small scales also become anisotropic although velocity gradient statistics follow constraints based on a state of local axisymmetry. In the direction of the magnetic field velocity gradients become much weaker while the vorticity component is dominant. The property of local axisymmetry leads to some interesting relations between different components of the dissipation and vorticity-variance tensors. Both large and small scales display trends towards quasi two-dimensionality, including great contrast between integral length scales in different directions, a ratio close to 3 between the mean squares of longitudinal and transverse velocity gradients in the plane, and a reduced intermittency typical of 2D turbulence.

A detailed study of the anisotropy in spectral space is also performed, as a function of wavenumbers parallel and perpendicular (k_1 and k_r respectively) to the magnetic field, through the use of 1D and axisymmetric spectra. As expected, the most interesting contribution in the spectral dynamics comes from the Joule dissipation, which is counteracted by viscous dissipation, nonlinear transfer, and pressure-strain effects. As the turbulence evolves 1D spectra in k_1 become increasingly concentrated in regions of low k_1, especially for the spectra of u_2 at later times. Radial spectra for u_2

in k_r show signs of a backward transfer in regions of small k_r. Axisymmetric spectra as a function of k_1 and k_r simultaneously show that turbulence kinetic energy is increasingly concentrated in a narrow crescent-like region with very small k_1 but $k_r \gg k_1$. The crescent-like shape results from the anisotropic axisymmetric spectra of Joule dissipation which tends to selectively remove energy from modes in spectral regions where $k_1 > k_r$.

While most of the effort in this study has been focused on simulations with $N = 1$, results at larger N are included, which leads to a stronger Joule dissipation and faster growth of length scales in the direction of the magnetic field. Simulations conducted with the same initial turbulence state but N varied over two orders of magnitude indicate that the development of Reynolds stress anisotropy scales with Joule time for about 1 τ_J, and peak anisotropy approaches values predicted at infinitely large N (before a reversal occurs). Other effects of large N include accelerated development of local axisymmetry for statistics of the velocity gradients, and increased dominance of Joule dissipation in the spectral dynamics.

In summary, although previous works on the subject of this chapter have been useful, numerical constraints arising from the physics of the effects of a magnetic field must be given careful consideration. In general, the present results on elongated domains confirm those seen in prior work on cubic domains of finite size up to a certain time span, but also provide new information at later times where results on cubic domains could be overwhelmed by numerical confinement effects. For example, from Fig. 4.3 one may infer that although results from simulations on cubic domains and on elongated domains may be largely in agreement as far as early or even intermediate times are concerned, the benefits of elonagated domains are very substantial if long-time behaviors are to be established with confidence. Figure 4.7 also shows quite clearly that the development of vortical structures under the magnetic field cannot be represented sufficiently unless the domain is long enough, the contrasts being increasingly dramatic at later times. Several of the key results in this chapter, including relations between contributions to dissipation and enstrophy from derivatives in different directions (Eq. 4.15), and the behavior of axisymmetric spectra at low wavenumbers (Fig. 4.14) of various terms in the spectrum tensor equation can be captured accurately only on elongated domains at long simulation times.

In this work, while the bulk of the computing power have been devoted to the use of elongated dimains, the Reynolds numbers for the (unforced) isotropic turbulence states to which the magnetic

field is applied have been modest. An important future goal is thus to simulate MHD effects acting on initially isotropic turbulence with an inertial range, which will require yet-larger simulations of greater computational cost. To this end, a larger simulation has been performed on a 32768×4096^2 grid with $N = 8$, and more detailed data analysis awaits. The understanding of MHD turbulence obtained in the work presented in this chapter lays the foundation for the next two chapters, on scalar mixing in MHD turbulence and the relaxation of strained MHD turbulence respectively.

CHAPTER 5
RELAXATION OF STRAINED MHD TURBULENCE

5.1 Introduction

In Chap. 4 the anisotropy development of initially isotropic turbulence subject to a magnetic field was studied. However since many flows in nature and engineering possess some degree of anisotropy, it would be interesting to see whether and how some anisotropy present in the initial state of turbulence affects the anisotropy development upon imposing a magnetic field. Such a scenario arises for example when one considers the conducting fluids that pass through an axisymmetrically contracting tunnel and then enter a straight section subjected to a uniform magnetic field. The contraction phase leads to anisotropy at all scales, but in the straight section the anisotropic turbulence has a tendency to partially return to an isotropic state, as reported in prior experimental and numerical work (Ayyalasomayajula and Warhaft, 2006; Clay and Yeung, 2016) in the absence of the magnetic field. Specifically these past studies showed that while the small scales largely return to isotropy, a degree of residual anisotropy persists in the large scales. However, for a conducting fluid, the presence of the magnetic field in the straight section may modify the relaxation process significantly. Since both the magnetic field and the axisymmetric contraction impose a preferred direction, the anisotropy development is expected to depend on whether the magnetic field is parallel or perpendicular to the direction of extensive strain. This chapter summarizes some key findings on the relaxation of strained MHD turbulence in numerical simulations.

5.2 Simulation set up and parameters

To obtain a realistic initial turbulent state, a pre-simulation is first performed in a manner similar to that discussed in Chap. 4.3. A time-dependent axisymmetric strain is then applied in the x_1 direction such that the fluid undergoes contractions as if it were directed into a wind tunnel with a $4:1$ area ratio, without a magnetic field. The numerical procedures of the axisymmetric contraction were documented in Clay and Yeung (2016) and Clay (2017) and are thus not repeated here. Once a $4:1$ area ratio is achieved, the mean strain due to the axisymmetric contraction is removed and the

Table 5.1: Parameters for simulations where the magnetic field is parallel to the direction of extensive strain (x_1). Pre-contraction denoted by subscript or superscript a while post-contraction denoted by subscript or superscript b. R_λ^0 is the Taylor-scale Reynolds number at the start of the pre-simulation. In the first block, the number of grid points and grid metric factors are N_α and β_α^b. In the second block, $L_\alpha = 2\pi/\beta_\alpha$ is the domain size. l_{11} and l_{22} are the longitudinal integral length scales in the x_1 and x_2 directions, while l_{21} is the transverse integral length scales in the x_1 direction. Grid spacing is $\Delta_\alpha = 2\pi/N_\alpha$ and η is the Kolmogorov length scales. The third block lists the post to pre-contraction ratios of turbulence kinetic energy K, viscous dissipation rate ϵ and mean-square of velocity $\langle u_\alpha^2 \rangle$. The fourth block shows ratios of variances of velocity gradient $u_{i,j} = \partial u_i/\partial x_j$ and the skewness (S) and flatness (F) of the longitudinal velocity gradients.

Run	5	5r	5rd1	5rd2	6	6d1	6d2	9	9d
R_λ^0	39.7	39.7	39.7	39.7	67.7	67.7	67.7	113	113
N_1	1024	2048	4096	8192	1024	4096	8192	4096	8192
$N_2 = N_3$	1024	1024	1024	1024	1024	2048	2048	4096	4096
β_1^b	1/8	1/8	1/16	1/32	1/4	1/16	1/32	1/8	1/16
$\beta_2^b = \beta_3^b$	$\frac{1}{2\sqrt{2}}$	$\frac{1}{2\sqrt{2}}$	$\frac{1}{2\sqrt{2}}$	$\frac{1}{2\sqrt{2}}$	$\frac{1}{\sqrt{2}}$	$\frac{1}{2\sqrt{2}}$	$\frac{1}{2\sqrt{2}}$	$\frac{1}{2\sqrt{2}}$	$\frac{1}{2\sqrt{2}}$
$(L_1/l_{11})_b$	121	115	236.9	477.1	75.3	307.5	591.4	168	333.4
$(L_1/l_{21})_b$	37.7	38.0	78.5	153.8	20.5	82.4	168.2	44.3	88.4
$(L_2/l_{22})_b$	46.6	48.4	46.0	47.1	26.3	50.4	51.5	54.3	55.8
$(\Delta_1/\eta)_b$	4.34	2.17	2.17	2.17	4.31	4.30	4.30	4.30	4.28
$(\Delta_2/\eta)_b$	1.53	1.53	1.53	1.53	1.52	1.52	1.52	1.52	1.52
K_b/K_a	1.57	1.56	1.57	1.56	1.57	1.57	1.57	1.59	1.58
$\langle\epsilon\rangle_b/\langle\epsilon\rangle_a$	2.13	2.13	2.13	2.13	1.85	1.84	1.83	1.54	1.52
$\langle u_1^2\rangle_b/\langle u_1^2\rangle_a$	0.202	0.200	0.207	0.201	0.222	0.223	0.221	0.244	0.245
$\langle u_2^2\rangle_b/\langle u_2^2\rangle_a$	2.25	2.25	2.25	2.25	2.24	2.24	2.24	2.26	2.25
$\langle u_{2,1}^2\rangle_b/\langle u_{1,1}^2\rangle_b$	4.27	4.28	4.27	4.27	3.05	3.05	3.05	2.27	2.27
$\langle u_{3,2}^2\rangle_b/\langle u_{2,2}^2\rangle_b$	2.98	2.98	2.98	2.98	2.96	2.96	2.96	2.90	2.90
$S(u_{1,1}^b)$	0.0175	0.0135	0.0137	0.0112	0.345	0.335	0.318	0.399	0.397
$S(u_{3,3}^b)$	-0.0613	-0.0607	-0.0603	-0.0577	-0.102	-0.097	-0.094	-0.178	-0.173
$F(u_{1,1}^b)$	6.53	6.64	6.64	6.71	9.72	9.64	9.59	11.2	11.2
$F(u_{3,3}^b)$	3.43	3.44	3.44	3.44	3.57	3.58	3.59	3.82	3.82

turbulence can be thought as entering a straight section. Note that no solid boundary is considered in this work, and the regions of interest are near the centerline of the contraction wind tunnel and the straight section, where actual effects of the wall are weak. At the same instant when the mean strain is removed, a magnetic field is applied either in the same x_1 direction (i.e. parallel to the extensive strain direction) or in the x_3 direction (i.e. perpendicular to the extensive strain direction, or parallel to one of the compressive strain directions).

In simulations of anisotropic turbulence, it is important to ensure that small scale resolution is adequate, while the domain size is sufficiently large to avoid finite domain size effects that arise from the use of periodic boundary conditions. It is useful to perform some type of convergence tests as in Chap. 4.3: if the evolution of statistics do not change much upon improving the resolution

Table 5.2: Parameters for simulations where the magnetic field is parallel to the direction of compressive strain (x_3). Pre-contraction denoted by subscript or superscript a while post-contraction denoted by subscript or superscript b. R_λ^0 is the Taylor-scale Reynolds number at the start of the pre-simulation. In the first block, the number of grid points and grid metric factors are N_α and β_α^b. In the second block, $L_\alpha = 2\pi/\beta_\alpha$ is the domain size. l_{11} and l_{22} are the longitudinal integral length scales in the x_1 and x_2 directions, while l_{21} is the transverse integral length scales in the x_1 direction. Grid spacing is $\Delta_\alpha = 2\pi/N_\alpha$ and η is the Kolmogorov length scales. The third block lists the post to pre-contraction ratios of turbulence kinetic energy K, viscous dissipation rate ϵ and mean-square of velocity $\langle u_\alpha^2 \rangle$. The fourth block shows ratios of variances of velocity gradient $u_{i,j} = \partial u_i/\partial x_j$ and the skewness (S) and flatness (F) of the longitudinal velocity gradients.

Run	1	1d1	1d2	1d3	1rd3	2	3
R_λ^0	39.7	39.7	39.7	39.7	39.7	67.7	113
$N_1 = N_2$	512	512	512	512	512	1024	2048
N_3	512	1024	2048	4096	4096	8192	16384
β_1^b	$1/4$	$1/4$	$1/4$	$1/4$	$1/2$	$1/2$	$1/2$
β_2^b	$1/\sqrt{2}$	$1/\sqrt{2}$	$1/\sqrt{2}$	$1/\sqrt{2}$	$1/\sqrt{2}$	$1/\sqrt{2}$	$1/\sqrt{2}$
β_3^b	$\frac{1}{\sqrt{2}}$	$\frac{1}{2\sqrt{2}}$	$\frac{1}{4\sqrt{2}}$	$\frac{1}{8\sqrt{2}}$	$\frac{1}{8\sqrt{2}}$	$\frac{1}{8\sqrt{2}}$	$\frac{1}{8\sqrt{2}}$
$(L_1/l_{11})_b$	66.3	59.0	59.9	59.9	29.7	35.9	41.5
$(L_1/l_{21})_b$	19.7	19.5	19.5	19.1	9.5	10.7	10.9
$(L_2/l_{22})_b$	23.7	22.0	24.4	22.8	22.7	27.3	25.5
$(L_3/l_{22})_b$	23.7	44.1	97.5	182.4	181.2	218.3	203.7
$(\Delta_1/\eta)_b$	4.33	4.34	4.34	4.34	2.17	2.15	2.15
$(\Delta_2/\eta)_b$	1.53	1.53	1.53	1.53	1.53	1.52	1.52
$(\Delta_3/\eta)_b$	1.53	1.53	1.53	1.53	1.53	1.52	1.52
K_b/K_a	1.59	1.57	1.56	1.56	1.57	1.56	1.59
$\langle\epsilon\rangle_b/\langle\epsilon\rangle_a$	2.12	2.12	2.13	2.12	2.12	1.86	1.54
$\langle u_1^2\rangle_b/\langle u_1^2\rangle_a$	0.207	0.200	0.200	0.202	0.197	0.216	0.241
$\langle u_2^2\rangle_b/\langle u_2^2\rangle_a$	2.26	2.25	2.25	2.25	2.26	2.25	2.28
$\langle u_{2,1}^2\rangle_b/\langle u_{1,1}^2\rangle_b$	4.26	4.27	4.27	4.27	4.28	3.06	2.28
$\langle u_{3,2}^2\rangle_b/\langle u_{2,2}^2\rangle_b$	2.97	2.98	2.97	2.98	2.98	2.95	2.90
$S(u_{1,1}^b)$	0.0226	0.0075	0.0175	0.0177	0.0512	0.4422	0.4930
$S(u_{3,3}^b)$	-0.0686	-0.0610	-0.0547	-0.0060	-0.0618	-0.1014	-0.1789
$F(u_{1,1}^b)$	6.52	6.47	6.56	6.58	6.81	10.87	12.72
$F(u_{3,3}^b)$	3.45	3.44	3.43	3.43	3.43	3.59	3.84

or elongating the domain size, the grids are deemed adequate. Generally the convergence tests are performed on smaller grids, which then provide guidance for simulations at larger problem sizes, usually at higher Reynolds numbers. Table 5.1 and Table 5.2 show the post-contraction statistics obtained on grids with different resolutions, domain sizes and the Reynolds numbers, for the magnetic field parallel and perpendicular to the extensive strain direction respectively. In Table 5.1, runs 5,6 and 9 are taken from Clay and Yeung (2016) (maintaining the same identifier for individual runs) and are used as baselines at three different Reynolds numbers. Other runs have improved small scale resolution ('r' in the run name) and/or elongated domain size ('d' in the run name) to examine their effects on strained MHD turbulence separately or jointly. It can be seen that improved resolution and/or domain size have only a weak effect on lower order quantities during the axisymmetric contraction, such as post to pre-contraction ratios of turbulence kinetic energy K, mean dissipation rate $\langle\epsilon\rangle$, Reynolds stress components and mean squares of velocity gradients, while higher order quantities such as skewness and flatness factors are more sensitive. The dependence of post-contraction statistics on resolution and Reynolds number follow similar trends as those in Clay and Yeung (2016). Furthermore, good agreement in post-contraction statistics between simulations performed on non-cubic grids and those on cubic grids suggests that axisymmetric contraction is properly simulated on the non-cubic grids. Here since the integral length scales are known to grow preferentially upon imposing the magnetic field (in the x_1 direction), the emphasis is on an elongated domain in the same direction.

The same naming convention is used in Table 5.2, which shows post-contraction statistics in the case when the magnetic field is applied in the x_3 direction, which is one of the directions of compressive strain. Since the axisymmetric contraction phase is free of MHD effects, the post-contraction statistics at the same Reynolds number are similar to those in Table 5.1. To allow room for the integral length scales to grow naturally in the magnetic field direction, the domain is elongated along the x_3 direction. Note that the x_1 direction is also slightly elongated, because integral length scales grow preferentially along the direction of extensive strain (x_1 direction) as axisymmetric contraction occurs. Since decaying turbulence is considered for both cases of the magnetic field being parallel or perpendicular to the extensive strain direction, resolution continues to improve with time, while the domain size may be of greater concern than resolution. As a result, the larger runs at higher Reynolds numbers use domains strongly elongated in the direction of the

magnetic field.

5.3 Anisotropy development

In the subsections to follow, results of strained MHD turbulence with the magnetic field parallel and perpendicular to the direction of extensive strain are presented respectively. For the parallel case, run 1 (Table 5.1) is first used with three magnetic interaction parameters $N = 0$, 1 and 4 to show the basic phenomenology of strained MHD turbulence with or without a magnetic field. Using the most elongated grids, results from runs '5rd2', '6d2' and '9d' (Table 5.1) are then presented to demonstrate the Reynolds number effects. For the case when the magnetic field is perpendicular to the extensive strain direction, results from runs '1rd3', '2' and '3' (Table 5.2) are used with a focus on the Reynolds number dependence of anisotropy development. Measures of anisotropy addressed in the discussions include anisotropy tensor of the Reynolds stress, which is dominated by the large scales, as well as the vorticity covariance tensor and the velocity gradient statistics representing the small scales. For all normalizations, the subscript b denotes the same time instant when the axisymmetric contraction is completed (i.e. post-contraction) and the magnetic field (either parallel or perpendicular to the direction of extensive strain) is applied.

5.3.1 Results of strained MHD turbulence when the magnetic field is parallel to the direction of extensive strain

To give an overview of the relaxation of strained turbulence with or without a magnetic field parallel to the extensive strain direction, Fig. 5.1 and 5.2 show, at three magnetic interaction parameters $N = 0$, 1, 4 (see the definition of the N at Chap. 4.3), the evolution of the transverse integral length scales, turbulence kinetic energy K, viscous dissipation $\langle\epsilon\rangle$ and Joule dissipation $\langle J\rangle$. A clear effect of the magnetic field is a strong increase in the integral length scales along the magnetic field direction (x_1 direction) as shown in Fig. 5.1. This observation is similar to those in simulations of MHD turbulence from an isotropic state, and is the main reason for the use of elongated domains. Free of numerical forcing, the turbulence decays in the relaxation of strained turbulence. Fig. 5.2 (a) shows that K decays slightly faster at early times when a magnetic field is imposed. However at later times, the decay rates are similar for all values of N. Since the time rate of change of

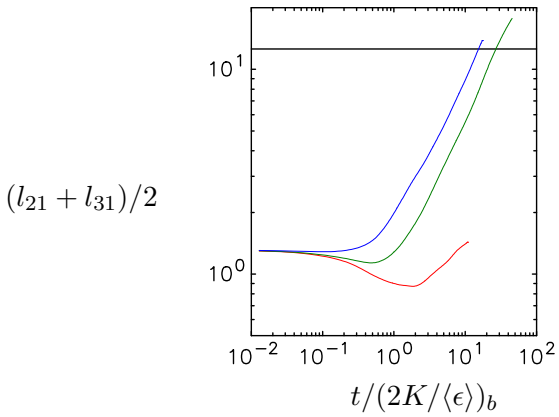

Figure 5.1: Evolution of the averaged transverse integral length scales l_{21} and l_{31} in the x_1 direction. Magnetic interaction parameter $N = 0$ (red), 1 (green) and 4 (blue). The horizontal solid line denotes $1/4$ of the domain size in the x_1 direction at 4π. Results are taken from run 5 in Table 5.1 of 1024^3 grids on a $16\pi \times (4\sqrt{2}\pi)^2$ domain.

turbulence kinetic energy K is given by

$$d\,K/d\,t = -\langle\epsilon\rangle - \langle J\rangle\ , \tag{5.1}$$

a larger decay rate of K suggests that the combined dissipations are larger. Figure 5.2 (b) shows that viscous dissipations are initially close for different N, but simulations with a larger N give lower values of $\langle\epsilon\rangle$ at later times. In comparison, Joule dissipation at early times is larger in simulation with a larger N, but its dependence on N becomes weaker at later times. The slightly larger decay rate of K at early times is due to the stronger Joule dissipation. At late times since Joule dissipation dominates viscous dissipation and values of $\langle J\rangle$ become close for different N, the decay rates for $N = 1$ and 4 are similar.

While Fig. 5.1 and 5.2 are useful in characterizing the evolution of strained MHD turbulence, the evolution of anisotropy is equally of great interest. Figure 5.3 shows the evolution of elements of the Reynolds stress anisotropy tensor $b_{ij} = \langle u_i u_j\rangle/(2K) - \delta_{ij}/3$ and the second and third invariants of the b_{ij} tensor, given by

$$\eta = (b_{ij}b_{ji}/6)^{1/2}\ ;\ \xi = (b_{ij}b_{jk}b_{ki}/6)^{1/3}\ , \tag{5.2}$$

where η here is not to be confused with the Kolmogorov length scale. Without a magnetic field (i.e. $N = 0$), the magnitudes of b_{11} and b_{22} decrease monotonically, where a value of zero denotes a per-

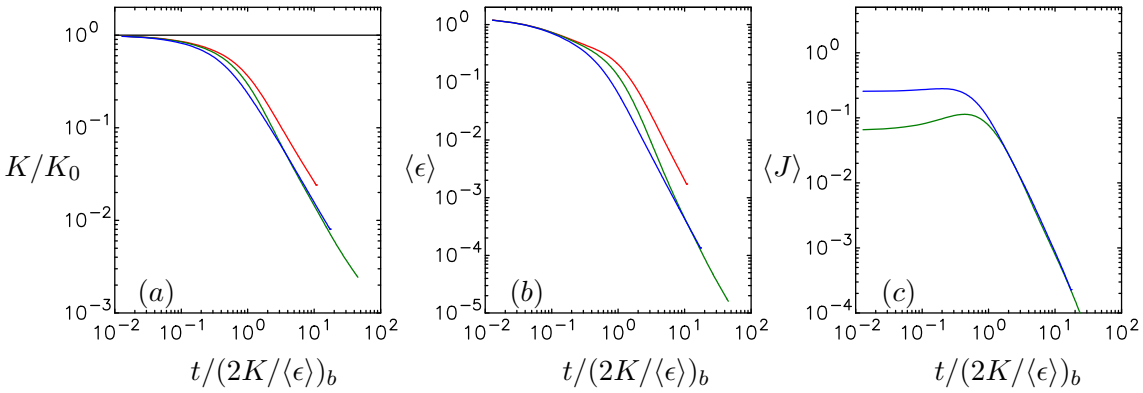

Figure 5.2: Evolution of (a) turbulence kinetic energy K normalized by the post-contraction value (denoted by K_b), (b) viscous dissipation rate $\langle\epsilon\rangle$ and (c) Joule dissipation rate $\langle J\rangle$. Magnetic interaction parameter $N = 0$ (red), 1 (green) and 4 (blue). Results are taken from run 5 in Table 5.1 of 1024^3 grids on a $16\pi \times (4\sqrt{2}\pi)^2$ domain.

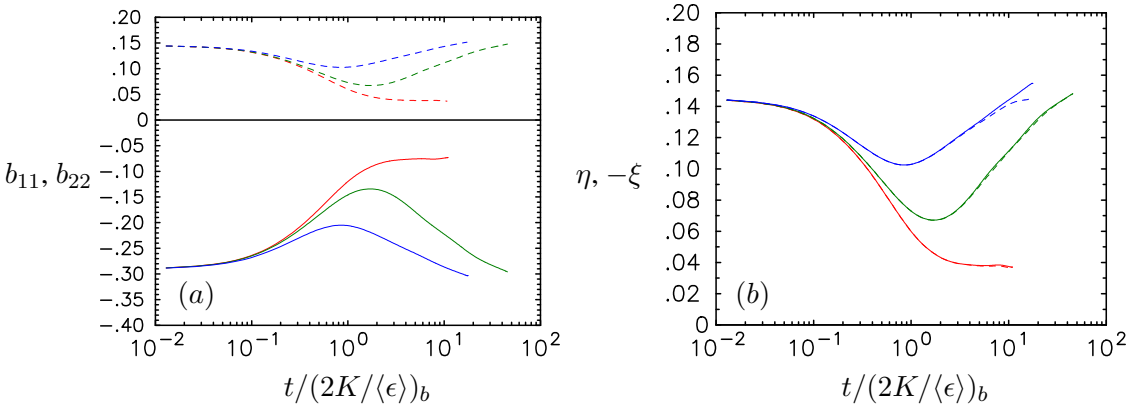

Figure 5.3: Evolution of (a) components of the Reynolds stress anisotropy tensor, and (b) second and third invariants of the Reynolds stress anisotropy tensor. Magnetic interaction parameter $N = 0$ (red), 1 (green) and 4 (blue). In (a) solid and dashed curves denote b_{11} and b_{22} and in (b) solid and dashed curves denote η and $-\xi$. Results are taken from run 5 in Table 5.1 of 1024^3 grids on a $16\pi \times (4\sqrt{2}\pi)^2$ domain.

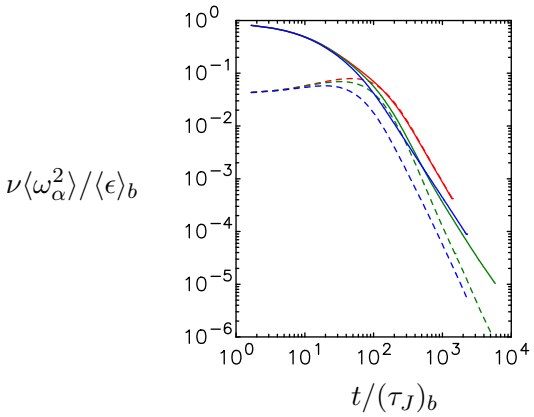

Figure 5.4: Evolution of components of the vorticity covariance tensor parallel (solid) and perpendicular (dashed) to the magnetic field direction. Magnetic interaction parameter $N = 0$ (red), 1 (green) and 4 (blue). Results are taken from run 5 in Table 5.1 of 1024^3 grids on a $16\pi \times (4\sqrt{2}\pi)^2$ domain.

fect isotropic state. However a persistent departure from zero suggests that the Reynolds stress still possesses some residual anisotropy that arises during the axisymmetric contraction. In comparison when a magnetic field is applied, b_{11} and b_{22} evolve non-monotonically as the degree of anisotropy initially weakens but becomes stronger at later times. This non-monotonic behavior results from the opposing effects of a return-to-isotropy trend by turbulence versus the highly anisotropic Joule dissipation. At late times the behaviors of b_{11} and b_{22} are similar to those in Fig. 4.2 (c), which suggests that Joule dissipation leads both isotropic and strained turbulence to a similar state, which was described as quasi-two-dimensional in Chap. 4. Since both the axisymmetric contraction and the magnetic field are applied in the same direction, the flow retains the same state of axisymmetry. In particular Fig. 5.3 (b) shows that the axisymmetric relation of $\eta = -\xi$ holds well, and from (a) it is clear that the axisymmetric state is characterized by two dominant Reynolds stress components perpendicular to the magnetic field.

To assess the anisotropy development in the small scales, Fig. 5.4 and 5.5 show the evolution of vorticity components and the ratios of velocity gradient variances. Since the small scale motions are also affected by the Lorentz force, the time is normalized by the Joule time $\tau_J \equiv \rho/(\sigma B_0^2)$ (see Chap. 4.5). In Fig. 5.4 at $t \approx 0$, vorticity component in extensive direction is larger than that in the compressive direction. However after about $100(\tau_J)_b$, the two components become almost equal in the absence of the magnetic field, which suggests that the small scales eventually return to isotropy completely. When a magnetic field is applied, the two vorticity components

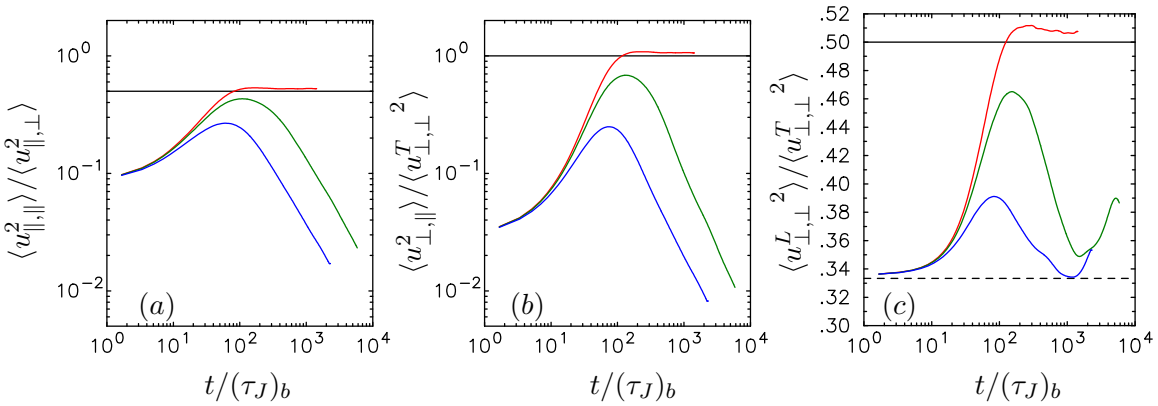

Figure 5.5: Evolution of ratios of velocity gradient variances of (a) $\langle u^2_{1,1}\rangle/\langle u^2_{1,3}\rangle$, (b) $\langle u^2_{2,1}\rangle/\langle u^2_{2,3}\rangle$, and (c) $\langle u^2_{2,2}\rangle/\langle u^2_{2,3}\rangle$. Magnetic interaction parameter $N = 0$ (red), 1 (green) and 4 (blue). The solid horizontal lines denote values expected at an isotropic state. The dashed horizontal line in (c) marks $1/3$. Results are taken from run 5 in Table 5.1 of 1024^3 grids on a $16\pi \times (4\sqrt{2}\pi)^2$ domain.

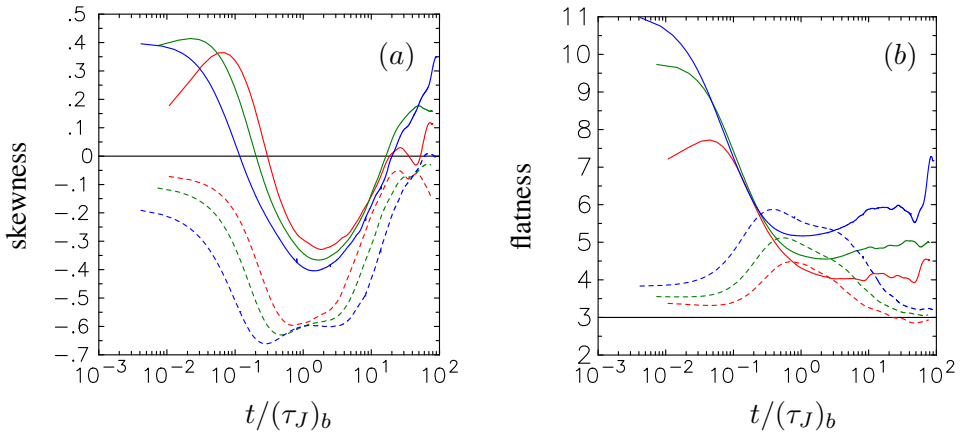

Figure 5.6: Evolution of the (a) skewness and (b) flatness of longitudinal velocity gradients. Solid curves for $\partial u_1/\partial x_1$ and dashed curves for $\partial u_3/\partial x_3$. Magnetic interaction parameter $N = 1$, and the Reynolds numbers ${R_\lambda}^0$ are at 39.7 (red), 67.7 (green) and 113 (blue). Results are taken from runs 5rd2, 6 and 9 in Table 5.1.

become closer at intermediate times, but at later times xxx the parallel component is much larger than the perpendicular ones at later times. Similarly Fig. 5.5 shows that while for $N = 0$ the ratios of velocity gradient variances approach values typical in isotropic turbulence, the magnetic field inhibits a return to isotropy in the small scales. Specifically, at later times velocity gradients along the magnetic field direction are strongly damped, and the small scales are axisymmetric, as $\langle u^2_{2,3}\rangle/\langle u^2_{2,2}\rangle = 1/3$ roughly holds as seen in Fig. 5.5 (c). The late-time behaviors in the small scales are very similar to the highly anisotropic state in MHD turbulence from isotropic initial conditions.

The results presented so far provide a basic characterization of the anisotropy development in strained MHD turbulence with an initial Reynolds number of 39.7. To examine the Reynolds num-

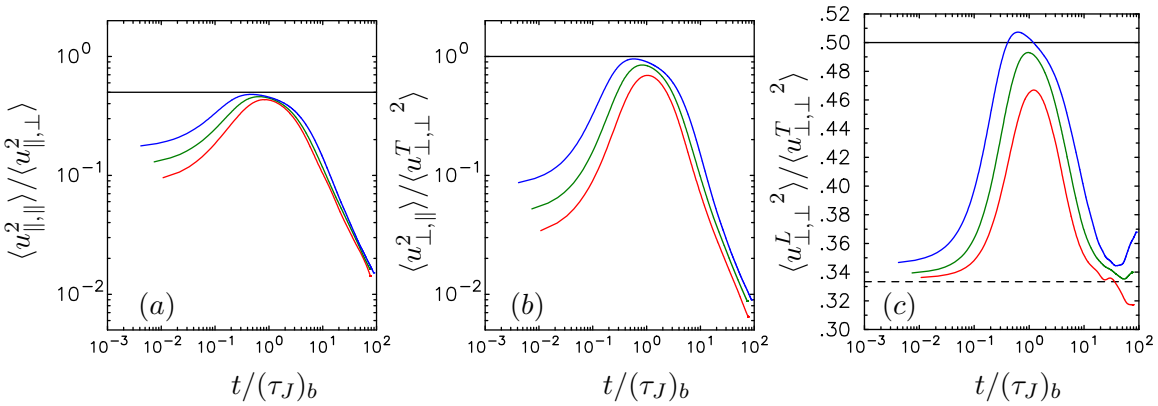

Figure 5.7: Evolution of ratios of velocity gradient variances of (a) $\langle u^2_{\parallel,\parallel}\rangle/\langle u^2_{\parallel,\perp}\rangle$, (b) $\langle u^2_{\perp,\parallel}\rangle/\langle {u^T_{\perp,\perp}}^2\rangle$, and (c) $\langle {u^L_{\perp,\perp}}^2\rangle/\langle {u^T_{\perp,\perp}}^2\rangle$. The solid horizontal lines denote values expected at an isotropic state. The dashed horizontal line in (c) marks $1/3$. Magnetic interaction parameter $N = 1$, and the Reynolds numbers ${R_\lambda}^0$ are at 39.7 (red), 67.7 (green) and 113 (blue). Results are taken from runs 5rd2, 6 and 9 in Table 5.1.

ber dependence of the statistics, two larger simulations of higher Reynolds numbers (67.7 and 113) have also been performed. Since the effects of increasing the Reynolds number are most evident in the small scales, the focus is on the velocity gradient statistics. Figure 5.6 shows the skewness and flatness factors of the longitudinal velocity gradients at different initial Reynolds numbers with the same $N = 1$. The skewness factors of the longitudinal velocity gradients both parallel and perpendicular to the magnetic field decrease at early times, but become close to zero or slightly positive at later times. The flatness factors of the velocity gradient parallel to the magnetic field decrease strongly but remain non-Gaussian, whereas the perpendicular component has a flatness factor close to a Gaussian value of 3 at the end the simulation, despite an obvious departure from Gaussianity at intermediate times. Again the late-time behaviors of these higher order statistics are similar to those reported in Table 4.4. The effect of increasing the Reynolds number is mainly for the flatness factors to attain larger values, which is consistent with the notion that the turbulence is more intermittent as the Reynolds number increases. For the ratios of the velocity gradient variances, Fig. 5.7 shows that the temporary return to isotropy at intermediate times is stronger as the Reynolds number increases.

In general, as a wider range of scales accompanies an increase of the Reynolds number, axisymmetric spectra can provide clearer contrasts between anisotropy in the large and small scales. Fig. 5.8 shows the axisymmetric energy spectra at selected time instants, from run '9d' in Table 5.1 with an initial Reynolds number of 113. At $t = 0$ the contours of the axisymmetric spectra show

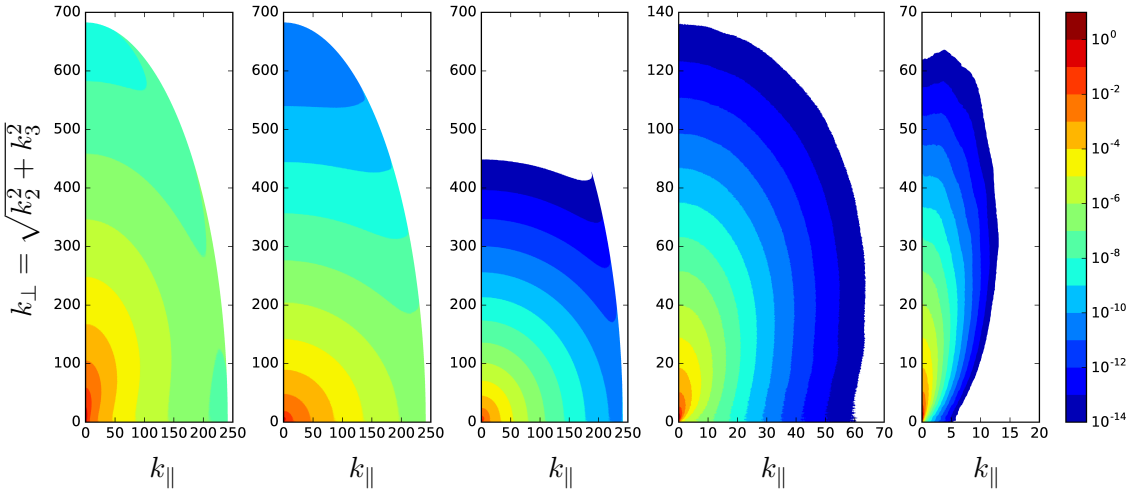

Figure 5.8: Evolution of axisymmetric energy spectra at $t/(2K/\langle\epsilon\rangle)_0 = 0$, 0.5, 2, 10, and 40 (from left to right). Results are taken rom run 9 in Table 5.1.

non-concentric circles, thus indicating anisotropy at all scales. This result is very similar to those in the post-contraction state reported in Clay and Yeung (2016). At early times, the small scales (those with a larger wavenumber magnitude $|k| = \sqrt{k_\parallel^2 + k_\perp^2}$) quickly develop circular contours while the large scales still show non-circular ones. This observation is consistent with a return to isotropy that only occurs at the small scales. At later times, the contours at all scales progressively resemble the crescent-like shape seen at late times in MHD turbulence with isotropic conditions (see Fig. 4.12), suggesting a high degree of anisotropy at all scales.

5.3.2 Results of strained MHD turbulence when the magnetic field is perpendicular to the direction of extensive strain

Since the previous subsection has showed results of the relaxation of strained MHD turbulence in the absence of a magnetic field ($N = 0$), the focus of the current subsection is on the effects of the Reynolds number while the magnetic interaction parameter is fixed at $N = 1$. Figure 5.9 shows the evolution of integral length scales at three Reynolds numbers of 39.7, 67.7 and 113. Both the longitudinal (a) and transverse (b) integral length scales along the magnetic field (x_3) direction grow strongly, while the longitudinal integral length scales perpendicular to the magnetic field (but parallel to the extensive strain direction) grow more slowly after a slight decrease at early times. Since the integral length scales along the magnetic field direction first reach $1/4$ of the domain size, the most critical direction is x_3, while the domain sizes in other directions can be considered

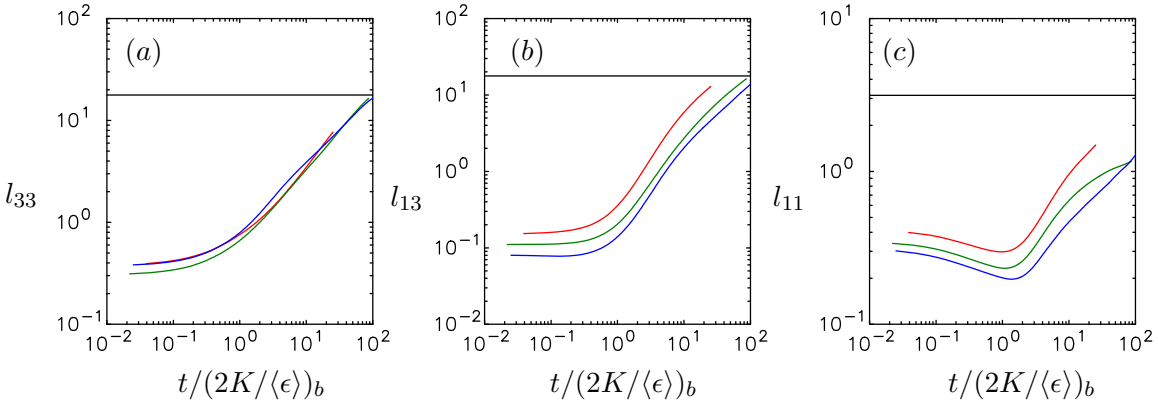

Figure 5.9: Evolution of integral length scales (a) l_{33}, (b) l_{13} and (c) l_{11}, where $L_{\alpha\alpha,\beta}$ denotes the α-th velocity component separated in the β direction. The initial Reynolds numbers ${R_\lambda}^0$ are at 39.7 (red), 67.7 (green) and 113 (blue), while magnetic interaction parameters are all at $N = 1$. The solid horizontal lines denote $1/4$ of the domain size in the corresponding direction. Results are taken from runs 1rd3, 2 and 3 in Table 5.2.

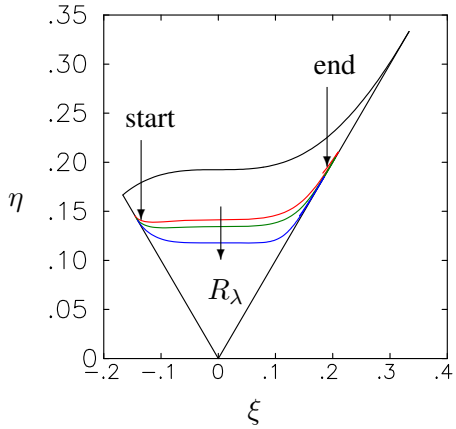

Figure 5.10: Anisotropy invariant map. The initial Reynolds numbers ${R_\lambda}^0$ are at 39.7 (red), 67.7 (green) and 113 (blue), while magnetic interaction parameters are all at $N = 1$. The black solid curves mark the boundary of the Lumley triangle (see discussions in the text). The middle arrows marked by R_λ points in the direction of increasing Reynolds number. The arrows on the side mark the start and end of the curves. Results are taken from runs 1rd3, 2 and 3 in Table 5.2.

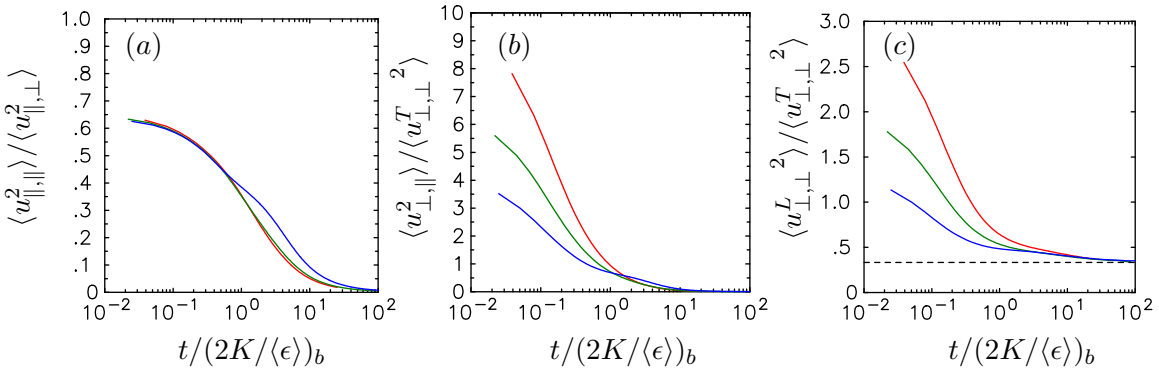

Figure 5.11: Evolution of ratios of velocity gradient variances (a) $\langle u^2_{\parallel,\parallel}\rangle/\langle u^2_{\parallel,\perp}\rangle$, (b) $\langle u^2_{\perp,\parallel}\rangle/\langle {u^T_{\perp,\perp}}^2\rangle$, and (c) $\langle {u^L_{\perp,\perp}}^2\rangle/\langle {u^T_{\perp,\perp}}^2\rangle$, where L and T denotes longitudinal and transverse respectively. The initial Reynolds numbers ${R_\lambda}^0$ are at 39.7 (red), 67.7 (green) and 113 (blue), while magnetic interaction parameters are all at $N = 1$. The dashed horizontal line in (c) marks $1/3$. Results are taken from runs 1rd3, 2 and 3 in Table 5.2.

adequate.

An important consequence in strained MHD turbulence with the magnetic field perpendicular to the extensive strain direction is that the axis of axisymmetry changes from the x_1 to x_3. Therefore the axisymmetric relation $\eta = -\xi$ for the Reynolds stress may no longer hold. Different states of turbulence can be shown in the anisotropy invariant map (AIM) with the so-called Lumley triangle (Lumley and Newman, 1977), within which all possible values of η and ξ reside. Figure 5.10 shows the anisotropy development in the Reynolds stress. The trajectory of (η, ξ) coordinates on the AIM starts from the left side of the Lumley triangle that expresses axisymmetric relations $\eta = -\xi$ with two similarly large Reynolds stress components, and ends on the right side of the Lumley triangle that expresses yet another axisymmetric relation $\eta = \xi$ but with a single larger Reynolds stress component. A closer look (not shown here) shows that the $\langle u_3^2\rangle$ component dominates which is along the magnetic field direction. At higher Reynolds number, the trajectory at intermediate times in Fig. 5.10 is closer to the origin, which represents an isotropic state. This observation is consistent with a stronger effect of return-to-isotropy by turbulence as the Reynolds number increases.

To see the anisotropy development in the small scales, Fig. 5.11 shows the evolution of the ratios of velocity gradient variances. While the Reynolds number has an effect on some of the ratios at the post-contraction state, the late-time behaviors are similar regardless of the Reynolds number. In particular, Fig. 5.11 (a) and (b) show that velocity gradients along the magnetic field direction decrease strongly, while (c) shows that the small scales assume local axisymmetry as the

ratio $\langle {u^L_{\perp,\perp}}^2 \rangle / \langle {u^T_{\perp,\perp}}^2 \rangle$ approaches $1/3$.

5.4 Summary

Building on previous studies of the relaxation of anisotropic turbulence subjected to axisymmetric contraction (Clay and Yeung, 2016), this chapter presents further results of how the relaxation process is modified with the presence of the magnetic field, either parallel or perpendicular to the direction of extensive strain. Since anisotropy of various degrees persists throughout the simulation for both cases, careful tests were performed to ensure that the domain size is sufficiently long to allow the turbulence structures to grow naturally, and the small scale resolution is adequate to faithfully simulate the fine scale motions.

When the magnetic field is parallel to the direction of extensive strain, the axis of axisymmetry remains the same and both the large and the small scales assume a state of axisymmetry. Nevertheless, there is a trend of return to isotropy at intermediate times for all scales. Since the small scales evolve fast in small time scales, their statistics can reach isotropic values, for example in the ratios of velocity gradient variances and in the circular contours at the high wavenumbers in the axisymmetric energy spectra, especially at higher Reynolds numbers. The late-time behaviors of both the large and small scales resemble those in MHD turbulence from isotropic initial conditions, which suggests that the initial anisotropy resulting from axisymmetric contraction is not strong enough to affect the dynamics at later times.

In comparison, when the magnetic field is along one of the compressive strain directions, The state of axisymmetry transitions from the case where two Reynolds stress components perpendicular to the magnetic field dominate, to the case where the only dominant Reynolds stress component is the one parallel to the magnetic field direction. Such a transition can be clearly seen in the anisotropy invariant map, and at higher Reynolds numbers the intermediate state becomes slightly closer to isotropic. One more distinctive feature is that with the change of axisymmetry, there is no return to isotropy at intermediate times, unlike the case when magnetic field and the axisymmetric contraction are applied in the same direction. Nevertheless some observations at late times are common to all MHD turbulence regardless of the initial conditions and whether the magnetic field is parallel or perpendicular to the extensive strain direction. Specifically, along the magnetic field direction the

integral length scales always grow strongly, and velocity gradients decrease substantially. Moreover the small scales always assume a local state of axisymmetry about the direction of the magnetic field.

The results presented in this chapter are useful in improving the understanding of MHD turbulence in general. The initial anisotropic condition that is obtained after axisymmetric contraction can be more relevant to actual flows since most of them possess some degree of anisotropy.

CHAPTER 6

PASSIVE SCALAR MIXING IN MHD TURBULENCE

6.1 Introduction

As discussed in Chap. 1, efficient mixing of scalars is a key property of turbulence, and has important consequences in nature and engineering. Often the scalars involved are of too low concentration to have a back reaction on the velocity field, and therefore are known as dynamically passive. Typical examples include a small temperature difference in the flow, and moisture content in the air. In general, mixing occurs in the small scales at the molecular level as turbulence breaks large-scale non-uniformities into increasingly smaller fragments. The relative strength of the viscous and molecular diffusion, characterized by the corresponding diffusivities ν and D, defines the Schmidt number $Sc \equiv \nu/D$. Moreover, the regime of the Schmidt number determines the smallest scales present in turbulence, as discussed in Chap. 2.3. In isotropic turbulence a wide range of Schmidt numbers has been studied extensively (Warhaft, 2000; Gotoh and Yeung, 2013). Yet scalar mixing in MHD turbulence, which occurs at low Sc due to high molecular diffusivity of liquid metals, has received little attention (Kassinos, Knaepen, and Carati, 2007; Kinet et al., 2008). In the case of MHD turbulence forced in the large scales, Kinet et al. (2008) considered two scalars with $Sc = 0.1$ and 1 without a mean scalar gradient. It was found that scalar variance decays slower in the presence of the magnetic field, and the scalar gradients parallel to the magnetic field become smaller than those in the perpendicular direction. Moreover, a departure from local isotropy was found in the scalar field. While the finding is useful in the understanding of scalar mixing in MHD turbulence, several improvements to methodologies employed in previous work can be made. First, an isotropic scalar field was initialized after the forced MHD turbulence reached a stationary state in the study of Kinet et al. (2008). Even though this set-up is a convenient extension to the study of scalar mixing after studies of the anisotropy development in the forced velocity field subjected to a magnetic field, often the scalars evolve simultaneously with the velocity field, and as a result it is arguably more physical to initialize the scalar field at the instant when a magnetic field is imposed. Second since the effects of the magnetic field do not appear explicitly in the governing equations of the scalars (Eq. 2.19) but

are felt through the velocities, the use of numerical forcing in the velocity field interferes with the Lorentz force that acts on all scales, and may thus affect scalar mixing unnaturally. Third, a mean scalar gradient coupled with velocity fluctuations acting upon the gradient produces scalar variance, and it is interesting to study how the scalar fluctuations in MHD turbulence develop in the presence of a source. Given all the considerations above, this chapter presents some preliminary results of passive scalar mixing in MHD turbulence with and without a mean scalar gradient.

6.2 Simulation set up and parameters

To study the simultaneous evolution of the velocity and scalar field subject to a magnetic field, the same procedures as described in Chap. 4.3 are used to prepare the initial conditions that represent physical turbulence states. In fact many of the key configurations already used for the velocity field can be used again for scalars. The initial condition for the scalars depend on whether a mean scalar gradient is present or not. Without a mean scalar gradient, the scalar field is initialized according to the "double delta" probability distribution (Eswaran and Pope, 1988b), which mimics a mixture with initially segregated species as commonly found in non-premixed combustion. The same initial condition for the scalars was successfully applied in studies of rotating turbulence (Yeung and Xu, 2004), and the effects of mixing can be seen in the relaxation of the PDF shape closer to a Gaussian distribution. In the case when a mean scalar gradient is supplied, scalar mixing is expected to depend on the relative orientation of the gradient and the magnetic field. In industrial applications, the magnetic field can be either parallel or perpendicular to the mean scalar gradient (Davidson, 2013), but a transverse magnetic field may require the domain size to be elongated in both the magnetic field and mean scalar gradient directions, and are thus computationally more expensive. In this work, for simplicity, only the case of a magnetic field parallel to the mean scalar gradient is considered. The general evolution equation of scalar variance $\langle \phi^2 \rangle$ in homogeneous turbulence is governed by

$$\frac{\langle \phi^2 \rangle}{d\,t} = -2\langle u_i \phi \rangle \frac{\partial \Phi}{\partial x_i} - 2D\langle \frac{\partial \phi}{\partial x_i} \frac{\partial \phi}{\partial x_i} \rangle \,. \tag{6.1}$$

As noted previously, the coupling of the scalar flux $\langle u_i \phi \rangle$ with the mean scalar gradient $\partial \Phi / \partial x_i$ in Eq. 6.1 produces scalar variance, while scalar dissipation $\langle \chi \rangle \equiv 2D\langle \frac{\partial \phi}{\partial x_i} \frac{\partial \phi}{\partial x_i} \rangle$ reduces scalar variance. To clearly see the effects of a mean scalar gradient, the scalar field is initialized as zero

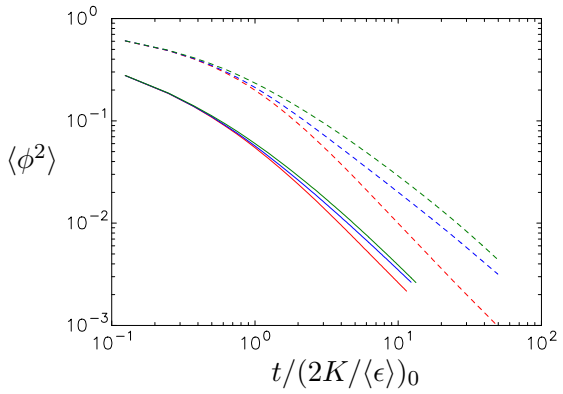

Figure 6.1: Evolution of scalar variance in the absence of a mean scalar gradient. Solid curves denote scalars with $Sc = 0.1$, and dashed curves denote scalars with $Sc = 1$. Magnetic interaction parameters are $N = 0$ (red), 1 (blue) and 4 (green). Results are taken from a 2048×256^2 grid on a $16\pi \times (2\pi)^2$ domain.

when the magnetic field is applied. For both initial conditions, the effects of the magnetic field on passive scalar mixing can be seen when comparing the evolution of scalar integral length scales, and statistics of scalar variance and gradients.

The introduction of the Schmidt number Sc adds to existing non-dimensional parameters of the Reynolds number and magnetic interaction parameter N. As a preliminary study with a focus on key effects of the magnetic field on scalar mixing, only the results with an initial Reynolds number of 21 are presented. The magnetic interaction parameters are mainly 0 or 1, although a larger value of 4 was used in some cases. The Schmidt numbers were $1/16$, 1 and 0.1, 1 for the case with and without a mean scalar gradient respectively. While mercury has a smaller $Sc \approx 0.02$ (Clay, 1973), the lower Sc values used here are still instructive to study low-Sc scalar mixing, whereas the $Sc = 1$ case allows an examination of the Schmidt number dependence. Much smaller Schmidt number down to $1/2048$ were studied in forced isotropic turbulence with (Yeung and Sreenivasan, 2014) and without (Yeung and Sreenivasan, 2013) a mean scalar gradient, and special treatments were applied to take account of the rapidly-evolving scalar field. However the Schmidt numbers simulated in this study are much larger than those in the past (yet are still of low values), and tests confirmed that special treatments are not necessary.

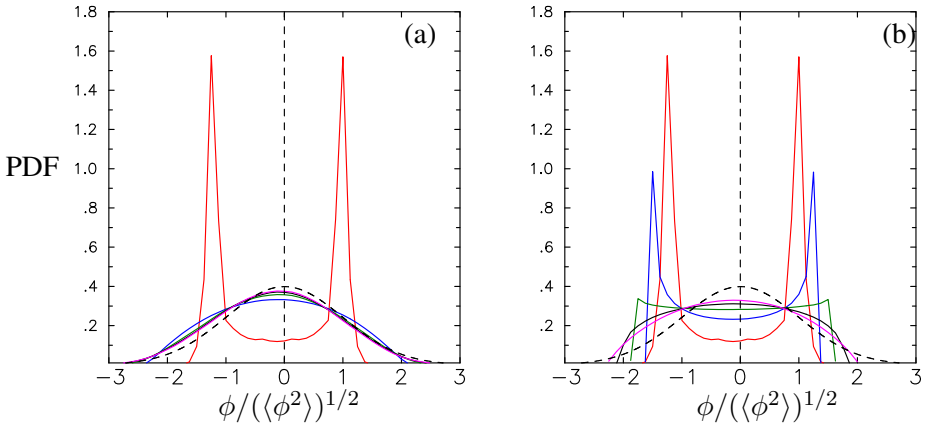

Figure 6.2: Relaxation of PDFs of $\phi/(\langle\phi^2\rangle)^{1/2}$ for (a) $Sc = 0.1$ (b) $Sc = 1$ from initial "double delta" shape to a distribution close to Gaussian (dashed curves). The same time instants are used at $t/\tau_\eta = 0$ (red),2 (blue),4 (green), 6 (black),8 (magenta). Results are taken from simulations at $N = 1$ on a 2048×256^2 grid.

6.3 Scalar mixing in MHD turbulence without a mean scalar gradient

In this configuration without a mean scalar gradient, the scalar field is initialized with a "double-delta" PDF, and the scalar variance is non-zero at $t = 0$. At later times scalar variance decreases monotonically as mixing occurs, but the rate of decay may depend on the Schmidt number Sc and whether a magnetic field is applied. Figure 6.1 (a) shows the evolution of scalar variances with $Sc = 0.1$ and 1 and for magnetic interaction parameters $N = 0$, 1 and 4. It is seen that scalar variances decay slower (scalar mixing is less effective) with a magnetic field for both Sc, and the effect is stronger at $Sc = 1$. Moreover, while the decay of scalar variances at later times seems to follow a power law regardless of N, at early times the scalar variances decrease strongly with $Sc = 0.1$. This observation suggests a rapid change in the PDFs of the scalar as shown in Fig. 6.2. It is seen the initial 'double delta" PDFs relax towards a distribution close to Gaussian for both Schmidt numbers, and the relaxation is much faster for $Sc = 0.1$, within a few Kolmogorov time scales. Since molecular diffusion is stronger at $Sc = 0.1$ than that at $Sc = 1$, the results suggest the effect of the magnetic field is weaker when molecular diffusion dominates.

To examine the departures from local isotropy in the scalar field, Fig. 6.3 shows the evolution of scalar gradient variances parallel ($\langle(\nabla_\parallel\phi)^2\rangle$) and perpendicular ($\langle(\nabla_\perp\phi)^2\rangle$) to the applied magnetic field with their ratios plotted in the inset. It is clear that the presence of the magnetic field introduces anisotropy in the small scales of the scalars, as the ratio of $\langle(\nabla_\parallel\phi)^2\rangle/\langle(\nabla_\perp\phi)^2\rangle$ deviate substantially

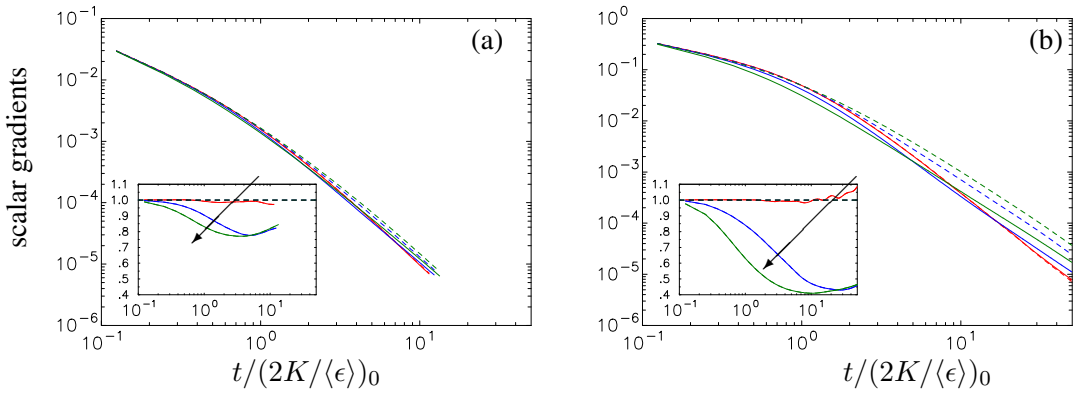

Figure 6.3: Evolution of scalar gradient variances with (a) $Sc = 0.1$ (b) $Sc = 1$. Solid curves denote $\langle(\nabla_\parallel\phi)^2\rangle$ and dashed curves denote $\langle(\nabla_\perp\phi)^2\rangle$. Inset shows ratios of $\langle(\nabla_\parallel\phi)^2\rangle/\langle(\nabla_\perp\phi)^2\rangle$. Arrow points along increasing magnetic interaction parameters of $N = 0$ (red), 1 (blue) and 4 (green). Results are taken from simulations at $N = 1$ on a 2048×256^2 grid.

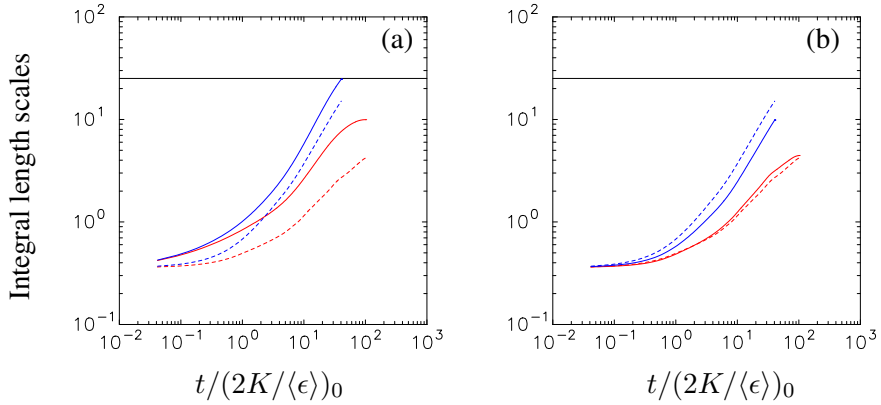

Figure 6.4: Evolution of integral length scales in the x_1 direction for (a) $Sc = 1/16$ (b) $Sc = 1$. Solid and dashed curves denote integral length scales of scalar and velocity respectively. Magnetic interaction parameter $N = 0$ (red) and $N = 1$ (blue). The horizontal solid line denotes $1/4$ of the domain size at 4π. Results are taken from 4096×512^2 grids on a $32\pi \times (4\pi)^2$ domain.

from the isotropic value of unity. Unlike the ratios between velocity gradients (e.g. Fig. 4.5), $\langle(\nabla_\parallel\phi)^2\rangle/\langle(\nabla_\perp\phi)^2\rangle$ does not decrease indefinitely but attains similar values for $N \neq 0$.

6.4 Scalar mixing in MHD turbulence with a uniform mean scalar gradient parallel to the magnetic field

The main focus of this chapter is on scalar mixing in MHD turbulence with a longitudinal mean scalar gradient, a topic with little previously published results. To allow integral length scales in both the velocity and the scalar to grow naturally, the simulation domain is elongated in all directions, of size $32\pi \times (4\pi)^2$. Figure. 6.4 and 6.5 show the evolution of the scalar and velocity integral length

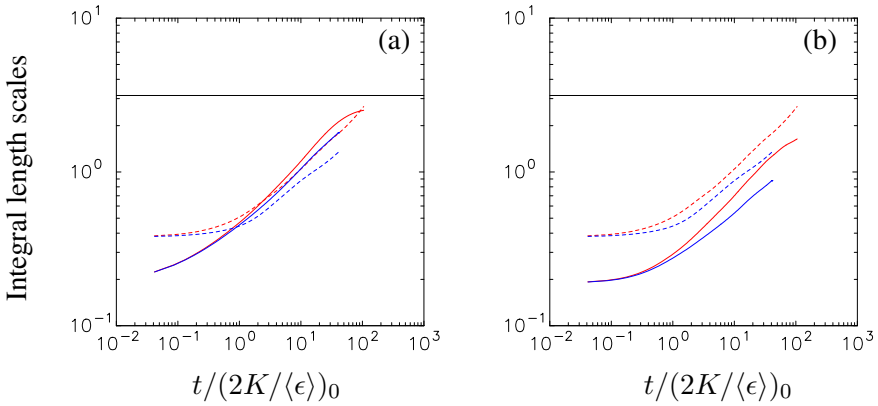

Figure 6.5: Evolution of averaged integral length scales in the x_2 and x_3 directions for (a) $Sc = 1/16$ (b) $Sc = 1$. Solid and dashed curves denote integral length scales of scalar and velocity respectively. Magnetic interaction parameter $N = 0$ (red) and $N = 1$ (blue). The horizontal solid line denotes $1/4$ of the domain size at $\pi/2$. Results are taken from 4096×512^2 grids on a $32\pi \times (4\pi)^2$ domain.

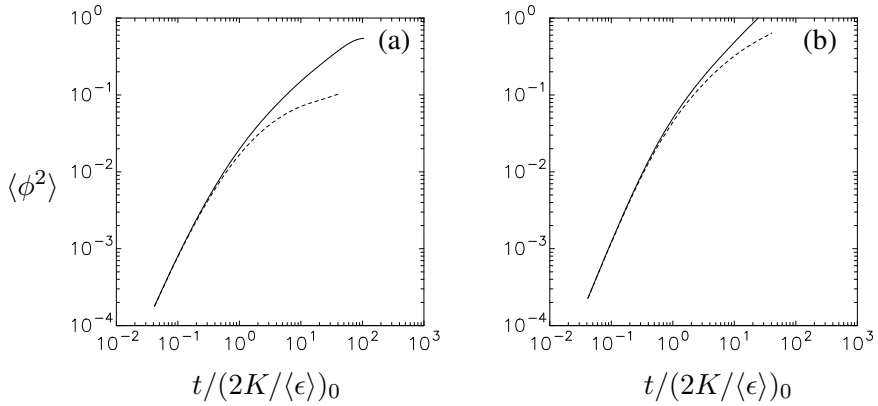

Figure 6.6: Evolution of scalar variances with (a) $Sc = 1/16$ (b) $Sc = 1$. Solid curves denote $N = 0$ and dashed curves denote $N = 1$. Results are taken from 4096×512^2 grids on a $32\pi \times (4\pi)^2$ domain.

scales in the parallel x_1 direction and the perpendicular directions respectively. The magnetic field is seen to make the integral length scales for both velocity and scalar grow faster in the magnetic field direction, but slightly slower in the perpendicular direction. However, the integral length scales depend on the Schmidt number. Specifically the integral length scales of the scalar with $Sc = 1/16$ tend to be larger than those of the velocity, which is consistent with previous findings in isotropic turbulence (Yeung and Sreenivasan, 2014). The rapid growth of the integral length scales confirm once again the importance of using elongated domains. As was the case in Chap. 4, simulations are terminated once any of the integral length scales exceed one quarter of the domain size, as shown in Fig. 6.4.

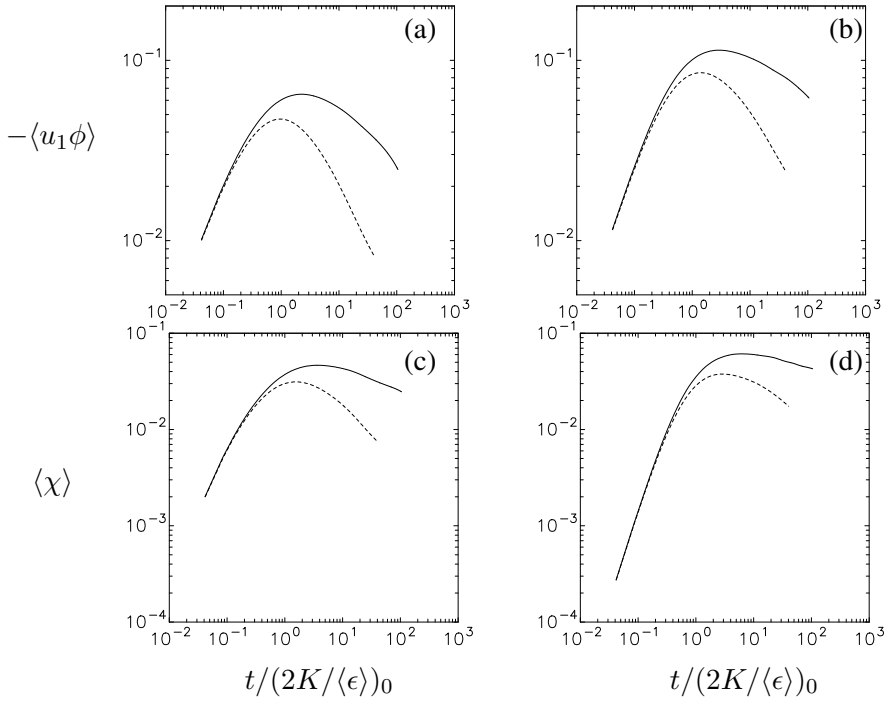

Figure 6.7: Evolution of (a, b) scalar production and (c, d) scalar dissipation. The Schmidt number $Sc = 1/16$ (a, c) and $Sc = 1$ (b, d). Solid curves denote $N = 0$ and dashed curves denote $N = 1$. Results are taken from 4096×512^2 grids on a $32\pi \times (4\pi)^2$ domain.

With the presence of a source, scalar variance grows from the initial value of zero, as shown in Fig. 6.6, but the growth rate decreases at later times, as suggested by the curves being convex. The magnetic field is seen to decrease the growth rate further, but the effects are only obvious after about one initial large-eddy turnover time, and are stronger for lower Schmidt number. To understand the evolution of scalar variance, Fig. 6.7 shows the evolution of the production and dissipation terms in Eq. 6.1, while their difference which gives the time rate of change of scalar variance, is shown in Fig. 6.8. It is interesting to note that both the production and dissipation terms have similar non-monotonic evolutions, and the magnetic field causes both terms to decrease at earlier times after reaching their respective maximal values. The convex appearance of the curves representing scalar variance evolution (Fig. 6.6) can also be explained by examining Fig. 6.8, which shows the time rate of change of scalar variance. While the time rate of change remains positive throughout the simulation, its value becomes close to zero at later times, especially at lower Schmidt number. Simulations on yet larger domains may be useful to see whether scalar variance would stay constant, or even decrease.

To examine the evolution of the small scales in the scalars, Fig. 6.9 shows the development of

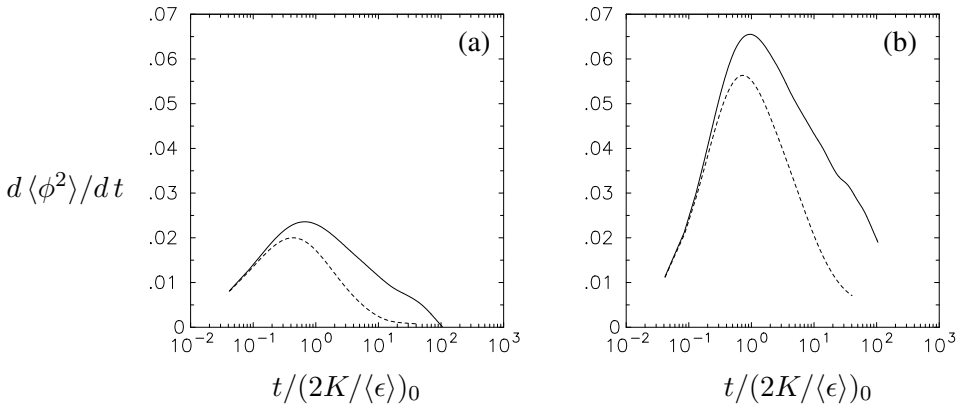

Figure 6.8: Evolution of the time rate of change of scalar variance for (a) $Sc = 1/16$ and (b) $Sc = 1$. Solid curves denote $N = 0$ and dashed curves denote $N = 1$. Results are taken from 4096×512^2 grids on a $32\pi \times (4\pi)^2$ domain.

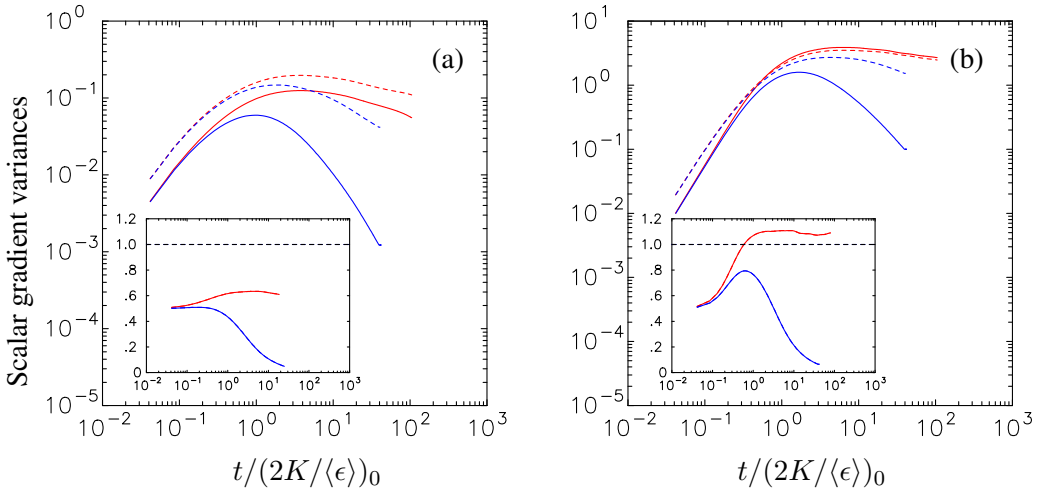

Figure 6.9: Evolution of the scalar gradient variances $\langle(\nabla_\parallel\phi)^2\rangle$ (solid) and $\langle(\nabla_\perp\phi)^2\rangle$ (dashed) where the insets show the ratio of $\langle(\nabla_\parallel\phi)^2\rangle/\langle(\nabla_\parallel\phi)^2\rangle$. Frame (a) $Sc = 1/16$ and (b) $Sc = 1$. Magnetic interaction parameter $N = 0$ (red) and $N = 1$ (blue). Results are taken from 4096×512^2 grids on a $32\pi \times (4\pi)^2$ domain.

the scalar gradient variances parallel $\langle(\nabla_\parallel\phi)^2\rangle$ and perpendicular $\langle(\nabla_\perp\phi)^2\rangle$ to the magnetic field, as well as their ratios in the insets. Unlike the case without a mean scalar gradient where the ratio of $\langle(\nabla_\parallel\phi)^2\rangle/\langle(\nabla_\parallel\phi)^2\rangle$ starts at unity, here the ratios at $t \approx 0$ are around 0.5. To understand the value of 0.5, note that the governing equation of the evolution of scalar θ (Eq. 2.19) can be simplified at the initial condition of zero scalar fluctuations. Specifically Eq. 2.19 becomes

$$\partial\phi/\partial t = -\mathbf{u}\cdot\nabla\Phi\ , \tag{6.2}$$

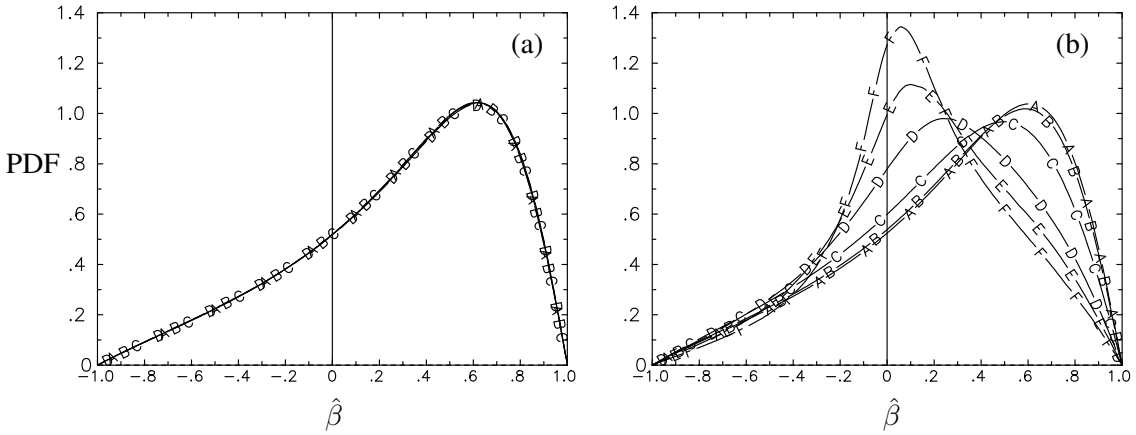

Figure 6.10: Evolution of the PDFs of the normalized intermediate strain rate $\hat{\beta}$ for (a) $N = 0$ and (b) $N = 1$. In (a), curves A-D denote $t/(2K/\langle\epsilon\rangle)_0 \approx 3.76$, 12.43, 25.54 and 45.25. In (b), curves A-F denote $t/(2K/\langle\epsilon\rangle)_0 \approx 0.52$, 1.30, 3.76, 12.43, 25.54 and 45.25. Results are taken from 4096×512^2 grids on a $32\pi \times (4\pi)^2$ domain.

which further reduces to

$$\partial\phi/\partial t = -u_1 \,, \tag{6.3}$$

in the case that the mean scalar gradient $\nabla\Phi = (1, 0, 0)$, i.e. along the x_1 direction. As a result, the following relations hold

$$\frac{\partial\phi}{\partial x_1} \approx -\frac{\partial u_1}{\partial x_1} t \tag{6.4}$$

$$\frac{\partial\phi}{\partial x_2} \approx -\frac{\partial u_1}{\partial x_2} t \,, \tag{6.5}$$

and hence

$$\frac{\langle(\nabla_\parallel\phi)^2\rangle}{\langle(\nabla_\perp\phi)^2\rangle} \approx \frac{\langle(\partial u_1/x_1)^2\rangle}{\langle(\partial u_1/x_2)^2\rangle} \approx \frac{1}{2} \,, \tag{6.6}$$

where the last equal sign results from relations in the velocity field of isotropic turbulence. At later times without the magnetic field, while the parallel component of the scalar gradient remains smaller than the perpendicular one at $Sc = 1/16$, the ratio exceeds unity at the larger $Sc = 1$, which shows a clear Schmidt number dependence. The presence of a magnetic field has a strong effect to the small scales of the scalars, leading to decreased scalar gradients along the magnetic field direction, similar to the velocity gradient, for both Schmidt numbers studied.

In the study of scalar mixing under a uniform mean scalar gradient, it is useful to examine the alignment between the fluctuating scalar gradient with the principal strain rate directions. Let α, β,

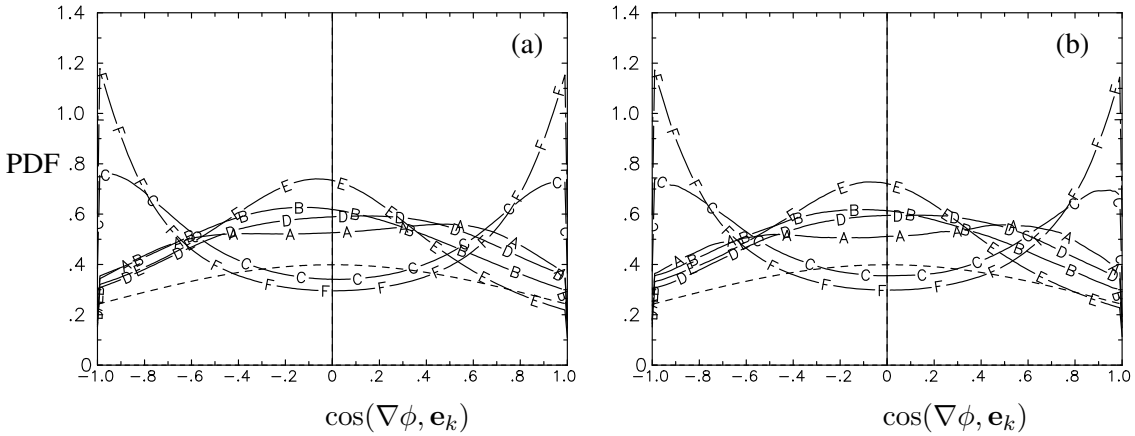

Figure 6.11: Evolution of the PDFs of directional cosines $\cos(\nabla\phi, \mathbf{e}_k)$ for $k = \alpha$, β and γ for $N = 0$, at $t/(2K/\langle\epsilon\rangle)_0$ of (a) 3.76 and (b) 45.25. Curves A-C represent eigenvectors $\mathbf{e}_\alpha$, $\mathbf{e}_\beta$, $\mathbf{e}_\gamma$ for $Sc = 1/16$, while curves D-F give corresponding data for $Sc = 1$. Results are taken from 4096×512^2 grids on a $32\pi \times (4\pi)^2$ domain.

and γ to denote the principal strain rates of the rate of strain tensor $s_{ij} \equiv (\partial u_i/\partial x_j + \partial u_j/\partial x_i)/2$ where $\alpha > \beta > \gamma$. Incompressibility gives $\alpha + \beta + \gamma = 0$, and it can be shown that the normalized principal strain rate $\hat{\beta} \equiv \sqrt{6}\beta/\sqrt{\alpha^2 + \beta^2 + \gamma^2}$ is bounded between -1 amd 1, which corresponds to the case of $\beta = \gamma$ and $\beta = \alpha$ respectively. Figure 6.10 shows the PDFs of $\hat{\beta}$ at different time instants with or without the magnetic field. In the absence of the magnetic field (frame (a)), the shape of the PDF does not change despite a decrease of Reynolds number in the decaying turbulence simulations. This independence of Reynolds number is a known feature of the intermediate principal strain rate (Vedula, Yeung, and Fox, 2001) in isotropic turbulence. Moreover the intermediate principal strain rate is more likely to be positive (extensive), which is consistent with previous work (Ashurst et al., 1987). However when a magnetic field is applied, Fig. 6.10 (b) shows that the shape of PDF changes significantly and at later times the PDF becomes more symmetric, with the peak probability occurring at $\beta = 0$. Such a scenario suggests that the magnetic field modifies the small scale structure strongly, as the most extensive principal strain α is now balanced by the most compressive strain γ.

In the analysis involving principal strains, the principal strain eigenvectors $\mathbf{e}_k$ where $k = \alpha$, β and γ can define a coordinate frame. To study the degree of geometric alignment between the fluctuating scalar gradient vector $\nabla\phi$ and the eigenvectors, Fig. 6.11 and 6.12 show the PDFs of their directional cosines $\cos(\nabla\phi, \mathbf{e}_k)$ at $N = 0$ and 1. Without the magnetic field, the PDFs are roughly symmetric, and the fluctuating scalar gradients are more likely to be aligned with the

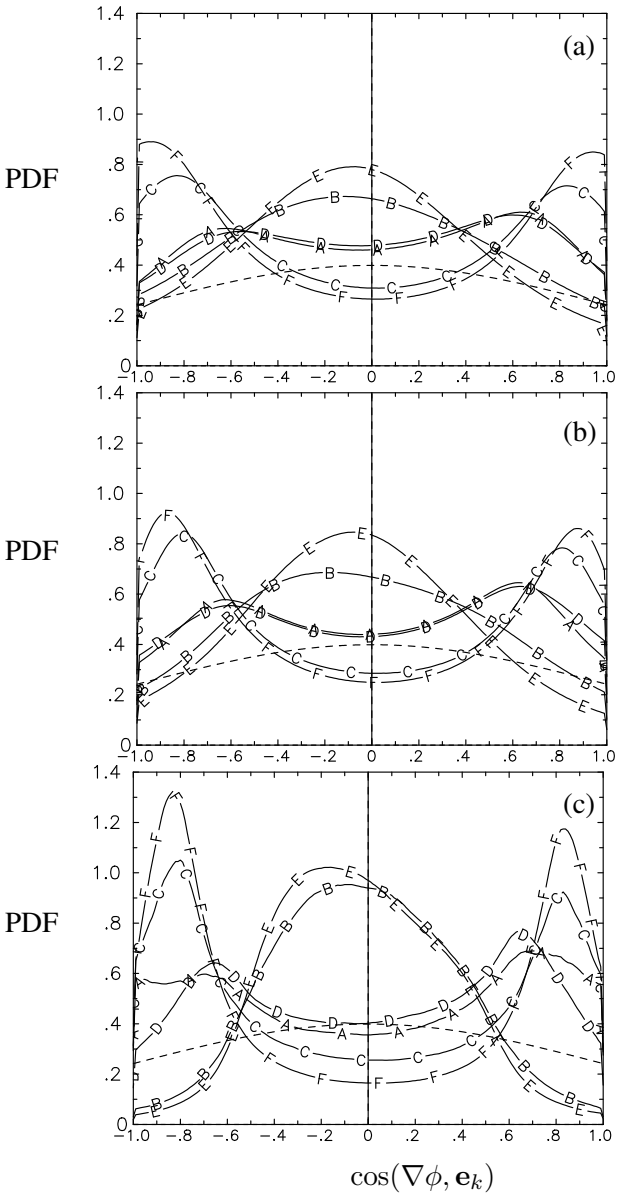

Figure 6.12: Evolution of the PDFs of directional cosines $\cos(\nabla\phi, \mathbf{e}_k)$ for $k = \alpha$, β and γ for $N = 1$, at $t/(2K/\langle\epsilon\rangle)_0$ of (a) 0.52, (b) 3.76 and (c) 45.25. Curves A-C represent eigenvectors $\mathbf{e}_\alpha$, $\mathbf{e}_\beta$, $\mathbf{e}_\gamma$ for $Sc = 1/16$, while curves D-F give corresponding data for $Sc = 1$. Results are taken from 4096×512^2 grids on a $32\pi \times (4\pi)^2$ domain.

eigenvector $\mathbf{e}_\gamma$ that corresponds to the most compressive principal strain rate, especially for the larger $Sc = 1$. Also the PDFs of $\cos(\nabla\phi, \mathbf{e}_k)$ show independence of the Reynolds number as those of $\hat{\beta}$. When the magnetic field is applied, the PDFs of $\cos(\nabla\phi, \mathbf{e}_k)$ change in a way such that a small angle is likely to exist between the fluctuating scalar gradients and the eigenvector $\mathbf{e}_\gamma$. The slight degree of asymmetry in the shape of the PDFs may be a result of inadequate statistical sampling, which can be improved when ensemble-averaging is applied over simulations that started with different random number seeds.

6.5 Summary

This chapter presents some preliminary results of passive scalar mixing in MHD turbulence, with a focus on the case when a uniform mean scalar gradient is applied parallel to the magnetic field direction. It is seen that magnetic field affects scalar mixing in general. In the absence of a mean scalar gradient, the scalar field is initialized by a "double-delta" PDF shape, which relaxes quickly to a Gaussian distribution, especially at a lower Schmidt number when molecular diffusivity is stronger. The magnetic field is seen to slow down scalar mixing, and the effect is stronger for a larger Schmidt number where the dynamics is not dominated by molecular diffusion. While the small scales of the scalars remain locally isotropic if the magnetic field is not applied, for $N \neq 0$ the scalar gradients parallel to the magnetic field direction become smaller than the perpendicular ones. When a mean scalar gradient is maintained parallel to the magnetic field, scalar variance develops from a zero initial condition, but a magnetic field slows down the growth of scalar variance. As for the small scales, the evolution of the scalar gradient variances depends on the Schmidt number at $N = 0$, but the parallel component always becomes much smaller than the perpendicular ones upon applying a magnetic field regardless of the Schmidt numbers. A closer look at the alignment of the fluctuating scalar gradients $\nabla\phi$ and the eigenvectors representing the principal strain rates shows that the magnetic field changes the preferred alignments. The PDFs of the normalized intermediate strain rate $\hat{\beta}$ are also affected by a magnetic field, as $\hat{\beta}$ is more likely to take a value of zero. It is expected the results presented here could motivate further research, including simulations at higher Reynolds numbers and the case when a mean scalar gradient is applied perpendicular to the magnetic field direction.

CHAPTER 7
CONCLUSIONS AND FURTHER WORK

This thesis presents a numerical study of turbulence structure with and without the effects of a magnetic field using large scale direct numerical simulations. For the small scales in isotropic turbulence, the results provide important clarifications both on the topological features of the extreme events of large fluctuating amplitude, and on the accurate characterization of the sign oscillation properties. Specifically, resolution effects in space and time are found to affect geometries of the extreme events strongly. Also it is suggested that measures in higher dimensions should be used to quantify the sign oscillations. In MHD turbulence, the development of anisotropy in the velocity and scalar fields is studied using simulations on elongated domains, which are found to be critical for reliable results. Since different configurations are considered (such as the different types of initial conditions and the presence of a mean scalar gradient) and many parameters are varied (such as the Reynolds number as well as the strengths of the magnetic field and the scalar molecular diffusivity), results reported in the thesis serve as a documentation of various aspects of MHD turbulence for the research community. In the following, summaries of the main conclusions in the thesis are given for each topic, followed by a brief discussion of future work.

7.1 Summary of the main conclusions

7.1.1 Resolution effects on the structures of extreme events

Visualizations are conducted using several single-time snapshots in simulations of different combinations of the Courant number C (at 0.15, 0.3 and 0.6), spatial resolution $k_{max}\eta$ (at 1.4, 2.7 and 5.4), and Reynolds numbers R_λ (390 and 650). Since the "chunky" structures (Yeung, Zhai, and Sreenivasan, 2015) associated with the extreme events vanish as the spatial and/or temporal resolutions are improved, their existence is considered spurious, and as a result is used as an indicator of whether the resolution is adequate. Present results indicate that $C = 0.15$ is generally adequate for all the spatial resolution and Reynolds numbers explored, while $C = 0.6$ is acceptable only when spatial resolution is much better (at $k_{max}\eta = 5.4$) than that often used, and also when the

Reynolds number is low. Since the 8192^3 simulation (Yeung, Zhai, and Sreenivasan, 2015) used $C = 0.6$ at $R_\lambda = 1300$ and $k_{max}\eta = 2$, the current results suggest the extreme events may not have been adequately resolved both spatially and temporally. The visualization results help clarify that topological features of the extreme events remain sheet-like for dissipation and filament-like for enstrophy, at least up to $R_\lambda = 650$. Furthermore, the results support the finding that resolution requirements become more demanding as Reynolds number is increased (Yakhot and Sreenivasan, 2005; Yeung, Sreenivasan, and Pope, 2018). Finer grids and smaller time steps must be employed when even larger simulations are attempted in the future.

7.1.2 Sign oscillation characteristics in the small-scales

Cancellation exponents, which quantify the sign oscillations, are computed using 1D, 2D and 3D measures for vorticity, longitudinal and transverse velocity gradients. Since 3D measures are hardly attainable in experiments, DNS results allow a direct assessment on whether measures in higher dimensions are needed to measure cancellation exponents for turbulence processes (Vainshtein et al., 1994). The results show that for vorticity and transverse velocity gradients, values of cancellation exponents measured in 2D and 3D are close to theoretical predictions, while 1D measure gives smaller cancellation exponent. In comparison, longitudinal velocity gradients have similar cancellation exponents, regardless of the dimensionality of the measure. To understand the reasons of the observed differences, cancellation exponents of vorticity are computed in low-R_m MHD turbulence, where the vortical structures grow strongly along the magnetic field direction. It is seen that increased degree of coherency leads to weakened sign-cancellation, and thus a smaller cancellation exponent. As a result, the results give the conclusion that the elongated vortical structures in isotropic turbulence, such as enstrophy filaments, are likely the cause of smaller cancellation exponents measured in 1D. It is also suggested that in general measures of higher dimensions should be used to characterize the sign oscillation property more accurately.

7.1.3 Turbulence structure subject to a magnetic field

In low-R_m MHD turbulence the velocity field is modified by the magnetic field via the Lorentz force, which introduces anisotropy at all scales. Diagonal elements of the Reynolds stress tensor initially have a larger component parallel to the magnetic field, but at later times the two perpen-

dicular components become larger. The small scales become anisotropic although velocity gradient statistics follow constraints based on a state of local axisymmetry. In the direction of the magnetic field velocity gradients become much weaker while the vorticity component is dominant. Both large and small scales display trends towards quasi two-dimensionality, while the spectral space axisymmetric spectra also become become highly anisotropic. The effects of a stronger magnetic field include faster growth of length scales in the direction of the magnetic field, accelerated development of local axisymmetry for statistics of the velocity gradients, and increased dominance of Joule dissipation in the spectral dynamics. A highlight of the work is the use of elongated domains, which provides new information at later times where results on cubic domains could be overwhelmed by numerical confinement effects (Zhai and Yeung, 2018).

7.1.4 Relaxation of strained MHD turbulence

The results show that the relaxation of strained turbulence (Clay and Yeung, 2016) is modified by a magnetic field, and the relative orientation of the magnetic field with respect to the extensive strain direction makes a difference. When the magnetic field is in the direction of extensive strain, the axis of axisymmetry remains the same and both the large and the small scales display a state of axisymmetry. Nevertheless, there is a trend of return to isotropy at intermediate times at all scales. The late-time behaviors of both the large and small scales resemble those in MHD turbulence from isotropic initial conditions. In comparison, when the magnetic field is in the compressive strain direction, axisymmetry breaks down initially although at later times a new state of axisymmetry develops about the direction of the magnetic field. Regardless of turbulence conditions prior to the activation of the magnetic field, rapid growth of the integral length scales along the magnetic field, accompanied by a state of local axisymmetry about the same direction in the small scales, is consistently observed.

7.1.5 Passive scalar mixing in MHD turbulence

Scalar mixing in MHD turbulence occurs at low Schmidt numbers where molecular diffusion is strong. In the absence of a mean scalar gradient, scalar field initialized corresponding to a "double-delta" PDF shape, relaxes quickly to a Gaussian distribution as mixing occurs. The magnetic field is seen to slow down scalar mixing, leading to a departure from local isotropy in the small scales of the

scalar field. When a mean scalar gradient is maintained parallel to the magnetic field, its coupling with the scalar flux acts as a source term in the equations of scalar variance evolution. As a result, scalar variance develops from a zero initial condition , but a magnetic field slows down the growth of scalar variance at later times. The same deviation from local isotropy as that in the absence of a mean scalar gradient is seen, where in the direction of the magnetic field scalar gradients decrease strongly. The results also show a magnetic field has an influence on the alignment of the fluctuating scalar gradients and the eigenvectors representing the principal strain rates.

7.2 Future work

There are several interesting directions of future work suggested by the numerical observations in this thesis. These aspects are given below, with discussions of numerical approach and scientific significance.

In Yeung, Zhai, and Sreenivasan (2015) the extreme events are found to display a "chunky" structure and evolve on a short time scale of a few Kolmogorov length scales. Since the "chunky" structures are now deemed spurious, previous conclusions on the temporal evolution of the extreme events require a re-assessment. One approach of the re-assessment is as follows: subcubes can be formed during the simulation (as opposed to post-processing as currently done), and a group of subcubes enclosing the extreme events can be written out from time to time. If the time interval between adjacent batches of saved subcubes is small, direct visualization of the collection subcubes can provide a movie of the evolution of the extreme events, where one can readily study how the extreme events and their topological features evolve in time. The choice of only saving a group of subcubes during the simulation avoids excessive I/O burden and alleviates data storage issues, which allows more frequent output of the subcubes. However, the overhead associated with forming subcubes, when accumulated over thousands of time steps, can be quite significant.

For decaying low magnetic Reynolds number MHD turbulence, the small scale resolution continues to improve as the turbulence decays. In fact at later times the energy of Fourier modes at high wavenumbers can drop down to nearly round-off levels, which results in inefficient use of computing resources. One possible solution, which involves some development work, is to remove the high wavenumber Fourier modes gradually and use a smaller grid accordingly as the simulation

progresses. For example, the simulation may start on a grid with 16384×2048^2 points, but decrease to a smaller grid of 8192×1024^2 points or less at late time. Since the simulations would then use less and less resources at later times, this solution may allow the use of a much larger grid during the pre-simulation, which can give a higher Reynolds number. Currently the highest Reynolds number at the time of the application of the magnetic field is about 160, which barely gives a limited inertial range (Yeung and Zhou, 1998). It would be important to know whether a tendency towards local isotropy remains if the flow is initially in a more turbulent state.

Another topic that require extensive code development is the general MHD turbulence, where the magnetic Reynolds number is no longer small, such as in the astrophysics community. As a result it is necessary to simultaneously simulate the magnetic field and solve additional equations for the fluctuating magnetic field. In such a scenario where the velocity and magnetic fields act on each other, anisotropy is expected to develop in the magnetic field in addition to the velocity field. Moreover, since fluctuations of the magnetic field give rise to the magnetic energy, the interplay between the kinetic and magnetic energies is interesting. Furthermore, the anisotropy development in both the velocity and the magnetic field may depend on the magnitude of the magnetic Reynolds number as well.

Studies in strained MHD turbulence can also be further expanded. Currently the magnetic field is applied after axisymmetric contraction, and therefore effects of strain and MHD take place separately. It is interesting to consider the combined effects when the two mechanisms capable of inducing anisotropy are applied concurrently. In particular, since MHD effects may lead to a reversal of anisotropy in the Reynolds stress tensor counter to the effects of axisymmetric contraction, the post-contraction state under MHD may well depend on the relative strengths of these two competing effects.

As already noted, the study of scalar mixing in MHD turbulence is preliminary. A natural extension is to consider how a magnetic field perpendicular to the direction of the mean scalar gradient affects scalar mixing. Since the scalar integral length scales grow preferentially in the directions of the magnetic field and the mean scalar gradient, the domain sizes may need to be elongated in both directions to allow the large scales to develop naturally. Even for configurations presented in this thesis, more detailed analyses can be performed. For example, the spectral transfers are responsible for breaking large scale non-uniformities into smaller fragments for efficient scalar mixing to

occur. The rates of spectral transfer in different directions, with or without a mean scalar gradient, may differ. Furthermore, the topology of large scalar gradients that contribute to extreme events in scalar dissipation can be studied. To this end, the techniques developed in forming the subcubes for dissipation and enstrophy can be easily extended to scalar dissipation, and the relationship among regions of extreme dissipation, enstrophy and scalar dissipation is of interest.

Appendices

APPENDIX A

EXTREME EVENTS IN COMPUTATIONAL TURBULENCE

P. K. Yeung, X. M. Zhai and K. R. Sreenivasan (2015) *Proceedings of the National Academy of Sciences of the United States of America* 112, pp. 12633-12638

Abstract

We have performed direct numerical simulations of homogeneous and isotropic turbulence in a periodic box with 8192^3 grid points. These are the largest simulations performed to-date aimed at improving our understanding of turbulence small-scale structure. We present some basic statistical results and focus on "extreme" events (whose magnitudes are several tens of thousands the mean value). The structure of these extreme events is quite different from that of moderately large events (of the order of ten times the mean value). In particular, vorticity occurs primarily in the form of tubes for moderately large events whereas they are much more "chunky" for extreme events (though probably overlaid on the traditional vortex tubes). We track the temporal evolution of extreme events and find that they are generally short-lived. Extreme magnitudes of energy dissipation rate and enstrophy occur simultaneously in space and remain so during their evolution.

APPENDIX B

CANCELLATION EXPONENTS IN ISOTROPIC TURBULENCE AND MAGNETOHYDRODYNAMIC TURBULENCE

X. M. Zhai, K. R. Sreenivasan and P. K. Yeung (2018) *Physical Review E* (submitted)

Abstract

Small scale characteristics of turbulence such as velocity gradients and vorticity fluctuate rapidly in magnitude and oscillate in sign. Much work exists on the characterization of magnitude variations, but far less on sign oscillations. While averages performed on large scales tend to zero because of the oscillatory character, those performed on increasingly smaller scales will vary with the averaging scale in some characteristic way. This characteristic variation at high Reynolds numbers is captured by the so-called cancellation exponent, which measures how local averages tend to cancel out as the averaging scale increases, in space or time. Past experimental work suggests that the exponents in turbulence depend on whether one considers quantities in full three-dimensional space or uses their one- or two-dimensional cuts. We compute cancellation exponents of vorticity and longitudinal as well as transverse velocity gradients in isotropic turbulence at Taylor-scale Reynolds number up to 1300 on 8192^3 grids. The 2D cuts yield the same exponents as those for full 3D, while the 1D cuts yield smaller numbers, suggesting that the results in higher dimensions are more reliable. We make the case that the presence of vortical filaments in isotropic turbulence leads to this conclusion. This effect is particularly conspicuous in magnetohydrodynamic turbulence, where an increased degree of spatial coherence develops along the imposed magnetic field.

APPENDIX C

THE EVOLUTION OF ANISOTROPY IN DIRECT NUMERICAL SIMULATIONS OF MHD TURBULENCE IN A STRONG MAGNETIC FIELD ON ELONGATED PERIODIC DOMAINS

X. M. Zhai and P. K. Yeung (2018) *Physical Review Fluids* 3, pp. 084602

Abstract

The response of initially isotropic turbulence to a strong magnetic field in the low magnetic Reynolds number regime has been studied using direct numerical simulations on elongated solution domains that are necessary for reliable results at long evolution times. Most results are obtained using a 16384×2048^2 periodic domain of aspect ratio 8, without numerical forcing, after a pre-simulation that creates the desired initial conditions before the magnetic field is applied. At early times, velocity fluctuations parallel to the magnetic field becomes dominant as a result of Joule dissipation being weaker in this direction. However, this anisotropy is reversed after several large-eddy time scales. Statistics of the velocity gradients indicate a strong trend towards local axisymmetry and quasi-two-dimensionality, with reduced intermittency. Scale-dependent anisotropy is studied in spectral space in terms of a wavenumber (k_1) along the magnetic field and a radial wavenumber (k_r) in the orthogonal plane. Axisymmetric spectra show that the Joule dissipation plays a dominant role in causing kinetic energy to be concentrated in a narrow spectral region at very low values of k_1, which would not be captured if the domain were cubic. Simulations spanning over two orders of magnitude variation in the magnetic interaction parameter (N) show that Reynolds stress anisotropy scales with the Joule time only for a short initial period. At large N, accelerated development of anisotropy leads to an even greater need for elongated domains which have not been employed frequently in the literature. Overall the results in this work provide both a confirmation of trends seen in simulations on cubic domains at earlier times and new observations at later times where the benefits of an elongated domain are clearly evident. A clear parameterization of Reynolds number effects still awaits larger simulations at inevitably higher cost.

APPENDIX D

EXTREME EVENTS AND SMALL-SCALE STRUCTURE IN COMPUTATIONAL TURBULENCE

X. M. Zhai, P. K. Yeung and K. R. Sreenivasan (Nov. 2015) *68^{th} Annual Meeting of the Division of Fluid Dynamics of The American Physical Society*, Boston, MA.

Abstract

Detailed analyses have been made of data from a direct numerical simulation of turbulence on a periodic domain with 8192^3 grid points designed to improve our understanding of small-scale structure and intermittency. At the Reynolds number of this simulation (1300 based on the Taylor scale) extreme events of dissipation and enstrophy as large as 10^5 times the mean value are observed. These events are shown to possess a form that is different from similar events at low Reynolds numbers. Extreme vorticity appears to be "chunky" in character, in contrast to elongated vortex tubes at moderately large amplitudes commonly reported in the literature. We track the temporal evolution of these extreme events and find that they are generally short-lived, which suggests frequent sampling on-the-fly is useful. Extreme magnitudes of energy dissipation rate and enstrophy are essentially coincident in space and remain so during their evolution. Numerical tests show sensitivity to small-scale resolution and sampling but not machine precision. The connections expected between indicators of fine-scale intermittency such as acceleration statistics and the anomalous scaling of high-order velocity structure functions are also investigated.

APPENDIX E

THE STRUCTURE OF MHD TURBULENCE UNDER AN EXTERNAL MAGNETIC FIELD: RESULTS FROM SIMULATIONS ON ELONGATED DOMAINS

X. M. Zhai and P. K. Yeung (Nov. 2016) *69^{th} Annual Meeting of the Division of Fluid Dynamics of The American Physical Society*, Portland, OR.

Abstract

Turbulence in an electrically conducting fluid in the limit of low magnetic Reynolds number is, because of the Lorentz force due to an external magnetic field, very different from classical turbulence at both the large scales and the small scales. The importance of minimizing finite domain-size effects on the large scale development has often tended to limit the Reynolds number reached in the past. In this work we use periodic domains stretched along the magnetic field with aspect ratio up to 8 and beyond. The initial state is obtained from decaying isotropic turbulence with large-eddy length scales of order 1% of the length of the domain. After a transient period the kinetic energy undergoes a power law decay while the integral length scales in the direction parallel to the magnetic field show preferential growth. At early times the parallel velocity component becomes stronger than the other two but this anisotropy is subsequently reversed under the combined effects of anisotropic Joule and viscous dissipation. The small scales show characteristics of quasi two-dimensional behavior in the transverse plane. Results over a range of magnetic interaction parameters and Reynolds numbers are compared with known theoretical predictions.

APPENDIX F

EFFECTS OF A STRONG MAGNETIC FIELD ON TURBULENCE SUBJECTED TO AXISYMMETRIC CONTRACTION.

X. M. Zhai, M. P. Clay and P. K. Yeung (Nov. 2017) *70^{th} Annual Meeting of the Division of Fluid Dynamics of The American Physical Society*, Denver, CO.

Abstract

Many engineering applications and laboratory experiments involve the flow of fluids subjected to axisymmetric mean strain associated with the effects of varying cross-sectional area. If the fluid is conducting and a magnetic field is present then the Lorentz force leads to further complexities. In this work we apply a uniform magnetic field to homogeneous turbulence after a time-dependent axisymmetric contraction (Clay & Yeung, *J. Fluid Mech.* **805**, 460-493 (2016)) designed to mimic experiments. A magnetic field along the extensional direction is observed to initially weaken the anisotropy that developed from the contraction, but at later times the flow shows a high degree of anisotropy resembling that seen in simulations with isotropic initial conditions. The small scales no longer return to isotropy although they remain statistically axisymmetric. The anisotropy development is analyzed by computing various terms (including the Joule dissipation tensor) in the Reynolds stress budget equation, and studying energy transfer in wavenumber space. We also compare results at different Reynolds numbers and magnetic interaction parameters.

APPENDIX G

CANCELLATION EXPONENT IN ISOTROPIC TURBULENCE AND MHD TURBULENCE

X. M. Zhai, P. K. Yeung and K. R. Sreenivasan (Nov. 2018) *71^{th} Annual Meeting of the Division of Fluid Dynamics of The American Physical Society*, Atlanta, GA.

Abstract

Small scale motions in fluid turbulence, such as velocity gradients and vorticity, have fluctuations of positive and negative signs. A form of singularity arises over a range of scales if sign oscillations occur no matter how small the scale size becomes. Known as sign-singularity, The so-called cancellation exponent gives a measures the efficiency of cancellations of opposite signs over some spatial regions which may be one, two, or three-dimensional in nature. Past experimental work suggests the exponents depend on the dimensionality considered. We compute cancellation exponents of vorticity, longitudinal and transverse velocity gradients in isotropic turbulence up to R_λ 1300 on 8192^2 grids. It appears that 2D and 3D measurements give similar values of cancellation exponent, while 1D measure is smaller for transverse velocity gradients and vorticity. We show that increased degree of spatial coherency, for example in elongated vortex structures along the magnetic field in MHD turbulence, results in substantially smaller cancellation exponents in one dimension. Likewise, presence of vortical filaments in isotropic turbulence leads to smaller cancellation exponents. Our results suggest that cancellation exponents should be measured in higher dimensions to avoid bias by coherent structures.

BIBLIOGRAPHY

Alberts-Chico, X., D. G. E. Grigoriadis, E. V. Votyakov, and S. Kassinos (2013). "Direct numerical simulation of turbulent liquid metal flow entering a magnetic field". *Fusion Engr. & Design* 88, 3108–3124.

Alemany, A, R Moreau, P. Sulem, and U Frisch (1979). "Influence of an external magnetic field on homogeneous MHD turbulence". *J. de Mecanique* 28, 2777313.

Ashurst, W. T., A. R. Kerstein, R. M. Kerr, and C. H. Gibson (1987). "Alignment of vorticity and scalar gradient with strain rate in simulated Navier-Stokes turbulence". *Phys. Fluids* 30, 2343–2353.

Ayyalasomayajula, S. and Z. Warhaft (2006). "Nonlinear interactions in strained axisymmetric high-Reynolds-number turbulence". *J. Fluid Mech.* 56, 273–307.

Bandaru, V., T. Boeck, D. Krasnov, and J. Schumacher (2016). "A hybrid finite difference–boundary element procedure for the simulation of turbulent MHD duct flow at finite magnetic Reynolds number". *J. Comput. Phys.* 304, 320–339.

Batchelor, G. K. (1946). "The Theory of Axisymmetric Turbulence". *Proc. Roy. Soc. Lond. A* 186, 480–502.

Bertozzi, A. L. and A. B. Chhabra (1994). "Cancellation exponents and fractal scaling". *Phys. Rev. E* 49.5, 4716.

Biskamp, D. (2003). *Magnetohydrodynamic Turbulence*. Cambridge University Press.

Boffetta, G. and R. E. Ecke (2012). "Two-dimensional turbulence". *Annu. Rev. Fluid Mech.* 44, 427–451.

Buaria, D. (2016). "Lagrangian investigations of turbulent dispersion and mixing using Petascale computing". PhD thesis. School of Aerospace Engineering, Georgia Institute of Technology.

Burattini, P., O. Zikanov, and B. Knaepen (2010). "Decay of magnetohydrodynamic turbulence at low magnetic Reynolds number". *J. Fluid Mech.* 657, 502–538.

Burattini, P., M. Kinet, D. Carati, and B. Knaepen (2008). "Anisotropy of velocity spectra in quasistatic magnetohydrodynamic turbulence". *Phys. Fluids* 20.6, 065110.

Canuto, C, M. Hussaini, A. Quarteroni, and T. Zang (1988). *Spectral Methods in Fluid Dynamics*. Springer-Verlag.

Caperan, P. and A. Alemany (1985). "Homogeneous low-magnetic-Reynolds-number MHD turbulence-Study of the transition to the quasi-two-dimensional phase and characterization of its anisotropy". *Journal de Mecanique Theorique et Appliquee* 4, 175–200.

Carbone, V, S Perri, E. Yordanova, P Veltri, R Bruno, Y. Khotyaintsev, and M. André (2010). "Sign-singularity of the reduced magnetic helicity in the solar wind plasma". *Phys. Rev. Lett.* 104, 181101.

Carbone, V. and R. Bruno (1997). "Sign singularity of the magnetic helicity from in situ solar wind observations". *Astrophys. J.* 488.1, 482.

Castillo, L., J. Dabiri, J. Naughton, and C. Meneveau (2013). "Foreword: a special issue on turbulence and wind energy". *J. Turb.* 14.4, 53–54.

Clay, J. P. (1973). "Turbulent mixing of temperature in water, air and mercury". PhD thesis. University of California at San Diego.

Clay, M. P. and P. K. Yeung (2016). "A numerical study of turbulence under temporally evolving axisymmetric contraction and subsequent relaxation". *J. Fluid Mech.* 805, 460–493.

Clay, M. P. (2017). "Strained Turbulence and Low-Diffusivity Turbulent Mixing Using High Performance Computing". PhD thesis. Georgia Institute of Technology.

Consolini, G. and A. T. Lui (1999). "Sign-singularity analysis of current disruption". *Geophys. Res. Lett.* 26.12, 1673–1676.

Cooley, J. W. and J. W. Tukey (1965). "An algorithm for the machine calculation of complex Fourier series". *Math. Comp.* 19, 297–301.

Corrsin, S. (1951). "On the spectrum of isotropic temperature fluctuations in an isotropic turbulence". *J. Appl. Phys.* 22, 469–473.

Davidson, P. A. (1997). "The role of angular momentum in the magnetic damping of turbulence". *J. Fluid Mech.* 336, 123–150.

Davidson, P. A. (2001). *An Introduction to Magnetohydrodynamics*. Cambridge University Press.

Davidson, P. A. (2013). *Turbulence in Rotating, Stratified and Electrically Conducting Fluids*. Cambridge University Press.

De Michelis, P, G Consolini, and A Meloni (1998). "Sign singularity in the secular acceleration of the geomagnetic field". *Phys. Rev. Lett.* 81.22, 5023.

Donzis, D. A. and K. R. Sreenivasan (2010). "The bottleneck effect and the Kolmogorov constant in isotropic turbulence". *J. Fluid Mech.* 657, 171–188.

Donzis, D. A. and P. K. Yeung (2010). "Resolution effects and scaling in numerical simulations of passive scalar mixing in turbulence". *Physica D* 239, 1278–1287.

Donzis, D. A., P. K. Yeung, and D. Pekurovsky (2008). "Turbulence simulations on $O(10^4)$ processors". In: *Proc. TeraGrid '08 Conf* (Las Vegas, NV).

Donzis, D. A., P. K. Yeung, and K. R. Sreenivasan (2008). "Dissipation and enstrophy in isotropic turbulence: scaling and resolution effects in direct numerical simulations". *Phys. Fluids* 20, 045108.

Du, Y., T. Tél, and E. Ott (1994). "Characterization of sign singular measures". *Physica D* 76.1-3, 168–180.

Eswaran, V. and S. B. Pope (1988a). "An examination of forcing in direct numerical simulations of turbulence". *Comput. Fluids* 16, 257–278.

Eswaran, V. and S. B. Pope (1988b). "Direct numerical simulation of the turbulent mixing of a passive scalar". *Phys. Fluids* 31, 506–520.

Favier, B., F. S. Godeferd, C. Cambon, A. Delache, and W. J. T. Bos (2011). "Quasi-static magnetohydrodynamic turbulence at high Reynolds number". *J. Fluid Mech.* 681, 434–461.

Favier, B., F. S. Godeferd, C. Cambon, and A. Delache (2010). "On the two-dimensionalization of quasistatic magnetohydrodynamic turbulence". *Phys. Fluids* 22.7, 075104.

Frisch, U. (1995). *Turbulence: the legacy of A. N. Kolmogorov*. Cambridge University Press.

Gallet, B. and C. R. Doering (2015). "Exact two-dimensionalization of low-magnetic-Reynolds-number flows subject to a strong magnetic field". *J. Fluid Mech.* 773, 154–177.

George, W. K. and H. J. Hussein (1991). "Locally axisymmetric turbulence". *J. Fluid Mech.* 233, 1–23.

Gotoh, T. and P. K. Yeung (2013). "Passive scalar transport in turbulence: A computational perpsective". In: *Ten Chapters in Turbulence*. Ed. by P. A. Davidson, Y. Kaneda, and K. R. Sreenivasan. Cambridge University Press.

Gotoh, T., Y. Watanabe, Y. Shiga, T. Nakano, and E. Suzuki (2007). "Statistical properties of four-dimensional turbulence". *Phys. Rev. E* 75.1, 016310.

Graham, J. P., P. D. Mininni, and A. Pouquet (2005). "Cancellation exponent and multifractal structure in two-dimensional magnetohydrodynamics: direct numerical simulations and Lagrangian averaged modeling". *Phys. Rev. E* 72.4, 045301.

Hentschel, H. and I. Procaccia (1983). "The infinite number of generalized dimensions of fractals and strange attractors". *Physica D* 8.3, 435–444.

Horne, E and P. D. Mininni (2013). "Sign cancellation and scaling in the vertical component of velocity and vorticity in rotating turbulence". *Phys. Rev. E* 88.1, 013011.

Imazio, P. R. and P. D. Mininni (2010). “Cancellation exponents in helical and non-helical flows”. *J. Fluid Mech.* 651, 241–250.

Ishida, T. and Y. Kaneda (2007). “Small-scale anisotropy in magnetohydrodynamic turbulence under a strong uniform magnetic field”. *Phys. Fluids* 19, 075104.

Ishihara, T., T. Gotoh, and Y. Kaneda (2009). “Study of high-Reynolds number isotropic turbulence by direct numerical simulation”. *Annu. Rev. Fluid Mech.* 41, 165–180.

Ishihara, T., K. Morishita, M. Yokokawa, A. Uno, and Y. Kaneda (2016). “Energy spectrum in high-resolution direct numerical simulations of turbulence”. *Phys. Rev. Fluids* 1 (8), 082403.

Iyer, K. P. (2014). “Studies of turbulence structure and turbulent mixing using Petascale computing”. PhD thesis. Georgia Institute of Technology.

Iyer, K. P., K. R. Sreenivasan, and P. K. Yeung (2017). “Reynolds number scaling of velocity increments in isotropic turbulence”. *Phys. Rev. E* 95.2, 021101.

Jimenez, J. (2003). “Computing high-Reynolds-number turbulence: will simulations ever replace experiments?” *J. Turb.* 4, 022.

Jimenez, J. and A. A. Wray (1998). “On the characteristics of vortex filaments in isotropic turbulence”. *J. Fluid Mech.* 373, 255–285.

Kaneda, Y, T Ishihara, M Yokokawa, K Itakura, and A Uno (2003). “Energy dissipation rate and energy spectrum in high resolution direct numerical simulations of turbulence in a periodic box”. *Phys. Fluids* 15, L21–L24.

Kassinos, S. C., B. Knaepen, and D. Carati (2007). “The transport of a passive scalar in magnetohydrodynamic turbulence subjected to mean shear and rotation”. *Phys. Fluids* 19, 015105.

Kawahara, G. (2005). “Energy dissipation in spiral vortex layers wrapped around a straight vortex tube”. *Phys. Fluids* 17.5, 055111.

Kerr, R. M. (1985). “Higher-order derivative correlations and the alignment of small-scale structures in isotropic numerical turbulence”. *J. Fluid Mech.* 153.APR, 31–58.

Kinet, M., P. Burattini, D. Carati, and B. Knaepen (2008). “Decay of passive scalar fluctuations in magnetohydrodynamic turbulence”. *Phys. Fluids* 20, 075105.

Knaepen, B. and R. Moreau (2008). “Magnetohydrodynamic turbulence at low magnetic Reynolds number”. *Annu. Rev. Fluid Mech.* 40, 23–45.

Kobayashi, H. (2006). “Large eddy simulation of magnetohydrodynamic turbulent channel flows with local subgrid-scale model based on coherent structures”. *Phys. Fluids* 18.4, 045107.

Kolmogorov, A. N. (1941). “The local structure of turbulence in an incompressible fluid with very large Reynolds numbers”. Dokl. Akad. Nauk SSSR 30, 301–305.

Kolmogorov, A. N. (1962). “A refinement of previous hypotheses concerning the local structure of turbulence in a viscous incompressible fluid at high Reynolds number”. *J. Fluid Mech.* 13, 82–85.

Lumley, J. L. and G. R. Newman (1977). “The return to isotropy of homogeneous turbulence”. *J. Fluid Mech.* 82, 161–178.

Mandelbrot, B. B. (1974). “Intermittent turbulence in self-similar cascades: divergence of high moments and dimension of the carrier”. *J. Fluid Mech.* 62.2, 331–358.

Martin, L., G De Vita, L Sorriso-Valvo, P Dmitruk, G Nigro, L Primavera, and V Carbone (2013). “Cancellation properties in Hall magnetohydrodynamics with a strong guide magnetic field”. *Phys. Rev. E* 88.6, 063107.

Mininni, P. D., D. Rosenberg, and A. Pouquet (2012). “Isotropization at small scales of rotating helically driven turbulence”. *J. Fluid Mech.* 699, 263–279.

Moffatt, H. K. (1967). “On the suppression of turbulence by a uniform magnetic field”. *J. Fluid Mech.* 28.03, 571–592.

Moin, P and K Mahesh (1998). “Direct numerical simulation: A tool in turbulence research”. *Annu. Rev. Fluid Mech.* 30, 539–578.

Monin, A. S. and A. M. Yaglom (1975). *Statistical Fluid Mechanics*. Vol. 1. MIT Press.

Montgomery, D. and L. Turner (1982). “Two-and-a-half-dimensional magnetohydrodynamic turbulence”. *Phys. Fluids* 25.2, 345–349.

Nelkin, M. (1999). “Enstrophy and dissipation must have the same scaling exponents in the high Reynolds number limit of fluid turbulence”. *Phys. Fluids* 11, 2202–2204.

Obukhov, A. M. (1949). “The structure of the temperature field in a turbulent flow”. *Dokl. Akad. Nauk. SSSR* 39, 391.

Oefelein, J., J. H. Chen, and R Sankaran (2009). “High-fidelity simulations for clean and efficient combustion of alternative fuels”. In: *J. Phys. Conf. Ser.* Vol. 180, 012033.

Okamoto, N., P. A. Davidson, and Y. Kaneda (2010). “On the decay of low-magnetic-Reynolds-number in an imposed magnetic field”. *J. Fluid Mech.* 651, 295–318.

Okamoto, N., K. Y. amd K. Schneider, and M. Farge (2014). “Small-scale anisotropic intermittency in magnetohydrodynamic turbulence at low magnetic Reynolds numbers”. *Phys. Rev. E* 89, 033013.

Ott, E., Y. Du, K. R. Sreenivasan, A Juneja, and A. K. Suri (1992). “Sign-singular measures: Fast magnetic dynamos, and high-Reynolds-number fluid turbulence”. *Phys. Rev. Lett.* 69.18, 2654.

Pope, S. B. (2000). *Turbulent Flows*. Cambridge University Press.

Pothérat, A. and K. Kornet (2015). "The decay of wall-bounded MHD turbulence at low R_m". *J. Fluid Mech.* 783, 605–636.

Reddy, K. S., R. Kumar, and M. K. Verma (2014). "Anisotropic energy transfers in quasi-static magnetohydrodynamic turbulence". *Phys. Plasmas* 21.10, 102310.

Reddy, K. S. and M. K. Verma (2014). "Strong anisotropy in quasi-static magnetohydrodynamic turbulence for high interaction parameters". *Phys. Fluids* 26.2, 025109.

Richardson, L. F. (1926). "Atmospheric diffusion shown on a distance neighbor graph". *Proc. Roy. Soc. London, Ser. A* 110, 709–737.

Rogallo, R. S. (1981). "Numerical experiments in homogeneous turbulence. *NASA Tech. Memo. 81315*, NASA Ames Research Center".

Rothschild, B. and T. Osborn (1988). "Small-scale turbulence and plankton contact rates". *J. Plankton Res.* 10.3, 465–474.

Schumann, U. (1976). "Numerical simulation of the transition from three-to two-dimensional turbulence under a uniform magnetic field". *J. Fluid Mech.* 74.01, 31–58.

Shaw, R. A. (2003). "Particle-turbulence interactions in atmospheric clouds". *Annu. Rev. Fluid Mech.* 35, 183–227.

She, Z.-S., E. Jackson, and S. A. Orszag (1990). "Intermittant Vortex Structures in Homogeneous Isotropic Turbulence". *Nature* 344.6263, 226.

Siggia, E. D. (1981). "Numerical study of small-scale intermittency in three-dimensional turbulence". *J. Fluid Mech.* 107, 375–406.

Smith, L. M. and V. Yakhot (1994). "Finite-size effects in forced two-dimensional turbulence". *J. Fluid Mech.* 274, 115–138.

Sommeria, J. and R. Moreau (1982). "Why, how, and when, MHD turbulence becomes two-dimensional". *J. Fluid Mech.* 118, 507–518.

Sorriso-Valvo, L, V Carbone, A Noullez, H Politano, A Pouquet, and P Veltri (2002). "Analysis of cancellation in two-dimensional magnetohydrodynamic turbulence". *Phys. Plasmas* 9.1, 89–95.

Sorriso-Valvo, L., G. De Vita, M. D. Kazachenko, S. Krucker, L. Primavera, S. Servidio, A. Vecchio, B. T. Welsch, G. H. Fisher, F. Lepreti, et al. (2015). "Sign singularity and flares in solar active region NOAA 11158". *Astrophys. J.* 801.1, 36.

Sreenivasan, K. R. (1991). "Fractals and multifractals in fluid turbulence". *Annu. Rev. Fluid Mech.* 23, 539–600.

Sreenivasan, K. R. and R. A. Antonia (1997). "The phenomenology of small-scale turbulence". *Annu. Rev. Fluid Mech.* 29.1, 435–472.

Sreenivasan, K. R., A Juneja, and A. K. Suri (1995). "Scaling properties of circulation in moderate-Reynolds-number turbulent wakes". *Phys. Rev. Lett.* 75.3, 433.

Sreenivasan, K. R. and P. Kailasnatth (1993). "An update on the intermittency exponent in turbulence". *Phys. Fluids A* 5, 2766–2769.

Teaca, B., M. K. Verma, B. Knaepen, and D. Carati (2009). "Energy transfers in anisotropic magnetohydrodynamic turbulence". *Phys. Rev. E* 79, 046312.

Tennekes, H. and J. L. Lumley (1972). *A First Course in Turbulence*. MIT Press.

Vainshtein, S. I., Y. Du, and K. R. Sreenivasan (1994). "Sign-singular measure and its association with turbulent scalings". *Phys. Rev. E* 49.4, R2521.

Vainshtein, S. I., K. R. Sreenivasan, R. T. Pierrehumbert, V. Kashyap, and A. Juneja (1994). "Scaling exponents for turbulence and other random processes and their relationships with multifractal structure". *Phys. Rev. E* 50.3, 1823.

Vedula, P., P. K. Yeung, and R. O. Fox (2001). "Dynamics of scalar dissipation in isotropic turbulence: a numerical and modeling study". *J. Fluid Mech.* 433, 29–60.

Verma, M. K. (2017). "Anisotropy in Quasi-Static Magnetohydrodynamic Turbulence". *Rep. Prog. Phys* 80.087001, 087001.

Vincent, A and M Meneguzzi (1991). "The satial structure and statistical properties of homogeneous turbulence". *J. Fluid Mech.* 225, 1–20.

Vorobev, A., O. Zikanov, P. A. Davidson, and B. Knaepen (2005). "Anisotropy of magnetohydrodynamic turbulence at low magnetic Reynolds number". *Phys. Fluids* 17, 125105.

Warhaft, Z (2000). "Passive scalars in turbulent flows". *Annu. Rev. Fluid Mech.* 32, 203–240.

Yakhot, V. and K. R. Sreenivasan (2005). "Anomalous scaling of structure functions and dynamic constraints on turbulence simulations". *J. Stat. Phys.* 121, 823–841.

Yeung, P. K., D. A. Donzis, and K. R. Sreenivasan (2012). "Dissipation, enstrophy and pressure statistics in turbulence simulations at high Reynolds numbers". *J. Fluid Mech.* 700, 5–15.

Yeung, P. K., S. S. Girimaji, and S. B. Pope (1989). "Straining and scalar dissipation on material surfaces in turbulence: implications for flamelets". *Comb. & Flame* 79, 340–365.

Yeung, P. K., S. B. Pope, and B. L. Sawford (2006). "Reynolds number dependence of Lagrangian statistics in large numerical simulations of isotropic turbulence". *J. Turb.* 7, 1–12.

Yeung, P. K. and K. R. Sreenivasan (2013). "Spectrum of passive scalars of high molecular diffusivity in turbulent mixing". *J. Fluid Mech.* 716, R14.

Yeung, P. K. and K. R. Sreenivasan (2014). "Direct numerical simulation of turbulent mixing at very low Schmidt number with a uniform mean gradient". *Phys. Fluids* 26, 015107.

Yeung, P. K., K. R. Sreenivasan, and S. B. Pope (2018). "Effects of finite spatial and temporal resolution in direct numerical simulations of incompressible isotropic turbulence". *Phys. Rev. Fluids* 3.6, 064603.

Yeung, P. K. and J. Xu (2004). "Effect of rotation on turbulent mixing: non-premixed passive scalars". *Phys. Fluids* 16, 93–103.

Yeung, P. K., X. M. Zhai, and K. R. Sreenivasan (2015). "Extreme events in computational turbulence". *Proc. Nat. Acad. Sci.* 112(41), 12633–12638.

Yeung, P. K. and Y. Zhou (1997). "Universality of the Kolmogorov constant in numerical simulations of turbulence". *Phys. Rev. E* 56, 1746–1752.

Yeung, P. K. and Y. Zhou (1998). "Numerical study of rotating turbulence with external forcing". *Phys. Fluids* 10, 2895–2909.

Zhai, X. M. and P. K. Yeung (2018). "The evolution of anisotropy in direct numerical simulations of MHD turbulence in a strong magnetic field on elongated periodic domains". *Phys. Rev. Fluids* 3.8, 084602.

Zikanov, O. and A. Thess (1998). "Direct numerical simulation of forced MHD turbulence at low magnetic Reynolds number". *J. Fluid Mech.* 358, 299–333.

VITA

Xiaomeng 'Shine' Zhai was born in Shangcai, Henan Province of the People's Republic of China. Shine's parents were the first generation college students in their family and they studied history and English respectively. Unlike his parents who like liberal arts, Shine developed interest in Formula One racing as a teenager, and he was particularly fascinated by the power of aerodynamics. In 2008, Shine attended the Hong Kong University of Science and Technology (HKUST) in the Department of Computer Science and Engineering, but later transferred his major of study to Mechanical Engineering out of the curiosity to understand aerodynamics better. After a semester-long eye-opening exchange study in the University of Illinois at Urbana Champaign in the fall of 2010, in 2012 he completed his studies and obtained the degree of Bachelor of Engineering in Mechanical Engineering at HKUST. He then joined the Daniel Guggenheim School of Aerospace Engineering at the Georgia Institute of Technology for a doctoral study into the turbulence problem, under the supervision of Prof. P.K. Yeung. Outside of research, Shine is genuinely interested in literature and music, especially Peking Opera recently.